Contract Report W-98-1
September 1998

US Army Corps of Engineers
Waterways Experiment Station

Water Quality Research Program

Sediment Flux Model for Manganese and Iron

by Dominic DiToro, Scott Lowe,
James Fitzpatrick, Richard Isleib, HydroQual, Inc.

Approved For Public Release; Distribution Is Unlimited

Prepared for Headquarters, U.S. Army Corps of Engineers

Water Quality
Research Program

Contract Report W-98-1
September 1998

Sediment Flux Model for Manganese and Iron

by Dominic DiToro, Scott Lowe,
James Fitzpatrick, Richard Isleib

HydroQual, Inc.
One Lethbridge Plaza
Mahwah, NJ 07430

Final report

Approved for public release; distribution is unlimited

Prepared for U.S. Army Corps of Engineers
Washington, DC 20314-1000

Under Work Unit No. 32694

Monitored by U.S. Army Engineer Waterways Experiment Station
3909 Halls Ferry Road, Vicksburg, MS 39180-6199

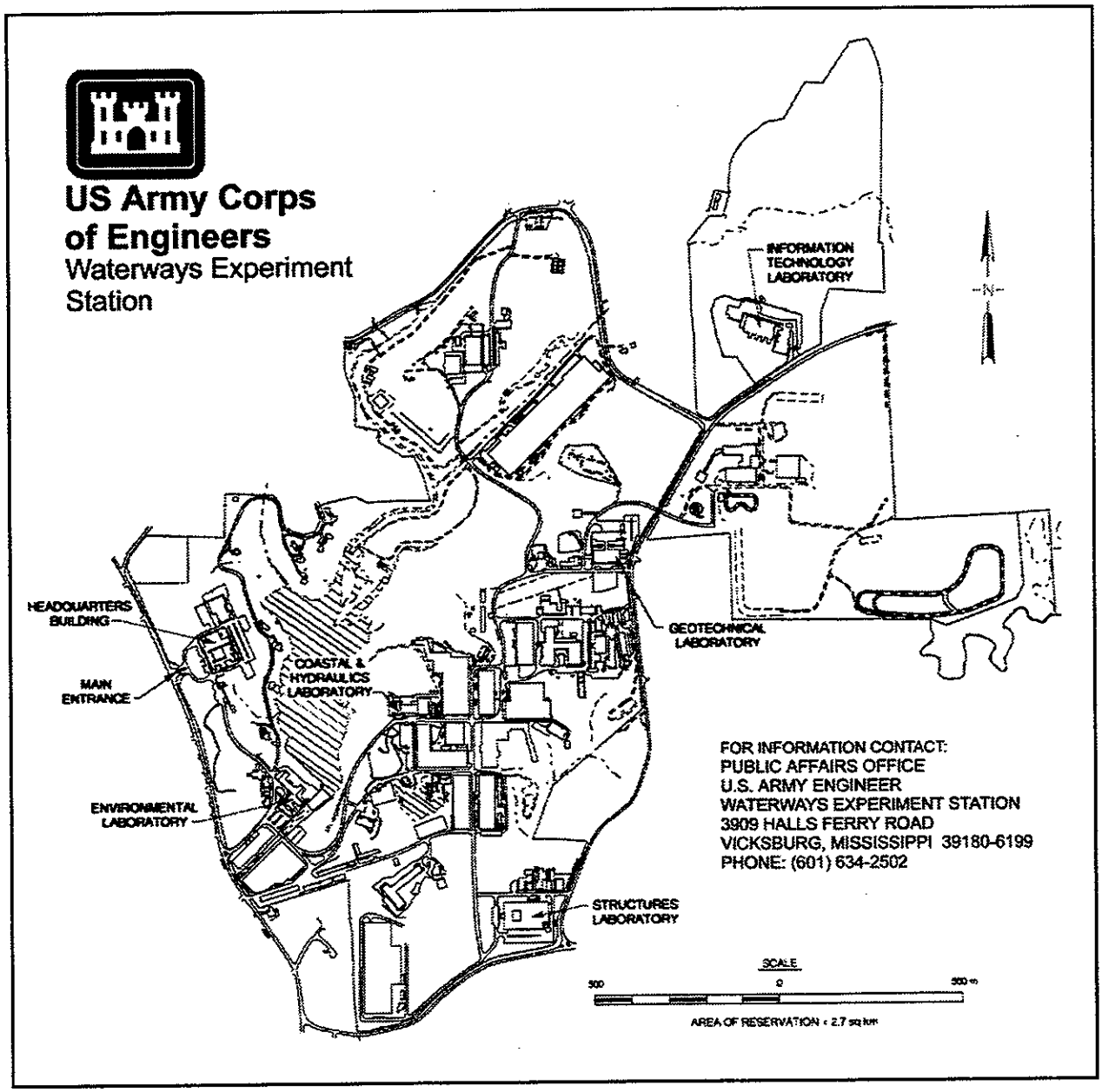

Waterways Experiment Station Cataloging-in-Publication Data

Sediment flux model for manganese and iron / by Dominic DiToro ... [et al.] ; prepared for U.S. Army Corps of Engineers ; monitored by U.S. Army Engineer Waterways Experiment Station.
172 p. : ill. ; 28 cm. -- (Contract report ; W-98-1)
Includes bibliographical references.
1. Estuarine sediments -- Mathematical models. 2. Marine sediments -- Mathematical models. 3. Lake sediments -- Mathematical models. 4. Soils -- Manganese content. 5. Soils -- Iron content. I. Di Toro, Dominic M. II. United States. Army. Corps of Engineers. III. U.S. Army Engineer Waterways Experiment Station. IV. Water Quality Research Program (U.S.) V. Series: Contract report (U.S. Army Engineer Waterways Experiment Station) ; W-98-1.
TA7 W34c no.W-98-1

Contents

Preface v

1—Executive Summary 1

2—Chemistry of Manganese and Iron 3

2.1 Manganese 3
2.2 Iron 6

3—Steady State Partitioning Model 9

3.1 Introduction 9
3.2 Manganese Flux Data 19
3.3 Conclusions 25

4—Solubility Control of Particulate Manganese 27

4.1 Introduction 27
4.2 Calcium Carbonate 27
4.3 Chemistry and Simplifications 28
4.4 Closed System 30
4.5 Sediment Model Equations and Solutions 33
4.6 Application to Long Island Sound 36
4.7 Manganese - Calcium - Alkalinity Flux Model 39
4.8 Chemistry and Simplifications 39
4.9 Sediment Model Equations and Solutions 42
Appendix: Equations and Solutions for $MnCO_3$, $CaCO_3$, Alkalinity and TIC 48

5—Time Variable Linear Partitioning Model 53

5.1 Introduction 53
5.2 Model Formulation 53
5.3 Review of MERL Data 59
5.4 Application of the Nutrient and Oxygen Flux Model 60
5.5 Manganese Model Application 62
5.6 Conclusions 65

6—Effect of pH 73

6.1 Introduction 73
6.2 pH in the Aerobic Layer 73
6.3 Effect of pH on the Manganese Flux 78
6.4 Effect of Varying Depositional Flux 81

7—Water Column and Sediment Interactions 87

7.1 Introduction 87
7.2 Model Formulation 90
7.3 Time Variable Model 98
7.4 Calibration 104

8—Application of Iron Flux Model to Onondaga Lake 119

8.1 Introduction 119
8.2 Model Configuration 123

9—Application to Croton Reservoir 151

9.1 Introduction 151
9.2 Model Setup 154
9.3 Summary 161

Bibliography 163

SF 298

Preface

The work reported herein was conducted as part of the Water Quality Research Program (WQRP), Work Unit No. 32694. The WQRP is sponsored by Headquarters, U.S. Army Corps of Engineers (HQUSACE), and is assigned to the U.S. Army Engineer Waterways Experiment Station (WES) under the purview of the Environmental Laboratory (EL). Funding was provided under Department of the Army Appropriation No. 96X3121, General Investigation. The WQRP is managed under the Environmental Resources Research and Assistance Programs (ERRAP). Dr. John Barko was Manager, ERRAP, and Mr. Robert Gunkel was Assistant Manager, ERRAP, for the WQRP. Technical Monitors during the study were Messrs. Pete Juhle and James Gottesman and Dr. John Bushman, HQUSACE.

Principal Investigator of the Work Unit was Dr. Carl F. Cerco, Water Quality and Contaminant Modeling Branch (WQCMB), Environmental Processes and Effects Division (EPED), EL.

This report was prepared by Drs. Dominic DiToro and Scott Lowe and Messrs. James Fitzpatrick and Richard Isleib of HydroQual Inc., Mahwah, NJ. Report review was provided by Drs. Barry Bunch and Patrick Deliman, WQCMB. Preparation of the report was under the general supervision of Dr. Mark Dortch, Chief, WQCMB, Dr. Richard E. Price, Chief, EPED, and Dr. John Harrison, Director, EL.

At the time of publication of this report, Dr. Robert W. Whalin was Director of WES, and COL Robin R. Cababa, EN, was WES Commander.

This report should be cited as follows:

DiToro, D., Lowe, S., Fitzpatrick, J., and Isleib, R. (1998). "Sediment Flux Model for Manganese and Iron," Contract Report W-98-1, U.S. Army Engineer Waterways Experiment Station, Vicksburg, MS.

The contents of this report are not to be used for advertising, publication, or promotional purposes. Citation of trade names does not constitute an official endorsement or approval of the use of such commercial products.

1

Executive Summary

This report presents a model of manganese and iron flux from sediments. The reaction kinetics for iron and manganese in the overlying water column are also developed. As shown below, the chemistry of iron and manganese are sufficiently similar so that a common model formulation can be used. The model is an extension of the nutrient and oxygen sediment flux model developed previously for application to Chesapeake Bay. It has subsequently been applied to freshwater lake sediments as well. Thus the model developed in this report is a comprehensive model for nutrients, oxygen and sulfide, and now iron and manganese.

The model is calibrated initially using two data sets which contained measured sediment manganese fluxes together with nutrient and oxygen fluxes. The detailed calibration used the results from an extensive three year nutrient addition experiment conducted using the MERL mesocosm experimental facility. This investigation included complete water column and sediment flux sampling. No comparable iron flux data sets could be located, presumably because aerobic sediment iron fluxes are small.

The model is calibrated initially in stand alone mode, in which the overlying water concentrations and the depositional fluxes of organic matter and particulate manganese are specified. The final stand alone calibration is made with the model coupled to an interactive water column volume, in which the kinetics of manganese oxidation are explicitly included. The interaction of the water column and sediment turns out to be a critical component in determining the magnitude and seasonal distribution of the sediment flux.

The iron and manganese sediment flux model is combined with a water column eutrophication model and applied to two lakes. Iron and manganese state variables and the appropriate reaction kinetics are added to the eutrophication model. The simulations reproduce the annual cycle of algal growth and stratification, summer anoxia and the increase of iron and manganese in the hypolimnion, and fall overturn and the return to low metals concentrations.

The sediment model required an adjustment to the anaerobic layer partition coefficient for iron, in order to match the data from the two lakes. No other iron model parameter needed changing. In contrast, the manganese model parameters were unchanged from the stand alone calibration values. This suggests that a possible extension to the model framework is to replace the empirical partition coefficient for iron with a formulation that explicitly calculates the pore water - solid phase partitioning

using a chemical model. The model already computes the iron and sulfide concentrations. The partitioning formulation would be replaced by an explicit computation of the formation of iron sulfide. An initial attempt at such a formulation is reported below for the formation of manganese carbonate.

2

Chemistry of Manganese and Iron

2.1 MANGANESE

The chemistry of manganese in surface waters and sediments has been studied for quite some time [Stumm and Morgan, 1970]. Manganese exists in two valances states: the +4 state $Mn(IV)$ in oxic waters and the +2 state $Mn(II)$ in anoxic waters. $Mn(IV)$ is very insoluble and precipitates to form manganese oxide, $MnO_2(s)$:

$$Mn(IV)^{4+} + 2H_2O \rightarrow MnO_2(s) + 4H^+ \tag{2.1}$$

which is the predominant form of manganese in oxic surface waters. It usually exists as a coating on particles [Jenne, 1968]. As the particles settle to the sediment, manganese is transported as well providing a source of manganese to the sediments.

In the oxic layer of the sediment, $MnO_2(s)$ is stable. However, particle mixing causes manganese containing particles to be transported to the anaerobic layer of the sediment where manganese oxide is thermodynamically unstable and a reduction reaction occurs. $Mn(IV)$ is reduced to $Mn(II)$. For this to occur, two electrons are required as shown by the reduction half reaction:

$$MnO_2(s) + 2e^- \rightarrow Mn(II)^{2+} - 4H^+ + 2H_2O \tag{2.2}$$

The primary source of electrons in sediments is decaying organic matter CH_2O and the oxidation half reaction is:

$$CH_2O + H_2O \rightarrow CO_2 + 4H^+ + 4e^- \tag{2.3}$$

The overall reduction reaction can be constructed by supplying the electrons required in eq.(2.2) from eq.(2.3) to form the redox reaction:

$$MnO_2(s) + \frac{1}{2}CH_2O + 2H^+ \rightarrow Mn(II)^{2+} + \frac{1}{2}CO_2 + \frac{3}{2}H_2O \tag{2.4}$$

In contrast to $Mn(IV)$, $Mn(II)$ is more soluble and exists in the mg/L range in sediment pore waters. As a consequence it can diffuse to the oxic layer of the sediment where it is subject to oxidation. The oxidation of $Mn(II)$ to $Mn(IV)$ occurs via the loss of two electrons:

$$Mn(II)^{2+} \rightarrow Mn(IV)^{4+} + 2e^- \tag{2.5}$$

For oxygen as the electron acceptor, the overall reaction can be found using the reduction half reaction for oxygen:

$$O_2 + 4H^+ + 4e^- \rightarrow 2H_2O \tag{2.6}$$

so that:

$$Mn(II)^{2+} + \frac{1}{2}O_2 + 2H^+ \rightarrow Mn(IV)^{4+} + H_2O \tag{2.7}$$

The $Mn(IV)^{4+}$ that is formed precipitates as manganese oxide, eq.(2.1), and the overall redox reaction is:

$$Mn(II)^{2+} + \frac{1}{2}O_2 + H_2O \rightarrow MnO_2(s) + 2H^+ \tag{2.8}$$

This is the reaction that occurs in the aerobic layer. The kinetics of this reaction have been examined [Morgan, 1967] and found to be slow in the normal pH ranges of surface waters (Fig.2.1). However the reaction can be bacterially mediated and proceed more rapidly [Jaquet et al., 1982; Dortch and Hamlin Tillman, 1995].

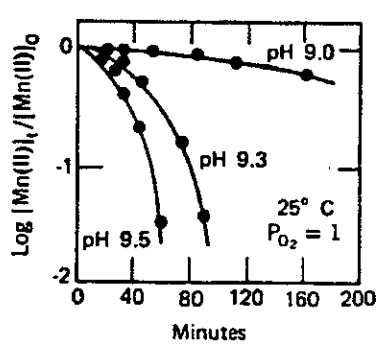

Fig. 2.1 Oxidation of Mn(II). Semi-logarithmic plots of normalized manganese concentration versus time

2.1.1 Solubility

Fig.2.2 presents a solubility diagram for manganese as a function of $pH + pe$ where pe is the activity of the electron which is a measure of the redox potential [Lindsay, 1979]. The pH of sediment pore water is typically $pH = 6$–8. The oxic layer has a $pe \sim 13$ in the presence of dissolved oxygen, whereas for the anoxic layer $pe \sim -3$, the redox potential at which sulfate reduction takes place.

For the oxic conditions $pH + pe \sim 20$, and manganese oxide, $MnO_2(s)$, is the predominant species. The concentration of manganese is predicted to be very low (

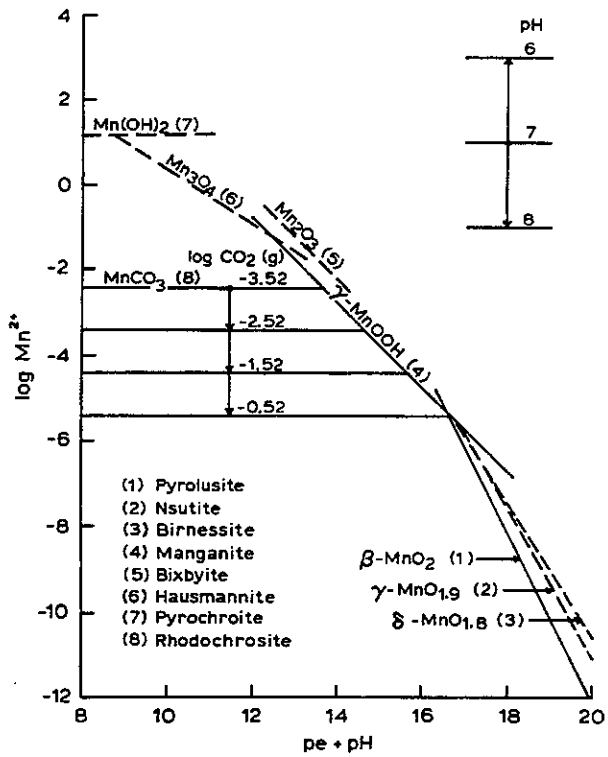

Fig. 2.2 Solubility of manganese minerals at $pH = 7$. The insert shows the effect of varying pH [Lindsay, 1979]

$< 10^{-7}M$, see Fig.2.2). Thus there should be no dissolved manganese in the oxic layer at equilibrium. We shall see below that the kinetics of the formation of manganese oxide, $MnO_2(s)$, controls the dissolved manganese concentration.

For anoxic conditions, $pH + pe < 10$ and the concentration is probably controlled by the solubility of manganese carbonate $MnCO_3\,(s)$ (rhodochrosite). It is unlikely that manganese sulfide $MnS(s)$ is present since iron sulfide $FeS(s)$ is present in most sediments and it is more insoluble than $MnS(s)$ [Emerson et al., 1983]. Typical pore water manganese concentrations are in the mg/L range or 10^{-4} M which is within the stability field of $MnCO_3\,(s)$ in Fig.2.2.

In addition, $Mn\,(II)$ will partition to sorption sites on the sediment particles. Thus not all of the $Mn\,(II)$ that is formed by the reduction of $MnO_2(s)$ remains in dissolved form even if manganese carbonate does not form. Some will sorb to sediment particles. Therefore the transfer of $Mn\,(II)$ from the anoxic to the oxic layer occurs via particle mixing which transports particulate Mn, and via the diffusion of soluble $Mn\,(II)$.

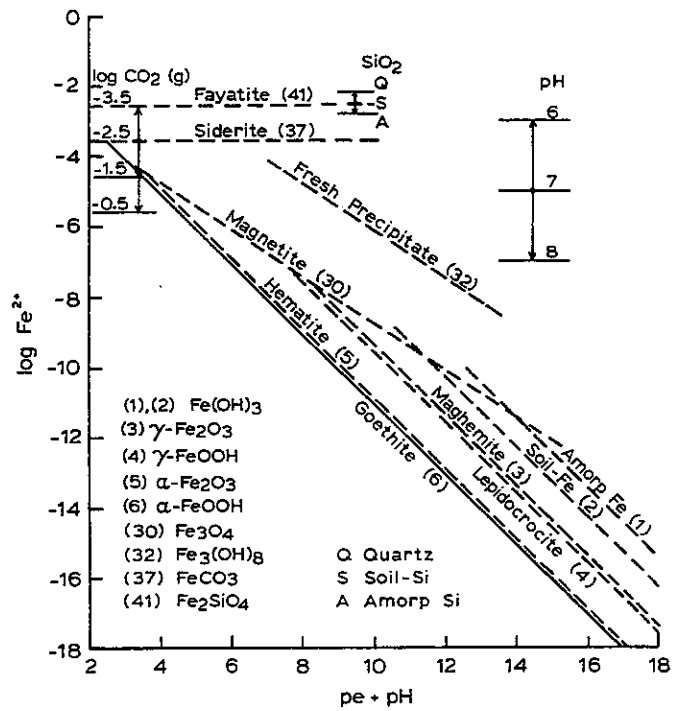

Fig. 2.3 Solubility of iron as a function of $pH + pe$ for $pH = 7$ [Lindsay, 1979].

2.2 IRON

Like manganese, the chemistry of iron in natural waters and sediments has also been extensively studied [Stumm and Morgan, 1970]. Iron exists in two valances states: the +3 state $Fe(III)$ in oxic waters and the +2 state $Fe(II)$ in anoxic waters. $Fe(III)$ is very insoluble and forms iron oxyhydroxide, $FeOOH(s)$, and eventually more insoluble iron oxides. Fig.2.3 presents a solubility diagram for iron as a function of $pH + pe$ [Lindsay, 1979]At equilibrium iron is more insoluble in oxic waters than manganese (Fig. 2.2). However iron carbonate (Siderite) and manganese carbonate have approximately the same solubility. Thus pore water iron concentrations should be comparable to manganese.

Like manganese, iron usually exists as a coating on particles. However, unlike manganese, there are other forms of particulate iron that exist in natural waters. Since the earth's crust is approximately 2% iron by weight [Lindsay, 1979], particles that run off into natural waters contain a large amount of iron. As the particles settle to the sediment, iron is transported as well. This is the source of iron to the sediments.

Not all iron in sediments is reactive. It is convenient to denote the reactive portion of oxic iron as $FeOOH(s)$ (Goethite), and to assume that it includes iron hydroxide, $Fe(OH)_3(s)$ as well since $Fe\,(OH)_3$ differs from $FeOOH\,(s)$ in water content only:

$$FeOOH\,(s) + H_2O \rightarrow Fe\,(OH)_3\,(s) \tag{2.9}$$

The term iron oxyhydroxide is meant to denote the sum of $FeOOH(s)$, $Fe(OH)_3(s)$, and any other reactive iron solid phases that are present [Canfield, 1989].

In the oxic layer of the sediment, $FeOOH(s)$ is stable. However, as particle mixing transports iron containing particles to the anaerobic layer of the sediment, iron oxyhydroxide is thermodynamically unstable and a reduction reaction occurs. $Fe(III)$ is reduced to $Fe(II)$. For this to occur, one electron is required as shown by the following reduction half reaction:

$$FeOOH(s) + e^- \rightarrow Fe(II)^{2+} - 3H^+ + 2H_2O \tag{2.10}$$

Again the source of electrons in sediments is organic matter, CH_2O (eq.2.3) and the overall reduction reaction can be written:

$$FeOOH(s) + \frac{1}{4}CH_2O + 2H^+ \rightarrow Fe(II)^{2+} + \frac{1}{4}CO_2 + \frac{7}{4}H_2O \tag{2.11}$$

By contrast to $Fe(III)$, $Fe(II)$ is more soluble and exists in the low mg/L range in sediment pore waters. As a consequence it can diffuse to the oxic layer of the sediment where it is subject to oxidation. The oxidation of $Fe(II)$ to $Fe(III)$ occurs via the loss of one electron:

$$Fe(II)^{2+} - e^- \rightarrow Fe(III)^{3+} \tag{2.12}$$

With oxygen as the electron acceptor, the overall reaction can be found using the half reaction for oxygen, eq.(2.6), followed by the precipitation of iron oxyhydroxide:

$$Fe(III)^{3+} + 2H_2O \rightarrow FeOOH(s) + 3H^+ \tag{2.13}$$

to yield the overall redox reaction:

$$Fe(II)^{2+} + \frac{1}{4}O_2 + \frac{3}{2}H_2O \rightarrow FeOOH(s) + 2H^+ \tag{2.14}$$

This is the reaction that occurs in the aerobic layer. The kinetics of this reaction have been examined and found to be rapid in the normal pH ranges of surface waters (Fig.2.4).Thus the chemistry of manganese and iron are quite similar. The oxidized forms are both insoluble and form oxides. The reduced forms are soluble in the mg/L range. Their concentrations in pore water are regulated by solid phases and sorption to particles. Their flux to the overlying water is controlled by the rate at which the reduced forms are oxidized in the aerobic layer. A rapid oxidation rate prevents escape since insoluble particles form. A reduced oxidation rate, or anoxic conditions in the

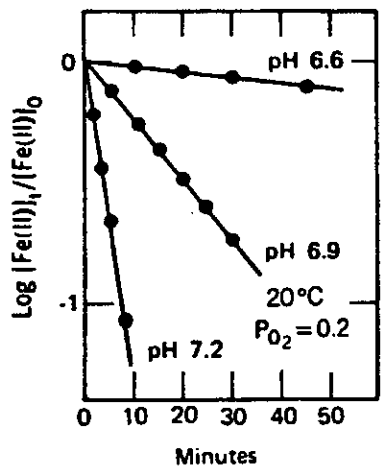

Fig. 2.4 Oxidation of Fe(II). Semi-logarithmic plot of the normalized iron concentration versus time.

overlying water, allows dissolved metal to escape as fluxes to the overlying water. Responses to lowered dissolved oxygen appear to be similar [Sundby et al., 1986]. Hence it is expected that the same framework for sediment flux models can be used for both manganese and iron. This is pursued in the next chapter.

3

Steady State Partitioning Model

3.1 INTRODUCTION

The chemistry of manganese discussed in section 2.1. The reactions that occur in the aerobic and anaerobic layer suggest a conceptual model for manganese fluxes from sediments that is illustrated in Fig. 3.1. This type of model has been suggested by a number of investigators [Sundby et al., 1986].It is instructive to think of the processes in temporal sequence, corresponding to the numbers in Fig. 3.1.

1. Particulate manganese dioxide $MnO_2(s)$settles to the aerobic layer of the sediment.

2. Particle mixing moves the particle downward into the anaerobic layer of the sediment.

3. Manganese dioxide is unstable in a reducing environment so it is reduced to soluble manganese (II) $Mn\,(II)$.

4. $Mn\,(II)$ diffuses to the aerobic layer.

5. Oxidation of $Mn\,(II)$ to manganese dioxide occurs in the aerobic layer which regenerates manganese dioxide $MnO_2(s)$.

6. However, the oxidation reaction converting $Mn\,(II)$ to $MnO_2(s)$ is competing with the diffusion of $Mn\,(II)$ to the overlying water.

7. If the oxidation of $Mn(II)$ is fast relative to its diffusion to the overlying water, then the only other sink is via burial by sedimentation. If, on the other hand, the oxidation of $Mn\,(II)$ is slow, then $Mn\,(II)$ escapes to the overlying water as a flux of soluble manganese, completing the cycle.

This conceptual model description is somewhat idealized since the processes all occur simultaneously. However, the main point is that the magnitude of the flux to the overlying water is due to a competition between the rate of oxidation of $Mn\,(II)$ to $MnO_2(s)$ in the aerobic layer, and the diffusion of $Mn\,(II)$ from the aerobic layer to the overlying water.

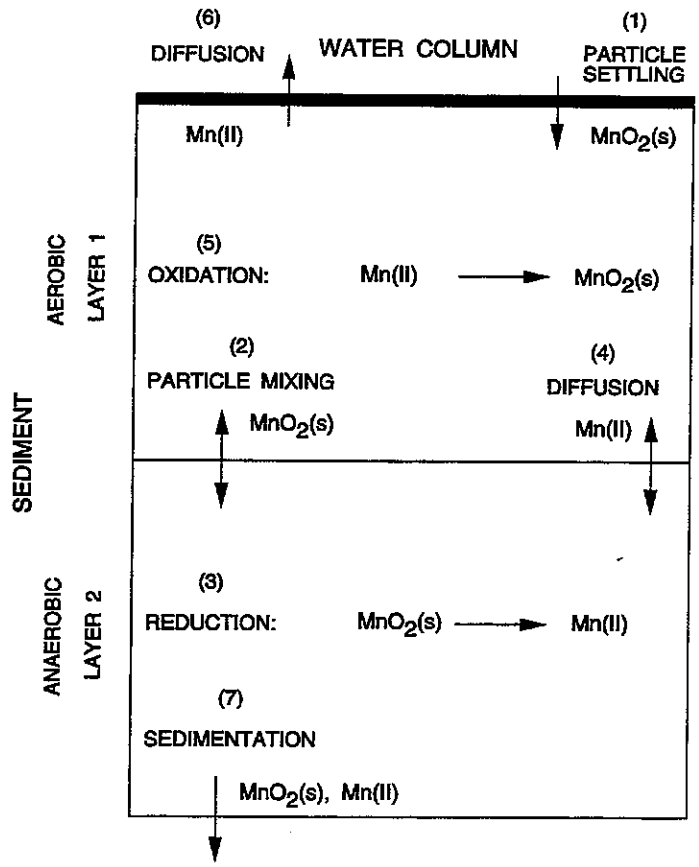

Fig. 3.1 Conceptual model for the flux of manganese from sediment.

3.1.1 Partitioning

In addition to the redox reactions discussed above, the chemistry of manganese (II) itself is also important. Since it is a divalent cation it can adsorb to sorption sites that are present in the sediment. In particular it can sorb to the freshly precipitated hydrous iron oxide [Dzombak and Morel, 1990] in the aerobic layer and to other sorption sites in the anaerobic layer.

Manganese (II) can also form solid species (see Fig. 2.2). A model formulation which explicitly considers the solubility of manganese carbonate is presented in Chapter 4. As we shall see, the result is a rather formidable set of equations.

For the model presented below, the formation of particulate manganese is modeled as a reversible partitioning reaction

$$Mn\,(II)_d \rightleftharpoons Mn\,(II)_p \tag{3.1}$$

where $Mn\,(II)_d$ and $Mn\,(II)_p$ are dissolved and particulate manganese (II) respectively. The rational for this choice is the same as that employed for the nutrients and oxygen flux model [Di Toro and Fitzpatrick, 1993]. First, the resulting equations can be solved analytically which is an important aid to understanding the model's behavior. Second, linear partitioning can sometimes be a realistic description of the relationship between dissolved and particulate chemical. It is the limiting case of the Langmuir model which is implicit in most surface complexation model formulations [Westall and Hohl, 1980; Dzombak and Morel, 1990]. Finally, the general problem of computing the chemical composition of pore water would involve using a numerical chemical equilibrium model [Jahnke et al., 1994]. Mass balance equations are required for the various chemicals that affect the pore water chemistry—for example hydrogen ion, carbon dioxide, and so on (e.g. [Di Toro, 1976]). Thermodynamic data are required for the relevant aqueous complexes, and the stable and metastable mineral phases, some of which are uncertain. Finally, sorption as well as precipitation reactions need to be considered. All this is necessary to compute the fraction of a chemical that is either dissolved or particulate.

The equivalent partitioning model employs only a partition coefficient π_{Mn}, the ratio of particulate to dissolved chemical concentration.

$$\pi_{Mn} = \frac{\left(Mn\,(II)_p\,/m\right)}{Mn\,(II)_d} \tag{3.2}$$

where $Mn\,(II)_p$ is the concentration of particulate manganese per unit sediment volume and m is the concentration of solids per unit sediment volume. Thus $Mn\,(II)_p\,/m$ is the concentration of manganese per unit sediment solids (e.g. μg Mn/g solids). Since $Mn\,(II)_d$ is the concentration of dissolved manganese per unit volume of pore water (e.g. μg Mn/L), π_{Mn} has the units of L/kg.

It is possible to build some level of chemical realism into the partitioning formulation. If necessary, π_{Mn} can be varied as a function of other physical and chemical parameters such as pH in order to produce more realistic behavior. The practical question is: does the added difficulty of including equilibrium chemistry into the model structure result in added realism? Whatever the answer, it is prudent to begin the modeling using linear partitioning and examine the utility of the results.

3.1.2 Model Formulation

The model structure is shown in Fig.3.2. It is an elaboration of the conceptual model presented in Fig.3.1. It is formulated in terms of manganese but it applies equally to iron since the redox chemistry of these two metals are similar. There are four dependent variables: $Mn(II)$ and $MnO_2(s)$ in layers 1 and 2. These concentrations are denoted by $Mn(1)$ and $Mn(2)$, and $MnO_2(1)$ and $MnO_2(2)$ respectively. They

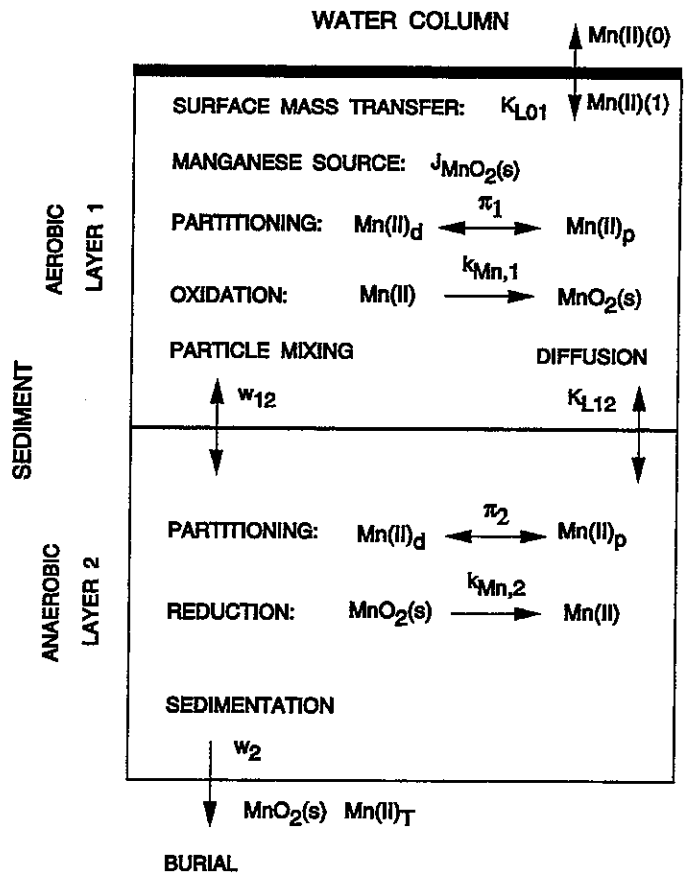

Fig. 3.2 Schematic of the manganese flux model

correspond to the total $Mn(II)$ and $Mn(IV)$ in each layer. The source of manganese to the sediment is the settling of particulate manganese oxide from the overlying water to the sediment. The flux is denoted by J_{MnO_2}.

Two reactions occur in the aerobic layer. $Mn(II)$ partitions to form particulate manganese. This reaction is parameterized with a linear partition coefficient, $\pi_{Mn,1}$. In addition, dissolved $Mn(II)$ is oxidized to $MnO_2(s)$ following eq.(2.8) with first order rate constant $k_{Mn,1}$. Thus the rate of $MnO_2\,(s)$ production in layer 1 per unit area is:

$$S_{MnO_2} = k_{Mn,1} H_1 f_{d1} Mn(1) \tag{3.3}$$

where H_1 is the depth of the aerobic layer and f_{d1} is the fraction of $Mn\,(1)$ that is dissolved. The depth of the aerobic layer H_1 is estimated from the ratio of the diffusion coefficient D_1 in layer 1 and the surface mass transfer coefficient s

$$H_1 = \frac{D_1}{s} \tag{3.4}$$

where the surface mass transfer coefficient is obtained from the sediment oxygen demand SOD computed by the oxygen portion of the sediment flux model, and the overlying water oxygen concentration $O_2(0)$.

$$s = \frac{SOD}{O_2(0)} \tag{3.5}$$

Thus the oxidation rate becomes

$$k_{Mn,1}H_1 = k_{Mn,1}\frac{D_1}{s} = \frac{\kappa^2_{Mn,1}}{s} \tag{3.6}$$

where

$$\kappa_{Mn,1} = \sqrt{k_{Mn,1}D_1} \tag{3.7}$$

which is the definition of a reaction velocity in layer 1. The rational for this definition and eq.(3.4) has been described [Di Toro and Fitzpatrick, 1993].

Two reactions also occur in the anaerobic layer. $Mn(II)$ partitions to form particulate manganese which is parameterized with a linear partition coefficient, $\pi_{Mn,2}$. This may be different from the aerobic layer partition coefficient $\pi_{Mn,1}$ due to differences in pH, the nature of the particles, the absence of freshly precipitated iron oxyhydroxides, and whatever else is influencing the extent of the formation of $Mn(II)$ particulates. In addition, $MnO_2(s)$ is reduced to $Mn(II)$ following eq.(2.4) with first order rate, $k_{Mn,2}$. Hence the source of $Mn(II)$ in the anaerobic layer is:

$$S_{Mn(II)} = k_{Mn,2}H_2MnO_2(2) = \kappa_{Mn,2}MnO_2(2) \tag{3.8}$$

where H_2 is the depth of the anaerobic layer and

$$\kappa_{Mn,2} = k_{Mn,2}H_2 \tag{3.9}$$

which is the definition of a reaction velocity in layer 2 [Di Toro and Fitzpatrick, 1993].

The mass transport between the overlying water and layer 1 is quantified via the surface mass transfer coefficient, K_{L01}, which is set equal to $s = SOD/O_2(0)$ (eq.3.5)

$$K_{L01} = s \tag{3.10}$$

as in the previous models for oxygen and nutrient fluxes[Di Toro and Fitzpatrick, 1993]. Particle mixing with mixing velocity w_{12} and diffusive exchange with mass transfer coefficient K_{L12} between layers 1 and 2 are included as before, as the loss of manganese by burial with sedimentation velocity w_2.

3.1.3 Equations and Solutions

The mass balance equations for the model follow from the reactions and transport processes discussed above. They are:

Layer 1 $Mn(II)$:

$$0 = H_1 \frac{dMn(1)}{dt} = -s\left(f_{d1}Mn(1) - Mn\left(0\right)\right) + K_{L12}(f_{d2}Mn(2) - f_{d1}Mn(1)) \\ +w_{12}(f_{p2}Mn(2) - f_{p1}Mn(1)) - w_2 Mn\left(1\right) - \frac{\kappa^2_{Mn,1}}{s} f_{d1}Mn(1) \tag{3.11a}$$

Layer 2 $Mn(II)$:

$$0 = H_2 \frac{dMn(2)}{dt} = -K_{L12}(f_{d2}Mn(2) - f_{d1}Mn(1)) \\ - w_{12}(f_{p2}Mn(2) - f_{p1}Mn(1)) - w_2\left(Mn(2) - Mn(1)\right) + \kappa_{Mn,2}MnO_2(2) \tag{3.11b}$$

Layer 1 $MnO_2\left(s\right)$:

$$0 = H_1 \frac{dMnO_2(1)}{dt} = \frac{\kappa^2_{Mn,1}}{s} f_{d1}Mn(1) + w_{12}(MnO_2(2) - MnO_2(1)) + J_{MnO_2} \tag{3.11c}$$

Layer 2 $MnO_2\left(s\right)$:

$$0 = H_1 \frac{dMnO_2(2)}{dt} = -\kappa_{Mn,2}MnO_2(2) \\ - w_{12}(MnO_2(2) - MnO_2(1)) - w_2\left(MnO_2(2) - MnO_2(1)\right) \tag{3.11d}$$

The particulate f_p and dissolved f_d fractions are computed from the partition coefficients and the concentration of sediment solids, m, in each layer

$$f_{d1} = \frac{1}{1 + m\pi_{Mn,1}} = 1 - f_{p1} \tag{3.12a}$$

$$f_{d2} = \frac{1}{1 + m\pi_{Mn,2}} = 1 - f_{p2} \tag{3.12b}$$

The solutions to these steady state equations (3.11a–3.11d) are found using the symbolic computation program MACSYMA [Macsyma, 1993]. The solutions are extremely complicated if the dissolved concentration in the overlying water $Mn\left(0\right)$ is included. However for $Mn\left(0\right) = 0$ the solutions are reasonably concise. The reason is that for this case only one equation (eq.3.11c) is inhomogeneous[1] with an external source of manganese. The rest are homogeneous equations with terms that are restricted to linear functions of the four unknowns. It turns out that the equations in such a set have relatively concise solutions.

[1] An equation is homogeneous if it has no forcing function. An inhomogeneous equation has a forcing function, in this case a constant.

The solutions of eqs.(3.11a–3.11d) for the case $Mn\,(0) = 0$ are:

$$Mn(2) = \frac{J_{MnO_2}\kappa_{Mn,2}}{(\kappa_{Mn,2} + w_2)\,(s f_{d1} r_{12} + w_2) + f_{d1}\frac{\kappa_{12}^2}{s} r_{12} w_2} \tag{3.13}$$

where r_{12} is the ratio of the layer 2 to layer 1 concentrations. It is found to be:

$$r_{12} \triangleq \frac{Mn(1)}{Mn(2)} = \frac{f_{d2}K_{L12} + f_{p2}w_{12}}{f_{d1}\left(K_{L12} + s + \frac{\kappa_{Mn,1}^2}{s}\right) + f_{p1}w_{12} + w_2} \tag{3.14}$$

The layer 1 solution is obtained using this relationship:

$$Mn(1) = r_{12}Mn(2) \tag{3.15}$$

The manganese flux follows from the relationship between surface mass transfer and dissolved layer 1 concentrations:

$$J[Mn] = s f_{d1} Mn(1) \tag{3.16}$$

Substituting eqs.(3.13 and 3.15) into this equation yields:

$$J[Mn] = s f_{d1} \frac{J_{MnO_2}\kappa_{Mn,2} r_{12}}{(\kappa_{Mn,2} + w_2)\,(s f_{d1} r_{12} + w_2) + f_{d1}\frac{\kappa_{12}^2}{s} r_{12} w_2} \tag{3.17}$$

which is the flux of manganese to the overlying water. Various special cases of this equation are examined below.

Once the $Mn\,(II)$ solutions are known the $MnO_2\,(s)$ concentrations are easily found. They are

$$MnO_2\,(1) = \frac{\left(f d_1 \frac{\kappa_{12}^2}{s} Mn\,(1) + J_{MnO_2}\right)(\kappa_{Mn,2} + w_{12} + w_2)}{(w_{12} + w_2)\,(\kappa_{Mn,2} + w_2)} \tag{3.18}$$

and

$$MnO_2\,(2) = \frac{Mn\,(2)\,(f_{d2}K_{L12} + f_{p2}w_{12} + w_2) - Mn\,(1)\,(f_{d1}K_{l12} + f_{p1}w_{12} + w_2)}{\kappa_{Mn,2}} \tag{3.19}$$

These solutions, eqs.(3.13–3.19) can be checked by evaluating the global mass balance equation

$$J_{MnO_2} = J\,[Mn] + w_2\,(Mn\,(2) + MnO_2\,(2)) \tag{3.20}$$

which states that the input of particulate manganese to the sediment J_{MnO_2} is either returned to the overlying water as a flux of dissolved manganese, or is buried as

```
/*      List the solutions
 jmn=jmneqz;
```

$$jmn = \frac{fd_1\, jmno2\, kmno2\, r12\, s}{\left(fd_1\, kmno2\, r12 + fd_1\, w_2\, r12\right) s + fd_1\, w_2\, kmn\, r12 + w_2\, kmno2 + w_2^{\,2}}$$

```
mn[1]=mn1eqz;
```

$$mn_1 = \frac{jmno2\, kmno2\, r12}{\left(fd_1\, kmno2\, r12 + fd_1\, w_2\, r12\right) s + fd_1\, w_2\, kmn\, r12 + w_2\, kmno2 + w_2^{\,2}}$$

```
mn[2]=mn2eqz:mn1eqz/r12;
```

$$mn_2 = \frac{jmno2\, kmno2}{\left(fd_1\, kmno2\, r12 + fd_1\, w_2\, r12\right) s + fd_1\, w_2\, kmn\, r12 + w_2\, kmno2 + w_2^{\,2}}$$

```
mno2[2]=mno22z;
```

$$mno2_2 = \frac{mn_2\left(fd_2\, k_{112} + fp_2\, w_{12} + w_2\right) - mn_1\left(fd_1\, k_{112} + fp_1\, w_{12} + w_2\right)}{kmno2}$$

```
r12=r12z;
```

$$r12 = \frac{fd_2\, k_{112} + fp_2\, w_{12}}{fd_1\, s + fd_1\, k_{112} + fd_1\, kmn + fp_1\, w_{12} + w_2}$$

```
/*      Evaluate the mass balance
 mb:jmno2-jmneqz-w[2]*(mn2eqz+mno22z);
```

$$-w_2\left(\frac{jmno2\, kmno2}{\left(fd_1\, kmno2\, r12 + fd_1\, w_2\, r12\right) s + fd_1\, w_2\, kmn\, r12 + w_2\, kmno2 + w_2^{\,2}} + \frac{mn_2\left(fd_2\, k_{112} + fp_2\, w_{12} + w_2\right) - mn_1\left(fd_1\, k_{112} + fp_1\, w_{12} + w_2\right)}{kmno2}\right) - \frac{fd_1\, jmno2\, kmno2\, r12\, s}{\left(fd_1\, kmno2\, r12 + fd_1\, w_2\, r12\right) s + fd_1\, w_2\, kmn\, r12 + w_2\, kmno2 + w_2^{\,2}} + jmno2$$

```
/*      Substitute the solutions for Mn(1) and Mn(2)
  ratsimp(ev(mb,mn[1]=mn1eqz,mn[2]=mn2eqz));
```

$$\frac{\left(fd_1\, w_2\, jmno2\, r12\, s + \left(fd_1\, w_2\, jmno2\, k_{112} + fd_1\, w_2\, jmno2\, kmn + \left(fp_1\, w_2\, w_{12} + w_2^{\,2}\right) jmno2\right) * r12 - fd_2\, w_2\, jmno2\, k_{112} - fp_2\, w_2\, w_{12}\, jmno2\right)}{\left(fd_1\, kmno2 + fd_1\, w_2\right) r12\, s + fd_1\, w_2\, kmn\, r12 + w_2\, kmno2 + w_2^{\,2}}$$

```
/*      Substitute for r12
   ratsimp(ev(%,r12=r12z));
```

$$0$$

Fig. 3.3 Algebraic evaluation of the global mass balance equation. Listing of the MACSYMA output [Macsyma, 1993].

either $Mn(II)$ or $MnO_2\,(s)$. The calculation, which is performed using MACSYMA [Macsyma, 1993], is presented in Fig.3.3.The solutions are listed, the mass balance equation is formed, and the results are simplified. The result, in the last line of the output, is zero which verifies that indeed eq.(3.20) is satisfied.

3.1.4 Simplified solutions

The steady state solution apportions the flux of manganese dioxide to the sediment J_{MnO_2} to either a flux of $Mn(II)$ to the overlying water $J\,[Mn]$ or to the burial of $MnO_2\,(s)$ and $Mn(II)$. The equations can be simplified considerably by examining a special case which, as shown subsequently, appears to be a reasonable representation of what actually occurs.

If the rate of reduction of $MnO_2\,(s)$ in the anaerobic layer is rapid, then $\kappa_{MnO_2} \rightarrow \infty$ and eq.(3.17) becomes

$$J\,[Mn] = \frac{J_{MnO_2}}{1+\beta} \tag{3.21}$$

where

$$\beta = \frac{w_2}{s f_{d1} r_{12}} \tag{3.22}$$

Thus β controls the fraction of incoming manganese that is recycled to the overlying water. It depends on the ratio of the burial velocity w_2 and the surface mass transfer coefficient s modified by the dissolved fraction in layer 1 f_{d1}, and r_{12}. The expression for r_{12} can be simplified slightly using the fact that the most of the manganese (II) in the sediment is in particulate phases. Thus

$$\begin{aligned} f_{p1} &\simeq 1 \\ f_{p2} &\simeq 1 \end{aligned} \tag{3.23}$$

and r_{12} becomes

$$r_{12} = \frac{f_{d2} K_{L12} + w_{12}}{f_{d1}\left(K_{L12} + s + \dfrac{\kappa_{Mn,1}^2}{s}\right) + w_{12} + w_2} \tag{3.24}$$

If the dissolved fractions: f_{d1} and f_{d2} are small enough and s is not small—note the $\kappa_{Mn,1}^2/s$ term—then

$$r_{12} \simeq \frac{w_{12}}{w_{12} + w_2} \rightarrow 1 \tag{3.25}$$

And since the particle mixing velocity w_{12} is usually large relative to the sedimentation velocity, w_2, then $r_{12} \rightarrow 1$ as indicated in eq.(3.25). Thus the fraction of incoming particulate $MnO_2\,(s)$ that is recycled to the overlying water is controlled by

$$\beta \simeq \frac{w_2}{s f_{d1}} \tag{3.26}$$

A large β corresponds to a small fraction recycled (eq.3.21). A large β occurs if the partitioning in the aerobic layer is large so that f_{d1} is small. To understand the magnitudes involved consider a typical sedimentation velocity of $w_2 = 10^{-5}$ m/d (0.36 cm/yr.). A typical surface mass transfer coefficient is $s = SOD/O_2(0) = (1\ \mathrm{g/m^2\text{-}d})/(10\ \mathrm{g/m^3}) = 0.1$ m/d. Thus for $\beta \sim 1$ which corresponds to recycling one half of the incoming flux, $f_{d1} \sim 10^{-4}$ and since (eq.3.12)

$$f_d \sim \frac{1}{m\pi_{Mn}} \tag{3.27}$$

and $m \sim 1$ kg/L a partition coefficient of $\pi_{Mn} \sim 10^4$ L/kg is required if fraction recycled is one half. If the partition coefficient is much larger, then none of the $MnO_2(s)$ flux to the sediment is recycled as a dissolved flux to the overlying water and $J[Mn] \to 0$. On the other hand, if π_{Mn} is much smaller, then the sediment traps very little Mn, all the incoming flux is recycled, and $J[Mn] \simeq J_{MnO_2}$.

3.1.4.1 Anoxic overlying water The largest manganese fluxes to the overlying water are observed if the overlying water concentration of dissolved oxygen approaches zero. Thus it is important to examine the solutions for this limiting case. For $O_2(0) \to 0$, $s = SOD/O_2(0) \to \infty$ and equations (3.13–3.16) approach

$$J[Mn] \underset{s\to\infty}{=} J_{MnO_2}\left(\frac{\kappa_{Mn,2}}{\kappa_{Mn,2}+w_2}\right)\left(\frac{f_{d2}K_{L12}+f_{p2}w_{12}}{f_{d2}K_{L12}+f_{p2}w_{12}+w_2}\right) \tag{3.28}$$

In this case, recycling will be complete if both of the bracketed expressions approach one. The first necessary condition is that

$$\kappa_{Mn,2} \gg w_2 \tag{3.29}$$

or, using the definition of the reaction velocity (eq.3.8), if

$$k_{Mn,2} \gg \frac{w_2}{H_2} \tag{3.30}$$

The term w_2/H_2 is the reciprocal of the residence time of $MnO_2(s)$ in the anaerobic layer. Therefore the condition in eq.(3.30) is that the reduction of $MnO_2(s)$ to $Mn(II)$ occurs rapidly relative to the residence time of $MnO_2(s)$ in H_2.

The second condition is that

$$f_{d2}K_{L12} + f_{p2}w_{12} \gg w_2 \tag{3.31}$$

which requires that the rate of transport of dissolved ($f_{d2}K_{L12}$) and particulate ($f_{p2}w_{12}$) manganese (II) to layer one is large relative to the rate at which it is buried w_2. This condition is necessary so that the manganese produced in layer 2 by the reduction of $MnO_2(s)$ to $Mn(II)$ is transported to layer 1 rather than buried. Once it is in layer1

it escapes to the overlying water without further modification since the depth of the aerobic layer $H_1$is approaching zero

$$\lim_{s\to\infty} H_1 = \lim_{s\to\infty} \frac{D_1}{s} = 0 \tag{3.32}$$

and no re-oxidation of $Mn\,(II)$ to $MnO_2\,(s)$ can occur.

3.1.4.2 Aerobic overlying water The other end of the spectrum is the behavior of $J\,[Mn]$ as $s \to 0$, corresponding to low SOD and high overlying water dissolved oxygen. To examine this case $J\,[Mn]$ (eqs.3.13–3.16) can be expanded in a Taylor series in s:

$$J\,[Mn] = J_{MnO_2}\frac{\kappa_{Mn,2}}{\kappa_{Mn,1}^2 w_2}s^2 + \cdots \tag{3.33}$$

The manganese flux decreases quadratically in s with a slope determined by the two reaction velocities and the sedimentation velocity.

The results of this section have shown that the model has reasonable limiting behavior at the extremes of the parameter values. It's ability to reproduce observations will be examined in the next section.

3.2 MANGANESE FLUX DATA

Two data sets will be examined using this model. This first is a relatively small number of manganese and nutrient flux measurements made at three Long Island Sound stations [Aller, 1980a]. The second is a large number of manganese [Hunt and Kelly, 1988] and nutrient flux measurements made at the MERL mesocosms [Nixon et al., 1986]. The analysis technique is to attempt to reproduce the observed relationship between the ammonia $J[NH_4]$ and manganese $J[Mn]$ fluxes. As shown in Fig.3.4 there is a proportional relationship between these two fluxes. The question is: what is the causal linkage.

3.2.1 Relationship between Manganese and Ammonia Fluxes

The parameter in the manganese model equations that can ultimately be related to the ammonia flux is the surface mass transfer coefficient: $s = SOD/O_2(0)$. This parameter controls both the rate of mass transfer from the pore water to the overlying water (eq.3.11a) and the depth of the aerobic layer, H_1(eq.3.6). As SOD increases or the overlying water dissolved oxygen decreases, one would expect that $J[Mn]$ would increase since both the rate of surface mass transfer increases and the depth of the aerobic zone decrease. The latter effect decreases the residence time in the aerobic layer and makes the oxidation of $Mn(II)$ to $MnO_2(s)$ less rapid (eq.3.6), enabling

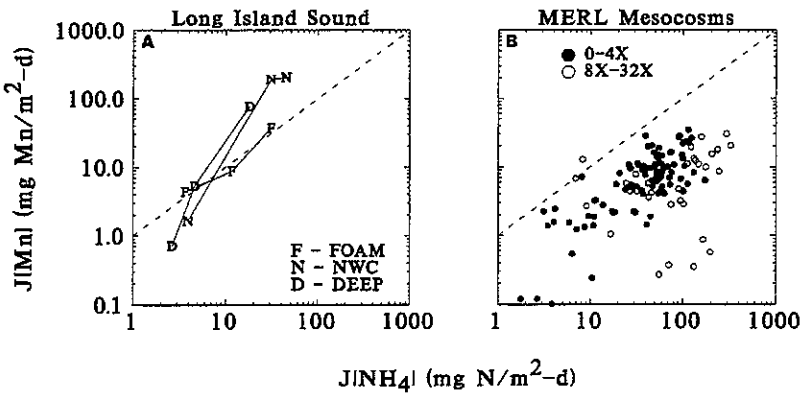

Fig. 3.4 Manganese versus ammonia flux. Data from Long Island Sound (A) and the MERL mesocosm experiment (B).

more $Mn(II)$ to escape to the overlying water. As shown in section 3.1.4.1 page 18, this is indeed how the steady state solution behaves.

The dependency of s on ammonia flux occurs because the ammonia flux and SOD are related [Di Toro and Fitzpatrick, 1993]. For the simple case with zero overlying water ammonia concentration, the relationship between ammonia diagenesis J_N—the rate at which organic matter is mineralized and ammonia is released to the pore water—and ammonia flux to the overlying water $J\,[NH_4]$ is

$$J[NH_4] = J_N \frac{s^2}{s^2 + \kappa^2_{NH_4,1}} \tag{3.34}$$

where s is the surface mass transfer coefficient and $\kappa_{NH_4,1}$ is the reaction velocity for nitrification in the aerobic layer. The SOD is related to ammonia diagenesis since as particulate organic matter decays to produce ammonia at a rate J_N, it also produces reduced organic carbon at a rate J_C. This, in turn, is eventually oxidized and results in SOD.

The temporal variation of SOD, and the fraction of reduced end-products that are buried, are the determined by the full sediment model equations [Di Toro and Fitzpatrick, 1993]. However an approximate analysis can be made as follows. The ratio between carbon and nitrogen produced by diagenesis is closely approximated by the Redfield ratio $a_{C,N}$, the stoichiometric composition of reactive organic matter

$$J_C = a_{C,N} J_N \tag{3.35}$$

If all the organic carbon were oxidized, the SOD would be

$$SOD = a_{O_2C} J_C = a_{O_2C} a_{C,N} J_N \tag{3.36}$$

where $a_{O_2,C}$ is the Redfield ratio of O_2 to carbon. It is the oxygen required to oxidize the organic carbon to CO_2. Hence the SOD can be computed from ammonia diagenesis J_N from eqs.(3.35–3.36). The equation which gives ammonia diagenesis as a function of ammonia flux and overlying water oxygen concentration is found by solving eqs.(3.34–3.36) simultaneously. The result is

$$J_N = \frac{1}{3}\left(\frac{\sqrt[3]{2a_{O2,N}^2}J[NH_4]^2}{d_1} + J[NH_4] + \frac{d_1}{\sqrt[3]{2a_{O2,N}^2}}\right) \tag{3.37}$$

where:

$$d_1 = \sqrt[3]{\begin{array}{c} 2a_{O2,N}^2 J[NH_4]^3 + 27J[NH_4][\kappa_{NH4,1}O_2(0)]^2 \\ +3^{\frac{3}{2}}J[NH_4]\kappa_{NH4,1}O_2(0)\sqrt{4a_{O2,N}^2 J[NH_4]^2 + 27[\kappa_{NH4,1}O_2(0)]^2} \end{array}} \tag{3.38}$$

This approximation assumes that all carbon diagenesis eventually becomes SOD, i.e. that losses due to sulfide fluxes and burial are negligible. From an analysis of Chesapeake Bay model fluxes, these losses amount to no more than 25% [Di Toro and Fitzpatrick, 1993].

The second source of error is due to the time lags that occur between the production of oxygen equivalents by carbon diagenesis and their eventual oxidation. These are caused by the formation and the subsequent oxidation of $FeS(s)$. From an analysis of the steady state version of the sediment model it is known that the time lag effect causes an error of approximately a factor of two between the carbon diagenesis estimated from SOD assuming steady state, and the actual flux [Di Toro and Fitzpatrick, 1993]. Thus although these errors are not negligible, the approximations can be used so long as the magnitude of the error involved is recognized.

Hence, for a specified ammonia flux $J[NH_4]$, ammonia diagenesis J_N is found (eq.3.37). The SOD is computed using eq.(3.36) and eq.(3.5) yields s which is used in eqs.(3.14–3.17) to compute $J[Mn]$. This establishes the relationship between ammonia and manganese fluxes.

3.2.2 Comparison to Data

The model computations are compared to the Long Island Sound data in Fig.3.5.The model parameters are listed in Table 3.1. Two cases are considered. The first results from assigning a slow oxidation rate (small $\kappa_{Mn,1}$). The input flux of particulate manganese J_{MnO_2} is specified to be 150 mg Mn/m^2–d for the Long Island Sound case since the flux of manganese from the sediment $J[Mn]$ is approximately this magnitude at the high ammonia fluxes (Fig.3.5A). The pore water and sediment data are plotted arbitrarily at an ammonia flux of 10 mg N/m^2-d for convenience. In order to reproduce the pore water and sediment manganese concentrations (Fig.3.5C,D) it is necessary to

Table 3.1 Parameter Values for linear partitioning model's application to Long Island Sound (LIS) and MERL

Parameters	Values				Units
	Small $\kappa_{Mn,1}$		Large $\kappa_{Mn,1}$		
	LIS	MERL	LIS	MERL	
J_{MnO_2}	150	20	50	10	mg Mn/m^2-d
$\kappa_{Mn,1}$	0.25		2.0		m/d
$\kappa_{MnO_2,2}$	0.1		0.1		m/d
$\pi_{Mn,1}$	200		200		L/kg
$\pi_{Mn,2}$	100		100		L/kg
m_1	1.0		1.0		kg/L
m_2	1.0		1.0		kg/L
K_{L12}	0.05		0.05		m/d
w_{12}	0.0012		0.0012		m/d
w_2	0.5		0.5		cm/yr
$\kappa_{NH_4,1}$	0.15		0.15		m/d
$[O_2(0)]$	5.0		5.0		mg/L
$a_{O_2,C} \times a_{C,N}$	2.54 × 5.68		2.54 × 5.68		mg O_2/mg N

recycle most of the incoming manganese to the overlying water (Fig.3.5B). Hence the oxidation reaction velocity $\kappa_{Mn,1}$ is set so that only a small fraction of the manganese (II) flux to the aerobic layer is oxidized to $MnO_2\,(s)$. As a result very little is trapped and the burial fraction is small (Fig.3.5B). Since most of the flux is being recycled, the variation in s which occurs as $J\,[NH_4]$ varies has little effect on the manganese flux as shown in Fig.3.5A.

An alternate calibration is shown in Fig.3.6. The oxidation reaction velocity $\kappa_{Mn,1}$ is increased from 0.25 to 2.0 m/d so that a larger fraction of the manganese (II) flux to the aerobic layer is oxidized to $MnO_2\,(s)$. As a consequence, the sediment manganese concentration is larger Fig.3.6C and so also is the pore water concentration Fig.3.6D because of the partitioning relationship (eq. 3.2). The oxidation rate is now in the range where the variation in s is affecting the fraction that is buried versus that recycled Fig.3.6 B. The burial fraction is predominant at low ammonia flux and the flux to the overlying water predominates at high ammonia flux.

A similar analysis for the MERL flux data, shown previously in Fig. 3.4, is presented in Fig.3.7 with similar results. The parameters are listed in Table 3.1. The flux of particulate manganese to the sediments appears to be smaller J_{MnO_2} = 10–20 mg Mn/m^2–d than the case of the Long Island Sound data J_{MnO_2} = 50–150 mg

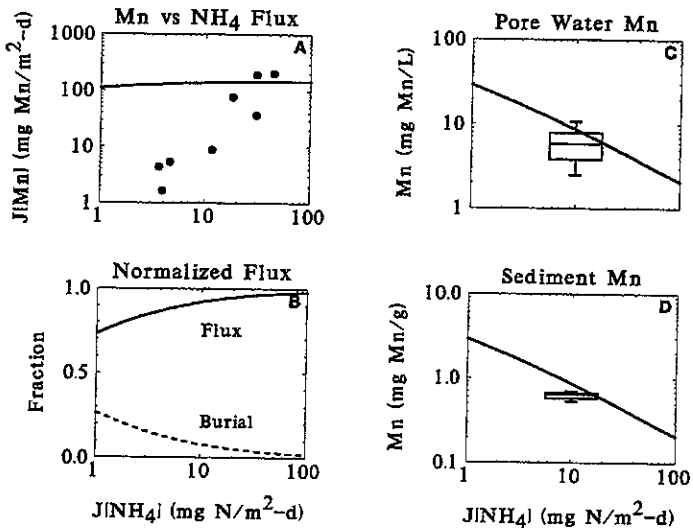

Fig. 3.5 Manganese linear partitioning model: slow oxidation rate. Comparison of model predictions (line) to data (points) from Long Island Sound as a function of the ammonia flux. (A) Manganese flux; (B) Mn flux normalized to depositional flux, (C) pore water Mn concentration, (D) solid phase Mn concentration.

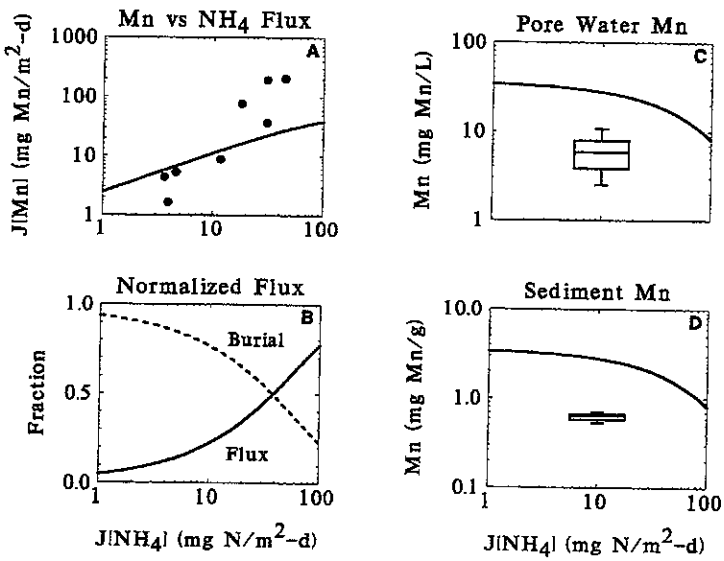

Fig. 3.6 Manganese linear partitioning model: rapid oxidation rate. Comparison of model predictions (line) to data (points) from Long Island Sound as a function of the ammonia flux. (A) Manganese flux; (B) Mn flux normalized to depositional flux, (C) pore water Mn concentration, (D) solid phase Mn concentration.

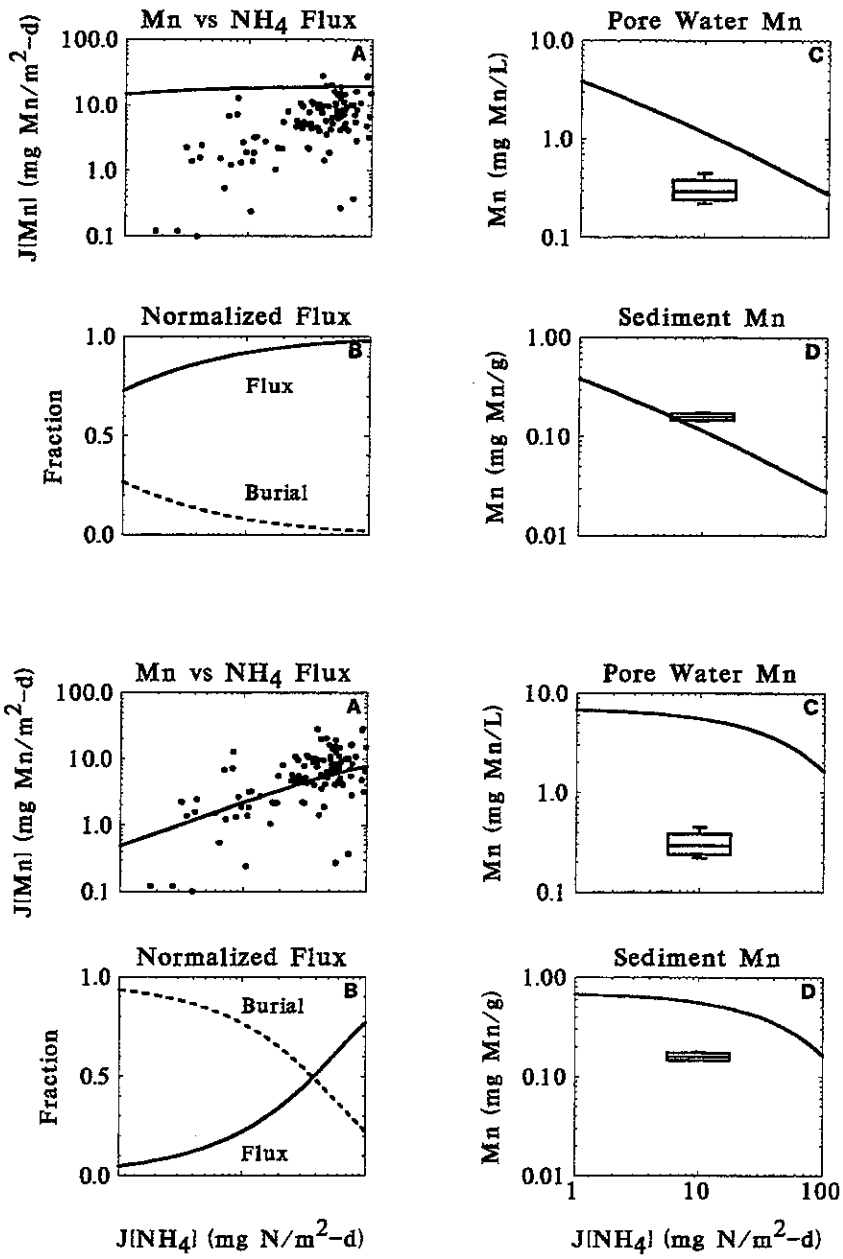

Fig. 3.7 Manganese linear partitioning model. Comparison of model predictions (line) to data (points) from the MERL experiment as a function of the ammonia flux. Top group: slow oxidation rate. Bottom group: rapid oxidation rate. (A) Manganese flux; (B) Mn flux normalized to depositional flux, (C) pore water Mn concentration, (D) solid phase Mn concentration.

Mn/m^2–d. As a consequence, the pore water and sediment manganese concentrations are also smaller.

3.3 CONCLUSIONS

The steady state linear partitioning model is reasonably successful in reproducing a major feature of the Long Island Sound and MERL data sets, namely the correlation between increasing ammonia and manganese fluxes. However, it cannot do so and be consistent with the pore water and sediment manganese concentrations at the same time. Perhaps the problem is the constant linear partition coefficient (eq. 3.2). For a steady state condition, there are only two possible exit pathways for the incoming manganese: either it escapes as a flux, or it is buried. Therefore, in order for the model to reproduce the observations it is necessary that it predicts a higher degree of burial at low ammonia fluxes and a larger manganese flux to the overlying water at high ammonia fluxes. If the actual partitioning were such that more manganese were sequestered at high ammonia fluxes, then perhaps the solid phase and pore water observations could be satisfied as well as the fluxes.

Consider the following possibility. Suppose the fraction of manganese that is particulate in the anaerobic layer is determined not only by the partitioning of $Mn\,(II)$ to sediment solids but also by the solubility of $MnCO_3(s)$. This is not a linear partitioning process. Rather it is controlled by a chemical equilibrium between manganese Mn^{2+} and carbonate ion CO_3^{2-} concentrations. Suppose further that the concentration of manganese carbonate increases with increasing ammonia flux. This mechanism might produce the necessary variation in partitioning.

The reason that the $MnCO_3(s)$ concentration might increase is as a consequence of increased alkalinity production associated with increased sulfate reduction. Sulfate reduction increases because more organic matter is being mineralized—this must be happening for the ammonia flux to increase—and the reduced organic carbon is being oxidized using sulfate as the electron acceptor.

$$CH_2O + \frac{1}{2}SO_4^{2-} \rightarrow \frac{1}{2}CO_2 + \frac{1}{2}HCO_3^- + \frac{1}{2}HS^- + \frac{1}{2}H_2O \tag{3.39}$$

This reaction produces alkalinity HCO_3^- as a consequence of the destruction of a strong acid cation SO_4^{2-}. The increased alkalinity causes an increased precipitation of $MnCO_3\,(s)$.

In the next chapter we shall explore the behavior of such a model using a much simplified yet reasonably realistic model which includes chemical equilibrium control of the solid phase.

4

Solubility Control of Particulate Manganese

4.1 INTRODUCTION

The model constructed in the previous chapter used linear partitioning to determine the fraction of manganese in the anaerobic layer that formed a solid phase. This is a critical mechanism since it influences the extent of burial. And the more burial that occurs the less is the flux to the overlying water. In this chapter we examine the behavior of a similar flux model, but one in which the precipitation of manganese carbonate is explicitly computed. One of the first models for the concentration of manganese in the pore water of a sediment was based on this idea [Holdren et al., 1975; Holdren, 1977].

In order to model the chemistry of manganese carbonate, we need to be able to model the chemical control of the carbonate concentration in pore water. Since calcium carbonate is the predominant inorganic carbon specie in sediments, its chemistry is considered first.

4.2 CALCIUM CARBONATE

Most freshwater and marine sediments contain large concentrations of calcium carbonate. Typical values are 10–100 mg $CaCO_3$/g or 1 to 10% of the dry weight. This is in the same order of magnitude as the organic carbon concentration in sediments. Calcium carbonate provides a buffer system for the pH in sediment pore water and also influences the concentration of carbonate ion. The objective of the model formulated in this section is to reproduce the observations of pore water and solid phase concentrations of calcium, alkalinity, and calcium carbonate. The model structure is shown in Fig.4.1.

The only chemical mechanism included in the model is the precipitation of calcium carbonate. Chemical speciation in the pore water is greatly simplified. Thus the model should be viewed more as a feasibility investigation into the methods and difficulties of including chemical equilibrium reactions into the sediment flux framework rather than a definitive model of calcium carbonate formation in sediments.

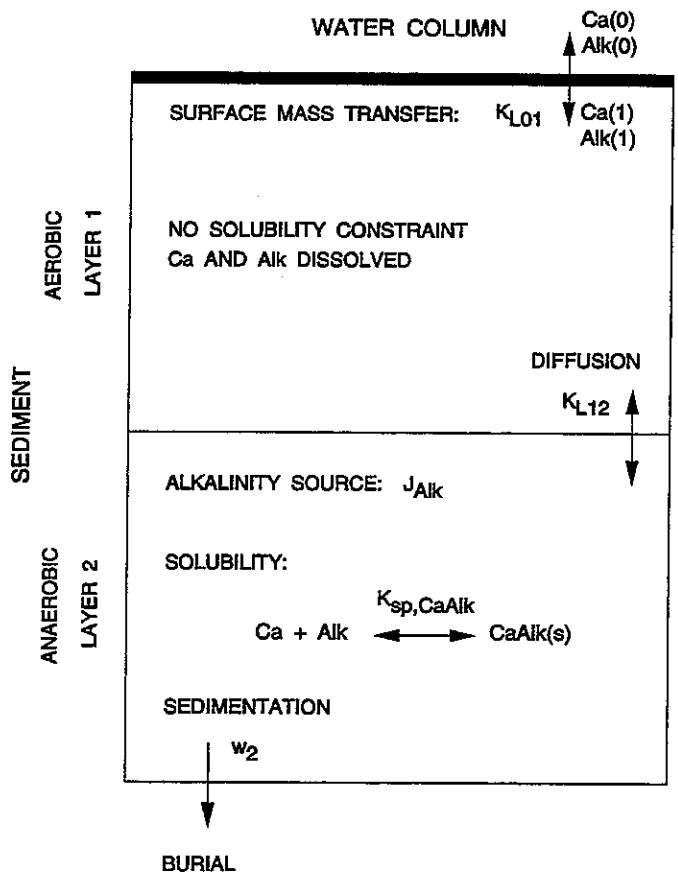

Fig. 4.1 Schematic diagram of the calcium and alkalinity flux model.

4.3 CHEMISTRY AND SIMPLIFICATIONS

A model of a chemical system is specified by the chemical components and the species formed by the components [Morel, 1983]. This type of system is termed a closed system since the concentration of the components are thought of as being constant and fixed. This is the normal situation considered in typical chemical equilibrium calculations. The use of components in model formulations also applies to systems that are open [Di Toro, 1976], i.e. systems which have external sources and sinks of the components.

The equilibrium chemistry of carbon dioxide, alkalinity and calcium in natural waters is well understood [Stumm and Morgan, 1981; Loewenthal and Marais, 1976; Morse and Mackenzie, 1990; Butler, 1991]. It is specified by three components: calcium Ca, alkalinity Alk, and total inorganic carbon TIC. However, using all these three components results in an equation set that is not conveniently solved. Therefore a simplified set of components and equations are used in the analysis presented below.

The equation that determines the solubility of calcium carbonate is

$$[Ca^{2+}][CO_3^{2-}] = K_{s1} \tag{4.1}$$

where the brackets [ ] denote molar concentrations and K_{s1} is the solubility product of calcium carbonate $CaCO_3\,(s)$. Ionic strength corrections are assumed to be included in K_{s1}. Since the objective of this exercise is to produce a tractable set of model equations, additional approximations are introduced. The concentration of Ca^{2+} is approximated with the concentration of total dissolved calcium denoted by $[Ca]$. This ignores the contributions of complexes of calcium with bicarbonate $CaHCO_3^+$ and other ligands to the total dissolved calcium.

$$[Ca] = \left[Ca^{2+}\right] + \left[CaHCO_3^+\right] + \cdots \simeq \left[Ca^{2+}\right] \tag{4.2}$$

The concentration of carbonate can be obtained using the definition of alkalinity

$$[Alk] = [HCO_3^-] + 2[CO_3^{2-}] + [OH^-] - [H^+] \tag{4.3}$$

In the pH range that is typical of sediment pore waters $pH = 7$–8 and for large enough alkalinity, $[Alk] > 0.1$ meq/L, and the bicarbonate ion makes up essentially all the alkalinity

$$[Alk] \simeq [HCO_3^-] \tag{4.4}$$

The deprotonation reaction for bicarbonate HCO_3^- which yields carbonate CO_3^{2-} is

$$HCO_3^- \leftrightarrow H^+ + CO_3^{2-} \tag{4.5}$$

and the mass action equation is

$$\frac{[H^+][CO_3^{2-}]}{[HCO_3^-]} = K_2 \tag{4.6}$$

where K_2 is the equilibrium constant for the reaction 4.5. Using eq.(4.4) for HCO_3^- yields

$$\frac{[H^+][CO_3^{2-}]}{[Alk]} = K_2 \tag{4.7}$$

Thus the carbonate concentration becomes

$$[CO_3^{2-}] = \frac{K_2[Alk]}{[H^+]} \tag{4.8}$$

Substituting this equation in the solubility mass action equation (4.1) yields

$$[Ca][Alk] = \frac{K_{s1}}{K_2}[H^+] \triangleq K_{CaAlk} \tag{4.9}$$

where K_{CaAlk} is the apparent solubility constant of $CaCO_3(s)$ in terms of total dissolved calcium $[Ca]$ and alkalinity $[Alk]$. It is an apparent or conditional solubility constant because it is a function of pH. The effect of decreasing pH, which increases H^+, increases the apparent solubility constant, as it should since $[CO_3^{2-}]$ is decreasing as pH decreases (eq.4.8).

This simplification reduces the number of components to two: Ca and Alk, and requires only that the pH be specified. This is a significant reduction in the complexity of the equations.

4.4 CLOSED SYSTEM

Consider, initially, a closed system with no inflows or outflows. Let Ca_T and Alk_T be the total concentrations of calcium and alkalinity in the system. The mass balance equations are

$$[Ca] + [CaCO_3(s)] = Ca_T \tag{4.10}$$

and

$$[Alk] + 2[CaCO_3(s)] = Alk_T \tag{4.11}$$

where $[CaCO_3(s)]$ is the concentration of calcium carbonate that forms. The term $2[CaCO_3(s)]$ in the alkalinity equation arises from the two equivalents of alkalinity in each mole of $CaCO_3(s)$—see eq.(4.3). Substituting these equations into the mass action eq.(4.9), dropping the brackets, and denoting $CaCO_3\ (s)$ by $CaCO_3$ for notational convenience yields

$$(Ca_T - CaCO_3)\,(Alk_T - 2CaCO_3) = K_{CaAlk} \tag{4.12}$$

which is a quadratic equation that can be solved for $CaCO_3$.

It is more convenient and instructive to solve, instead, for dissolved calcium Ca_d

$$Ca_d = Ca_T - CaCO_3 \tag{4.13}$$

Finding the equation for Ca_d yields

$$Ca_d^2 - (Ca_T - \frac{1}{2}Alk_T)Ca_d - \frac{K_{CaAlk}}{2} = 0 \tag{4.14}$$

The point is that the concentration of dissolved calcium is a function only of the difference $Ca_T - \frac{1}{2}Alk_T$

$$Ca_x \triangleq Ca_T - \frac{1}{2}Alk_T \tag{4.15}$$

which we define as the excess calcium Ca_x. Hence, the equation for Ca_d is

$$Ca_d^2 - (Ca_x)Ca_d - \frac{K_{CaAlk}}{2} = 0 \tag{4.16}$$

The reason that the dissolved calcium concentration Ca_d is only a function of excess calcium is a reflection of the chemical fact that changing the concentration of solid phase calcium carbonate in a solution that is already saturated—i.e. already in equilibrium with $CaCO_3\,(s)$—does not affect the concentration of dissolved calcium. The system is already saturated with respect to calcium carbonate so that solid calcium carbonate is present and adding more solid calcium carbonate does not cause any chemical change. The equation for calcium carbonate does not have this property since the concentration of calcium carbonate depends on *both* the concentration of total calcium and alkalinity.

To see that excess calcium is independent of $CaCO_3$, note that adding a quantity $\Delta CaCO_3$ of calcium carbonate to the system increases Ca_T by $\Delta CaCO_3$ and increases Alk_T by $2\Delta CaCO_3$ since each mole of calcium carbonate is two moles of alkalinity. However the excess calcium, Ca_x (eq.4.15) is unchanged and therefore, so is the dissolved calcium concentration since it depends only on the excess calcium concentration (eq. 4.16).

The solution for dissolved calcium is found by solving eq.(4.16)

$$Ca_d = \frac{Ca_x}{2}\left(1 \pm \sqrt{1 + \frac{2K_{CaAlk}}{Ca_x^2}}\right) \tag{4.17}$$

Once the dissolved calcium is known, the concentration of calcium carbonate follows from eq.(4.10)

$$CaCO_3 = Ca_T - Ca_d \tag{4.18}$$

We shall see in section 4.5 that the form of the solutions for the equations that result from the sediment flux model are similar.

4.4.1 Solution Behavior

The concentration of calcium carbonate is determined by the difference between the total and dissolved calcium, eq.(4.10) which in turn is determined by the excess calcium (eq.4.17). It is instructive to examine the solution in terms of the two independent variables: total calcium and alkalinity, Ca_T and Alk_T.

A simple way of understanding the solution is to obtain the relationship between the concentrations of Ca_T and Alk_T for a fixed concentration of $CaCO_3$. The solubility constraint is

$$[Ca][Alk] = (Ca_T - CaCO_3)(Alk_T - 2CaCO_3) = K_{CaAlk} \tag{4.19}$$

For a fixed concentration of $CaCO_3$ this equation gives a relationship between Ca_T and Alk_T

$$Ca_T = \frac{K_{CaAlk}}{Alk_T - 2CaCO_3} + CaCO_3 \tag{4.20}$$

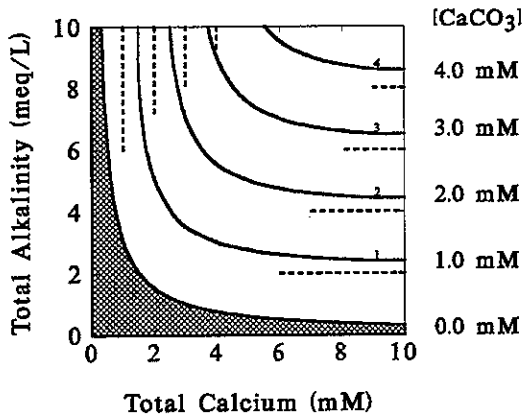

Fig. 4.2 Concentration of $CaCO_3\,(s)$ as a function of total alkalinity and total calcium concentrations. $CaCO_3 = 0$ in the shaded region. The dotted lines are the stoichiometric limits to the quantity of $CaCO_3\,(s)$ that can form as Ca_T or $Alk_T \rightarrow \infty$.

For various concentrations of $CaCO_3$, the relationship between Ca_T and Alk_T is shown in Fig.4.2.

The lack of symmetry in Fig.4.2, which is implied by eq.(4.9), is due to the requirement that two moles of alkalinity are required to form one mole of calcium carbonate whereas only one mole of calcium suffices. If the graph were constructed with the axes: Ca_T and $2Alk_T$, then the graph would be symmetric in Ca_T and Alk_T.

There is a range of Ca_T and Alk_T over which no precipitation occurs. This is signaled by the mathematics if either of the resulting dissolved concentrations are negative. That is, if either dissolved concentration, computed from the relationships

$$Ca_d = Ca_T - CaCO_3 < 0 \tag{4.21}$$

or

$$Alk_d = Alk_T - 2CaCO_3 < 0 \tag{4.22}$$

are negative, that signals that the solubility constraint, eq.(4.9) cannot be satisfied with chemically reasonable, i.e. positive, concentrations and the only realistic solution is $CaCO_3 = 0$. The solubility constraint (eq.4.19) becomes

$$(Ca_T - CaCO_3)\,(Alk_T - 2CaCO_3) = (Ca_T)\,(Alk_T) \leq K_{CaAlk} \tag{4.23}$$

which means that the solution is undersaturated with respect to calcium carbonate. The shaded region in Fig.4.2 is where no $CaCO_3$ can form. For larger concentrations, calcium carbonate forms as shown.

This example illustrates an important point. When computing the solutions of a chemical equilibrium problem from the algebraic equations that result from the mass

balance and mass action equations, the solution must be tested to insure that it is physically realistic, namely that all the computed concentrations—the solid phase and dissolved concentrations—are positive. The mathematical solutions of sets of equations where the inequalities that express the range of possibilities—saturated and unsaturated conditions, e.g.

$$(Ca_T)\,(Alk_T) \leq K_{CaAlk} \tag{4.24}$$

are replaced by equalities. e.g.

$$(Ca_T)\,(Alk_T) = K_{CaAlk} \tag{4.25}$$

which are only true if the solid phase precipitates, do not necessarily result in positive concentrations. We shall see that the need to test the realism of the solutions extends to the more complicated settings examined below.

4.5 SEDIMENT MODEL EQUATIONS AND SOLUTIONS

The model formulation is shown in Fig.4.1. The dependent variables are $Alk(1)$ and $Alk(2)$, the total alkalinity in layer 1 and layer 2 respectively; $Ca(1)$ and $Ca(2)$, the total calcium in the same sequence; and $CaCO_3(2)$, the calcium carbonate in layer 2. Calcium carbonate precipitation in layer 1 is not considered since the layer is usually much thinner than layer 2. The mass balance and mass action equations are as follows.

Layer 1 Alkalinity

$$0 = s\,[Alk(0) - Alk(1)] + K_{L12}\,[Alk(2)_d - Alk(1)] \tag{4.26}$$

Layer 2 Alkalinity

$$0 = K_{L12}\,[Alk(2)_d - Alk(1)] - w_2\,[2CaCO_3(2)] + J_{Alk} \tag{4.27}$$

Layer 1 Calcium

$$0 = s\,[Ca(0) - Ca(1)] + K_{L12}\,[Ca(2)_d - Ca(1)] \tag{4.28}$$

Layer 2 Calcium

$$0 = K_{L12}\,[Ca(2)_d - Ca(1)] - w_2\,[CaCO_3(2)] \tag{4.29}$$

$CaCO_3\,(s)$ Solubility

$$Ca(2)_d Alk(2)_d = K_{CaAlk} \tag{4.30}$$

where

$$Ca\,(2)_d = Ca(2) - \ CaCO_3(2) \tag{4.31}$$

and

$$Alk\,(2)_d = Alk(2) - 2\ CaCO_3(2) \tag{4.32}$$

are the dissolved calcium and alkalinity in layer 2. Since no calcium carbonate is allowed to precipitate in layer 1, the total concentrations: $Ca(1)$ and $Alk(1)$ are equal to the dissolved concentrations.

The solution to these equations can be found as follows. The variables: $Alk(1)$, $Alk(2)$, $Ca(1)$, and $Ca(2)$ are eliminated from the five simultaneous equations (4.26-4.30). The resulting equation for $CaCO_3(2)$ is a quadratic equation of the form

$$aCaCO_3 + bCaCO_3 + c = 0 \tag{4.33}$$

where

$$a = 2(s + K_{L12})^2 w_2^2 \tag{4.34}$$

$$b = -w_2(s + K_{L12})\left[(2Ca(0) + Alk(0))\, sK_{L12} + J_{Alk}\,(s + K_{L12})\right] \tag{4.35}$$

$$c = -sK_{L12}\left\{sK_{L12}\left[K_{CaAlk} - Alk(0)Ca(0)\right] - J_{Alk}Ca(0)\,(s + K_{L12})\right\} \tag{4.36}$$

It is remarkable that the solution to these five simultaneous equations is reduced to the solution of a quadratic equation, as it is for the closed system analyzed in the last section (eq.4.14). This suggests that so long as the chemistry can be simplified to the point that the equations for a closed system reduce to a manageable result, then the open system equations can also be solved at the same level of algebraic difficulty. We shall see subsequently that this observation continues to be true for more complex systems.

4.5.1 Simplified Solution

Before examining the solution of eq.(4.33) it is instructive to consider the limiting case where $K_{CaAlk} \rightarrow 0$ which corresponds to a completely *insoluble* calcium carbonate. In fact, this is a somewhat unrealistic assumption as can be seen in Fig.4.2 where the dotted lines represent the contours for the $K_{CaAlk} \rightarrow 0$ case, Nevertheless the resulting solution is instructive. For $K_{CaAlk} = 0$, eq.(4.30) requires that either $Ca\,(2)_d$ or $Alk\,(2)_d$ be zero or, using the definitions (eqs.4.31–4.32)

$$CaCO_3(2) = \frac{1}{2}Alk(2) \tag{4.37}$$

or

$$CaCO_3(2) = Ca(2) \tag{4.38}$$

The conditions are that either all the alkalinity (eq.4.37) or all the calcium (eq.4.38) becomes calcium carbonate, whichever is the least abundant. Assuming that alkalinity

is in the shortest supply so that eq.(4.37) is true, eqs.(4.26-4.27) become

$$0 = s\left[Alk(0) - Alk(1)\right] + K_{L12}\left[-Alk(1)\right] \tag{4.39}$$

and

$$0 = K_{L12}\left[-Alk(1)\right] - w_2[2CaCO_3(2)] + J_{Alk} \tag{4.40}$$

Solving eq.(4.39) for $Alk(1)$ yields

$$Alk(1) = \frac{s}{s + K_{L12}} Alk(0) \tag{4.41}$$

and solving eq.(4.40) for $CaCO_3(2)$ yields

$$CaCO_3(2) = \frac{1}{2w_2}\left[J_{Alk} + \left(\frac{1}{s} + \frac{1}{K_{L12}}\right)^{-1} Alk(0)\right] \tag{4.42}$$

To understand this solution consider the burial flux of calcium carbonate $w_2 CaCO_3\,(2)$

$$J_{CaCO_3(s)} = w_2 CaCO_3(2) = \frac{1}{2}\left[J_{Alk} + \left(\frac{1}{s} + \frac{1}{K_{L12}}\right)^{-1} Alk(0)\right] \tag{4.43}$$

The concentration of calcium carbonate is determined by a balance between the loss by burial $w_2\ CaCO_3(2)$ and the sources of alkalinity to the sediment on the right hand side of eq.(4.43). As the right hand side of eq.(4.43) increases, the concentration $CaCO_3\,(2)$ increases so that eq.(4.43) remains true.

A portion of the alkalinity transferred to the sediment is via diffusion from the overlying water. The reciprocal of the sum of the reciprocals of the mass transfer coefficients $\left(\frac{1}{s} + \frac{1}{K_{L12}}\right)^{-1}$ is the total mass transfer resistance for transferring overlying water alkalinity $Alk(0)$ to the anaerobic layer. This source is added to the source of alkalinity due to sulfate reduction J_{Alk}. Since $CaCO_3$ is assumed to be completely insoluble, both of these sources of alkalinity are transformed entirely into calcium carbonate. The $\frac{1}{2}$ reflects the two moles of alkalinity that are required to make one mole of calcium carbonate, eq.(4.3).

If the calcium is in shortest supply, then eq.(4.38) is true. Using this result and solving eqs.(4.28-4.29) for $J_{CaCO_3(s)}$ yields

$$J_{CaCO_3(s)} = w_2 CaCO_3(2) = \left(\frac{1}{s} + \frac{1}{K_{L12}}\right)^{-1} Ca(0) \tag{4.44}$$

where the calcium carbonate concentration is now determined by a balance between the loss of calcium via sedimentation of calcium carbonate $w_2\ CaCO_3(s)$ and the source of calcium from the overlying water $\left(\frac{1}{s} + \frac{1}{K_{L12}}\right)^{-1} Ca(0)$.

4.6 APPLICATION TO LONG ISLAND SOUND

The data for this application comes from observations of fluxes from three stations in Long Island Sound ([Aller, 1980b]–[Aller and Yingst, 1980]). The parameters required for the calcium-alkalinity flux model are the usual transport parameters as well as those specific to these components. These are listed in Table 4.1.

Table 4.1 Transport parameter values for the calcium carbonate model

Variable	Value	Units
$Ca(0)$	9	mM
$Alk(0)$	2	mM
K_{CaAlk}	10–30	mM^2

In addition to the source of alkalinity from the overlying water there is also a sediment source of alkalinity, J_{Alk}. This is computed from the ammonia flux using eqs.(3.5–3.38) given above to obtain s and J_N. Redfield stoichiometry (eq.3.35) is used to compute the carbon diagenesis, J_C. If it is assumed that all carbon diagenesis reduces sulfate to sulfide then the following formula applies

$$CH_2O + \frac{1}{2}SO_4^{2-} \rightarrow HCO_3^- + \frac{1}{2}H_2S + H_2O \tag{4.45}$$

Therefore each mole of organic carbon reacted produces one equivalent of bicarbonate alkalinity. However, this conclusion depends on which end-product is assumed for the sulfide formed. For example if HS^- forms then

$$CH_2O + \frac{1}{2}SO_4^{2-} \rightarrow \frac{1}{2}CO_2 + \frac{1}{2}HCO_3^- + \frac{1}{2}HS^- + \frac{1}{2}H_2O \tag{4.46}$$

and one concludes that only 1/2 mole of alkalinity forms. If iron sulfide is the final repository of the sulfide, which is assumed in the sulfide and oxygen flux model [Di Toro and Fitzpatrick, 1993], then the reaction is

$$CH_2O + \frac{4}{9}FeOOH + \frac{4}{9}SO_4^{2-} \rightarrow \frac{1}{9}CO_2 + \frac{8}{9}HCO_3^- + \frac{4}{9}FeS + \frac{7}{9}H_2O \tag{4.47}$$

which is almost a 1 to 1 molar ratio between CH_2O mineralized and alkalinity HCO_3^- produced. The difference between eq.(4.45) and eq.(4.47) is the $1/9^{th}$ mole of organic matter required to reduce the $Fe(III)$ to $Fe(II)$ which does not produce alkalinity. An analysis of the pore water relationships in Chesapeake Bay sediments indicates that a 1 to 1 stoichiometry is actually observed [Di Toro and Fitzpatrick, 1993]. We adopt this stoichiometry for the calculations presented below.

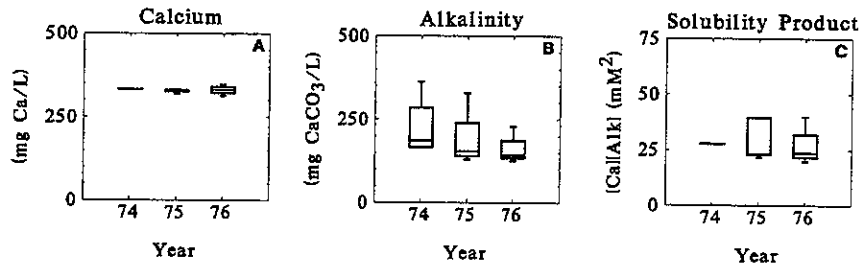

Fig. 4.3 Pore water concentration of (A) dissolved calcium Ca, (B) alkalinity Alk, and (C) the apparent solubility product $Ca \times Alk$ from three Long Island Sound stations.

4.6.1 Chemical Parameters

The only chemical parameter required K_{CaAlk} is the apparent solubility of $CaCO_3$. Fig.4.3 presents the pore water data for dissolved calcium Ca and alkalinity Alk from three Long Island Sound stations. The product: $Ca \times Alk = K_{CaAlk}$ is also presented. It ranges from approximately 20 $(\text{mM})^2$ to over 40 $(\text{mM})^2$. This sets the range for K_{CaAlk}. With the parameters established, the model is evaluated by specifying an ammonia flux and computing the resulting concentrations. The additional parameter values are presented in Table 4.2.

Table 4.2 Parameter values for the calcium carbonate model

Variable	Value
$Ca(0)$	9 mM
$Alk(0)$	2 mM
K_{CaAlk}	10–30 mM^2

4.6.2 Results

Fig.4.4 presents the results for K_{CaAlk} = 10–30 $(\text{mM})^2$. Alkalinity flux increases as ammonia flux increases (Fig.4.4A). This is due to the increased production of alkalinity as a consequence of the increase in sulfate reduction in response to the increase in organic matter deposition that must have occurred to fuel the increase in ammonia flux (eq.4.45). For $K_{CaAlk} = 30$ $(\text{mM})^2$ the solubility of $CaCO_3\,(s)$ is exceeded for $J[NH_4]$ > 10 mg N/m^2-d and $CaCO_3(s)$ starts to form (Fig 4.4E). At that point the calcium flux changes from zero to negative (Fig.4.4B) which is the flux into the sediment that is required to support the burial of $CaCO_3\,(s)$. Also the flux of alkalinity from the sediment to the overlying water increases less rapidly (Fig.4.4A) since a portion is

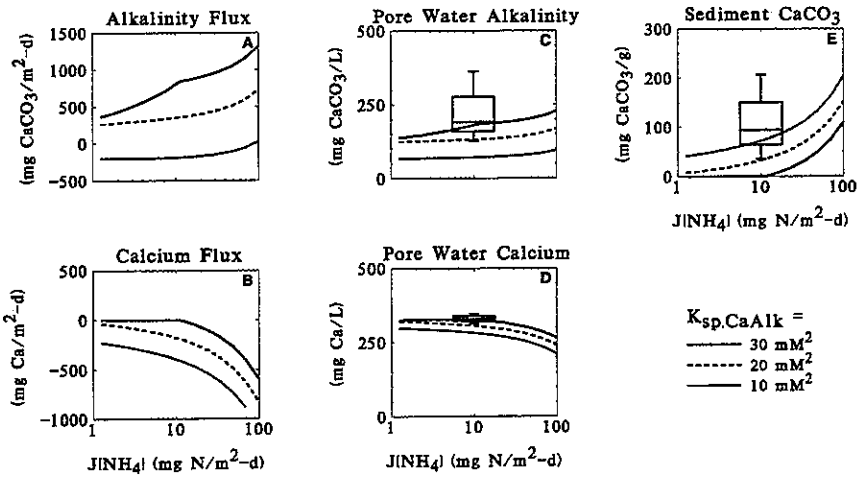

Fig. 4.4 Comparison of model results to Long Island Sound pore water data for various apparent solubility products K_{CaAlk}.

being buried. For smaller solubility products, K_{CaAlk} = 10–20 (mM)^2, $CaCO_3(s)$ forms over the entire range of $J[NH_4]$ investigated (Fig.4.4E) and therefore there is a corresponding calcium flux to the sediment (Fig.4.4B).

Pore water concentrations are compared in Fig.4.4C–D. The data are plotted at $J[NH_4]$ = 10 mg N/m^2-d for convenience only. The annual average ammonia flux is actually somewhat larger. Alkalinity and calcium are reproduced for K_{CaAlk} = 30 (mM)^2. Calcium concentrations as essentially equal to the overlying water concentrations whereas the alkalinity is larger, due to the additional source that results from sulfate reduction.

The concentration of $CaCO_3(s)$ is computed to increase from less than 10 mg $CaCO_3$ (s)/g (1% of dry weight) to over 100 mg $CaCO_3$ (s)/g (10%). Long Island Sound sediments contain between 25 and 200 mg/g. The model reproduces the observations for the lower values of the solubility constant. This is in contrast to the pore water results. Perhaps there is an additional source of calcium carbonate to the sediments, e.g., $CaCO_3(s)$ from bivalve shells, which accounts for the additional $CaCO_3(s)$.

Nevertheless, the model is reasonably successful in reproducing the general features of the data. Pore water calcium concentrations are predicted to be close to the overlying water value, 9 mM = 326 mg/L, whereas alkalinity is predicted to be larger than the overlying value of 2 meq = 100 mg/L. Calcium carbonate concentrations are predicted to be in the range of 10 to 100 mg/g which is the range of the observations. These results are obtained using transport parameters that are calibrated from Chesapeake Bay sediment flux data, suggesting that these parameters are also representative

for these Long Island Sound sediments. In particular, the sedimentation velocity for these sediments is quite close to 0.5 cm/yr. used for these calculations.

4.7 MANGANESE - CALCIUM - ALKALINITY FLUX MODEL

A model is formulated in which the pore water and solid phase concentration of manganese are controlled by the solubility of manganese carbonate. To this end, the calcium carbonate model is included as part of the formulation. The rest of the model parallels the linear partitioning model presented in Chapter 3.

4.8 CHEMISTRY AND SIMPLIFICATIONS

The simplification of the manganese carbonate chemistry parallels that for calcium. The concentration of $Mn(II)^{2+}$ is approximated by the concentration of total dissolved manganese, Mn. This ignores the complexes of manganese with bicarbonate and other ligands. The concentration of carbonate can be approximated using alkalinity as formulated in section 4.3, eq.(4.8). The mass action equation for the solubility of $MnCO_3(s)$ is:

$$[Mn][Alk] = \frac{K_{sp,MnCO_3}}{K_2}[H^+] \triangleq K_{MnAlk} \tag{4.48}$$

Pore water data from Chesapeake Bay sediments [Bricker et al., 1977] and Long Island Sound [Aller, 1980b] are shown in Fig.4.5. $MnAlk$ apparent solubility products are similar for both sets, ranging from 0.1 to 1.0 mM^2.

4.8.1 Equations and Solutions for Manganese and Calcium Carbonate

The mass balance and mass action equations for a closed system which include manganese carbonate as well as calcium carbonate are:

Alkalinity mass balance:

$$Alk_T - 2CaAlk - 2MnAlk - Alk_d = 0 \tag{4.49}$$

Calcium mass balance:

$$Ca_T - Ca_d - CaAlk = 0 \tag{4.50}$$

Manganese mass balance:

$$Mn_T - Mn_d - MnAlk = 0 \tag{4.51}$$

$CaCO_3(s)$ Solubility:

$$Ca_d Alk_d = K_{CaAlk} \tag{4.52}$$

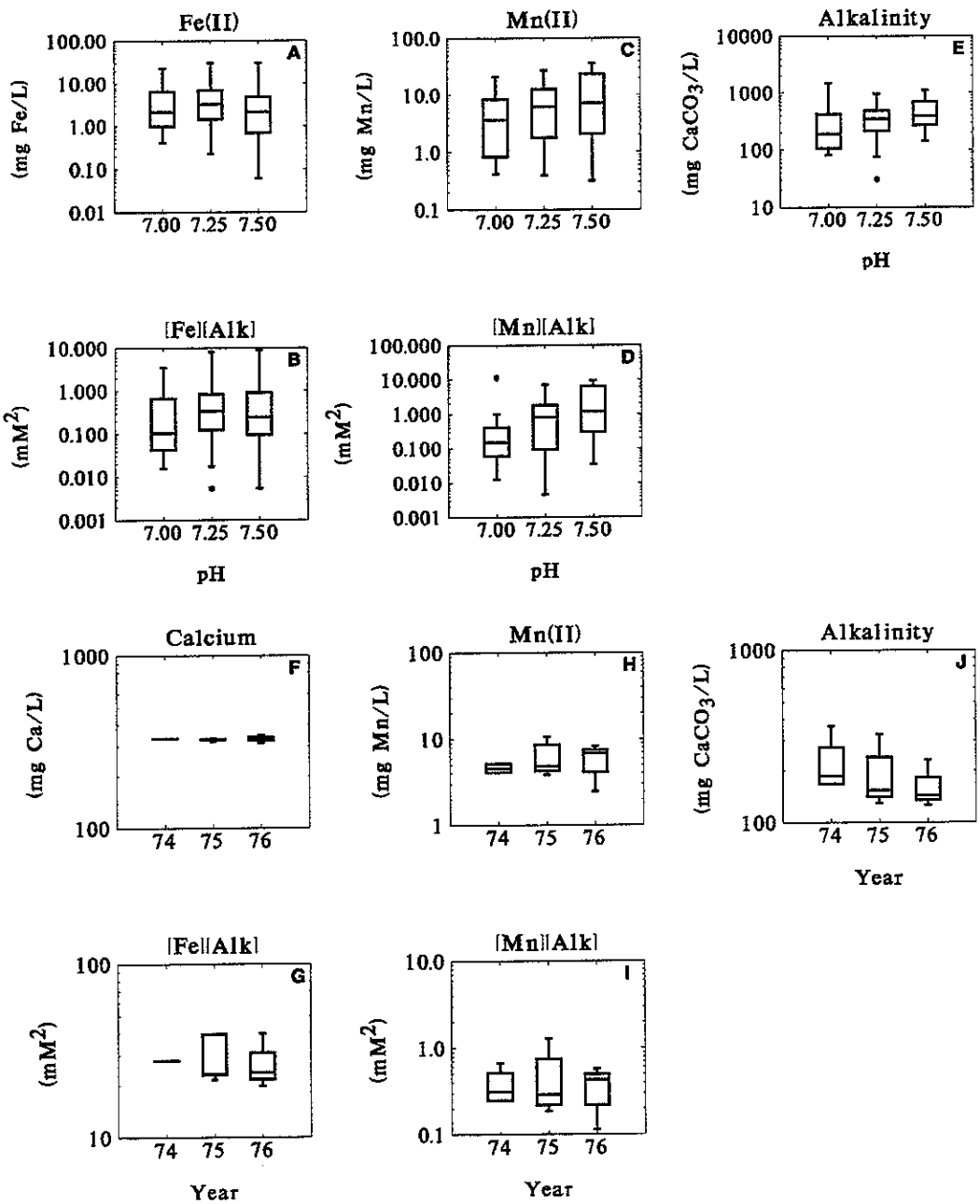

Fig. 4.5 Top: Pore water data from Chesapeake Bay sediments [Bricker et al., 1977]. Bottom: Pore water data from Long Island Sound [Aller, 1980a]

$MnCO_3(s)$ Solubility:

$$Mn_d Alk_d = K_{MnAlk} \tag{4.53}$$

where Alk_T and Alk_d are the total and dissolved alkalinity; Mn_T and Mn_d are the total and dissolved manganese, and Ca_T and Ca_d are the total and dissolved calcium. Eliminating all the independent variables except $MnAlk$ yields a quadratic equation of the form:

$$aMnAlk^2 + bMnAlk + c = 0 \tag{4.54}$$

with coefficients:

$$a = -4(K_{MnAlk} + K_{CaAlk}) \tag{4.55}$$

$$b = 2(2K_{MnAlk}Mn_T + 4K_{CaAlk}Mn_T - 2Ca_T K_{MnAlk} + Alk_T K_{MnAlk}) \tag{4.56}$$

$$c = -2(2K_{CaAlk}Mn_T^2 - 2Ca_T K_{MnAlk}Mn_T + Alk_T K_{MnAlk}Mn_T - K_{MnAlk}) \tag{4.57}$$

The equation for $CaAlk$ is also quadratic:

$$aCaAlk^2 + bCaAlk + c = 0 \tag{4.58}$$

with:

$$a = 2 \tag{4.59}$$

$$b = 2MnAlk - Ca_T - Alk_T \tag{4.60}$$

$$c = -2Ca_T MnAlk - K_{CaAlk} + Alk_T Ca_T \tag{4.61}$$

It is remarkable that adding manganese as a component and $MnCO_3(s)$ as a solid phase does not materially complicate the solution. It requires only the solutions of quadratic equations.

The solution procedure is to solve the quadratic eq.(4.54) for $MnAlk$ which yields two solutions. For each of these solutions, two solutions for $CaAlk$ are found from eq.(4.58). For each of the four possible solutions the dissolved concentrations are computed. Then the solutions are checked for the following conditions.

1. Are all concentrations positive?
2. Are there no oversaturated solids?
3. If both of these conditions are true, then the feasible solution has been found.
4. If no feasible solution is found, then either $CaAlk$ and/or $MnAlk$ are zero and the solution is undersaturated with either or both of these solids.

4.8.2 Results

An example computation is presented below in Tables 4.3 and 4.4. The calcium concentration is kept constant, Ca = 300 mg/L = 7.5 mM which is approximately the concentration in overlying water for the Long Island Sound sediment data. The solubility products are: $K_{CaAlk} = 10$ (mM)^2 and $K_{MnAlk} = 0.4$ (mM)^2. Total alkalinity is varied from 1 to 20 mM and total manganese from 0.05 to 0.5 mM. These ranges are representative for the data considered above. Note that the alkalinity is much larger than the manganese concentrations. The tables 4.3 and 4.4 have alkalinity varying in the vertical direction and manganese in the horizontal direction.

The computed solid phase concentrations, $MnAlk$ and $CaAlk$, and the computed solubility products are given in Table 4.3. $CaAlk$ forms as Alk_T is increased. Its concentration is not affected by the concentration of Mn_T. $MnAlk$ also forms as Alk_T and Mn_T are increased. Its concentration is affected by both independent variables: Alk_T and Mn_T. Note that if the aqueous phase is undersaturated with either solid—the solubility product is less than K_{CaAlk} or K_{MnAlk}—then no solid phase forms. The dissolved concentrations are listed in Table 4.4. They are all positive as required by the feasibility conditions.

4.9 SEDIMENT MODEL EQUATIONS AND SOLUTIONS

The structure of the manganese flux model is illustrated in Fig.4.6. The oxidation of $Mn(II)$ to $MnO_2(s)$ occurs in the aerobic layer, and the reduction or $MnO_2(s)$ to $Mn(II)$ occurs in the anaerobic layer. The partitioning of $Mn(II)$ in the anaerobic layer is controlled by the solubility of $MnCO_3(s)$. In order to calculate the carbonate concentration, the influence of $CaCO_3(s)$ must also be considered. Both these reactions are shown as the solubility of $MnAlk$ and $CaAlk$, as discussed above.

Hence, the equations for the sediment model are a combination of the equations for the linear partitioning model for manganese, with the addition of the equations for calcium, from the calcium-alkalinity model, and a solubility equation for $MnAlk$. The equations and the solution procedures are listed in the Appendix. Once again, the solutions are found from the roots of quadratic equations. They are very similar to the closed system equations, although the coefficients of the equations are much more involved. Nevertheless, no essential complexity is introduced and the numerical solutions are straightforward.

4.9.1 Results

A calibration to the Long Island Sound data is shown in Fig.4.7. The additional parameter values are presented in Table 4.5. The observed pore water alkalinity (Fig.4.7C),

Table 4.3 Concentration and solubility products of $MnAlk$ and $CaAlk$ as a function of Alk_T and Mn_T

Concentrations

Alk_T (mM)	$MnAlk$ (mM)					
1.0000	0	0	0	0	0	0.699
1.8206	0	0	0	0	0.0309	0.2094
3.3145	0	0	0	0	0.0777	0.2566
6.0342	0	0	0	0.0389	0.1525	0.3325
10.9856	0	0.0045	0.0504	0.1230	0.2382	0.4207
20.0000	0.0198	0.0490	0.0952	0.1685	0.2847	0.4688

Alk_T (mM)	$CaAlk$ (mM)					
1.0000	0	0	0	0	0	0
1.8206	0.4101	0.4101	0.4101	0.4101	0.3844	0.2348
3.3145	1.6152	1.6152	1.6152	1.6152	1.5548	1.4146
6.0342	3.5210	3.5210	3.5210	3.4971	3.4266	3.3132
10.9856	5.6321	5.6309	5.6190	5.5998	5.5689	5.5184
20.0000	6.7445	6.7429	6.7404	6.7364	6.7299	6.7195
Mn_T (mM)	0.0500	0.0792	0.1256	0.1991	0.3155	0.5000

Solubility products of $MnAlk$ and $CaAlk$

Alk_T (mM)	$[Mn][Alk]$ (mM)^2					
1.0000	0.0500	0.0792	0.1256	0.1991	0.3155	0.4000
1.8206	0.0705	0.1118	0.1771	0.2808	0.4000	0.4000
3.3145	0.0850	0.1347	0.2134	0.3382	0.4000	0.4000
6.0342	0.1257	0.1992	0.3156	0.4000	0.4000	0.4000
10.9856	0.2677	0.4000	0.4000	0.4000	0.4000	0.4000
20.0000	0.4000	0.4000	0.4000	0.4000	0.4000	0.4000

Alk_T (mM)	$[Ca][Alk]$ (mM)^2					
1.0000	7.5000	7.5000	7.5000	7.5000	7.5000	6.9756
1.8206	10.000	10.000	10.000	10.000	10.000	10.000
3.3145	10.000	10.000	10.000	10.000	10.000	10.000
6.0342	10.000	10.000	10.000	10.000	10.000	10.000
10.9856	10.000	10.000	10.000	10.000	10.000	10.000
20.0000	10.000	10.000	10.000	10.000	10.000	10.000
Mn_T (mM)	0.0500	0.0792	0.1256	0.1991	0.3155	0.5000

Table 4.4 Dissolved concentration of Mn, Alk and Ca as a function of Alk_T and Mn_T

Alk_T (mM)	Mn (mM)					
1.0000	0.0500	0.0792	0.1256	0.1991	0.3155	0.4301
1.8206	0.0500	0.0792	0.1256	0.1991	0.2846	0.2906
3.3145	0.0500	0.0792	0.1256	0.1991	0.2378	0.2434
6.0342	0.0500	0.0792	0.1256	0.1601	0.1629	0.1675
10.9856	0.0500	0.0748	0.0752	0.0760	0.772	0.0793
20.0000	0.0302	0.303	0.304	0.0305	0.0308	0.0312

Alk_T (mM)	Alk (mM)					
1.0000	1.0000	1.0000	1.0000	1.0000	1.0000	0.9301
1.8206	1.4105	1.4105	1.4105	1.4105	1.4105	1.3764
3.3145	1.6993	1.6993	1.6993	1.6993	1.6820	1.6433
6.0342	2.5132	2.5132	2.5132	2.4982	2.4550	2.3885
10.9856	5.3535	5.3502	5.3163	5.2627	5.1784	5.046
20.0000	13.236	13.208	13.164	13.095	12.985	12.812
Mn_T (mM)	0.0500	0.0792	0.1256	0.1991	0.3155	0.5000

Alk_T (mM)	Ca (mM)					
1.0000	7.5000	7.5000	7.5000	7.5000	7.5000	7.5000
1.8206	7.0899	7.0899	7.0899	7.0899	7.1156	7.2652
3.3145	5.8848	5.8848	5.8848	5.8848	5.9452	6.0854
6.0342	3.9790	3.9790	3.9790	4,0029	4.0734	4.1868
10.9856	1.8679	1.8691	1.8810	1.9002	1.9311	1.9816
20.0000	0.7555	0.7571	0.7596	0.7636	0.7701	0.7805
Mn_T (mM)	0.0500	0.0792	0.1256	0.1991	0.3155	0.5000

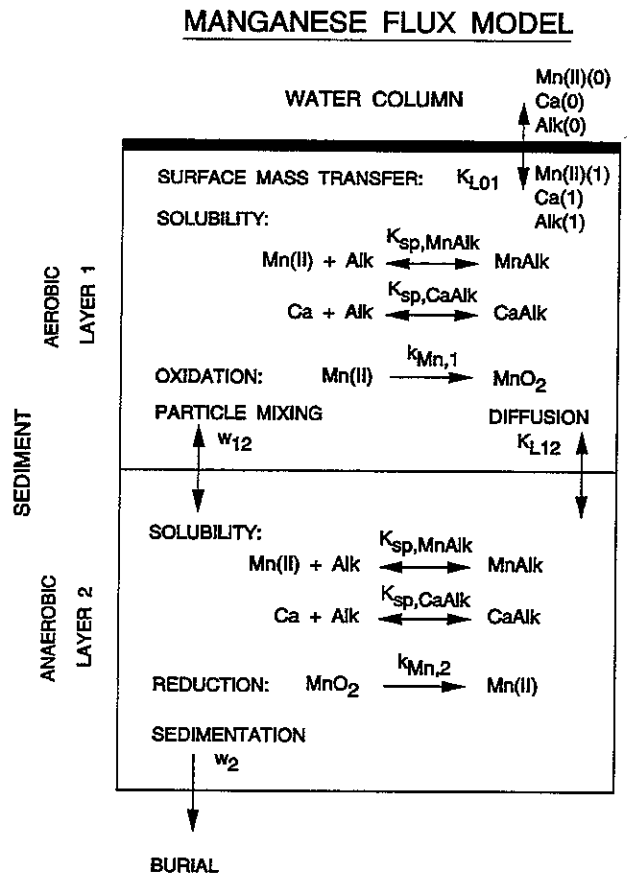

Fig. 4.6 Schematic diagram of the $Mn - Ca - Alk$ Model

calcium (Fig.4.7D), and $CaCO_3(s)$ (Fig.4.7E) are reproduced by the model calculations. The data are plotted at $J[NH_4] = 10$ mg/m^2-d for convenience. The fit is actually slightly better than the model for $CaCO_3(s)$ alone, Fig.4.4.

The manganese results are shown in Fig.4.8. Pore water manganese is reproduced reasonably closely (C) while the computed concentration of $MnCO_3(s)$ is higher than the observation (D). The manganese flux varies with respect to ammonia flux (A,B). However it is still not as pronounced as the observations (E).

4.9.2 Conclusions

The inclusion of manganese carbonate precipitation as the speciation reaction that controls manganese partitioning in the anaerobic layer has slightly improved the model results. However if the results are compared to the linear partitioning case—compare Fig. 3.6 to Fig.4.8—it is clear that the model is producing substantially the same results. The addition of the chemical control on partitioning in the anaerobic layer has

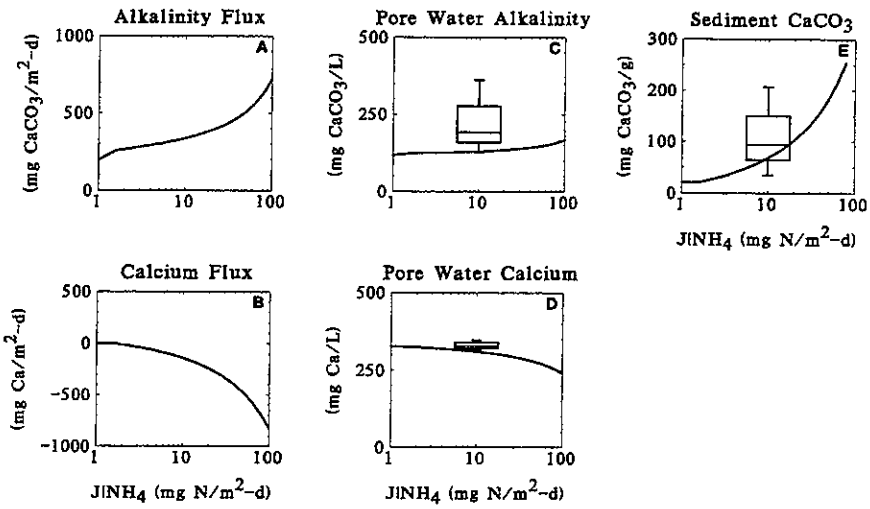

Fig. 4.7 Comparison of model and data from Long Island Sound. Pore water calcium, alkalinity, and sediment calcium carbonate concentrations.

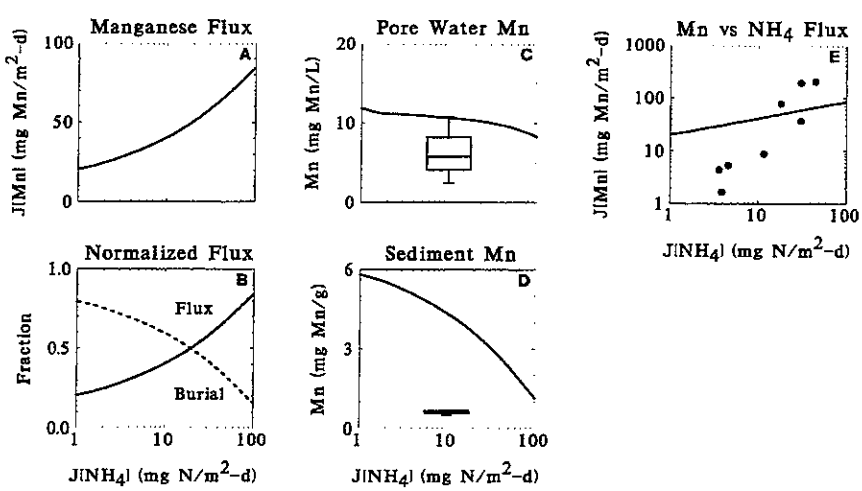

Fig. 4.8 Comparison of model and Long Island Sound data. Pore water and sediment manganese concentrations. Manganese versus ammonia flux.

Table 4.5 Parameter values for the $MnCO_3$ and $CaCO_3$ model

Variable	Value	Units
$\kappa_{Mn,1}$	0.03	m/d
$\kappa_{Mn,2}$	10	m/d
pi_1	300	L/kg
K_{CaCO_3}	20	mM^2
K_{CaCO_3}	0.5	mM^2

not fundamentally changed the model's behavior, at the cost of an order of magnitude increase in complexity of the resulting equations. Thus, this approach is abandoned and the linear partitioning formulation is retained.

The next step is to examine the time variable version of the model, which is presented in the next chapter.

Appendix: Equations and Solutions for $MnCO_3$, $CaCO_3$, Alkalinity and TIC

The mass balance equations are:

Layer 1 Alkalinity

$$K_{L12}\left(-2MnAlk - 2\,CaAlk + Alk\,(2) - Alk\,(1)\right) - \left(Alk\,(1) - Alk\,(0)\right)\,s = 0 \quad \text{(A.1)}$$

Layer 2 Alkalinity

$$\begin{aligned} 0 &= -w_2\,(2MnAlk + 2\,CaAlk) \\ &\quad -K_{L12}\left(-2MnAlk - 2\,CaAlk + Alk\,(2) - Alk\,(1)\right) + J_{Alk} \end{aligned} \quad \text{(A.2)}$$

Layer 1 Calcium

$$-Ca\,(1)\;s + Ca\,(0)\;s + \left(-CaAlk + Ca\,(2) - Ca\,(1)\right)\,K_{L12} = 0 \quad \text{(A.3)}$$

Layer 2 Calcium

$$-\left(-CaAlk + Ca\,(2) - Ca\,(1)\right)\,K_{L12} - w_2\,CaAlk = 0 \quad \text{(A.4)}$$

Layer 1 $Mn(II)$

$$\begin{aligned} 0 &= -\left(Mn\,(1)\;f_d - Mn\,(0)\right)\,s + w_{12}\,\left(MnAlk - Mn\,(1)\;f_p\right) \\ &\quad +K_{L12}\left(-MnAlk - Mn\,(1)\;f_d + Mn\,(2)\right) - \kappa_1\,Mn\,(1)\;f_d \end{aligned} \quad \text{(A.5)}$$

Layer 2 $Mn(II)$

$$\begin{aligned} 0 &= -w_{12}\,\left(MnAlk - Mn\,(1)\;f_p\right) - w_2 MnAlk \\ &\quad -K_{L12}\left(-MnAlk - Mn\,(1)\;f_d + Mn\,(2)\right) + \kappa_2\,MnO_2\,(2) \end{aligned} \quad \text{(A.6)}$$

Layer 1 $MnO_2(s)$

$$J_{MnO_2} + \kappa_1\,Mn\,(1)\;f_d + \left(MnO_2\,(2) - MnO_2\,(1)\right)\,w_{12} = 0 \quad \text{(A.7)}$$

Layer 2 $MnO_2(s)$

$$-\left(MnO_2\,(2) - MnO_2\,(1)\right)\,w_{12} - MnO_2\,(2)\;w_2 - \kappa_2\,MnO_2\,(2) = 0 \quad \text{(A.8)}$$

The mass action equations are

Layer 2 $CaCO_3(s)$ Solubility

$$\left(Ca\,(2) - CaAlk\right)\,\left(-2MnAlk - 2\,CaAlk + Alk\,(2)\right) - K_{sp,CaCO_3} = 0 \quad \text{(A.9)}$$

Layer 2 $MnCO_3(s)$ Solubility

$$(-2MnAlk - 2\,CaAlk + Alk\,(2))\;(Mn\,(2) - MnAlk) - K_{sp,MnCO_3} = 0 \qquad \text{(A.10)}$$

The first step in the solution is to solve for all the dependent variables except $CaAlk\,(2)$ and $MnAlk(2)$ using the mass balance equations. The solutions are

$$Alk\,(1) = \frac{Alk(0)\;s - 2\,K_{L12}MnAlk - 2\,CaAlk\,K_{L12} + Alk(2)\;K_{L12}}{s + K_{L12}} \qquad \text{(A.11)}$$

$$Ca\,(1) = \frac{Ca\,(0)\;s - CaAlk\,K_{L12} + Ca\,(2)\;K_{L12}}{s + K_{L12}} \qquad \text{(A.12)}$$

$$Mn\,(1) = \frac{Mn(0)\;s - K_{L12}MnAlk + w_{12}\,MnAlk + Mn(2)\;K_{L12}}{f_d\,s + w_{12}\,f_p + f_d\,K_{L12} + \kappa_1\,f_d} \qquad \text{(A.13)}$$

$$Alk\,(2) = \frac{\begin{array}{c} 2\,K_{L12}MnAlk\,s - 2\,w_2MnAlk\,s + 2\,CaAlk\,K_{L12}\,s \\ +Alk(0)\;K_{L12}\,s - 2\,w_2\,CaAlk\,s + J_{Alk}\,s \\ -2\,w_2\,K_{L12}MnAlk\;-2\,w_2\,CaAlk\,K_{L12} + J_{Alk}\,K_{L12} \end{array}}{K_{L12}\,s} \qquad \text{(A.14)}$$

$$Ca\,(2) = \frac{CaAlk\,K_{L12}\,s + Ca\,(0)\;K_{L12}\,s - w_2\,CaAlk\,s - w_2\,CaAlk\,K_{L12}}{K_{L12}\,s} \qquad \text{(A.15)}$$

$$Mn\,(2) = \frac{\left\{\begin{array}{c} \kappa_2\left(\begin{array}{c} Mn\,(0)\;w_{12}\,f_p\,s + f_d\,J_{MnO_2}\,s - w_{12}\,f_d\,MnAlk\,s \\ -w_2\,f_dMnAlk\,s + w_{12}\,J_{MnO_2}\,f_p - w_2\,w_{12}MnAlk\,f_p \end{array}\right) \\ +w_2\left(\begin{array}{c} Mn\,(0)\;w_{12}\,f_p\,s - w_{12}\,f_d\,MnAlk\,s - w_2\,f_dMnAlk\,s \\ -w_2\,w_{12}MnAlk\,f_p \end{array}\right) \\ +\kappa_2\,f_d\,K_{L12}\;(MnAlk\,s + Mn\,(0)\;s + J_{MnO_2} - w_2MnAlk) \\ +w_2\,f_d\,K_{L12}\;(MnAlk\,s + Mn\,(0)\;s - w_2MnAlk) \\ +\kappa_1\,\kappa_2\,f_d\;(Mn\,(0)\;s + J_{MnO_2} - w_2MnAlk) \\ +\kappa_1\,w_2\,f_d\,K_{L12}MnAlk - \kappa_1\,w_2\,f_d\;(w_{12} + w_2)MnAlk \end{array}\right\}}{w_2\,f_d\,K_{L12}\,s + \kappa_2\,f_d\,K_{L12}\,s + \kappa_1\,w_2\,f_d\,K_{L12}} \qquad \text{(A.16)}$$

$$MnO_2\,(1) = \frac{\begin{array}{c} (w_{12} + w_2 + \kappa_2) \\ (J_{MnO_2}\,s + Mn\,(0)\;\kappa_1\,s + \kappa_1\,J_{MnO_2} - \kappa_1\,w_2MnAlk) \end{array}}{w_{12}\;(w_2\,s + \kappa_2\,s + \kappa_1\,w_2)} \qquad \text{(A.17)}$$

$$MnO_2\,(2) = \frac{J_{MnO_2}\,s + Mn(0)\;\kappa_1\,s + \kappa_1\,J_{MnO_2} - \kappa_1\,w_2MnAlk}{w_2\,s + \kappa_2\,s + \kappa_1\,w_2} \qquad \text{(A.18)}$$

The mass action equations are used to solve for $CaAlk$ and $MnAlk$. Only the layer two solutions that are needed in these equations. They are written in the following form in order to substitute for various parameter groups and to isolate the dependency

on $CaAlk$ and $MnAlk$:

$$Alk(2) = \mathcal{J}_{a0} + \mathcal{J}_{ac} CaAlk(2) + \mathcal{J}_{am} MnAlk(2) \tag{A.19}$$

$$Ca(2) = \mathcal{J}_{c0} + \mathcal{J}_{cc} CaAlk(2) + \mathcal{J}_{cm} MnAlk(2) \tag{A.20}$$

$$Mn(2) = \mathcal{J}_{m0} + \mathcal{J}_{mc} CaAlk(2) + \mathcal{J}_{mm} MnAlk(2) \tag{A.21}$$

where the notation denotes the Jacobian ($\mathcal{J}$) of the equation (a, c, m for Alk, Ca, Mn) with respect to the variables c, m for $CaAlk$, $MnAlk$, or 0 for the constant term.

$$\mathcal{J}_{a0} = \frac{Alk(0)\ K_{L12}\, s + J_{Alk}\, s + J_{Alk}\, K_{L12}}{K_{L12}\, s} \tag{A.22}$$

$$\mathcal{J}_{ac} = \frac{2\ (K_{L12}\, s - w_2\, s - w_2\, K_{L12})}{K_{L12}\, s} \tag{A.23}$$

$$\mathcal{J}_{am} = \frac{2\ (K_{L12}\, s - w_2\, s - w_2\, K_{L12})}{K_{L12}\, s} \tag{A.24}$$

$$\mathcal{J}_{c0} = Ca\,(0) \tag{A.25}$$

$$\mathcal{J}_{cc} = \frac{K_{L12}\, s - w_2\, s - w_2\, K_{L12}}{K_{L12}\, s} \tag{A.26}$$

$$\mathcal{J}_{cm} = 0 \tag{A.27}$$

$$\mathcal{J}_{m0} = \frac{\begin{array}{c} Mn(0)\ w_2\, w_{12}\, f_p\, s + Mn(0)\ \kappa_2\, w_{12}\, f_p\, s + \kappa_2\, f_d\, J_{MnO_2}\, s \\ + Mn(0)\ w_2\, f_d\, K_{L12}\, s + Mn(0)\ \kappa_2\, f_d\, K_{L12}\, s + Mn(0)\ \kappa_1\, \kappa_2\, f_d\, s \\ + \kappa_2\, w_{12}\, J_{MnO_2}\, f_p + \kappa_2\, f_d\, K_{L12}\, J_{MnO_2} + \kappa_1\, \kappa_2\, f_d\, J_{MnO_2} \end{array}}{f_d\, K_{L12}\ (w_2\, s + \kappa_2\, s + \kappa_1\, w_2)} \tag{A.28}$$

$$\mathcal{J}_{mc} = 0 \tag{A.29}$$

$$\mathcal{J}_{mm} = \frac{\begin{array}{c} w_2\, f_d\, K_{L12}\, s + \kappa_2\, f_d\, K_{L12}\, s - w_2\, w_{12}\, f_d\, s - \kappa_2\, w_{12}\, f_d\, s \\ - w_2^2\, f_d\, s - \kappa_2\, w_2\, f_d\, s - w_2^2\, w_{12}\, f_p - \kappa_2\, w_2\, w_{12}\, f_p \\ - w_2^2\, f_d\, K_{L12} - \kappa_2\, w_2\, f_d\, K_{L12} + \kappa_1\, w_2\, f_d\, K_{L12} - \kappa_1\, w_2\, w_{12}\, f_d \\ - \kappa_1\, w_2^2\, f_d - \kappa_1\, \kappa_2\, w_2\, f_d \end{array}}{f_d\, K_{L12}\ (w_2\, s + \kappa_2\, s + \kappa_1\, w_2)} \tag{A.30}$$

An important relationship among these coefficients is:

$$\mathcal{J}_{ac} = 2\mathcal{J}_{cc} \tag{A.31}$$

$$\mathcal{J}_{am} = 2\mathcal{J}_{cc} \tag{A.32}$$

Using these equations and substituting into the mass action equations yields quadratic equations for both $CaAlk$ and $MnAlk$. The form is:

$$aCaAlk^2 + bCaAlk + c = 0 \tag{A.33}$$

and similarly for $MnAlk$. The coefficients for $MnAlk(2)$ are denoted by the subscript Mn:

$$\begin{aligned} a_{Mn} &= 2K_{CaAlk} + 2\mathcal{J}_{mm}^2 K_{CaAlk} + \mathcal{J}_{mm}(-4K_{CaAlk} - 2K_{MnAlk}) \\ &\quad +2K_{MnAlk} + \mathcal{J}_{cc}(-2K_{MnAlk} + 2\mathcal{J}_{mm}K_{MnAlk}) \end{aligned} \tag{A.34}$$

$$\begin{aligned} b_{Mn} &= \mathcal{J}_{m0}(-4K_{CaAlk} + 4\mathcal{J}_{mm}K_{CaAlk} - 2K_{MnAlk} \\ &\quad +\mathcal{J}_{c0}(2K_{MnAlk} - 2\mathcal{J}_{mm}K_{MnAlk}) \\ &\quad +\mathcal{J}_{a0}(-K_{MnAlk} + \mathcal{J}_{mm}K_{MnAlk} \end{aligned} \tag{A.35}$$

$$\begin{aligned} c_{Mn} &= -(-2\mathcal{J}_{m0}^2 K_{CaAlk} + K_{MnAlk} \\ &\quad +\mathcal{J}_{m0}(-(\mathcal{J}_{a0}K_{MnAlk}) + 2\mathcal{J}_{c0}K_{MnAlk})) \end{aligned} \tag{A.36}$$

and for $CaAlk(2)$ which are denoted by the subscript Ca:

$$a_{Ca} = 2 - 4\mathcal{J}_{cc} + 2\mathcal{J}_{cc}^2 \tag{A.37}$$

$$\begin{aligned} b_{Ca} &= \mathcal{J}_{a0}(-1 + \mathcal{J}_{cc}) + (-2 + 2\mathcal{J}_{cc})\mathcal{J}_{c0} + 2MnAlk(2) \\ &\quad -4\mathcal{J}_{cc}MnAlk(2) + 2\mathcal{J}_{cc}^2 MnAlk(2) \end{aligned} \tag{A.38}$$

$$c_{Ca} = -(-(\mathcal{J}_{a0}\mathcal{J}_{c0}) + K_{CaAlk} + \mathcal{J}_{c0}(2MnAlk(2) - 2\mathcal{J}_{cc}MnAlk(2)) \tag{A.39}$$

The solution procedure is to solve the quadratic equation for $MnAlk(2)$ which yields two solutions. For each of these solutions, two solutions for $CaAlk(2)$ are found. For each of the four possible solutions the rest of the variables are computed. Then the solutions are checked for the following conditions. Are all concentrations positive? Are there no oversaturated solids? If both of these conditions are true, then the feasible solution has been found. If no feasible solution is found, then either $CaAlk$ and/or $MnAlk$ are zero and the solution is undersaturated with either or both of these solids.

5

Time Variable Linear Partitioning Model

5.1 INTRODUCTION

This chapter presents the formulation and application of the time variable version of the linear partitioning manganese flux model presented in Chapter 3. The MERL data set is used for calibration and comparison.

5.2 MODEL FORMULATION

The time variable manganese flux model is a straightforward extension of the steady state model discussed in Chapter 3. The time variation introduces an additional feature besides the need to consider the derivatives in eqs.(3.11a–3.11d). It is related to the variation in the thickness of the aerobic and anaerobic layers and the mass balance consequences.

5.2.1 Entrainment Flux

The time variable form of the mass balance equations can be derived by considering the rate of change of the mass of the constituent being considered in each layer. For a concentration c_1 and a depth H_1 the product $H_1 c_1$ is the mass/unit area, e.g. mg/m^2, in layer 1. The mass balance equations equate the rate of change of the mass to the sources and sinks

$$\frac{d\,(H_1 c_1)}{dt} = S_1 \tag{5.1a}$$

$$\frac{d\,(H_2 c_2)}{dt} = S_2 \tag{5.1b}$$

where S_1 and S_2 represent all the source-sink terms. Consider what happens if the layer thickness changes and there are no sources or sinks. The situation is illustrated in Fig. 5.1. Eqs.(5.1) become

$$\frac{d\,(H_1 c_1)}{dt} = 0 \tag{5.2a}$$

$$\frac{d\,(H_2 c_2)}{dt} = 0 \tag{5.2b}$$

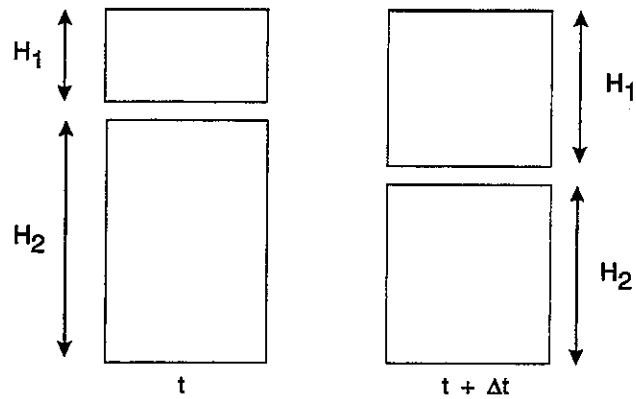

Fig. 5.1 Volume changes from t to $t + \Delta t$.

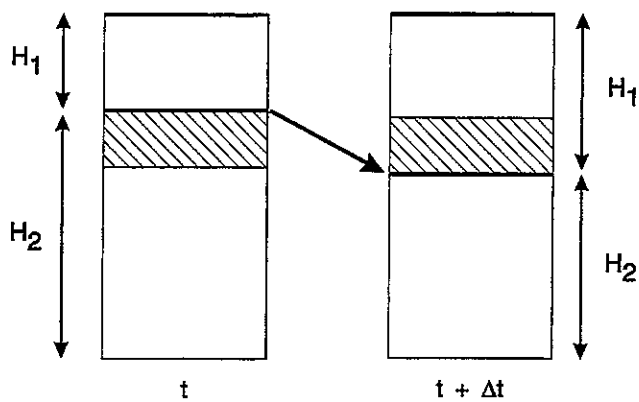

Fig. 5.2 Entrainment of layer 2 mass (shaded region) into layer 1 during the time step Δt as H_1 increases.

and the solutions are

$$H_1(t)\, c_1\,(t) \;=\; H_1(0)\, c_1\,(0) \tag{5.3a}$$

$$H_2(t)\, c_2\,(t) \;=\; H_2(0)\, c_2\,(0) \tag{5.3b}$$

That is, the mass in each layer remains constant over the time interval Δt. Therefore the volumes are not connected in any way. As the volume expands or contracts, the concentrations decrease or increase, respectively, to keep the mass constant.

However, this is not the correct result if the depth of one layer is changing at the expense of the other. In the sediment, the motion of the H_1–H_2 boundary causes an entrainment of mass into and out of the layers. This is illustrated in Fig. 5.2.Consider the sediment column at time t. Suppose that during the time Δt the H_1–H_2 boundary moves downward as illustrated. For this case H_1 is increasing and $dH_1/dt > 0$. Then the shaded layer of sediment, which was in H_2 at time t, moves into H_1 at time $t+\Delta t$.

This amounts to a loss of mass from H_2 and a gain for H_1. Thus the mass balance equations become

$$\frac{d(H_1c_1)}{dt} = +c_2\frac{dH_1}{dt} \tag{5.4a}$$

$$\frac{d(H_2c_2)}{dt} = -c_2\frac{dH_1}{dt} \tag{5.4b}$$

For the case that the boundary moves upward and $dH_1/dt < 0$ the source and sink terms are reversed

$$\frac{d(H_1c_1)}{dt} = -c_1\left|\frac{dH_1}{dt}\right| = +c_1\frac{dH_1}{dt} \tag{5.5a}$$

$$\frac{d(H_2c_2)}{dt} = +c_1\left|\frac{dH_1}{dt}\right| = -c_1\frac{dH_1}{dt} \tag{5.5b}$$

Mass is lost from top layer and gained by the bottom layer. The absolute value signs are employed to emphasize that the amount of mass entrained is determined by the magnitude of dH_1/dt and not its sign.

It is possible to write eqs.(5.5) as one set of equations by defining the functions

$$\dot{H}_1^+ = \begin{cases} \dfrac{dH_1}{dt} & \text{if } \dfrac{dH_1}{dt} \geq 0 \\ 0 & \text{if } \dfrac{dH_1}{dt} < 0 \end{cases} \tag{5.6a}$$

$$\dot{H}_1^- = \begin{cases} -\dfrac{dH_1}{dt} & \text{if } \dfrac{dH_1}{dt} \leq 0 \\ 0 & \text{if } \dfrac{dH_1}{dt} > 0 \end{cases} \tag{5.6b}$$

where the dot denotes the time derivative. A straightforward way of computing this function is to use the magnitude of the derivative so that positive and negative terms subtract as appropriate to give zero[1].

$$\dot{H}_1^+ = +\frac{1}{2}\left(\frac{dH_1}{dt} + \left|\frac{dH_1}{dt}\right|\right) = +\frac{1}{2}\left(\dot{H}_1 + \left|\dot{H}_1\right|\right) \tag{5.7a}$$

$$\dot{H}_1^- = -\frac{1}{2}\left(\frac{dH_1}{dt} - \left|\frac{dH_1}{dt}\right|\right) = -\frac{1}{2}\left(\dot{H} - \left|\dot{H}_1\right|\right) \tag{5.7b}$$

[1]A straightforward implimentation of eq.(5.6) involves the use of `if()` statements. For compilers that parallelize computations it is imperative that `if()` statements be avoided. The `abs()` function is faster and accomplishes the same thing.

Using these functions the mass balance equations which include entrainment can be written as

$$\frac{d\left(H_1 c_1\right)}{dt} = +c_2 \dot{H}_1^+ - c_1 \dot{H}_1^- \tag{5.8a}$$

$$\frac{d\left(H_2 c_2\right)}{dt} = -c_2 \dot{H}_1^+ + c_1 \dot{H}_1^- \tag{5.8b}$$

and employing the chain rule for the derivatives yields

$$H_1 \frac{dc_1}{dt} + c_1 \frac{dH_1}{dt} = +c_2 \dot{H}_1^+ - c_1 \dot{H}_1^- \tag{5.9a}$$

$$H_2 \frac{dc_2}{dt} + c_2 \frac{dH_2}{dt} = -c_2 \dot{H}_1^+ + c_1 \dot{H}_1^- \tag{5.9b}$$

and finally

$$H_1 \frac{dc_1}{dt} = +c_2 \dot{H}_1^+ - c_1 \left(\dot{H}_1 + \dot{H}_1^-\right) \tag{5.10a}$$

$$H_2 \frac{dc_2}{dt} = -c_2 \left(\dot{H}_2 + \dot{H}_1^+\right) + c_1 \dot{H}_1^- \tag{5.10b}$$

where $\dot{H}_1 = dH_1 dt$ and $\dot{H}_2 = dH_2 dt$.

5.2.2 Layer Thickness

The time derivative of the aerobic layer thickness $\dot{H}_1$ is computed from the equation specifying H_1(eq.3.4) and from substituting $s = SOD/O_2\left(0\right)$

$$H_1 = \frac{D_1\left[O_2\left(0\right)\right]}{SOD} \tag{5.11}$$

Taking the derivative of this equation yields

$$\frac{dH_1}{dt} = \frac{SOD \dfrac{d\left(D_1\left[O_2\left(0\right)\right]\right)}{dt} - \left(D_1\left[O_2\left(0\right)\right]\right)\dfrac{dSOD}{dt}}{SOD^2} \tag{5.12}$$

$$= \frac{1}{SOD}\left(\frac{d\left(D_1\left[O_2\left(0\right)\right]\right)}{dt} - \frac{dSOD}{dt} H_1\right) \tag{5.13}$$

The variation in H_2 comes from the assumption of a constant active layer depth H_T

$$H_T = H_1 + H_2 \tag{5.14}$$

Differentiating with respect to t yields

$$0 = \frac{dH_1}{dt} + \frac{dH_2}{dt} \tag{5.15}$$

or

$$\frac{dH_2}{dt} = -\frac{dH_1}{dt} \tag{5.16}$$

which simply states that as H_1 increases H_2 decreases and vise versa.

5.2.3 Model Equations

The linear partitioning model as described in Chapter 3 is the basis for the time variable version. The mass balance equations for the model are based on eqs.(3.11a–3.11d) with the addition of the entrainment terms.

Layer 1 $Mn(II)$:

$$\begin{aligned} H_1\frac{dMn(1)}{dt} &= -s\left(f_{d1}Mn(1) - Mn\,(0)\right) + K_{L12}(f_{d2}Mn(2) - f_{d1}Mn(1)) \\ &+w_{12}(f_{p2}Mn(2) - f_{p1}Mn(1)) - w_2Mn\,(1) - \frac{\kappa^2_{Mn,1}}{s}f_{d1}Mn(1) \\ &+Mn\,(2)\,\dot{H}_1^+ - Mn\,(1)\left(\dot{H}_1 + \dot{H}_1^-\right) \end{aligned} \tag{5.17a}$$

Layer 2 $Mn(II)$:

$$\begin{aligned} H_2\frac{dMn(2)}{dt} &= -K_{L12}(f_{d2}Mn(2) - f_{d1}Mn(1)) \\ &-w_{12}(f_{p2}Mn(2) - f_{p1}Mn(1)) - w_2\left(Mn(2) - Mn(1)\right) \\ &+\kappa_{Mn,2}MnO_2(2) - Mn(2)\left(\dot{H}_2 + \dot{H}_1^+\right) + Mn(1)\dot{H}_1^- \end{aligned} \tag{5.17b}$$

Layer 1 $MnO_2\,(s)$:

$$\begin{aligned} H_1\frac{dMnO_2(1)}{dt} &= \frac{\kappa^2_{Mn,1}}{s}f_{d1}Mn(1) - w_2MnO_2(1) \\ &+w_{12}(MnO_2(2) - MnO_2(1)) + J_{MnO_2} \\ &+MnO_2(2)\dot{H}_1^+ - MnO_2(1)\left(\dot{H}_1 + \dot{H}_1^-\right) \end{aligned} \tag{5.17c}$$

Layer 2 $MnO_2\,(s)$:

$$\begin{aligned} H_1\frac{dMnO_2(2)}{dt} &= -\kappa_{Mn,2}MnO_2(2) \\ &-w_{12}(MnO_2(2) - MnO_2(1)) - w_2\left(MnO_2(2) - MnO_2(1)\right) \\ &-MnO_2(2)\left(\dot{H}_2 + \dot{H}_1^+\right) + MnO_2(1)\dot{H}_1^- \end{aligned} \tag{5.17d}$$

The numerical scheme used to solve these equations is the same implicit integration technique that is used for the nutrient model equations [Di Toro and Fitzpatrick, 1993]. Since there are four equations matrix notation will be used. Equations (5.17) are written as

$$\mathbf{H}(t)\frac{d\mathbf{c}(t)}{dt} = \mathbf{A}(\mathbf{t})\mathbf{c}(t) + \mathbf{b}(t) \tag{5.18}$$

where the bold face symbols denote vectors (lower case) and matrices (upper case). The manganese concentration state variable vector is

$$\mathbf{c}(t) = \begin{bmatrix} Mn(1) \\ Mn(2) \\ MnO_2(1) \\ MnO_2(2) \end{bmatrix} \tag{5.19}$$

The matrix $\mathbf{A}(t) = [a_{ij}]$ has elements

$$a_{11} = -sf_{d1} - f_{12} - w_2 - \frac{\kappa^2_{Mn,1}}{s} f_{d1} - \left(\dot{H}_1 + \dot{H}_1^-\right) \tag{5.20a}$$

$$a_{12} = f_{21} + \dot{H}_1^+ \tag{5.20b}$$

$$a_{21} = f_{12} + w_2 + \dot{H}_1^- \tag{5.20c}$$

$$a_{22} = -f_{21} - w_2 - \left(\dot{H}_2 + \dot{H}_1^+\right) \tag{5.20d}$$

$$a_{24} = \kappa_{Mn,2} \tag{5.20e}$$

$$a_{31} = \frac{\kappa^2_{Mn,1}}{s} f_{d1} \tag{5.20f}$$

$$a_{33} = -w_{12} - w_2 - \left(\dot{H}_1 + \dot{H}_1^-\right) \tag{5.20g}$$

$$a_{34} = w_{12} + \dot{H}_1^+ \tag{5.20h}$$

$$a_{43} = w_{12} + w_2 + \dot{H}_1^- \tag{5.20i}$$

$$a_{44} = -\kappa_{Mn,2} - w_{12} - w_2 - \left(\dot{H}_2 + \dot{H}_1^+\right) + \dot{H}_1^- \tag{5.20j}$$

where f_{12} and f_{21} are the effective mass transfer coefficients from layer 1 to layer 2 and from layer 2 to layer 1 respectively

$$f_{12} = K_{L12} f_{d1} + w_{12} f_{p1} \tag{5.21a}$$

$$f_{21} = K_{L12} f_{d2} + w_{12} f_{p2} \tag{5.21b}$$

and all other a_{ij}'s are zero. The forcing function is

$$\mathbf{b}(t) = \begin{bmatrix} sMn(0)(t) \\ 0 \\ J_{MnO_2}(t) \\ 0 \end{bmatrix} \tag{5.22}$$

and $\mathbf{H}(t)$ is a diagonal matrix of layer depths.

$$\mathbf{H}(t) = \text{diag}\left[\ H_1(t) \quad H_2(t) \quad H_1(t) \quad H_2(t)\ \right] \tag{5.23}$$

A finite difference equation is used to solve eq.(5.18). An implicit forward in time scheme [Hamming, 1962] is used for the concentrations since some of the coefficients in $\mathbf{A}$ can become quite large, e.g. $\kappa^2_{Mn,1}/s$ if s is small, and an explicit scheme would require an unacceptably small Δt to remain stable. The $\mathbf{A}$ and $\mathbf{H}$ matrices are evaluated at time level t for the terms coupled to the other state variables such as s. Otherwise, the equation set would be nonlinear and more difficult to solve. The resulting finite difference equation is

$$\mathbf{H}(t)\frac{\mathbf{c}(t+\Delta t) - \mathbf{c}(t)}{\Delta t} = \mathbf{A}(t)\mathbf{c}(t+\Delta t) + \mathbf{b}(t) \tag{5.24}$$

which can be factored

$$(\mathbf{H}(t) - \Delta t\mathbf{A}(t))\,\mathbf{c}(t+\Delta t) = \mathbf{H}(t)\mathbf{c}(t) + \Delta t\mathbf{b}(t) \tag{5.25}$$

and solved

$$\mathbf{c}(t+\Delta t) = (\mathbf{H}(t) - \Delta t\mathbf{A}(t))^{-1}\,(\mathbf{H}(t)\mathbf{c}(t) + \Delta t\mathbf{b}(t)) \tag{5.26}$$

by inverting the matrix as shown, or, using a more efficient linear equation solver [Press et al., 1989] applied to eq.(5.25). It requires the solution of four simultaneous linear equations instead of the two required for the other variables such as ammonia or oxygen [Di Toro and Fitzpatrick, 1993] because the equations for $Mn(II)$ and $MnO_2(s)$ in the two layers are coupled. This presents no essential difficulty, however, and the implementation is straightforward.

5.3 REVIEW OF MERL DATA

The MERL mesocosms are large outdoor tanks approximately 1.8 meters in diameter and have a water depth of 5.0 meters. Narragansett Bay water flows through at a rate to establish a detention time of approximately 30 days. The tanks have a mixer to reproduce the vertical mixing regime in Narragansett Bay and, in particular, the lack of stratification. Sediments are obtained using a large box cores which maintains the

vertical orientation and the top 40 cm are placed into containers in the bottom of the tanks [Nixon et al., 1986].

The data to be analyzed below comes from the Nutrient Addition Experiment. Its purpose was to examine the consequences of nutrient enrichment to coastal estuaries. The duration was approximately 2 1/4 years over three calendar years. The nutrient dosing was increased in a geometric series, 1X, 2X, 4X, 8X, 16X, and 32X, in addition to three control tanks, denoted as 0X. The nutrients added were inorganic nitrogen, phosphorus, and silica in a molar ratio of 12.8 N : 1.0 P : 0.91 Si to match the stoichiometry of sewage entering the bay [Nixon et al., 1986]. Areal loading rates of total nitrogen to the tanks varied from 23 mg N/m^2-d for the controls, 63 mg N/m^2-d for 1X, 103 mg N/m^2-d for 2X and so on geometrically to 1308 mg N/m^2-d for the 32X [Kelly et al., 1985]. As a result, mean annual water column dissolved inorganic nitrogen (DIN) concentration increased from 56 to 4200 μg N/L; mean annual chlorophyll$_a$ ranged from 4 to 70 μg/L, and total system carbon production ranged from 0.55 to 2.2 g C/m^2-d [Nixon et al., 1986].

Sediment processes were also examined during the experiment. Sediment oxygen demand, nutrient fluxes, pore water and solid phase concentrations were also measured. In addition, manganese flux and sediment compositional data were collected [Hunt and Kelly, 1988]. These are the data that were compared to the steady state model results in Figs.3.4 and 3.7.

Since the manganese flux model is coupled to the nutrient and oxygen flux model—the manganese flux model requires s and the depth of the aerobic layer H_1—the nutrient and oxygen data and model performance is evaluated below.

5.4 APPLICATION OF THE NUTRIENT AND OXYGEN FLUX MODEL

The sediment model is applied in stand alone mode when it is being initially calibrated. That is, it is not dynamically coupled to the overlying water, as it would be if it were being used as part of a larger coupled water quality-sediment model. Therefore the overlying water concentrations are specified externally. In addition, the average annual depositional flux of particulate organic nitrogen to the sediment J_{PON} is specified and Redfield stoichiometry is assumed in specifying the carbon, phosphorus and silica fluxes.

For application to the MERL dataset, the magnitudes of J_{PON} are chosen to fit the measured ammonia fluxes. The kinetic and transport parameter values are set to the values obtained from the calibration to the Chesapeake Bay data set [Di Toro and Fitzpatrick, 1993]. The required depositional fluxes are shown in Fig.5.3. Fluxes vary from less than 50 to 130 mg N/m^2-d, less than a 3 fold variation.

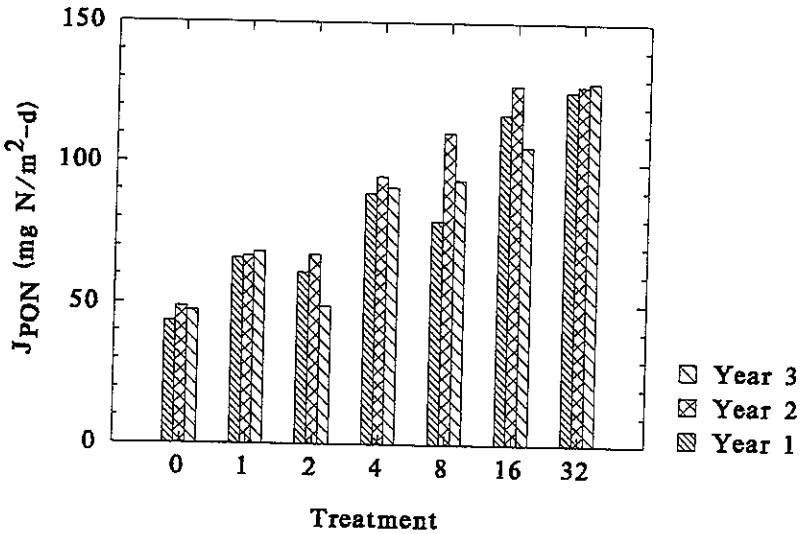

Fig. 5.3 Depositional flux of particulate organic nitrogen.

In order to run the model it is necessary to specify the initial state of the sediment, i.e. the concentrations of all the state variables. Since these concentrations were not measured—indeed it would be difficult if not impossible to measure the concentrations in the aerobic layer—they must be arrived at in another way. The objective is to produce the initial conditions in the sediments at the start of the experiment. The method chosen is to equilibrate the model by cycling the model until a periodic steady state is achieved. The same forcing functions are used for each annual cycle. Since the objective is to simulate the state of the sediments at the start of the experiment, the obvious choice is the inputs for the first year from the control tanks. That is, the overlying water concentrations observed in a control tank and the depositional flux which reproduces the ammonia flux for that tank are used to initialize all the tanks. This is equivalent to assuming that the state of the sediments in the year when they were collected is similar to that which is produced by a cyclical repetition of the conditions which were observed in the control tank for the first year of the experiment. Since the controls are a reasonable replication of Narragansett Bay, this seems not to be an unreasonable assumption.

It is also a very convenient and parsimonious way of proceeding. The initial conditions are not externally specified by some arbitrary means. Therefore, they are not an additional set of calibration parameters that need to be determined by fitting to the observations. This greatly reduces the degrees of freedom in the model and renders the calibration less of a curve fitting exercise. Also the initial conditions are consis-

tent with all the parameters used in the model. Thus, initially all the sediments have the same concentrations as the control. The differences in subsequent behavior occur solely due to the increased nutrient loading applied during the experiment.

The resulting ammonia fluxes are shown in Fig.5.4. The seasonal variation is reasonably well reproduced except for 32X. However, the negative fluxes during the winter, which increase as loading increases, are not captured, and we have no good explanation for these observations.

The oxygen fluxes are shown in Fig.5.5. The results are remarkably good. The absolute magnitudes and the seasonal variations are reproduced up to 32X. Since the manganese model requires the surface mass transfer coefficient $s = SOD/[O_2(0)]$, it is important that the oxygen flux be reproduced by the model.

5.5 MANGANESE MODEL APPLICATION

The manganese flux model is run as follows. The nutrient portion is run as described above. The overlying water concentrations of dissolved manganese are shown in Fig. 5.8 for all the tanks. For the equilibration phase the dissolved manganese concentrations for all the tanks are set to the average of the overlying water concentration of the control tanks, which is shown in the top two panels of Fig.5.8. These conditions are cycled periodically until the sediment has come into equilibrium. For the particulate manganese, the sediments are equilibrated using a constant depositional flux which is calculated from a water column settling velocity and the average particulate concentrations, shown in Fig. 5.9 for all the tanks. The overlying water particulate concentration is assumed to be constant as shown.

Once equilibrium has been reached, the nutrient loadings are increased in accordance with the various loading levels and the model is run for the three years of the experiment. The overlying water dissolved manganese concentrations are set at the observed values for the three years (Fig. 5.8). The particulate manganese concentrations are continued at the same constant value as used during the equilibration phase (Fig. 5.9).

Thus, it is assumed that water column processes during the experiment do not change the depositional flux of manganese to the sediment. This is only an approximation since the overlying water concentrations vary as dosing varies. However, overall the variation is not too large so that the assumption of a constant flux from the overlying water appears to be a reasonable first approximation. The consequences of this assumption is evaluated below when the overlying water is explicitly included in the model.

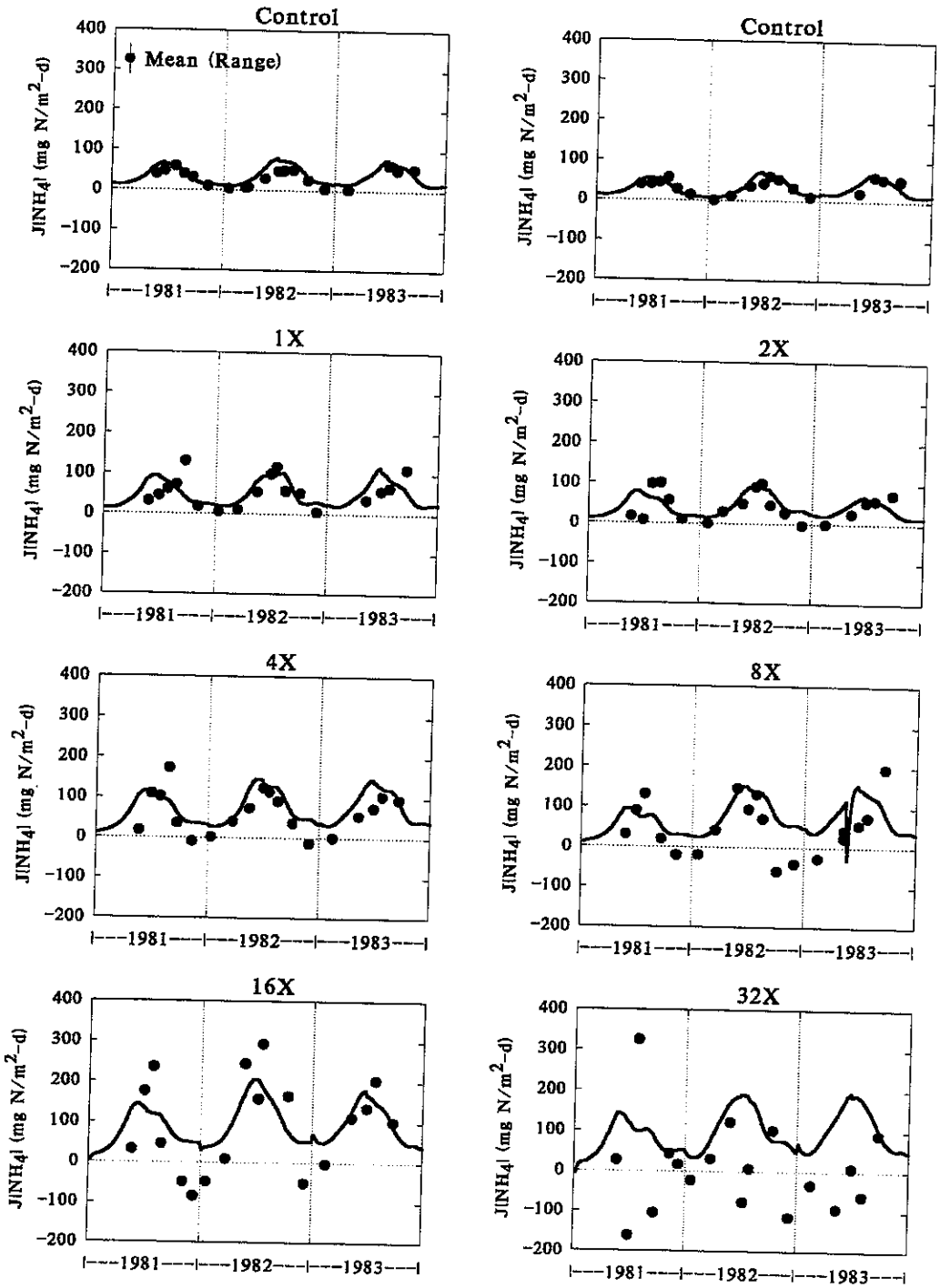

Fig. 5.4 Comparison of modeled and observed ammonia flux versus time for all the treatments.

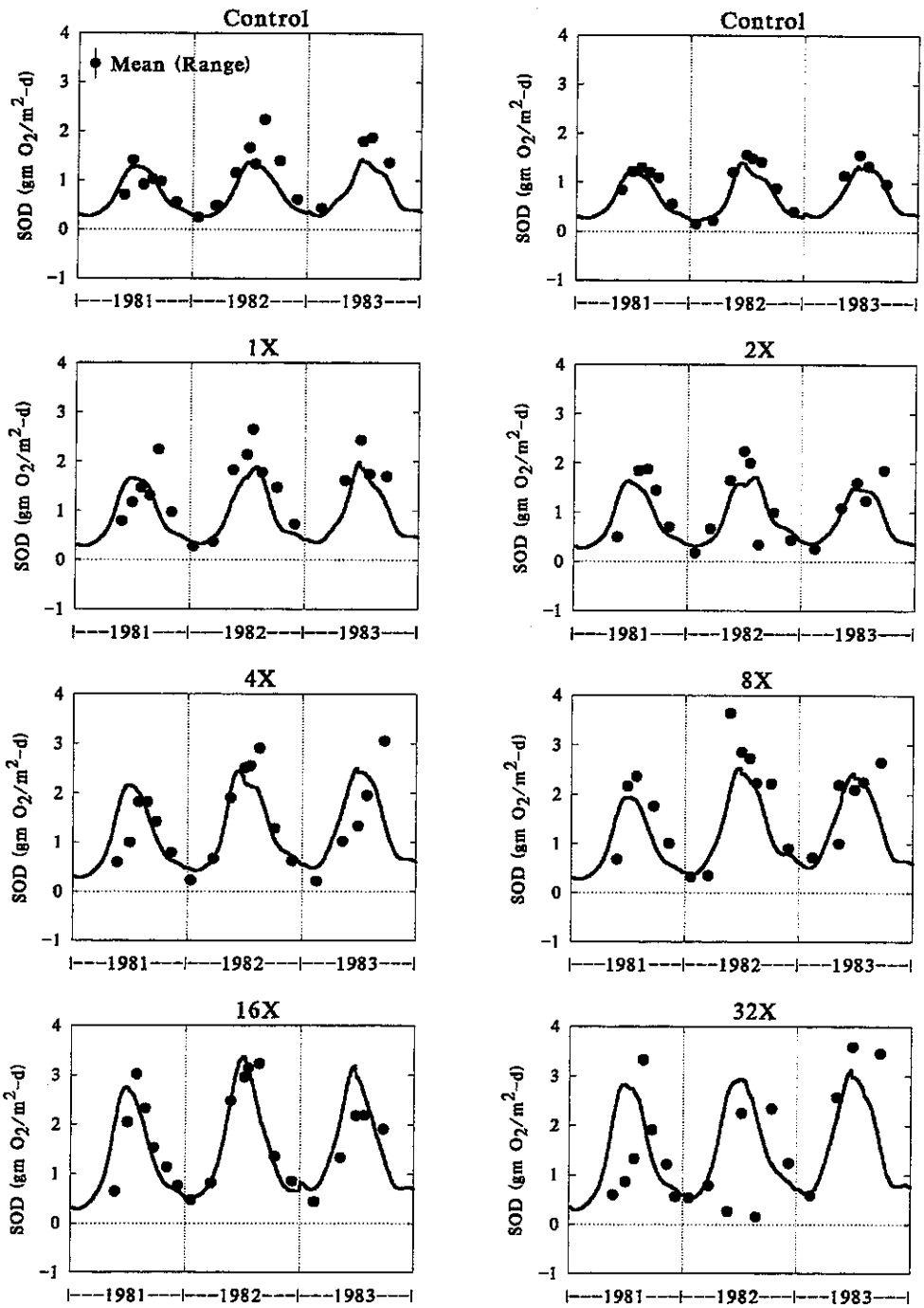

Fig. 5.5 Comparison of modeled and observed *SOD* versus time for all the treatments.

A comparison of the model and observed fluxes is shown in Fig. 5.10. The parameters are listed in Tables 5.1 and 5.2. The general shape of the seasonal variation of the manganese fluxes is reproduced quite nicely. This variation is due solely to the variation in s since the flux of particulate manganese to the sediment is held constant (Fig. 5.9). This is one reason for using the constant manganese depositional flux.

The variation in annual average manganese flux due to differing loading rates is examined in Fig. 5.6. The model captures the trend of increasing flux as nutrient loading increases for the first (Fig. 5.6A) and third (Fig. 5.6C) years. However the sharp increases in the second year for the 0X to 4X tanks (Fig. 5.6B) are not reproduced.

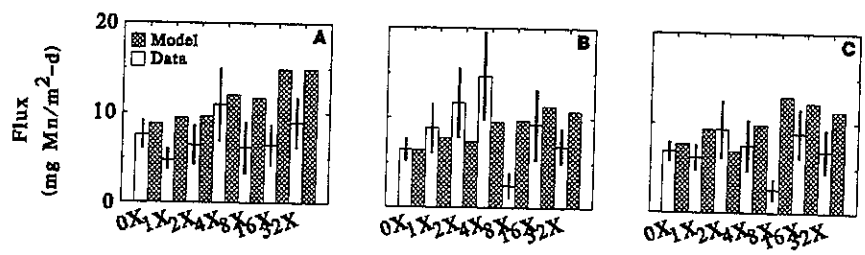

Fig. 5.6 Average annual manganese flux for the three years of the experiment. Comparison of model and data.

The variation of manganese fluxes with respect to temperature, overlying water dissolved oxygen, and ammonia flux for both the data and the model are presented in Fig. 5.11. The data exhibit a more pronounced variation with respect to temperature and ammonia flux than does the model. This is consistent with the findings of the steady state model (Fig. 3.7).

The pore water and solid phase concentrations are compared in Fig.5.7. The model concentrations are slightly higher than the observations, as was the case with the steady state model (Fig. 3.7).

5.6 CONCLUSIONS

The time variable version of the model captures many of the features exhibited by the data: a strong seasonal variation (Fig.5.10); an increasing manganese flux with increasing nutrient inputs (Fig.5.6); and a slight depletion of the sediment manganese concentration, as a consequence of the increased manganese flux (Fig.5.7). However, the modeled relationship between manganese and ammonia fluxes is still less than observed (Fig.5.11), and the inter-annual variations are not quite resolved.

The problem may be that the pH variation exhibited in the MERL experiments, and which is known to significantly affect the oxidation rate of manganese (II) to

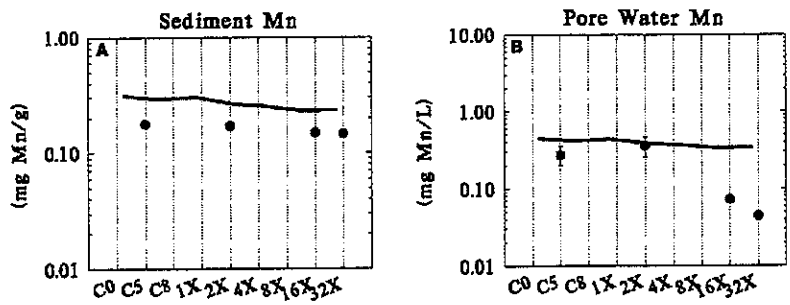

Fig. 5.7 Comparison of pore water and solid phase concentrations.

manganese (IV), has not been taken into account. This is addressed in the next section.

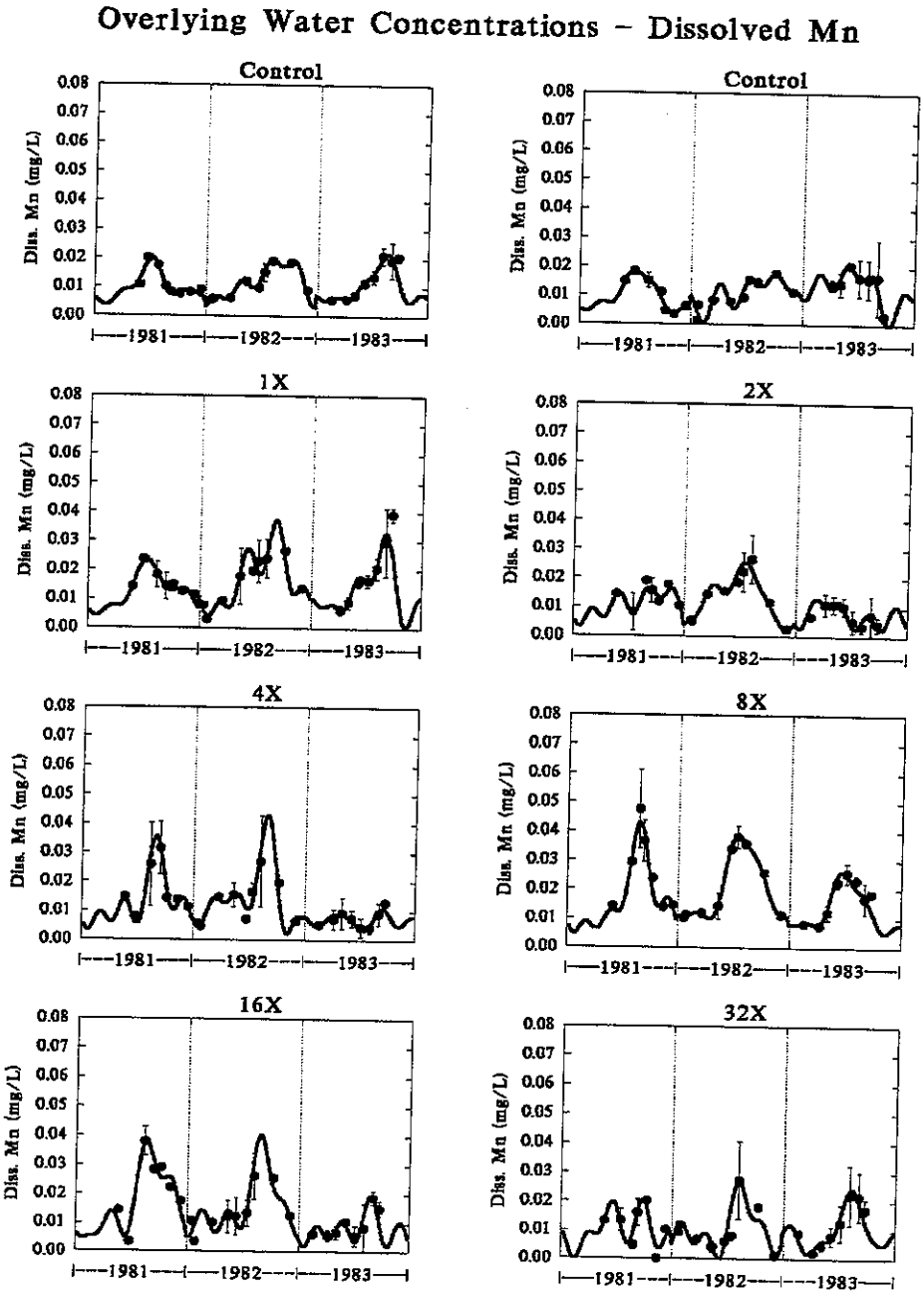

Fig. 5.8 Dissolved manganese concentrations in the overlying water

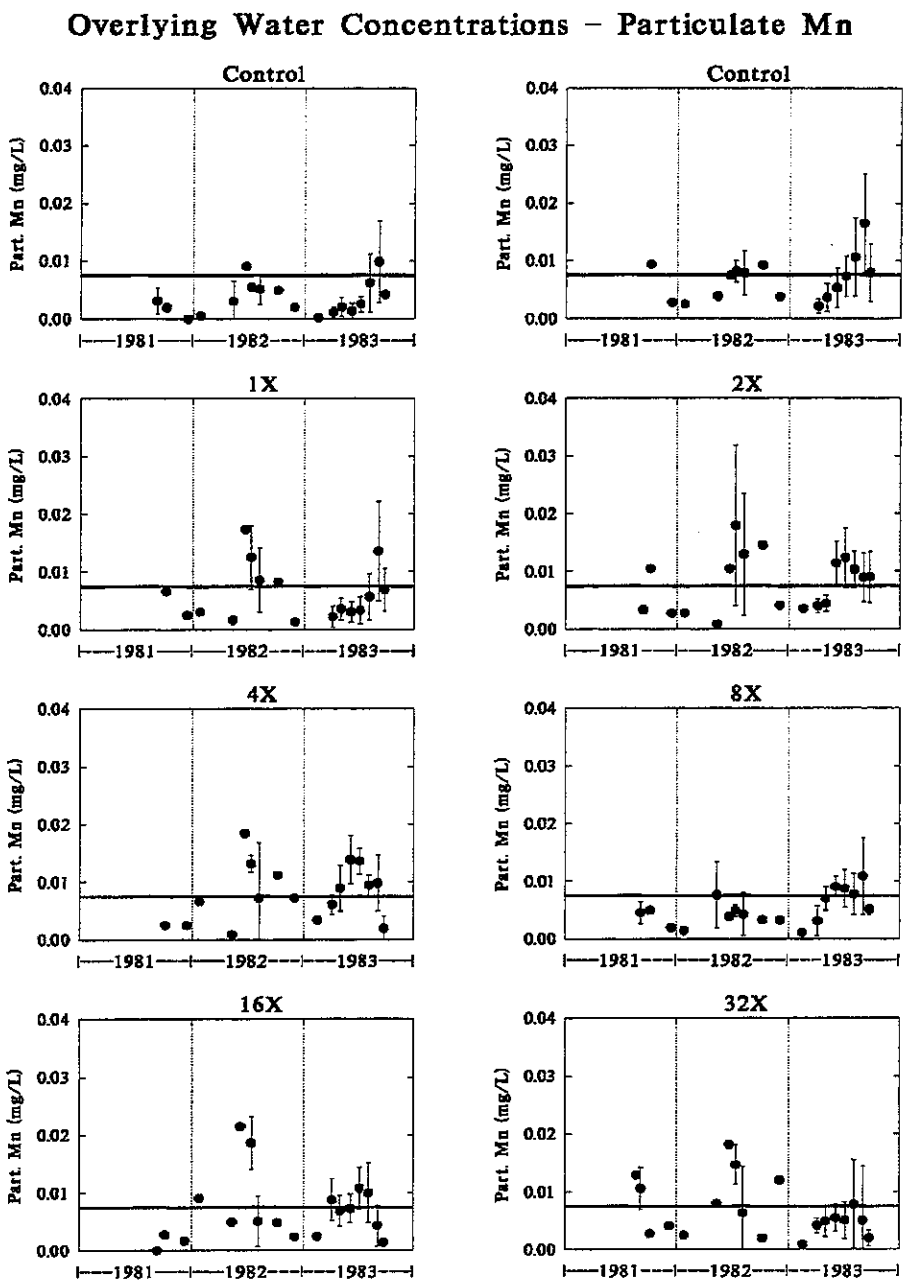

Fig. 5.9 Particulate concentrations in the overlying water. Line is the concentration used in the model for the depositional flux.

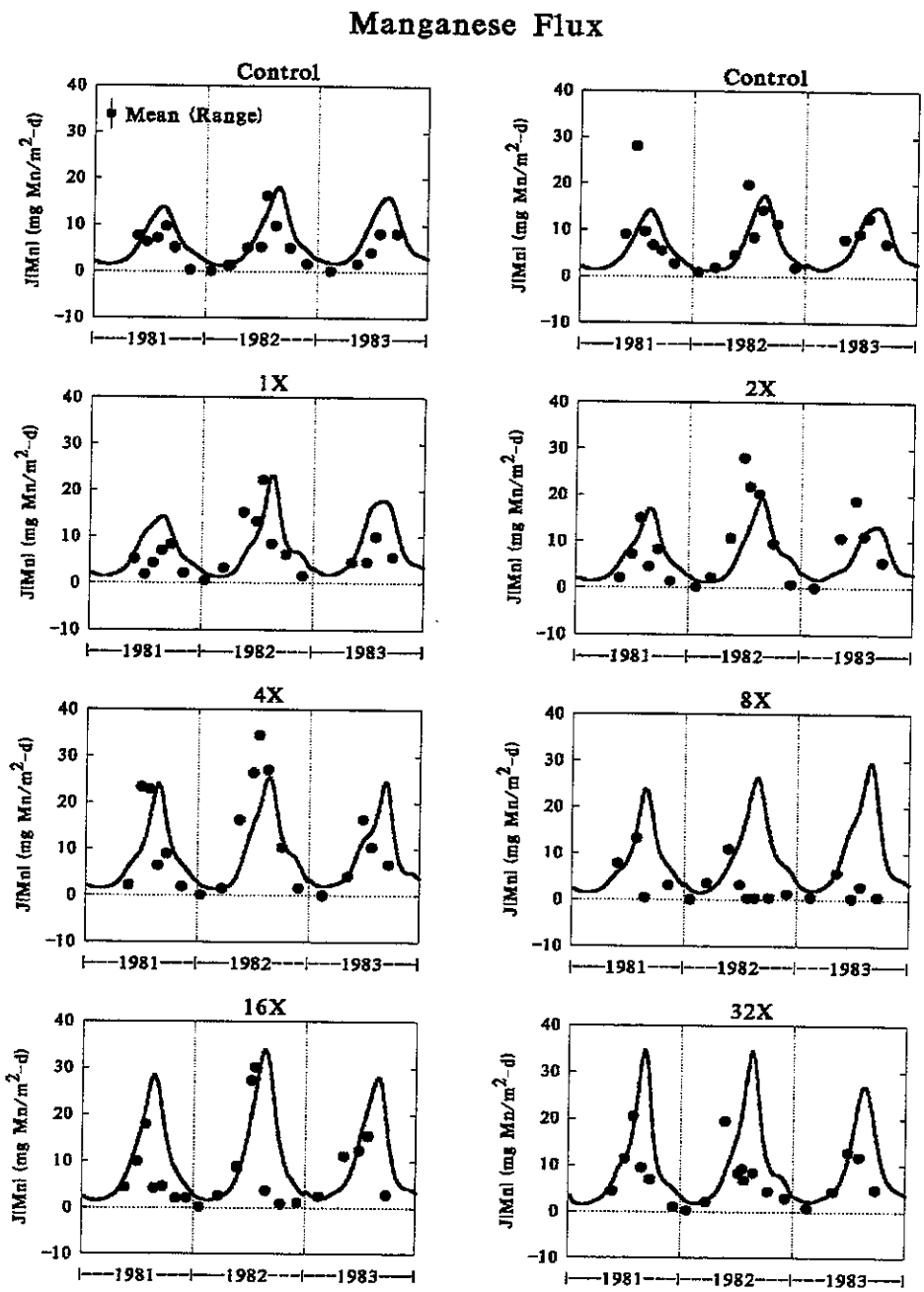

Fig. 5.10 Comparison of observed and modeled manganese fluxes.

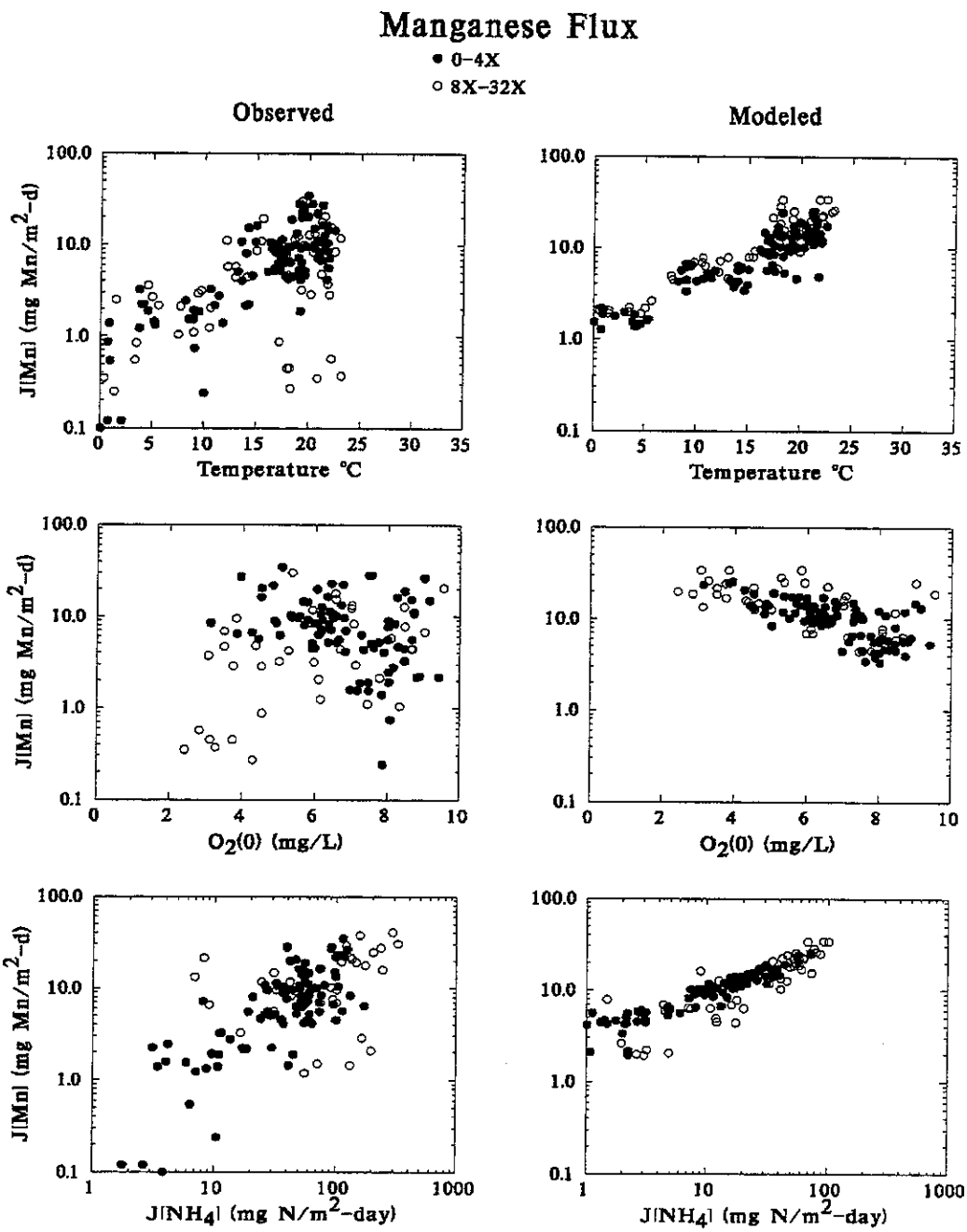

Fig. 5.11 Comparison of modeled and observed fluxes versus temperature, overlying water O_2 concentration, and ammonia flux $J[NH_4]$.

Table 5.1 Sediment Model Parameters for MERL Application

m_1 (kg/L) 0.5	m_2 (kg/L) 0.5	w_2 (m/d) 6.85×10^{-6}	H_2 (m) 0.10	H_0 (m) 5.	t_0 d 27.4
D_d (m^2/d) 5.0E-03	θ_{D_d} – 1.08	D_p (m^2/d) 1.2×10^{-4}	θ_{D_p} – 1.15	D_{d0} (m^2/d) 1.0×10^{-4}	$\theta_{D_{d0}}$ – 1.08
$\kappa_{NH_4,1}$ (m/d) 0.131	π_{NH_4} (L/kg) 1.00	θ_{NH_4} – 1.123	K_{M,NH_4} (mg N/L) 0.728	$\theta_{K_{M,NH_4}}$ – 1.125	K_{M,NH_4,O_2} (mg O_2/L) 0.74
$\kappa_{NO_3,1}$ (m/d) 0.10	$\kappa_{NO_3,2}$ (m/d) 0.25	θ_{NO_3} – 1.080			
$\kappa_{H_2S,d1}$ (m/d) 0.2	$\kappa_{H_2S,p1}$ (m/d) 0.4	$\pi_{H_2S,1}$ (L/kg) 100.0	$\pi_{H_2S,2}$ (L/kg) 100.0	θ_{H_2S} – 1.0800	K_{M,H_2S,O_2} (mg O_2/L) 4.0
k_{Si} (/d) 0.5	$[\mathrm{Si}]_{sat}$ (mg Si/L) 40.	$\Delta\pi_{\mathrm{Si},1}$ – 10.0	$\pi_{\mathrm{Si},2}$ (L/kg) 100.0	θ_{Si} – 1.100	$K_{M,P\mathrm{Si}}$ (mg Si/L) 5.0×10^4
$\Delta\pi_{PO_4,1}$ – 20.0	$\pi_{PO_4,2}$ (L/kg) 20.0	$O_2(0)_{\pi,PO_4}$ (mg O_2/L) 2.0	K_{M,D_p,O_2} (mg O_2/L) 4.0	$O_2(0)_{\pi,\mathrm{Si}}$ (mg O_2/L) 1.0	
$\Delta\pi_{Mn,1}$ – 3.	$\pi_{Mn,2}$ (L/kg) 700.	$O_2(0)_{\pi,Mn}$ (mg O_2/L) 2.0			
$\kappa_{MnO_2,1}$ (m/d) 0.0	$\theta_{MnO_2,1}$ – 1.08	$\kappa_{MnO_2,OH,1}$ (m/d) 0.01	$\theta_{MnO_2,OH,1}$ – 1.08	κ_{MnO_22} (m/d) 0.1	θ_{MnO_22} – 1.08
Alk_0 (meq/L) 2.0	pH_2 – 7.5	Alk_2 (meq/L) 3.0	$f_{\mathrm{colloidal}}$ – 0.5	K_S (/d) 0.03	$D_{p,\min}$ (m^2/d) 3×10^{-6}
$w_{MnO_2,in}$ (m/d) 2.0	θ_{J_N} – 1.15				

Table 5.2 Diagenesis Parameters for MERL Application

f_{PON_1}	k_{PON_1}	θ_{PON_1}	f_{PON_2}	k_{PON_2}	θ_{PON_2}
–	(/d)	–	–	(/d)	–
0.65	0.035	1.10	0.25	0.0018	1.15
f_{POC_1}	k_{POC_1}	θ_{POC_1}	f_{POC_2}	k_{POC_2}	θ_{POC_2}
–	(/d)	–	–	(/d)	–
0.65	0.035	1.10	0.20	0.0018	1.15
f_{POP_1}	k_{POP_1}	θ_{POP_1}	f_{POP_2}	k_{POP_2}	θ_{POP_2}
–	(/d)	–	–	(/d)	–
0.65	0.035	1.10	0.20	0.0018	1.15
f_{PON_3}	k_{PON_3}	θ_{PON_3}			
–	(/d)	–			
0.10	0.0	1.17			
f_{POC_3}	k_{POC_3}	θ_{POC_3}			
–	(/d)	–			
0.15	0.0	1.17			
f_{POP_3}	k_{POP_3}	θ_{POP_3}			
–	(/d)	–			
0.15	0.0	1.17			
$a_{C,N}$	$a_{C,P}$	$a_{C,\mathrm{Si}}$			
(mg C/mg N)	(mg C/mg P)	(mg C/mg Si)			
5.68	41	2.5			

6

Effect of pH

6.1 INTRODUCTION

The purpose of this chapter is to examine the effect of pH variations on the flux of manganese from the sediment. The rate of the oxidation reactions for both manganese and iron are strongly affected by the pH (Fig.2.1–2.4) so it is reasonable to expect that this effect is important. Since the oxidation reaction takes place in the aerobic layer of the sediment, this is where the pH is required. Since the layer 1 pH depends on the conditions in the overlying water and in the anaerobic layer, and on the magnitudes of the mass transfer coefficients that affect the aerobic layer, it must be computed as part of the model.

6.2 pH IN THE AEROBIC LAYER

The pH in the aerobic layer (layer 1) is determined by the layer 1 alkalinity Alk_1 and inorganic carbon TIC_1 concentrations. These, in turn, are determined by the mass fluxes of alkalinity and inorganic carbon from the adjacent layers and internal sources and sinks. For the sake of simplicity, we assume that neither internal sources nor sinks of Alk and TIC are significant. Any other assumption would require a consideration of the acid-base reactions in the layer as well as any TIC and alkalinity sources. Because the layer is quite thin, it is likely that their effects are not large. Therefore alkalinity and TIC are assumed to be conservative variables in layer 1. The schematic diagram is presented in Fig. 6.1.

The mass balance equations that result for this model are

$$s\left(Alk_0 - Alk_1\right) + K_{L12}\left(Alk_2 - Alk_1\right) = 0 \tag{6.1}$$

and

$$s\left(TIC_0 - TIC_1\right) + K_{L12}\left(TIC_2 - TIC_1\right) = 0 \tag{6.2}$$

where s and K_{L12} are the mass transfer coefficients for layer 0–1 and layer 1–2 respectively and subscripts are used to identify the layer. Solving these eqs.(6.1–6.2) for the layer 1 concentrations yields

$$Alk_1 = \alpha Alk_0 + (1-\alpha)\, Alk_2 \tag{6.3}$$

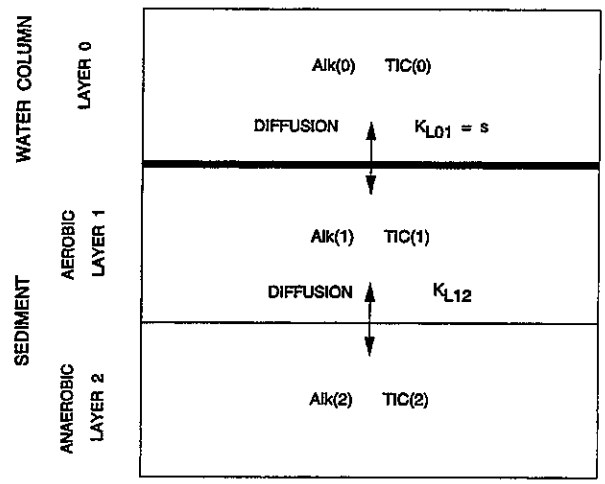

Fig. 6.1 Schematic diagram of the model for the aerobic layer 1 pH.

and

$$TIC_1 = \alpha TIC_0 + (1-\alpha)\, TIC_2 \tag{6.4}$$

where

$$\alpha = \frac{s}{s + K_{L12}} \tag{6.5}$$

Once Alk_1 and TIC_1 are known, the pH is computed using the equations that describe the carbon dioxide system [Stumm and Morgan, 1996].

The mass balance equations for the carbon dioxide system are

$$[TIC] = [CO_2] + \left[HCO_3^-\right] + \left[CO_3^{2-}\right] \tag{6.6}$$

$$[Alk] = \left[HCO_3^-\right] + 2\left[CO_3^{2-}\right] \tag{6.7}$$

and the mass action equations are

$$\frac{\left[HCO_3^-\right]\left[H^+\right]}{[CO_2]} = K_1 \tag{6.8}$$

$$\frac{\left[CO_3^{2-}\right]\left[H^+\right]}{\left[HCO_3^-\right]} = K_2 \tag{6.9}$$

Eliminating $[H^+]$, $\left[HCO_3^-\right]$ and $\left[CO_3^{2-}\right]$ yields

$$K_1K_2\,(Alk - 2TIC) + K_1H\,(Alk - TIC) + H^2 Alk = 0 \tag{6.10}$$

which relates the pH to the alkalinity and inorganic carbon concentrations. The square brackets and charges are dropped from the notation for convenience.

The aerobic layer alkalinity and TIC concentrations are given by eqs.(6.3–6.4). For the alkalinity, both Alk_0 and Alk_2 are known by measurement. However, the TIC's

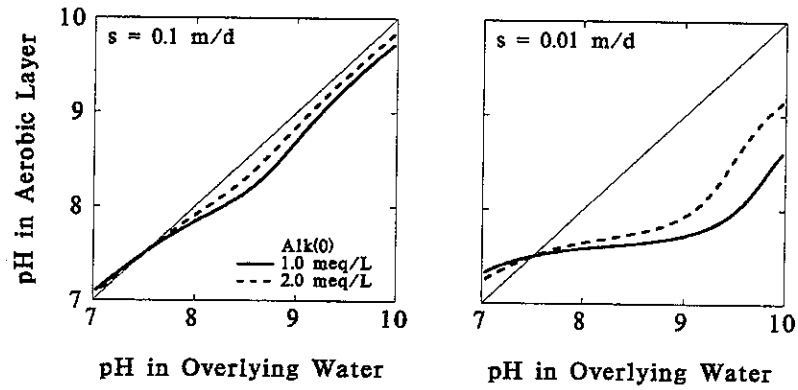

Fig. 6.2 Aerobic layer pH_1 as a function of overlying water pH_0. Assumed conditions: anaerobic layer $pH_2 = 7.5$; alkalinity $Alk_2 = 3$ meq/L; and layer 1–2 mass transfer coefficient $K_{L12} = 0.01$ m/d. Remaining parameters: s and Alk_0, are noted in the figure.

are not measured. They can be computed from the respective pHs and alkalinities. Using eq.(6.10) to solve for TIC yields

$$TIC = \frac{Alk\left(K_1\left(K_2 + H\right) + H^2\right)}{K_1\left(2K_2 + H\right)} \tag{6.11}$$

Using the relationship between pH and hydrogen ion concentration yields

$$H_0 = 10^{-pH_0} \tag{6.12}$$

which, together with Alk_0, determine TIC_0 using eq.(6.11). A similar procedure is applied to layer 2 to obtain TIC_2 using pH_2 and Alk_2. Then eq.(6.4) yields TIC_1. Since the layer 1 alkalinity and TIC are now known, eq.(6.10) can be solved for H_1 to obtain the pH_1. The result is

$$H_1 = \frac{K_1\left(TIC_1 - Alk_1\right) \pm \sqrt{4Alk_1\left(2TIC_1 - Alk_1\right)K_1K_2 + \left(TIC_1 - Alk_1\right)^2 K_1^2}}{2Alk_1} \tag{6.13}$$

and

$$pH_1 = -\log_{10}\left[H_1\right] \tag{6.14}$$

An example computation is given in Fig.6.2 which presents the pH in layer 1 as a function of the pH in the overlying water, for various overlying water alkalinities, for two values of the surface mass transfer coefficient s.

It is useful to understand what is determining pH_1. A part of the behavior has a straightforward rationalization. For a large surface mass transfer coefficient $s = 0.1$

m/d the aerobic layer pH_1 tracks the overlying water pH_0 since the mixing transports both the overlying water alkalinity and TIC to the aerobic layer. For the smaller surface mass transfer coefficient $s = 0.01$ m/d the aerobic layer pH_1 remains close to the anaerobic layer $pH_2 = 7.5$ since it is more isolated from the aerobic layer.

What is puzzling, however, is why the aerobic layer pH_1 varies as it does with varying overlying water alkalinity $Alk\,(0)$. Increasing the alkalinity from $Alk\,(0) = 1$ meq/L to 2 meq/L brings the overlying water alkalinity closer to the alkalinity of the *anaerobic* layer $Alk\,(2) = 3$ meq/L. One would expect that making the alkalinity in the overlying water closer to the alkalinity of the anaerobic layer would bring the pH in the aerobic layer closer to the *anaerobic* layer pH as well. But the reverse happens. The aerobic layer pH_1 becomes more like the *overlying water* pH_0.

The key to understanding this result in particular, and the CO_2 system in general, is to form the ratio of eq.(6.7) to eq.(6.6)

$$\frac{[Alk]}{[TIC]} = \frac{[HCO_3^-] + 2\,[CO_3^{2-}]}{[CO_2] + [HCO_3^-] + [CO_3^{2-}]} \tag{6.15a}$$

$$= \frac{[HCO_3^-]\left(1 + \dfrac{2K_2}{[H^+]}\right)}{[HCO_3^-]\left(\dfrac{[H^+]}{K_1} + 1 + \dfrac{K_2}{[H^+]}\right)} \tag{6.15b}$$

$$= \frac{\left(1 + \dfrac{2K_2}{[H^+]}\right)}{\left(\dfrac{[H^+]}{K_1} + 1 + \dfrac{K_2}{[H^+]}\right)} \tag{6.15c}$$

so that the pH is determined by the ratio of alkalinity to inorganic carbon $[Alk]\,/\,[TIC]$ and not the individual values.

This relationship is shown in Fig. 6.3.

Note that small changes in $[Alk]\,/\,[TIC]$ result in large changes in pH due to the lack of buffering capacity in the $pH = 7$–9 range [Stumm and Morgan, 1996]. As pH approaches pK_1 or pK_2 buffering is increased and the relationship flattens out.

The role of $[Alk]\,/\,[TIC]$ in determining the pH is illustrated in Fig. 6.4. The two panels represent the alkalinity, TIC, and $[Alk]\,/\,[TIC]$ ratio for a change in overlying water alkalinity from $Alk\,(0) = 1$ meq/L to 2 meq/L. An extreme case, $pH_0 = 10$, is chosen corresponding to the right hand side of Fig. 6.2 to amplify the differences.

The first two groups of bars present the concentration of Alk and TIC in the three layers. The center bars present the alkalinity and TIC concentrations, Alk_1 and TIC_1, computed from the adjacent Alk_0 and Alk_2, and TIC_0 and TIC_2 concentrations respectively using eqs.(6.3–6.4). For the third group of bars, the unfilled bars present Alk_0/TIC_0 and Alk_2/TIC_2 respectively. Note that they are the same for the two cases

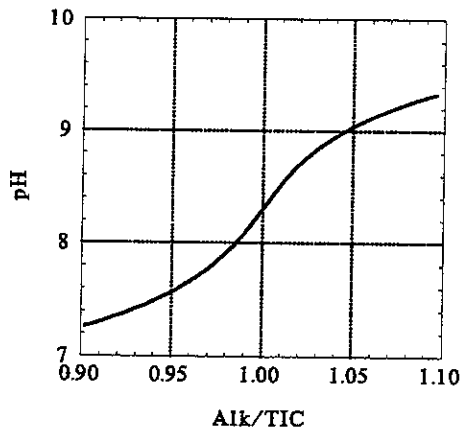

Fig. 6.3 pH as a function of $[Alk]/[TIC]$. Parameters: $K_1 = 10^{-6.3}$, $K_2 = 10^{-10.3}$.

since pH_0 and pH_2 are held constant and there is a one-to-one relationship between pH and Alk/TIC. The filled bars present Alk_1/TIC_1 for the two cases. Increasing Alk_0 results in an increase in Alk_1/TIC_1 and, therefore an increase in pH_1 as shown in Fig. 6.2. The difference between the two cases is small but because pH is such a sensitive function of Alk/TIC the pH varies appreciably.

Since the graphical presentation does not clearly indicate why the behavior is occurring, perhaps the algebraic relationships can provide the rationale. The equations that determine the result are

$$\frac{Alk_1}{TIC_1} = \frac{\alpha Alk_0 + (1-\alpha)\,Alk_2}{\alpha TIC_0 + (1-\alpha)\,TIC_2} \tag{6.16}$$

$$= \frac{\alpha Alk_0 + (1-\alpha)\,Alk_2}{\alpha r_0^{-1} Alk_0 + (1-\alpha)\,r_2^{-1} Alk_2} \tag{6.17}$$

where $r_0 = Alk_0/TIC_0$ and $r_2 = Alk_2/TIC_2$. Factoring this expression and grouping the terms yields

$$\frac{Alk_1}{TIC_1} = \frac{1+\beta}{r_0^{-1} + r_2^{-1}\beta} \tag{6.18}$$

where

$$\beta = \frac{K_{L12}}{s}\frac{Alk_2}{Alk_0} \tag{6.19}$$

The limiting cases are

$$\frac{Alk_1}{TIC_1} \underset{\beta\to 0}{\longrightarrow} r_0 = \frac{Alk_0}{TIC_0} \tag{6.20}$$

or

$$pH_1 \underset{\beta\to 0}{\longrightarrow} pH_0 \tag{6.21}$$

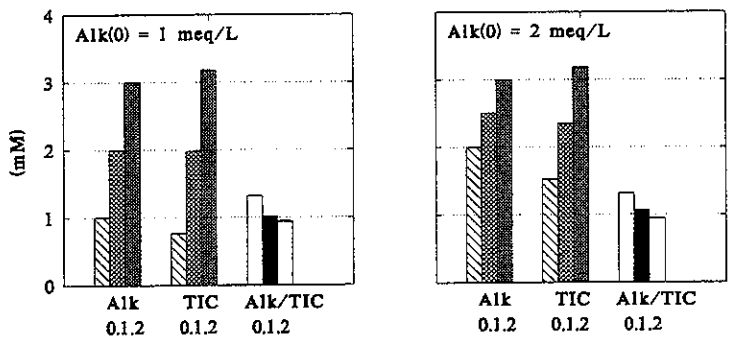

Fig. 6.4 The effect of overlying water alkalinity. Example computation for $pH_0 = 10$, $pH_2 = 7.5$, $Alk_2 = 3.0$ meq/L, $s = K_{L12} = 0.01$ m/d. Bars represent Alk, TIC, and Alk/TIC for layers 0,1,2. The filled bar represents Alk/TIC for layer 1 which determines pH_1.

Alternately

$$\frac{Alk_1}{TIC_1} \underset{\beta\to\infty}{\to} r_2 = \frac{Alk_2}{TIC_2} \tag{6.22}$$

or

$$pH_1 \underset{\beta\to\infty}{\to} pH_2 \tag{6.23}$$

Thus the behavior of the aerobic layer pH is determined by the magnitude of β. A large β can occur if K_{L12} is large relative to s so that layer 2 is transported into layer 1 and $pH_1 \to pH_2$. This is obvious case.

Alternately a large Alk_2 relative to Alk_0 also increases β. What is happening in this case is more subtle and explains the results in Fig.6.2. Decreasing Alk_0 causes a decrease in TIC_0 since pH_0 is assumed to be fixed. Hence more TIC_2 is transported into layer 1, making layer 1 more like layer 2 so that again $pH_1 \to pH_2$.

What prompted this exercise was the need to understand the results in Fig. 6.2: namely that increasing $Alk_0 \to Alk_2$ caused the pH_1 to more closely resemble pH_0. The reason is that increasing Alk_0 causes an increase in TIC_0 which makes TIC_1 more like TIC_0 and therefore Alk_1/TIC_1 more like Alk_0/TIC_0 and hence pH_1 more like pH_0.

6.3 EFFECT OF pH ON THE MANGANESE FLUX

The pH in the aerobic layer can now be calculated using the equations developed in the previous section, eqs.(6.3–6.5) and (6.13). The results are shown in Fig. 6.5. The solid line is an interpolation of the data points in the overlying water, which are also shown. The dashed line is the computed pH in the aerobic layer. The dotted line

is at the pH of the anaerobic layer, which is assumed to be at $pH = 7.5$, consistent with pore water observations. The alkalinities are $Alk_0 = 2.0$ meq/L and $Alk_2 = 3.0$ meq/L, which are also estimated from observations. The remaining parameters: s and K_{L12} are from the simulation to be presented below.

For the controls, 1X, and 2X loadings, there is little computed variation in pH_1. The reason is that surface mass transfer coefficient $s = SOD/O_2(0)$ is small, corresponding to a comparatively small SOD (Fig.5.5), so the aerobic layer resembles the anaerobic layer. However, for the more heavily loaded tanks, the SOD increases, s increases and the aerobic layer starts to be influenced by the overlying water pH, which is varying. Hence the variation in pH_1 is more substantial for these tanks, sometimes approaching one-half pH unit, which would correspond to one order of magnitude in oxidation reaction rate variation, as shown subsequently. It is for this reason—the expected importance of the pH variation in the aerobic layer—that this refinement is added to the model.

6.3.1 Reaction Kinetics

The incorporation of pH dependent reaction kinetics is straightforward. The aerobic layer reaction rate

$$-\frac{\kappa_{Mn,1}^2}{s} O_2(0)\, f_{d1} Mn(1) \tag{6.24}$$

is replaced by a pH dependent expression

$$-\frac{\kappa_{Mn,1}^2}{s} \left[OH^-\right]^2 O_2(0)\, f_{d1} Mn(1) \tag{6.25}$$

where the dependency on $[OH^-]^2$ is from an analysis of experimental results [Morgan, 1967]. This is expressed as follows

$$-\frac{\kappa_{Mn,1}^2}{s} \left(10^{2(pH_1-7)}\right) O_2(0)\, f_{d1} Mn(1) \tag{6.26}$$

The pH is normalized to $pH = 7$ so that the numerical value of the reaction velocity $\kappa_{Mn,1}$ corresponds to $pH_1 = 7$. This procedure is useful so that the magnitude of $\kappa_{Mn,1}$ has some specific meaning. The $+2$ in the exponent results for the dependency on $[OH^-]^2$

$$\left[OH^-\right]^2 = \left(\frac{K_W}{[H^+]}\right)^2 = \left(\frac{K_W}{10^{-pH}}\right)^2 = K_W^2 10^{2pH} \tag{6.27}$$

where $K_W = [H^+][OH^-]$,the ionization constant for water. With the kinetics modified, it remains only to rerun the model using the computed pH_1 and examine the results.

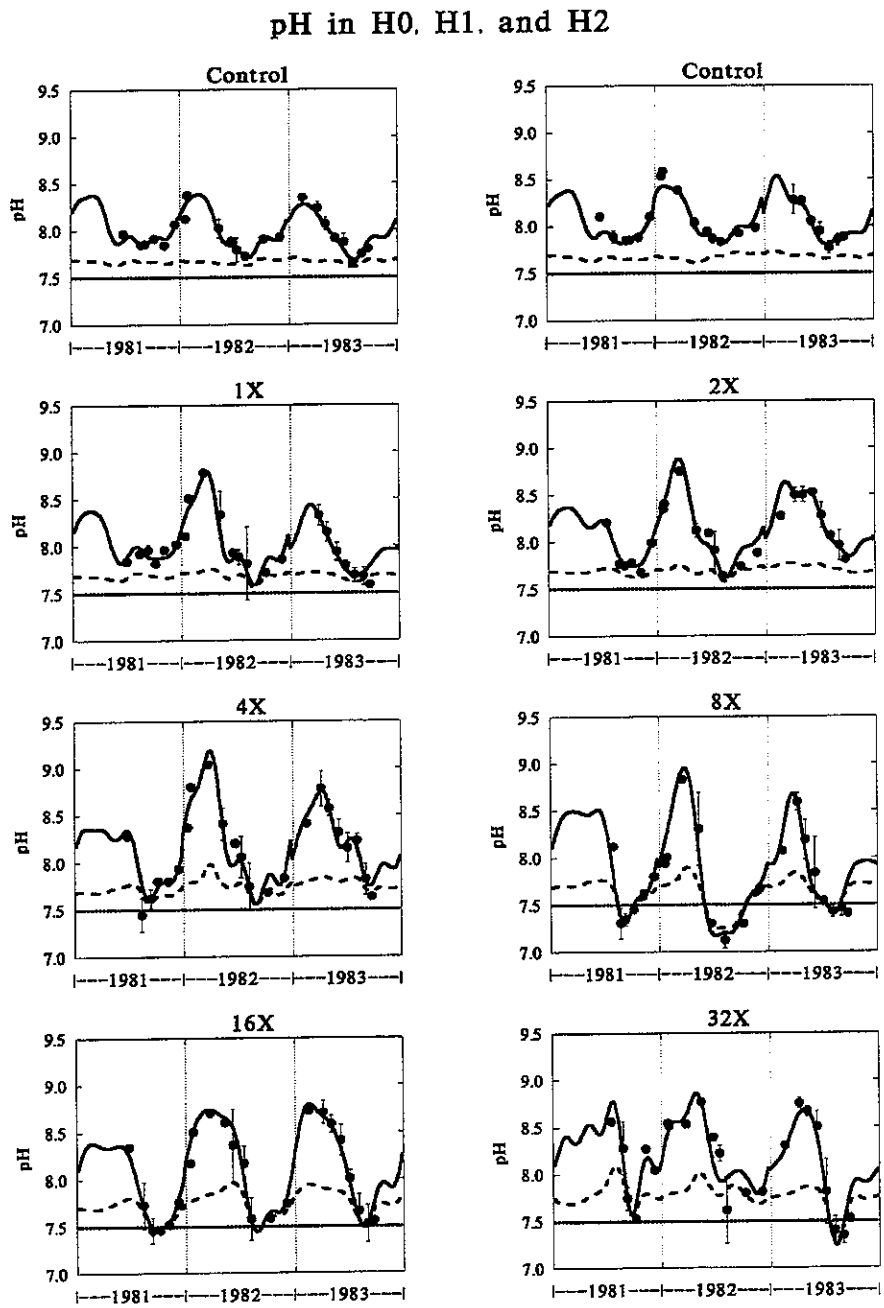

Fig. 6.5 *pH* in the overlying water (solid line is interpolated to the data points), aerobic layer (computed – dashed line), and anaerobic layer (assumed constant – dotted line).

6.3.2 Application to MERL

The consequences of this modification are shown in Figs. (6.6–6.7). There are almost no discernible differences. Perhaps this should not have been too surprising if one considers the steady state solutions for manganese flux equations: eqs.(3.21–3.22 and 3.26) in section 3.1.4 and eq.(3.28) in section 3.1.4.1. These highlight the importance of s and f_{d1} and not the oxidation rate $\kappa_{Mn,1}$ except in the case that s is small (eq.3.33).

Actually the pH is important, as we shall see in the next chapter. But it is important in the overlying water where the variation is larger and so also is its effect on the oxidation rate.

6.4 EFFECT OF VARYING DEPOSITIONAL FLUX

There is one more source of variation that has not been taken into account yet: the variation in the overlying water particulate manganese concentrations. The flux of manganese to the sediment is

$$J_{MnO_2} = w_0 \left[Mn_p\left(0\right)\right] \tag{6.28}$$

where w_0 is the settling velocity from the overlying water to the sediment and $[Mn_p(0)]$ is the concentration of particulate manganese in the overlying water. Fig. (6.8) presents $[Mn_p(0)]$ and the interpolated function used to compute the depositional flux (eq. 6.28). The results are shown in Figs. (6.9 and 6.10). Again the differences are small, suggesting that the time variation of $[Mn_p(0)]$ is not critical.

But, as we shall see in the next chapter, the *magnitude* of the particulate flux J_{MnO_2} is of critical importance. The question to be addressed next is: how is J_{MnO_2} to be specified in model applications to natural bodies of water. Presumably, through the use of eq.(6.28). So the question becomes: how is $[Mn_p(0)]$ to be computed. We examine this in the next chapter.

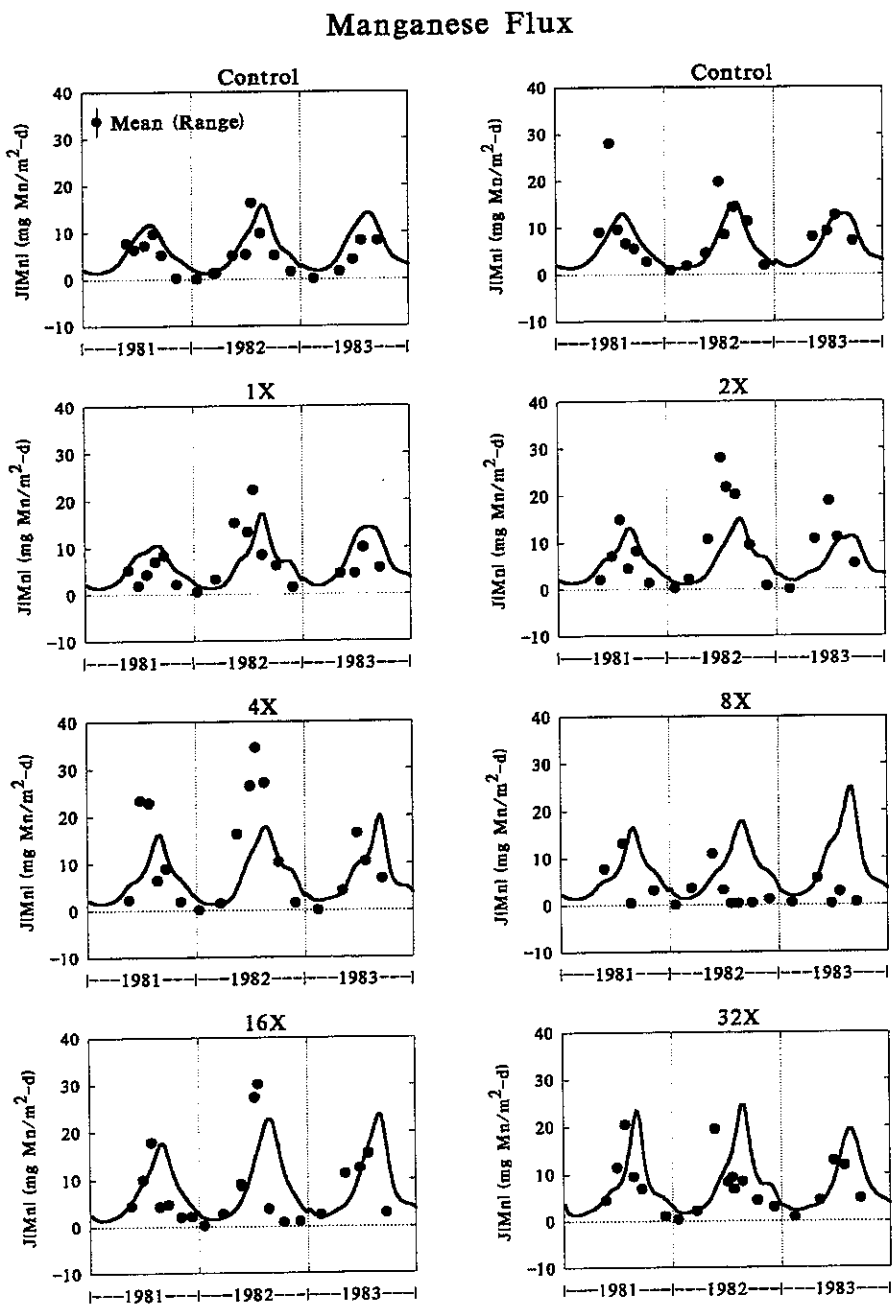

Fig. 6.6 Comparison of observed and modeled manganese fluxes.

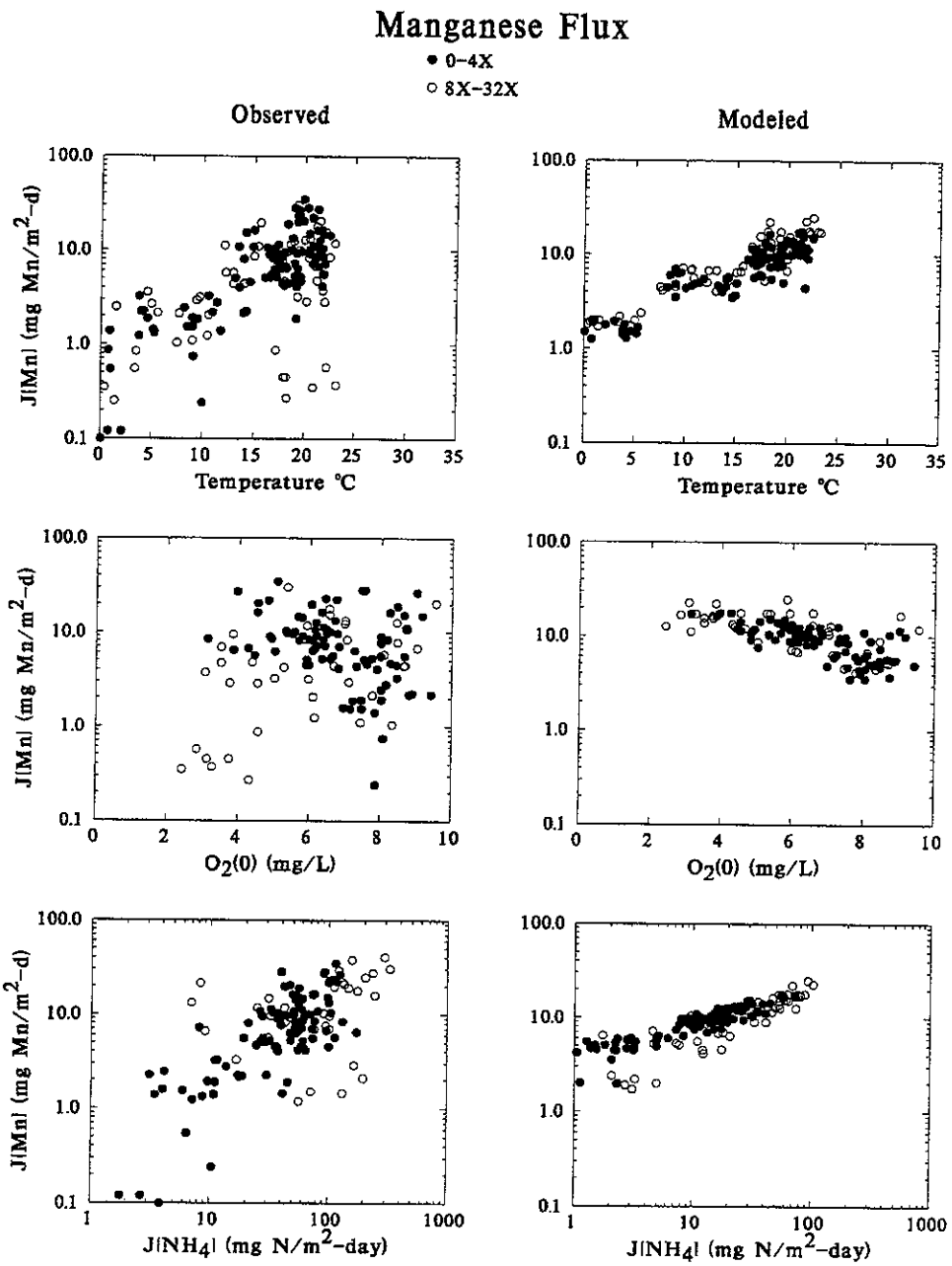

Fig. 6.7 Comparison of modeled and obsdrved fluxes versus temperature, overly water O_2 concentration and ammonia flux $J[NH_4]$.

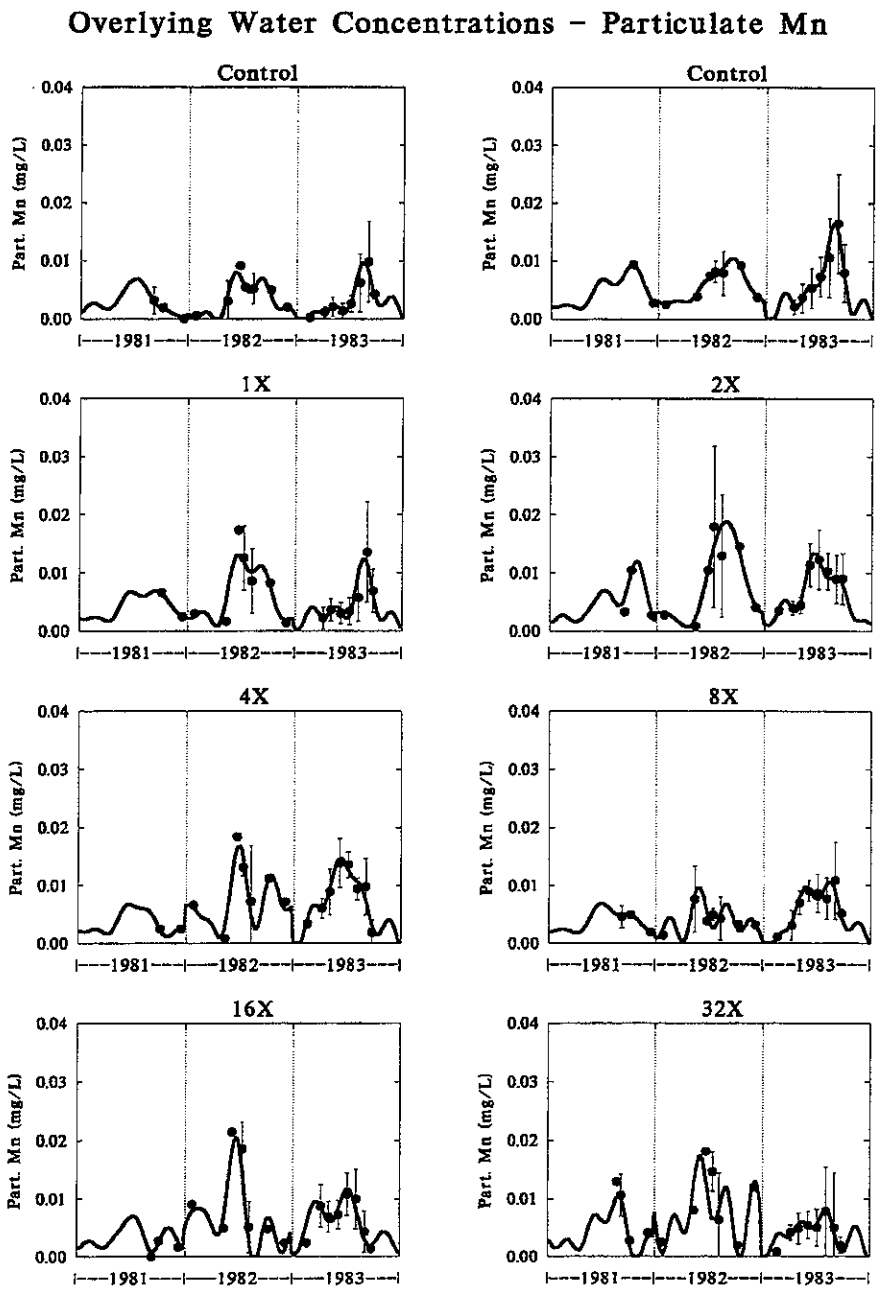

Fig. 6.8 Particulate manganese concentration in the overlying water.

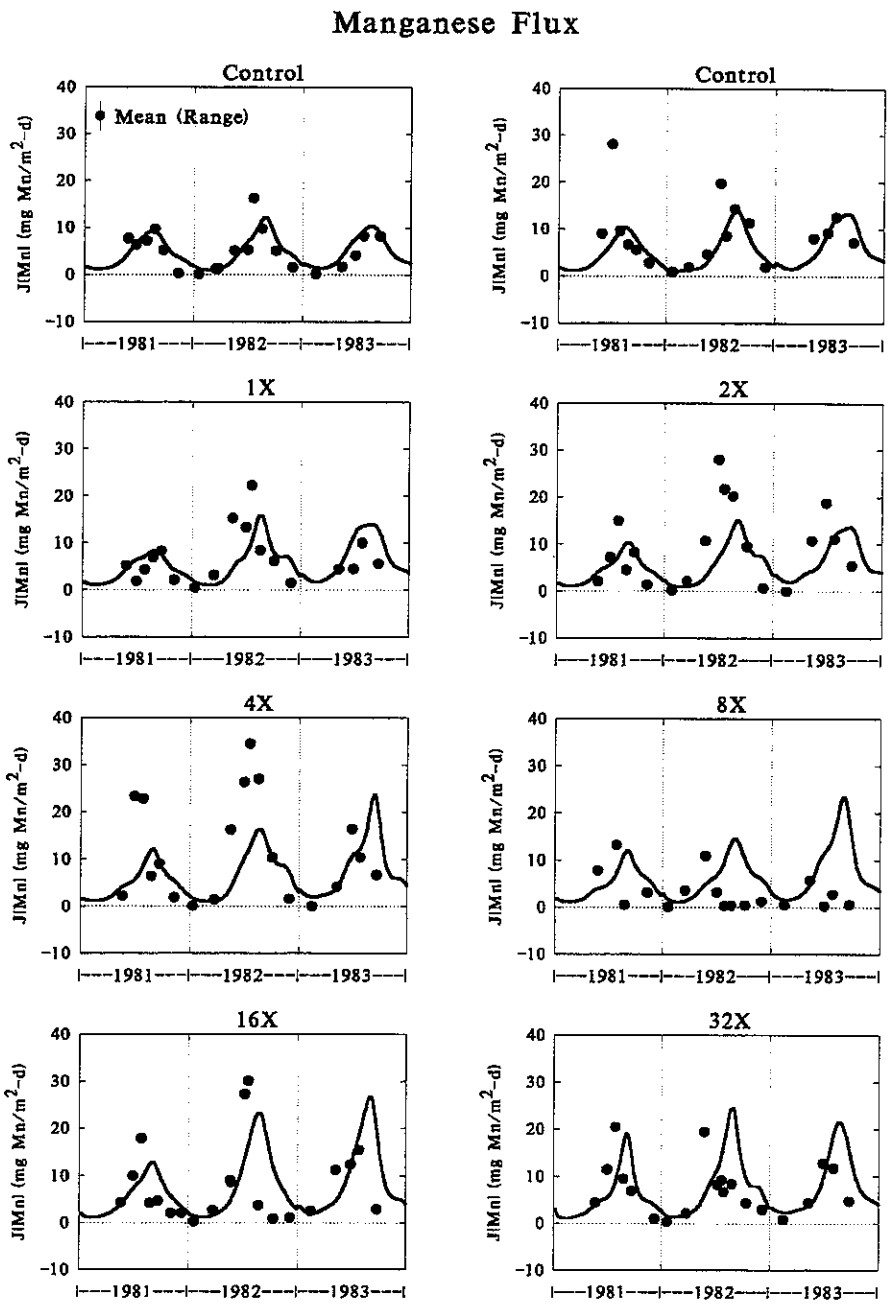

Fig. 6.9 Manganese flux to the overlying water. Run with *pH* dependent oxidation rate in the aerobic layer and observed overlying water particulate manganese concentrations.

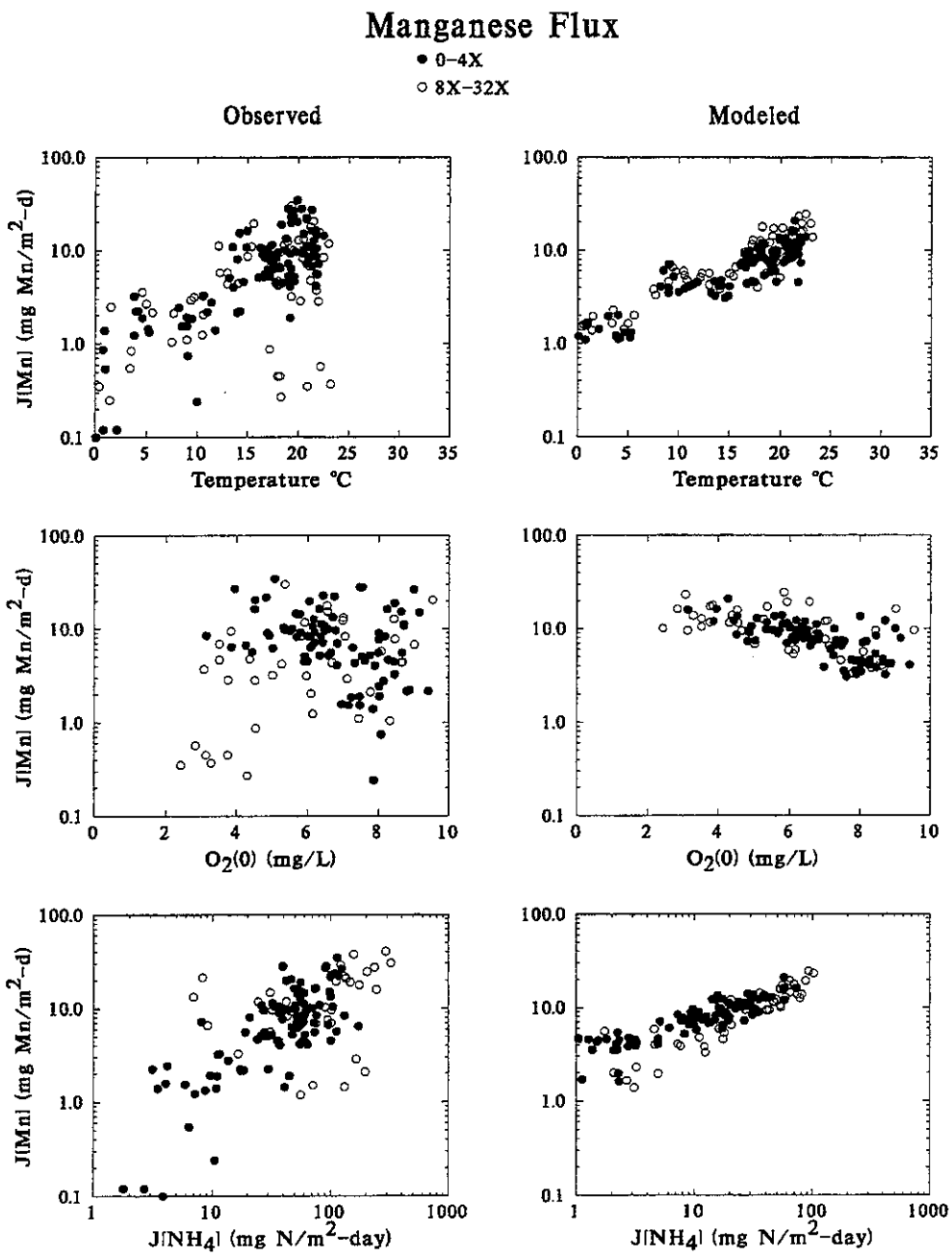

Fig. 6.10 Manganese flux versus T, $O_2(0)$, and $J[NH_4]$. Run with pH dependent oxidation rate in the aerobic layer and observed overlying water particulate manganese concentrations.

7

Water Column and Sediment Interactions

7.1 INTRODUCTION

The flux of dissolved manganese from the sediment to the overlying water is fueled by the depositional flux of particulate manganese from the overlying water to the sediment. In the previous chapters this flux J_{MnO_2} was either specified as a constant input parameter (Chapters 2–5) or computed using a settling velocity w_0 applied to the observed overlying water particulate concentration Mn_p (Chapter 6). This is a useful approach for model development and calibration. However, for actual applications it is necessary to be able to predict the water column manganese concentrations as well.

This chapter present an extension of the manganese and iron flux model which includes the overlying water as an integral part of the model. This formulation is the prototype for the actual coupled water column-sediment model that is applied to two lakes in the two subsequent chapters.

The addition of a third layer to the model is conceptually and computationally straightforward. Since the application is initially to the MERL data set, the water column layer is modeled as one completely mixed volume. The transport terms for this layer, in addition to those from the aerobic layer, is simply the advective inflow and outflow.

It is in the kinetic formulation that some choices need to be made. The question is: what controls the speciation between dissolved and particulate manganese in the water column. For the sediment aerobic layer, two reactions are considered: partitioning of $Mn\,(II)$ to sediment solids, and the oxidation reaction which converts $Mn\,(II)$ to $MnO_2\,(s)$. Clearly the oxidation reaction is important since the overlying water is usually oxic and that reaction occurs fairly rapidly. The question is: does the partitioning reaction need to be considered? The question is examined next.

7.1.1 Partitioning of Manganese (II)

The principle species of manganese (II) in water are the divalent cation Mn^{2+} and its hydrolysis product $Mn(OH)^+$ (see Chapter 2 and [Lindsay, 1979]). One expects, based on the partitioning behavior of other divalent metal cations, that manganese (II) should partition to particles in general and to hydrous iron oxides in particular.

In principle there is no difficulty in allowing both the partition reaction

$$Mn_d \leftrightarrow Mn_p \tag{7.1}$$

and the oxidation reaction

$$Mn\,(II) \rightarrow MnO_2\,(s) \tag{7.2}$$

to occur simultaneously in the water column. After all, this is exactly the formulation that is used in the sediment aerobic layer. The issue is: can the partition coefficient be determined in some independent way, or can it be shown that the partitioning reaction is insignificant relative to the oxidation reaction in the production of particulate manganese.

An estimate of the expected partition coefficients can be made using a linear free energy relationship [Brezonik, 1994]. The idea is that the variation in the equilibrium constant for a series of chemical species reacting with one ligand can be used to predict the variation in the equilibrium constant for another ligand. The usual choice for sorption reactions is the equilibrium constant for metal hydrolysis [Baes and Mesmer, 1976]

$$K_{MOH} = \frac{[M^{2+}]\,[OH^-]}{[MOH^+]} \tag{7.3}$$

which can be compared to the intrinsic sorption constants to hydrous iron oxide [Dzombak and Morel, 1990], and the sorption constants to sediment organic carbon [Mahony et al., 1996]. The relationships are presented in Fig. 7.1A.Manganese (II) has the

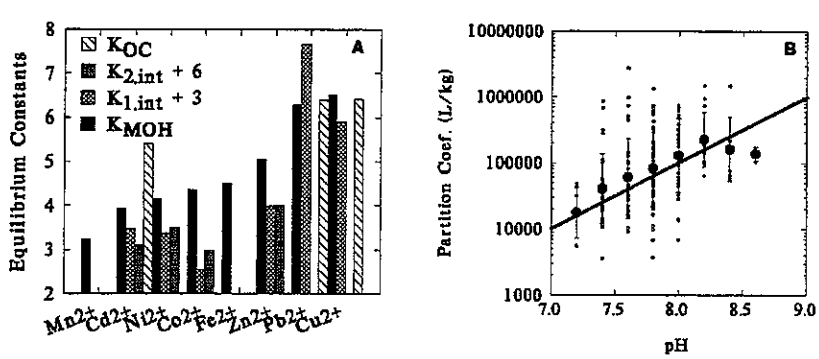

Fig. 7.1 (A) Linear free energy relationship between the first hydrolysis constants of metal ions, the intrinsic constants of sorption to hydrous iron oxide, and the partition coefficient to organic carbon at $pH = 7$. (B) Partition coefficients versus overlying water pH for the MERL data set.

smallest hydrolysis constant of the cations listed and, therefore, it is expected to have a comparatively small partition coefficient to hydrous iron oxide and particulate or-

Table 7.1 Manganese and Cadmium Partition Coefficients

pH	Observed π_{Mn} (L/kg)	Estimated $\pi_{Mn,OC}$ (L/kgOC)	Measured $\pi_{Cd,OC}$ (L/kgOC)
7	10^4	10^5–10^6	$10^{5.40}$
8	10^5	10^6–10^7	$10^{5.96}$

ganic carbon. Iron (II) is in the middle range so it would be expected to have sorption characteristics that are similar to Ni^{2+} and Zn^{2+}.

Fig. 7.1B presents the observed partition coefficient for manganese π_{Mn} from the MERL experiment, computed from the overlying water particulate $[Mn_p]$ and dissolved $[Mn_d]$ manganese concentrations and the concentration of suspended solids m

$$\pi_{Mn} = \frac{[Mn_p]/m}{[Mn_d]} \tag{7.4}$$

This computation assumes that all the particulate manganese is the result of sorption onto suspended solids and not a result of the oxidation of $Mn\,(II)$. It can be thought of as the partition coefficient that is necessary in order to explain the observed magnitude of particulate manganese. The results for $pH = 7$ and 8 are show in Table 7.1. The magnitudes of π_{Mn} are quite large. At $pH = 7$, $\pi_{Mn} = 10^4$ L/kg (Fig. 7.1B). If the particles were between 1 and 10% organic carbon, the weight fraction of organic carbon would be in the range $f_{OC} = 0.01$–0.1. The range in the organic carbon normalized partition coefficient

$$\pi_{Mn,OC} = \frac{\pi_{Mn}}{f_{OC}} \tag{7.5}$$

would be 10^5–10^6 L/kg OC. For $pH = 8$ the range would be $\pi_{Mn,OC} = 10^6$–10^7 L/kg OC.

For cadmium the measured organic carbon normalized partition coefficients are $\pi_{Cd,OC} = 10^{5.4}$ and $10^{5.96}$ L/kgOC at $pH = 7$ and 8 respectively [Mahony et al., 1996]. Thus $\pi_{Mn,OC}$ would need to be at least as large as $\pi_{Cd,OC}$, for $f_{OC} = 0.1$, and a factor of ten larger for $f_{OC} = 0.01$, in order to account for the partition coefficients shown in Fig. 7.1B. But manganese has a hydrolysis equilibrium constant, $10^{3.24}$, which is approximately one-half order of magnitude *smaller* than for cadmium, $10^{3.92}$. Thus it is unlikely that partitioning alone is the mechanism that generates particulate manganese. Of course, the partition coefficient estimated from the linear free energy relationship could be used in the model, but its influence would be small as demonstrated by the results in Table 7.1.

7.2 MODEL FORMULATION

The model formulation is shown in Fig. 7.2. The water column segment is linked to

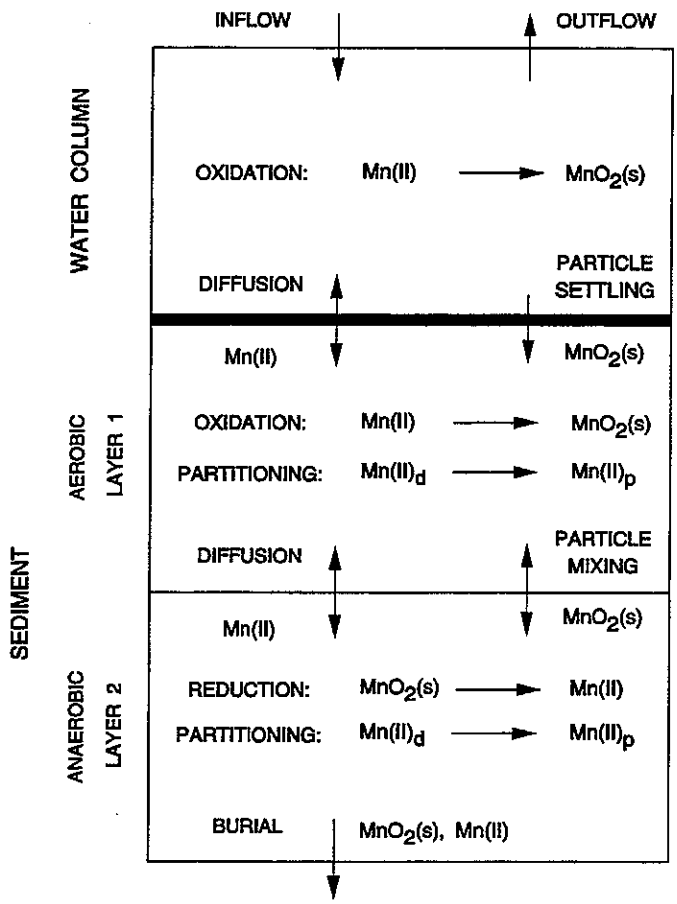

Fig. 7.2 Schematic of the manganese sediment flux model including the overlying water.

the aerobic layer by the transport terms: the diffusive exchange and particle settling. The oxidation of $Mn\,(II)$ is included. The water column transport is represented by an advective flow, which is the conventional representation for a completely mixed lake model, for example [Thomann and Mueller, 1987; Schnoor, 1996; Chapra, 1997]. The model equations that result for the water column concentrations are:
Layer 0 $Mn(II)$:

$$H_0 \frac{dMn(0)}{dt} = s\left(f_{d1} Mn(1) - Mn\,(0)\right) - \kappa_{Mn,0} Mn(0) + q_0\left(Mn\,(0)_i - Mn\,(0)\right) \quad (7.6)$$

Layer 0 $MnO_2\,(s)$:

$$H_0\frac{dMnO_2(0)}{dt} = \kappa_{Mn,0}Mn(0) - w_1 MnO_2\,(0) + q_0\,(MnO_2\,(0)_i - MnO_2\,(0)) \quad (7.7)$$

where

$$\kappa_{Mn,0} = k_{Mn,0}H_0 \quad (7.8)$$

the usual expression for a reaction velocity.

The terms in equations (7.6–7.7) represent the flux from the sediment to the overlying water

$$J\,[Mn] = s\,(f_{d1}Mn(1) - Mn\,(0)) \quad (7.9)$$

the oxidation of $Mn\,(II)$ to $MnO_2\,(s)$, the inflowing source of dissolved manganese $q_0 Mn\,(0)_i$ and the loss by outflow $q_0 Mn\,(0)$. The flow rate q_0 is included as an overflow rate (m/d)

$$q_0 = \frac{Q}{A} \quad (7.10)$$

where Q is the volumetric flow rate (m^3/d) and A is the surface area of the water column (m^2), so that the units of q_0 (m/d) are consistent with the other mass transport coefficients in the equations.

The layer 1 $Mn\,(1)$ equation (5.17a) is coupled to the layer 0 equation through $Mn\,(0)$ in eq. (5.17a) which is now computed using eq.(5.17a). In addition the source term in the layer 1 $MnO_2\,(1)$ eq.(5.17c) becomes

$$J_{MnO_2} = w_1 MnO_2\,(0) \quad (7.11)$$

which couples the sediment to the overlying water particulate concentration computed by eq.(7.7). Thus the sediment manganese mass balance equations become
Layer 1 $Mn(II)$:

$$\begin{aligned} H_1\frac{dMn(1)}{dt} &= -s\,(f_{d1}Mn(1) - Mn\,(0)) + K_{L12}(f_{d2}Mn(2) - f_{d1}Mn(1)) \quad (7.12)\\ &+w_{12}(f_{p2}Mn(2) - f_{p1}Mn(1)) - w_2 Mn\,(1) - \frac{\kappa^2_{Mn,1}}{s}f_{d1}Mn(1)\\ &+Mn\,(2)\,\dot{H}_1^+ - Mn\,(1)\left(\dot{H}_1 + \dot{H}_1^-\right) \end{aligned}$$

Layer 2 $Mn(II)$:

$$\begin{aligned} H_2\frac{dMn(2)}{dt} &= -K_{L12}(f_{d2}Mn(2) - f_{d1}Mn(1)) \quad (7.13)\\ &-w_{12}(f_{p2}Mn(2) - f_{p1}Mn(1)) - w_2\,(Mn(2) - Mn(1))\\ &+\kappa_{Mn,2}MnO_2(2) - Mn(2)\left(\dot{H}_2 + \dot{H}_1^+\right) + Mn(1)\dot{H}_1^- \end{aligned}$$

Layer 1 $MnO_2\,(s)$:

$$H_1\frac{dMnO_2(1)}{dt} = \frac{\kappa^2_{Mn,1}}{s}f_{d1}Mn(1) - w_2MnO_2(1) + w_{12}(MnO_2(2) - MnO_2(1)) + w_1MnO_2\,(0) + MnO_2(2)\dot{H}_1^+ - MnO_2(1)\left(\dot{H}_1 + \dot{H}_1^-\right) \tag{7.14}$$

Layer 2 $MnO_2\,(s)$:

$$H_1\frac{dMnO_2(2)}{dt} = -\kappa_{Mn,2}MnO_2(2) - w_{12}(MnO_2(2) - MnO_2(1)) - w_2\,(MnO_2(2) - MnO_2(1)) - MnO_2(2)\left(\dot{H}_2 + \dot{H}_1^+\right) + MnO_2(1)\dot{H}_1^- \tag{7.15}$$

The result is six coupled equations in the six unknown concentrations of $Mn(II)$ and $MnO_2\,(s)$ in the three layers.

7.2.1 Analytical Solutions

The steady state equations: eqs.(7.6–7.15) with $dMn/dt = 0$ and $dMnO_2/dt = 0$, can be solved analytically for the general case, but the solutions are too unwieldy to be useful. For the special case where the loss by burial in layer 2 is small relative to the loss by outflow in layer 0 and $w_2 = 0$ is a reasonable approximation, the equations can be solved and reduced to simple expressions.

The steady state equations are

Layer 0 $Mn(II)$:

$$0 = s\,(f_{d1}Mn(1) - Mn\,(0)) - \kappa_{Mn,0}Mn(0) + q_0\,(Mn\,(0)_i - Mn\,(0)) \tag{7.16a}$$

Layer 0 $MnO_2\,(s)$:

$$0 = \kappa_{Mn,0}Mn(0) - w_1MnO_2\,(0) + q_0\,(MnO_2\,(0)_i - MnO_2\,(0)) \tag{7.16b}$$

Layer 1 $Mn(II)$:

$$0 = -s\,(f_{d1}Mn(1) - Mn\,(0)) + K_{L12}(f_{d2}Mn(2) - f_{d1}Mn(1)) + w_{12}(f_{p2}Mn(2) - f_{p1}Mn(1)) - \frac{\kappa^2_{Mn,1}}{s}f_{d1}Mn(1) \tag{7.16c}$$

Layer 1 $MnO_2\,(s)$:

$$0 = \frac{\kappa^2_{Mn,1}}{s}f_{d1}Mn(1) + w_{12}(MnO_2(2) - MnO_2(1)) + w_1MnO_2\,(0) \tag{7.16d}$$

Layer 2 $Mn(II)$:

$$0 = -K_{L12}(f_{d2}Mn(2) - f_{d1}Mn(1)) - w_{12}(f_{p2}Mn(2) - f_{p1}Mn(1)) \tag{7.16e}$$

Layer 2 $MnO_2\,(s)$:

$$0 = -\kappa_{Mn,2}MnO_2(2) - w_{12}(MnO_2(2) - MnO_2(1)) \tag{7.16f}$$

These six simultaneous equations (7.16) can be solved analytically to yield a remarkably simple and instructive set of solutions. The layer 0 concentrations are

$$Mn\,(0) = Mn\,(0)_i \frac{w_1 + q_0}{w_1 + q_0 + \kappa_{Mn,0}} + MnO_2\,(0)_i \frac{w_1}{w_1 + q_0 + \kappa_{Mn,0}} \tag{7.17}$$

$$MnO_2\,(0) = Mn\,(0)_i \frac{\kappa_{Mn,0}}{w_1 + q_0 + \kappa_{Mn,0}} + MnO_2\,(0)_i \frac{\kappa_{Mn,0} + q_0}{w_1 + q_0 + \kappa_{Mn,0}} \tag{7.18}$$

Note that

$$Mn\,(0) + MnO_2\,(0) = Mn\,(0)_i + MnO_2\,(0)_i \tag{7.19}$$

which follows from a mass balance around the entire water column-sediment system

$$q_0\,(Mn\,(0)_i + MnO_2\,(0)_i) = q_0\,(Mn\,(0) + MnO_2\,(0)) \tag{7.20}$$

The mass flux of inflowing manganese must be equal to the only loss terms for manganese, namely the layer 0 outflows. This is why the assumption $w_2 = 0$ simplifies the situation dramatically.

7.2.1.1 Limiting Forms The concentrations of $Mn\,(II)$ and $MnO_2\,(s)$ that result in the water column (eqs.7.17–7.18) are controlled by ratios involving $\kappa_{Mn,0}$, q_0, and w_1 which are all parameters for water column processes: oxidation, outflow and settling to the sediment. No sediment process parameters are involved. This is a surprising result which requires an explanation.

The water column concentrations are linear functions of the inflowing concentrations weighted by ratios with the sum of $\kappa_{Mn,0}$, q_0, and w_1 in the denominator. Consider first what happens if the flow rate through the water column q_0 is large. Then the solutions become

$$\begin{aligned} Mn\,(0) &= Mn\,(0)_i \frac{w_1 + q_0}{w_1 + q_0 + \kappa_{Mn,0}} + MnO_2\,(0)_i \frac{w_1}{w_1 + q_0 + \kappa_{Mn,0}} \\ &\underset{\text{as } q_0 \to \infty}{\longrightarrow} Mn\,(0)_i \frac{q_0}{q_0} + MnO_2\,(0)_i \frac{w_1}{q_0} \\ &\longrightarrow Mn\,(0)_i \end{aligned} \tag{7.21}$$

$$\begin{aligned} MnO_2(0) &= Mn(0)_i \frac{\kappa_{Mn,0}}{w_1 + q_0 + \kappa_{Mn,0}} + MnO_2(0)_i \frac{\kappa_{Mn,0} + q_0}{w_1 + q_0 + \kappa_{Mn,0}} \\ &\underset{\text{as } q_0 \to \infty}{\to} Mn(0)_i \frac{\kappa_{Mn,0}}{q_0} + MnO_2(0)_i \frac{q_0}{q_0} \\ &\to MnO_2(0)_i \end{aligned} \tag{7.22}$$

i.e. there is no change in the water column concentrations; they remain at the inflow values. This is entirely reasonable. The large inflow provides an infinite supply of $Mn(II)$ and $MnO_2(s)$ so that whatever happens in the sediment has no effect.

Consider what happens if the settling velocity w_1 is large

$$\begin{aligned} Mn(0) &= Mn(0)_i \frac{w_1 + q_0}{w_1 + q_0 + \kappa_{Mn,0}} + MnO_2(0)_i \frac{w_1}{w_1 + q_0 + \kappa_{Mn,0}} \\ &\underset{\text{as } w_1 \to \infty}{\to} Mn(0)_i \frac{w_1}{w_1} + MnO_2(0)_i \frac{w_1}{w_1} \\ &\to Mn(0)_i + MnO_2(0)_i \end{aligned} \tag{7.23}$$

$$\begin{aligned} MnO_2(0) &= Mn(0)_i \frac{\kappa_{Mn,0}}{w_1 + q_0 + \kappa_{Mn,0}} + MnO_2(0)_i \frac{\kappa_{Mn,0} + q_0}{w_1 + q_0 + \kappa_{Mn,0}} \\ &\underset{\text{as } w_1 \to \infty}{\to} Mn(0)_i \frac{\kappa_{Mn,0}}{w_1} + MnO_2(0)_i \frac{\kappa_{Mn,0} + q_0}{w_1} \\ &\to 0 \end{aligned} \tag{7.24}$$

This is a more interesting result: all the inflowing manganese appears as dissolved $Mn(II)$.

The explanation can be arrived at by considering the constraint imposed by mass balance. Since the settling velocity is becoming large, the particulate concentration in the water column is approaching zero. Therefore all the inflowing manganese must escape via the dissolved concentration in the water column since—and this is why the simplification $w_2 = 0$ is so powerful—there is no other loss pathway. So the dissolved concentration increases to what is necessary to satisfy mass balance, namely the total inflowing concentration of manganese, both particulate and dissolved.

The converse situation occurs if the oxidation rate $\kappa_{Mn,0}$ is large

$$\begin{aligned} Mn(0) &= Mn(0)_i \frac{w_1 + q_0}{w_1 + q_0 + \kappa_{Mn,0}} + MnO_2(0)_i \frac{w_1}{w_1 + q_0 + \kappa_{Mn,0}} \\ &\xrightarrow[\text{as } \kappa_{Mn,0} \to \infty]{} Mn(0)_i \frac{w_1}{\kappa_{Mn,0}} + MnO_2(0)_i \frac{w_1}{\kappa_{Mn,0}} \\ &\to 0 \end{aligned} \tag{7.25}$$

$$\begin{aligned} MnO_2(0) &= Mn(0)_i \frac{\kappa_{Mn,0}}{w_1 + q_0 + \kappa_{Mn,0}} + MnO_2(0)_i \frac{\kappa_{Mn,0} + q_0}{w_1 + q_0 + \kappa_{Mn,0}} \\ &\xrightarrow[\text{as } \kappa_{Mn,0} \to \infty]{} Mn(0)_i \frac{\kappa_{Mn,0}}{\kappa_{Mn,0}} + MnO_2(0)_i \frac{\kappa_{Mn,0}}{\kappa_{Mn,0}} \\ &\to Mn(0)_i + MnO_2(0)_i \end{aligned} \tag{7.26}$$

All the dissolved manganese in the water column oxidizes to particulate manganese which must increase in concentration to the total inflowing manganese concentration so that the outflowing flux equals the inflowing flux.

7.2.1.2 Other Layers The sediment concentrations of $Mn(II)$ and $MnO_2(s)$ in layers 1 and 2 are also reasonably concise expressions

$$Mn(1) = \frac{Mn(0)_i (s(w_1 + q_0) + \kappa_{Mn,0} w_1) + MnO_2(0)_i w_1 (s + q_0 + \kappa_{Mn,0})}{s f_{d1} (w_1 + q_0 + \kappa_{Mn,0})} \tag{7.27a}$$

$$MnO_2(1) = MnO_2(2) \frac{w_{12} + \kappa_{Mn,2}}{w_{12}} \tag{7.27b}$$

$$Mn(2) = Mn(1) \frac{f_{d1} K_{L12} + f_{p1} w_{12}}{f_{d2} K_{L12} + f_{p2} w_{12}} + MnO_2(2) \frac{\kappa_{Mn,2}}{f_{d2} K_{L12} + f_{p2} w_{12}} \tag{7.27c}$$

$$MnO_2(2) = \frac{\begin{aligned} &(Mn(0)_i + MnO_2(0)_i) \left(\left(\frac{\kappa_{Mn,1}^2}{s} + \kappa_{Mn,0} \right) w_1 s + \kappa_{Mn,0} \frac{\kappa_{Mn,1}^2}{s} w_1 \right) \\ &+ q_0 s \left(\frac{\kappa_{Mn,1}^2}{s} Mn(0)_i + w_1 MnO_2(0)_i \right) \end{aligned}}{\kappa_{Mn,2} s (w_1 + q_0 + \kappa_{Mn,0})} \tag{7.27d}$$

The importance of the various parameter groupings will be examined using the numerical results presented below as a guide.

7.2.1.3 Manganese Flux The most surprising result of all is the solution for the sediment flux of $Mn\,(II)$. It is obtained by evaluating the defining equation

$$J\,[Mn] = s\,(f_{d1}Mn(1) - Mn\,(0)) \tag{7.28}$$

using the solutions for $Mn\,(1)$ and $Mn\,(0)$ given above (eqs.7.17 and 7.27a) and using eq.(7.18) to substitute for the resulting expression. The result is

$$J\,[Mn] = w_1 MnO_2\,(0) \tag{7.29}$$

It is equal to the flux of particulate $MnO_2\,(s)$ that settles from the water column to the sediment. There is a complete recycling of the particulate flux to the sediment as a dissolved flux from the sediment.

This remarkable prediction appears to be substantiated by the MERL experimental observations. Fig.7.3 compares the manganese flux $J\,[Mn]$ to the particulate manganese concentration in the overlying water $Mn(0)_p$. The point by point comparison (Fig.7.3A) shows no apparent relationship although the linear regression line included in the figure does indicate that a relationship exists. If the data are grouped (Fig.7.3B) a clear relationship emerges. The line corresponds to a settling velocity of $w_1 = 1.0$ m/d.

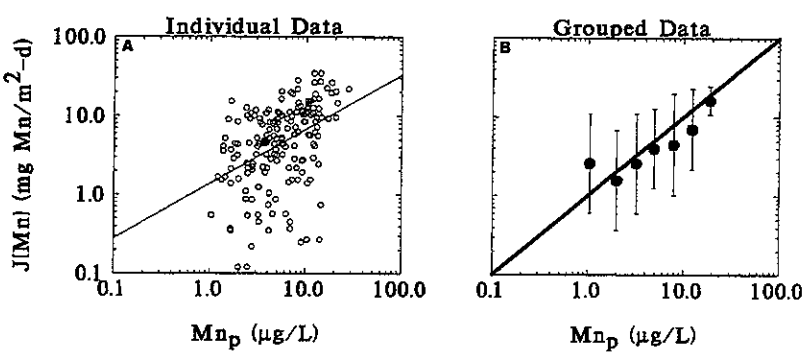

Fig. 7.3 (A) The observed manganese flux $J\,[Mn]$ versus the particulate manganese concentration in the overlying water $Mn(0)_p$. Only data for which $Mn(0)_p > 1\mu$g/L are included in order to reduce the influence of analytical errors at low concentrations. The linear regression line is shown. (B) The data are grouped in 0.2 $\log_{10}$ units. The mean $\pm$ the standard deviation is shown. The line corresponds to a settling velocity of $w_1 = 1$ m/d.

We can understand the flux solution, eq.(7.29), by examining what happens if no $MnO_2\,(s)$ forms in the water column. This happens if no particulate manganese flows

into the water column, $MnO_2(0)_i = 0$, and no manganese dioxide forms by oxidation of $Mn(II)$, so that $\kappa_{Mn,0} = 0$. For this case the concentrations in the overlying water (eqs.7.17–7.18) become

$$MnO_2(0) = 0 \tag{7.30}$$

$$Mn(0) = Mn(0)_i \tag{7.31}$$

The pore water concentration in the aerobic layer equilibrates with the overlying water concentration (eq.7.27c)

$$Mn(1)_d = f_{d1} Mn(1) = Mn(0) \tag{7.32}$$

and all the other sediment concentrations adjust accordingly to this concentration. Since there are no mass balance consequences—these concentrations can be any value whatever without a need to remove manganese to maintain mass balance—no flux from the sediment is generated.

Note that no other solution is possible. If the pore water concentration in layer 1 was different from the layer 0 concentration, that would imply that a flux of manganese is present either from or to the overlying water. But if that occurred, then the sediment concentrations would either be continually depleted or build up indefinitely, neither of which is a steady state solution. Therefore the zero flux case is the only allowable solution.

If $MnO_2(0) \neq 0$ so that there is a flux $w_1 MnO_2(0)$ to the sediment, then a flux from the sediment is necessary for mass balance to be maintained. Since the only possible flux is a dissolved flux $J[Mn]$ back to the overlying water—a burial flux has been eliminated as a possibility by assuming $w_2 = 0$—the concentrations adjust to exactly return this incoming flux (eq.7.29).

This remarkable result: that the sediment flux is controlled by water column processes and, in particular, the particulate concentration and settling velocity, was eventually noticed after many numerical simulations were performed. It provided the motivation for seeking analytical solutions to establish the precise form of the dependence. The solutions for the general case, $w_2 \neq 0$, are too complex to be useful, but removing the possibility of a burial flux simplifies the solutions so that the relationship between the particulate flux to the sediment and the recycled dissolved flux emerges. The utility of these analytical solutions to help in the understanding of the time variable numerical results is examined next.

7.3 TIME VARIABLE MODEL

The complete model includes the overlying water and the sediment mass balance equations. The equations are discussed first, followed by the a sequence of numerical calculations of increasing complexity and realism.

7.3.1 Vector-Matrix Equation

The equations used for the numerical calculations are expressed in vector-matrix form. They comprise the two layer model (eqs. 5.18–5.23) with the addition of the water column as the third layer. The manganese concentration state variable vector is

$$\mathbf{c}(t)=\begin{bmatrix} Mn\,(1) \\ Mn\,(2) \\ MnO_2\,(1) \\ MnO_2\,(2) \\ Mn\,(0) \\ MnO_2\,(0) \end{bmatrix} \tag{7.33}$$

where two additional rows have been added for the water column concentrations. The matrix $\mathbf{A}(t) = [a_{ij}]$ has elements

$$a_{11} = -sf_{d1} - f_{12} - w_2 - \frac{\kappa_{Mn,1}^2}{s}\left(10^{2(pH_1-7)}\right) O_2\,(0)\, f_{d1} - \left(\dot{H}_1 + \dot{H}_1^-\right) \tag{7.34a}$$

$$a_{12} = f_{21} + \dot{H}_1^+ \tag{7.34b}$$

$$a_{15} = s \tag{7.34c}$$

$$a_{21} = f_{12} + w_2 + \dot{H}_1^- \tag{7.34d}$$

$$a_{22} = -f_{21} - w_2 - \left(\dot{H}_2 + \dot{H}_1^+\right) \tag{7.34e}$$

$$a_{24} = \kappa_{Mn,2} \tag{7.34f}$$

$$a_{31} = \frac{\kappa_{Mn,1}^2}{s}\left(10^{2(pH_1-7)}\right) O_2\,(0)\, f_{d1} \tag{7.34g}$$

$$a_{33} = -w_{12} - w_2 - \left(\dot{H}_1 + \dot{H}_1^-\right) \tag{7.34h}$$

$$a_{34} = w_{12} + \dot{H}_1^+ \tag{7.34i}$$

$$a_{36} = w_1 \tag{7.34j}$$

$$a_{43} = w_{12} + w_2 + \dot{H}_1^- \tag{7.34k}$$

$$a_{44} = -\kappa_{Mn,2} - w_{12} - w_2 - \left(\dot{H}_2 + \dot{H}_1^+\right) + \dot{H}_1^- \tag{7.34l}$$

$$a_{51} = s f_{d1} \tag{7.34m}$$

$$a_{55} = -s - H_0/t_0 - \kappa_{Mn,0}\left(10^{2(pH_0-7)}\right) O_2(0) \tag{7.34n}$$

$$a_{65} = \kappa_{Mn,0}\left(10^{2(pH_0-7)}\right) O_2(0) \tag{7.34o}$$

$$a_{66} = -H_0/t_0 - w_1 \tag{7.34p}$$

where f_{12} and f_{21} are the effective mass transfer coefficients from layer 1 to layer 2 and from layer 2 to layer 1 respectively as before (eq.5.21a–5.21b) and all other a_{ij}'s are zero. The forcing function is

$$\mathbf{b}(t) = \begin{bmatrix} 0 \\ 0 \\ 0 \\ 0 \\ q_0 Mn(0)_i \\ q_0 MnO_2(0)_i \end{bmatrix} \tag{7.35}$$

with the only sources being the $Mn(II)$ and $MnO_2(s)$ flowing into layer 1. The diagonal matrix of layer depths, $\mathbf{H}(t)$, now includes the overlying water segment depth

$$\mathbf{H}(t) = \mathrm{diag}\left[\ H_1(t),\ \ H_2(t),\ \ H_1(t),\ \ H_2(t),\ \ H_0,\ \ H_0\ \right] \tag{7.36}$$

An implicit finite difference equation (eq.5.26) is used to solve these equations.

7.3.2 Comparison to Steady State Results

How useful are the steady state solutions in understanding the behavior of the time variable model? The first step is to check the results of the time variable model when it is configured to be a steady state computation. This is accomplished by disabling all the time varying elements. Thus all the parameters that cause the reaction rates to vary with temperature (the θ's) are set equal to one. This includes the nutrient and oxygen model parameters—for example the diagenesis reactions. The inflowing concentrations $Mn(0)_i$ and $MnO_2(0)_i$ are set to constant average values. The only time variation that is allowed to remain is that induced by the varying overlying water dissolved oxygen variation $O_2(0)$. The reason is to ascertain the effect of just this source of variation. The burial velocity is set to zero as well to correspond to the steady state solutions.

The time variable model is initialized by cycling the inputs for the first year until a periodic steady state is achieved. Then average concentrations are computed. In addition, annual average parameters and forcing functions are computed and the steady state equations are evaluated using these values, which are presented in Table 7.2. This procedure is followed for all the time variable-steady state comparisons.

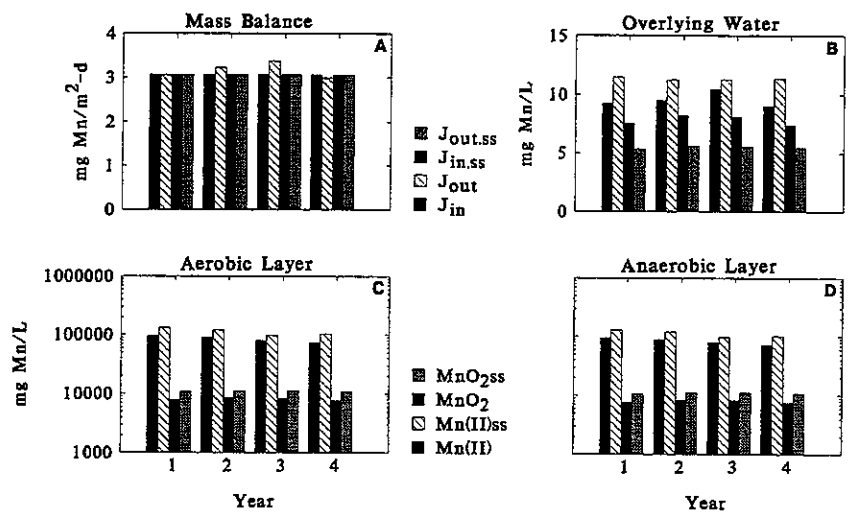

Fig. 7.4 Comparison of steady state and time variable solutions. Annual averages for the periodic steady state initialization, and the three years of simulation. (A) Mass balances: flux in (J_{in}) and flux out (J_{out}). (B) Overlying water concentrations. (C) Aerobic layer. (D) Anaerobic layer. The subscript "ss" indicates the steady state analytical solution.

The results are compared to the annual average fluxes and concentrations in Fig.7.4 as year 1. The subsequent years 2–4 represent the results of the simulation of the three year MERL experiment. The mass balances are checked in Fig.7.4A. Since the year one results are for an equilibrated model, the inflowing flux balances the out-flowing flux perfectly. However, the year 2 and 3 time variable model results show an imbalance with the outflow being larger than the inflow. This is occurring because the sediment is releasing more manganese than is settling to the sediment during this period. The cause is the change in overlying water conditions at the onset of the experiment. Of course the steady state solutions are perfectly in balance since they are the result that would be expected after the system has adjusted to the changed conditions.

The steady state and annual average concentrations for the overlying water (B), aerobic layer (C), and anaerobic layer (D) are somewhat different, reflecting the lack of steady state conditions in the time variable results. However the magnitudes are correct, which suggests that the steady state solutions can be used to guide calibration and to explain the time variable results.

Table 7.2 Steady State Sediment Model Parameters

Treatment	0.000	2.000	4.000	8.000	32.000
pH	8.093	8.143	8.234	7.864	8.254
T	10.644	10.972	10.840	11.062	10.861
H_0	5.000[a]	5.000	5.000	5.000	5.000
t_0	27.400[b]	27.400	27.400	27.400	27.400
s	0.089[c]	0.119	0.171	0.208	0.223
$\kappa_{Mn,0}$	0.963[c]	1.051	1.056	0.924	0.973
q_0	0.182[c]	0.182	0.182	0.182	0.182
w_1	2.000[c]	2.000	2.000	2.000	2.000
$Mn\,(0)_i$	9.332[d]	9.332	9.332	9.332	9.332
$MnO_2\,(0)_i$	7.481[d]	7.481	7.481	7.481	7.481
$\frac{Mn\,(0)_{ss}}{Mn\,(0)}$	11.232[d]	10.927	10.909	11.371	11.197
$\frac{MnO_2\,(0)_{ss}}{MnO_2\,(0)}$	8.863[d]	9.878	10.381	11.521	10.608
f_{d1}	5.581[d]	5.886	5.904	5.441	5.616
f_{p1}	7.603[d]	8.359	8.163	8.382	8.476
w_{12}	0.000951	0.000951	0.000951	0.000951	0.000951
K_{L12}	0.999	0.999	0.999	0.999	0.999
$\kappa^2_{Mn,1}/s$	0.048[c]	0.069	0.093	0.105	0.122
$\frac{J[Mn]_{ss}}{J[Mn]}$	1.42×10^{-7}[c]	1.58×10^{-7}	1.39×10^{-7}	1.42×10^{-7}	8.09×10^{-8}
$\frac{Mn\,(1)_{ss}}{Mn\,(1)}$	11.161[e]	11.771	11.808	10.883	11.233
$\frac{MnO_2\,(1)_{ss}}{MnO_2\,(1)}$	7.549[e]	8.625	8.446	8.964	8.812
H_2	143.275[d]	115.267	83.988	66.813	64.660
w_2	99.925[d]	91.045	69.484	63.885	58.630
f_{d2}	11.394[d]	11.942	11.935	10.987	11.325
f_{p2}	7.884[d]	8.593	8.340	8.521	8.600
$\kappa_{Mn,2}$	0.00879[a]	0.00902	0.00927	0.00941	0.00947
$\frac{Mn\,(2)_{ss}}{Mn\,(2)}$	0.00100[c]	0.00100	0.00100	0.00100	0.00100
$\frac{MnO_2\,(2)_{ss}}{MnO_2\,(2)}$	141.012[d]	114.090	83.422	66.443	64.375
	98.342[d]	90.108	69.006	63.519	58.363
	11.161[d]	11.771	11.808	10.883	11.233
	7.721[d]	8.468	8.249	8.439	8.528

[a] (m) [b] (d) [c] (m/d) [d] (mg Mn/m^3) [e] (mg Mn/m^2-d)

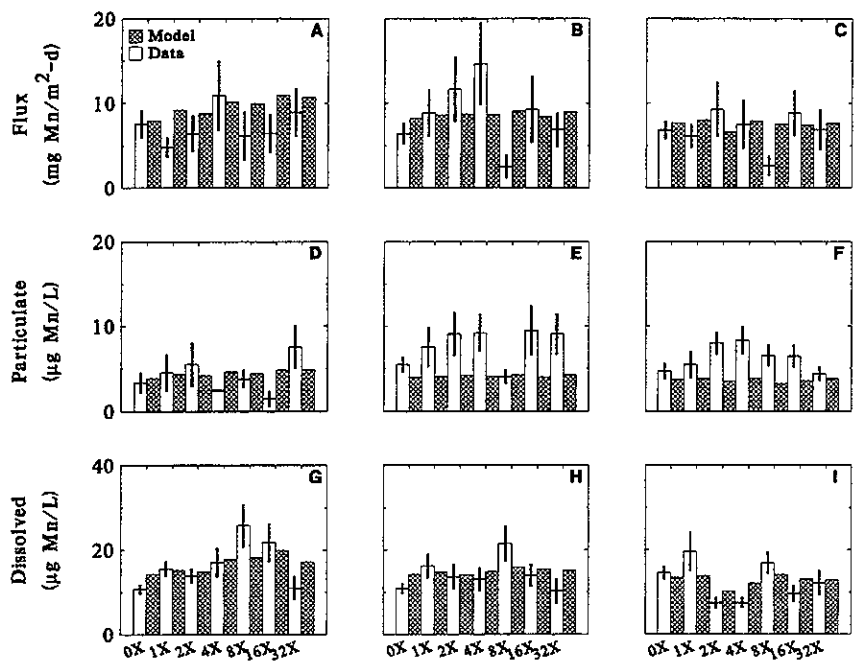

Fig. 7.5 Comparison of annual average observations and time variable model results. (A,D,G) 1981, (B,E,H) 1982, (C,F,I) 1983.

The annual average results from the time variable model are compared to the observations in Fig.7.5.

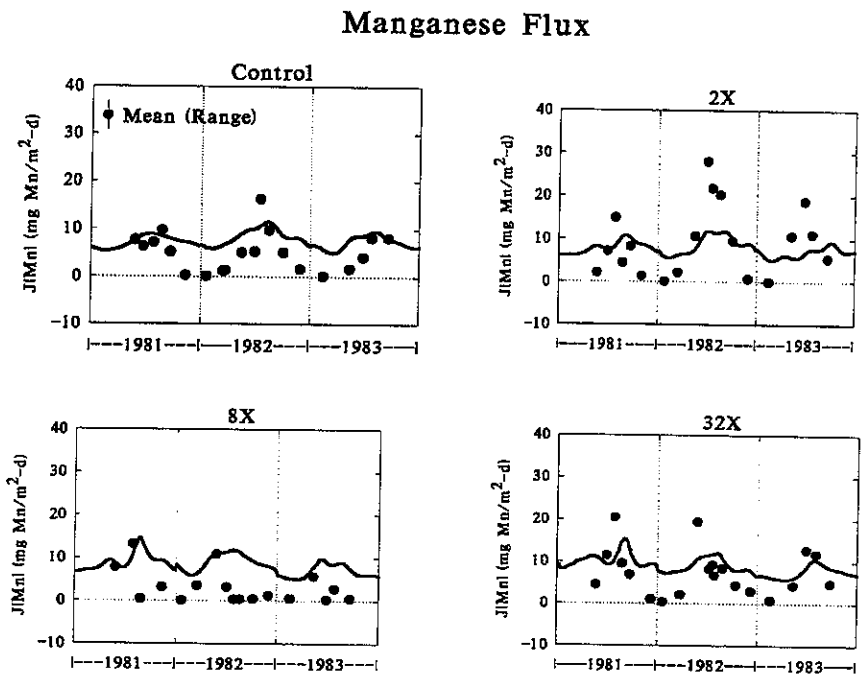

Fig. 7.6 Manganese fluxes for the control, 2X, 8X, and 32X treatment.

7.3.2.1 Effect of Dissolved Oxygen Variation It is instructive to examine the time variable results in more detail since there is only one source of time variation in the computation: the varying overlying water dissolved oxygen concentration. The variation in manganese flux from the sediment $J[Mn]$ is shown in Fig. 7.6 for the control and three treatments. The variation, which is not insignificant, is due in part to the variation in $s = SOD/O_2(0)$ and the variation in the depth of the aerobic layer H_1 that results from the variation in $O_2(0)$.

Overlying water dissolved oxygen concentration also affects the rate at which dissolved manganese (II) oxidizes and forms particulate manganese dioxide $MnO_2(0)$. The result is a variation in the particulate manganese concentration shown in Fig.7.7. Since the flux to the sediment is $w_1 MnO_2(0)$, its variation also induces an additional variation in $J[Mn]$ (Fig.7.6). The combination of the varying oxidation rate and the varying flux from the sediment produces a variation in the overlying water dissolved manganese concentration $Mn(0)$ as shown in Fig.7.7.

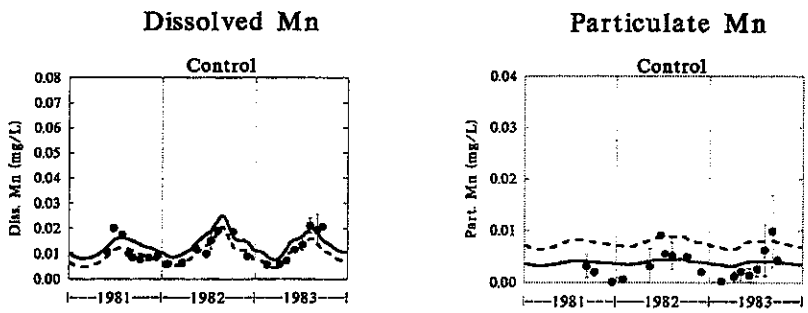

Fig. 7.7 Variation in overlying water dissolved and particulate manganese. The definitions of the solid and dashed lines are the same as in Fig.965.0008 and Fig.965.0009 to be discussed subsequently.

7.4 CALIBRATION

The calibration of the three layer model to the MERL data set is presented in this section. The particulate and dissolved concentrations $MnO_2\,(0)_i$ and $Mn\,(0)_i$ in the inflow to the water column for the three years are obtained from the average particulate and dissolved concentration in the control tank's water columns (Fig.7.8). The idea is that the control tanks are replicating the bay and therefore the concentrations in the control tanks are similar to what is in the inflow to the other tanks. For the latter part of the third year the actual inflowing concentrations were determined and these are included in Fig.7.8. They are similar to the control tank concentrations.

The pH in the three layers of the model is shown in Fig.7.9. The method used to compute the aerobic layer pH_1 is presented in Chapter 6. The rest of the inputs have been described in Chapter 5.

7.4.1 Model Results

The model is equilibrated to a periodic steady state by using the average water column concentrations of the control tanks for the inflowing concentrations and cycling the model. The same input is used for each cycle with the ending condition for the previous year is used as the initial conditions. The idea is to simulate the state of the sediments before the nutrient enrichment experiment commenced. The presumption is that the behavior of the first year of the controls is characteristic of the average situation in Narragansett Bay in general. Once the computation is initialized, the treatment loadings are initiated and the model is run for the three years.

The annual average data and model results for manganese fluxes, water column particulate and dissolved concentrations, are shown in Fig.7.10. The model parameters are listed in Table 5.1.

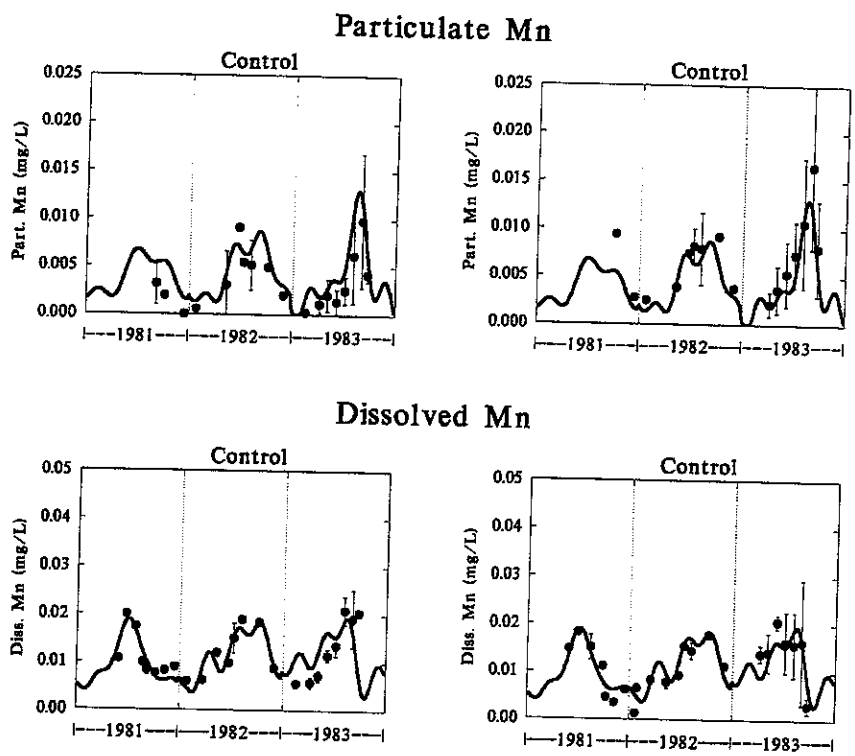

Fig. 7.8 Concentration of particulate and dissolved manganese in two control mesocosms. The lines are fitted to both data sets and they are used as the inflowing concentrations.

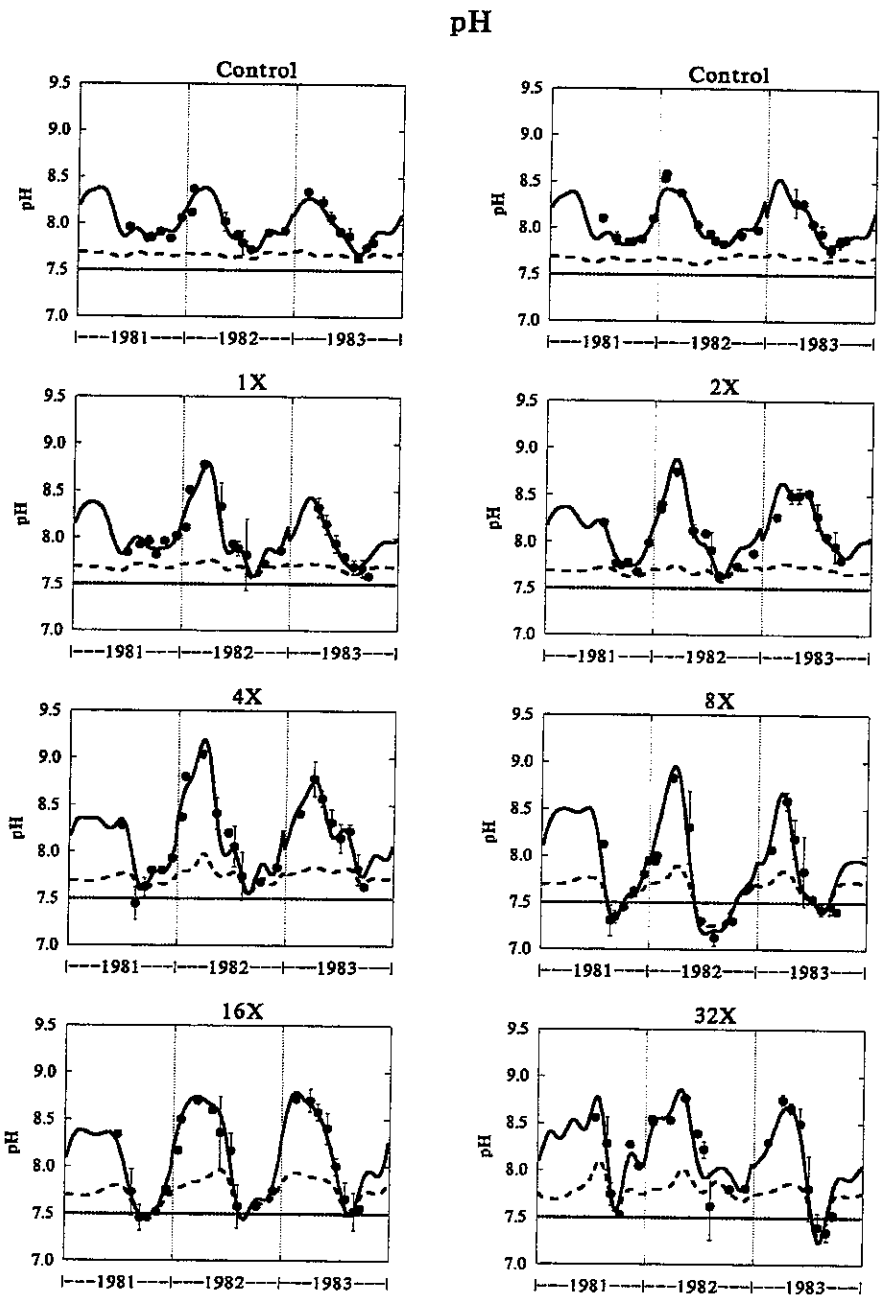

Fig. 7.9 Water column (solid line – fitted to the data), aerobic layer (dashed line – computed using the equations listed in section ref phmethod), and assumed constant anaerobic layer pH (dotted line).

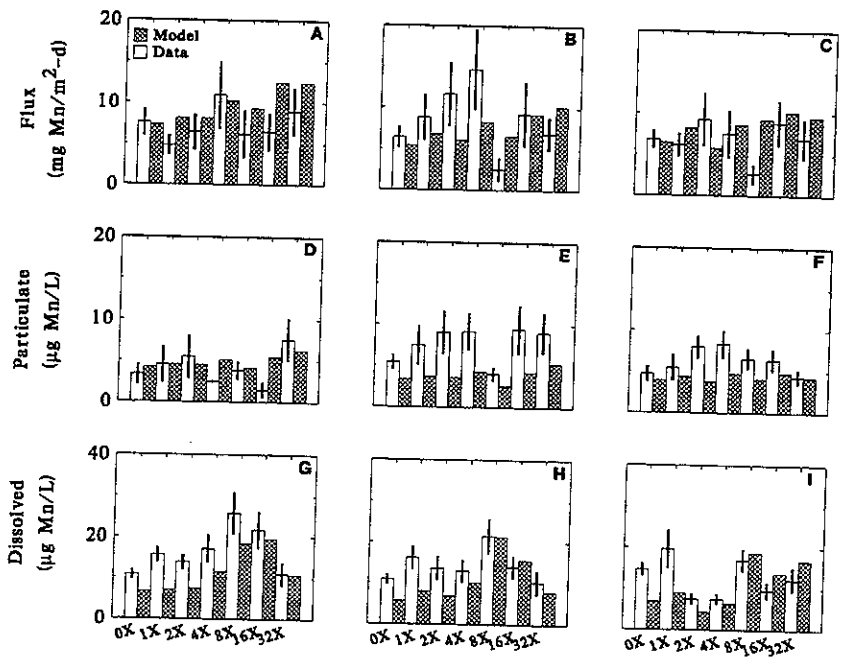

Fig. 7.10 Comparison of average annual data and model results: 1981 (A,D,G); 1982 (B,E,H); 1983 (C,F,I). Manganese flux (A,B,C). Water column particulate (D,E,F) and dissolved (G,H,I) manganese.

The manganese fluxes (A–C) increase with increased nutrient loading from the control (0X) to the most heavily loaded (32X). The magnitude and pattern are reproduced for the first and third year. The large flux increases in the 1X to 4X treatments for the second year (B) are not reproduced. These correspond to the large increase in particulate concentration (E).

The time variable computed and observed concentrations in the overlying water are shown in Figs.7.11 and 7.12.

Two sets of model computations are presented. The dashed lines are the model computed dissolved $Mn\,(0)$ and particulate $MnO_2\,(0)$ concentrations. These results correspond to the assumption that all the particulate manganese is filterable and would be quantified as particulate manganese. The solid lines are the concentrations that are computed if a fraction of the particulate manganese, $f_{\text{colloidal}}$, is not filterable. The reason for this modification is discussed below in the next section.

The model correctly computes the seasonal variation of dissolved manganese and the pattern of increasing concentrations to the 8X treatment and decreasing thereafter (Figs.7.11). The differences between the dashed and solid lines are not large and the data do not clearly favor one over the other. There is a systematic under-prediction of the dissolved manganese during the winter and spring of each year. We have no explanation for this discrepancy. The increase in pH_0 that occurs (Fig.7.9) causes a rapid increase in the rate at which the dissolved $Mn\,(0)$ oxidizes to particulate $MnO_2\,(0)$. The particulate manganese settles from the water column to the sediment where it remains for a period of time and then is recycled to the overlying water as a flux.

The manganese fluxes which result are shown in Fig.7.13. The model reproduces the observed seasonal variation as well as the increase in flux as the tanks are enriched from 1X to 32X. The flux to the water column causes the dissolved concentration to increase which produces the seasonal pattern.

As a result of the formation of particulate manganese in the water column, its settling to the sediment, and its release to the water column, there is a seasonal variation in the total manganese concentration in the water column as shown in Fig.7.14. It might be supposed that the variation in total manganese concentration is also influenced by the variation in input concentrations, Fig.7.8. However, this is not the case. It is possible to suppress the seasonal variation in the inflowing water by using constant input concentrations, which are the yearly average of the concentrations used previously (Fig.7.8), and are shown in Fig.7.15.The resulting total manganese concentrations are shown in Fig.7.16. The concentrations are almost indistinguishable from the results using the time variable inputs (Fig.7.14). This is also true for all the other model outputs. Thus the temporal variation in total manganese in the water column is generated by the migration of manganese from the sediment to the water column and back again during the annual cycle.

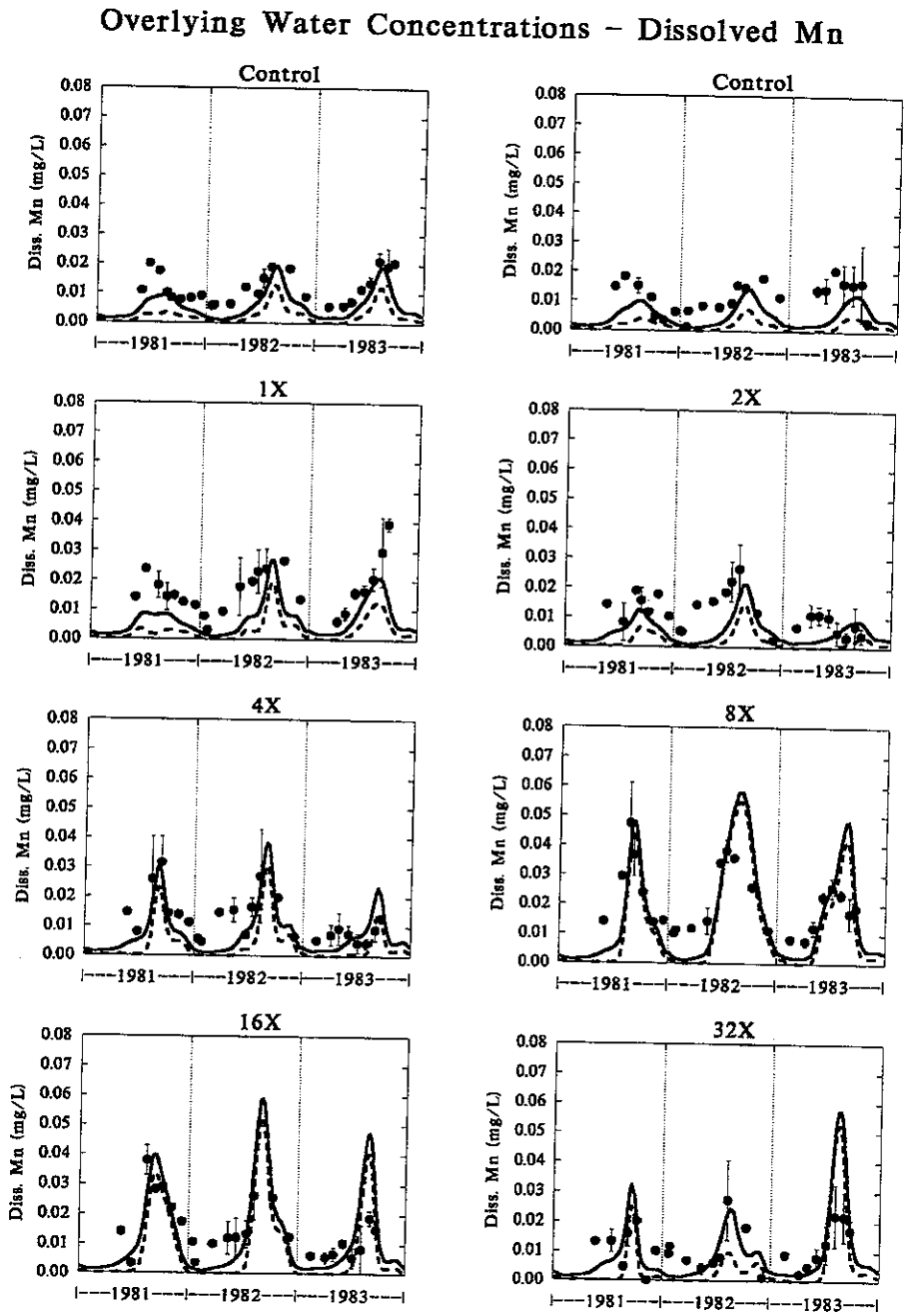

Fig. 7.11 Computed dissolved $Mn(0)$ (dashed line) and non-filterable $Mn(0) + f_{colloidal} MnO_2(0)$ (solid line) manganese in the water column compared to observations.

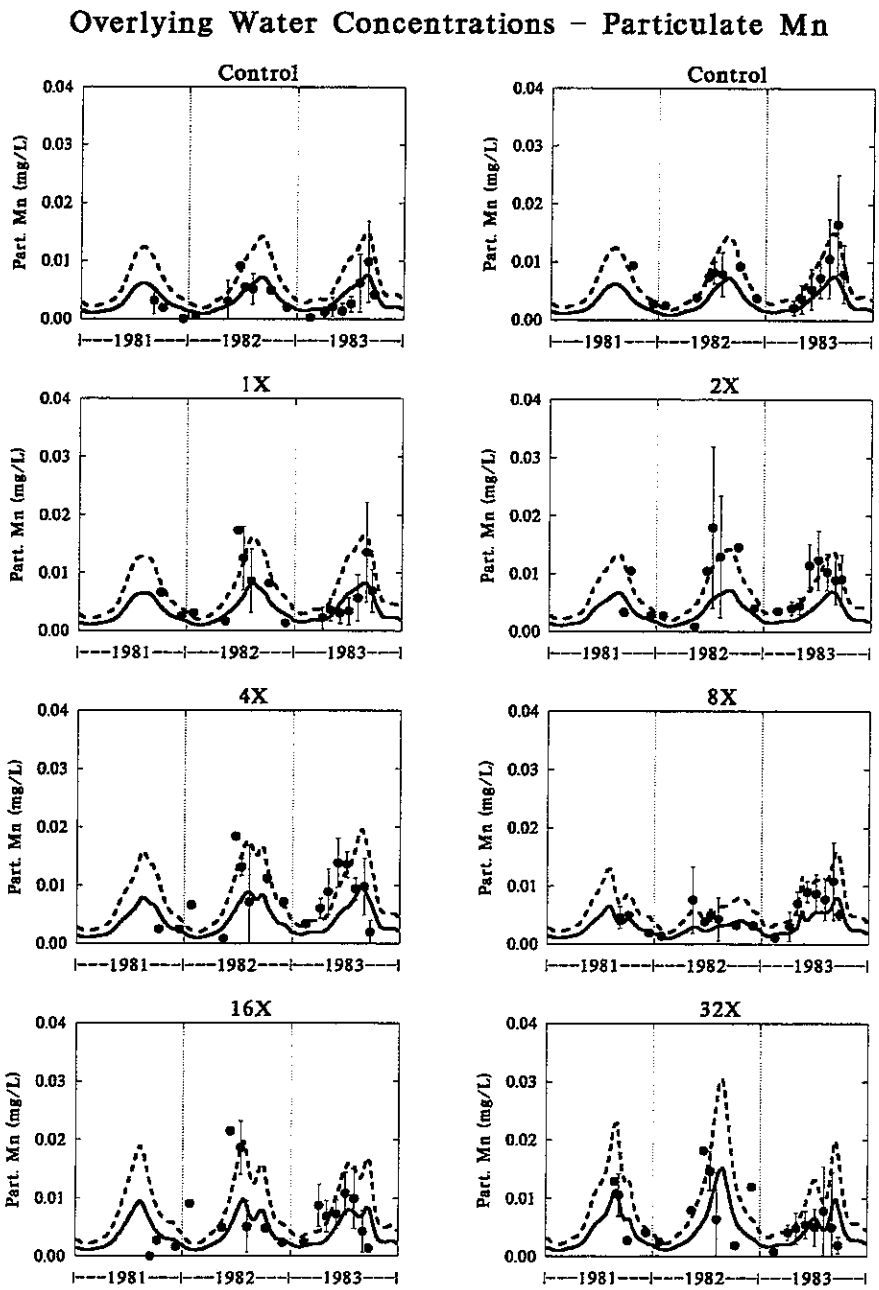

Fig. 7.12 Computed particulate $MnO_2(0)$ (dashed line) and filterable $MnO_2(0)$ – $f_{colloidal}MnO_2(0)$ (solid line) manganese in the water column compared to observations.

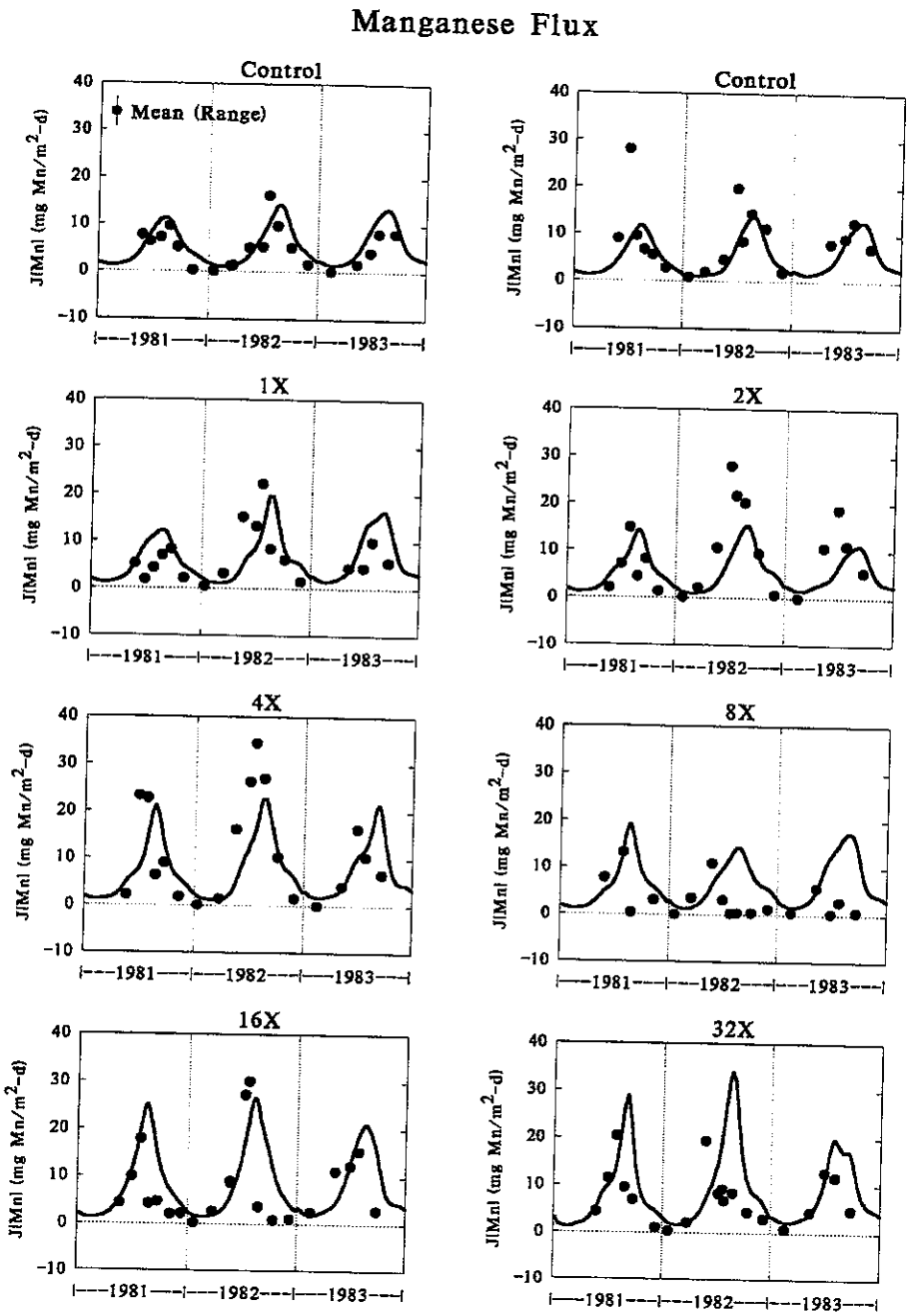

Fig. 7.13 Manganese flux versus time for all the treatments.

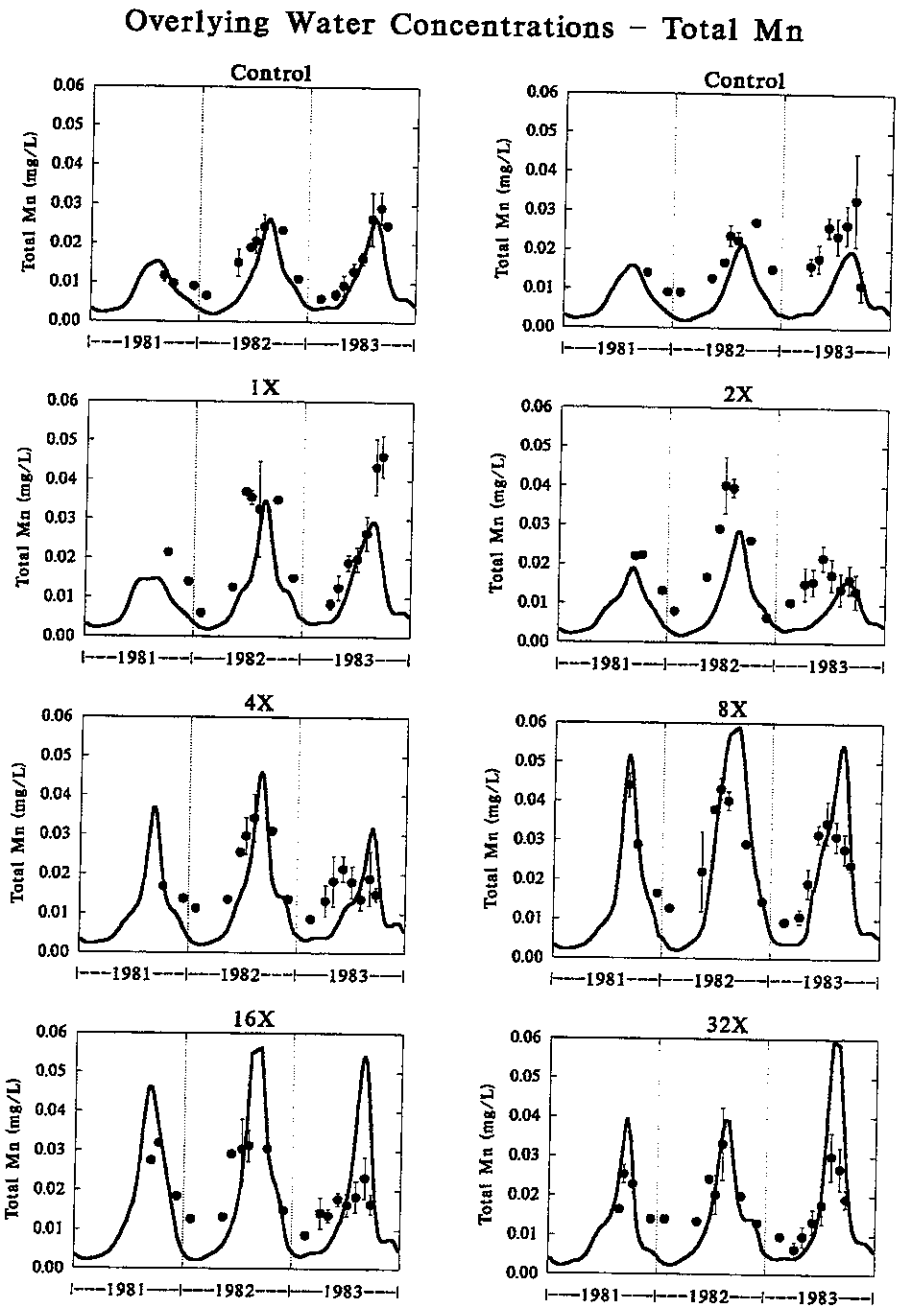

Fig. 7.14 Total manganese concentration in the water column. Comparison of observations and model output.

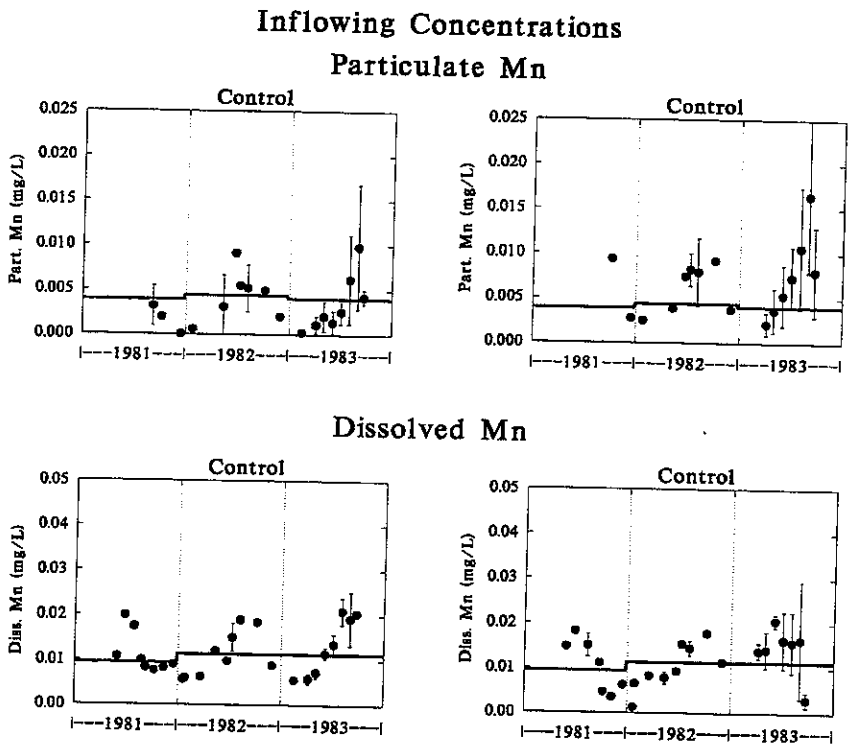

Fig. 7.15 Inflowing concentrations for the constant concentration case.

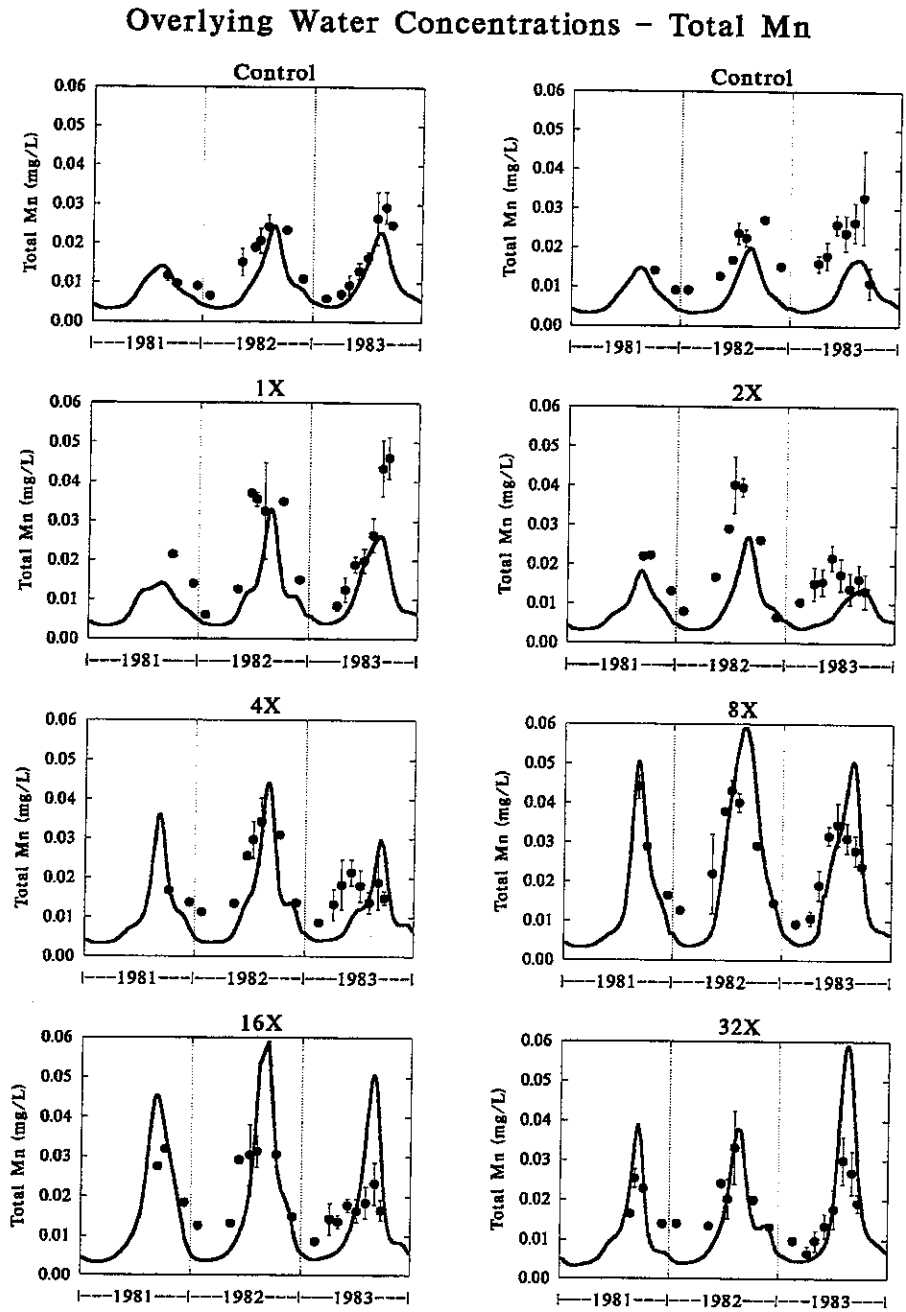

Fig. 7.16 Total manganese concentration in the water column. Comparison of observations and model output. Constant inflow concentrations.

7.4.2 Colloidal Fraction

The suggestion that a fraction of the particulate manganese is non-filterable and is quantified as dissolved manganese is not based on the model's ability to reproduce the observed particulate and dissolved manganese concentrations. In fact, the dashed lines (no colloidal manganese) capture the magnitude of the peak concentrations better than the solid lines (Figs.7.12) and the use of a colloidal fraction does not appear to significantly change the fit to the dissolved data (Fig.7.11). However if the data are analyzed in another way then a problem appears.

The fraction of manganese in the water column that is particulate is given by

$$f_p = \frac{MnO_2\,(0)}{MnO_2\,(0) + Mn\,(0)} \tag{7.37}$$

The variation in f_p as a function of the pH is shown in Fig.7.17. The upper solid

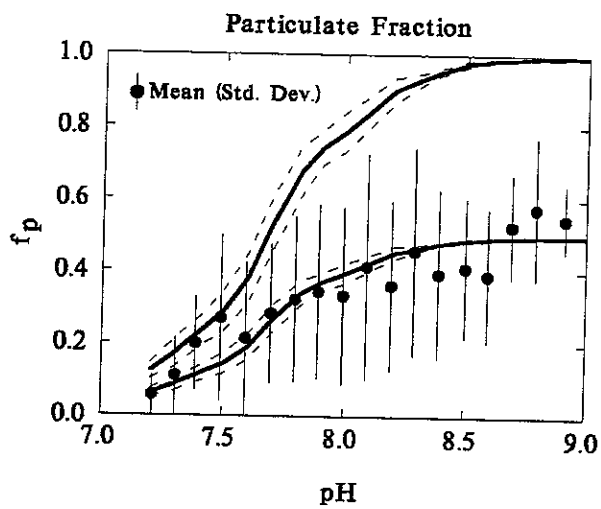

Fig. 7.17 Particulate fraction versus pH in the water column. Model results assuming $f_{colloidal} = 0$ (upper lines) and $f_{colloidal} = 1/2$ (lower lines). The dashed lines are the range in model results for that pH interval.

and dashed lines are the model average and range over each pH interval. assuming that all the particulate manganese $MnO_2\,(0)$ is filterable and would be measured as particulate manganese. The model kinetics predict that all the manganese should be particulate $f_p \simeq 1$ above $pH = 8.5$. However the observations rarely exceed a particulate fraction of $f_p = 0.5$. Since the pH dependency of the oxidation kinetics is experimentally observed, another explanation for this discrepancy is required.

The hypothesis is that the particulate manganese is composed of a colloidal fraction, which cannot be separated by filtration. It is known that freshly precipitated

manganese dioxide is largely in the colloidal particle size range so that this assumption is not without support [Pankow, 1979]. To be consistent, the colloidal fraction is assumed not to settle to the sediment so that w_1 is replaced by $w_1(1 - f_{\text{colloidal}})$ in eqs.(7.6–7.15).

The lower solid and dashed lines in Fig.7.17 are the model results assuming that 50% of the particulate manganese is colloidal ($f_{\text{colloidal}} = 0.5$) and therefore would not be filterable. The measured dissolved $Mn_d(0)$ and particulate $Mn_p(0)$ manganese concentrations—the dashed lines in Figs.7.11–7.12—are computed from the truly particulate and dissolved concentration using

$$Mn_d(0) = Mn(0) + f_{\text{colloidal}} MnO_2(0) \tag{7.38}$$

$$Mn_p(0) = MnO_2(0) - f_{\text{colloidal}} MnO_2(0) \tag{7.39}$$

The supposition that a colloidal fraction is erroneously measured as a dissolved specie is commonly used as an explanation for the observed decrease in partition coefficient as the concentration of particles increase [Gschwend and Wu, 1985] although an alternate explanation has been offered [Di Toro, 1985]. That effect is not much different from the observations in Fig.7.17 where the particulate fraction does not exceed $f_p = 0.5$, corresponding to a lower partition coefficient, whereas the expectation is that $f_p \rightarrow 1$ which corresponds to a high partition coefficient.

7.4.3 Effect of Anaerobic Layer Depth

The depth of the anaerobic layer H_2 is an important parameter in the sediment model since it controls the time constant—the characteristic time for the model to equilibrate to new conditions—for conservative species such as phosphorus [Di Toro and Fitzpatrick, 1993]. It is true for the manganese model as well. The reason is that the anaerobic layer provides a large storage volume for manganese and achieving steady state requires that the concentration $Mn(2)$ in H_2 be equilibrated. This can happen in two ways. Either the flux to or from the sediment $J[Mn]$,or the burial flux $w_2(Mn(2) + MnO_2(2))$, provides the route for which $Mn(2)$ adjusts. The time variable model results (Fig.7.4) presented in section 7.3.2 had $H_2 = 1$ cm. As a result, steady state was achieved relatively rapidly, even without a loss by burial since the comparisons to the analytical model steady state solutions are made with $w_2 = 0$. The question remains: what is the appropriate H_2 for the MERL nutrient exchange experiment.

The manganese concentration in the anaerobic layer near the end of year three of the simulation is compared to observations in Fig.7.18. These simulation are performed with $H_2 = 10$ cm. There is a notable decline in observed sediment manganese concentration at the higher enrichment levels which the model does not capture. The same results for $H_2 = 2$ cm. are shown in Fig.7.19.The decline in $Mn(2)$ with in-

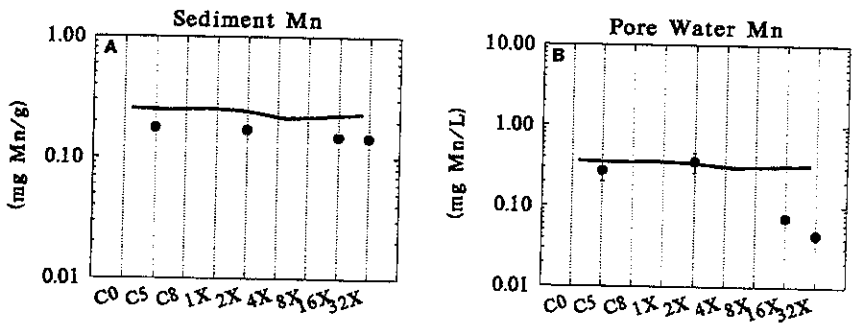

Fig. 7.18 Sediment and pore water manganese concentrations at the end of year 3. Solid line is the model computation. $H_2 = 10$ cm.

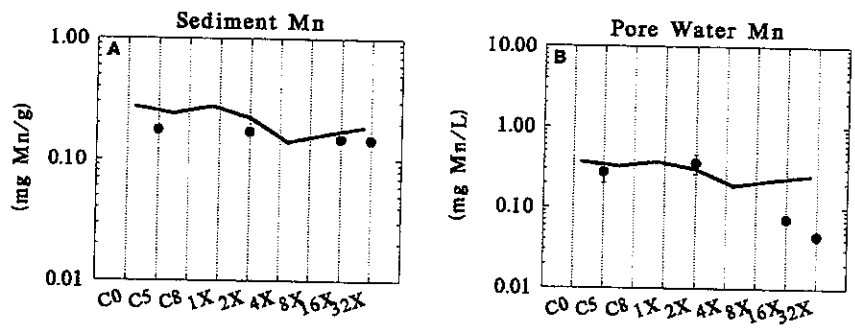

Fig. 7.19 Sediment and pore water manganese concentrations at the end of year 3. Solid line is the model computation. $H_2 = 2$ cm.

creasing nutrient inputs is the result of increasing fluxes of Mn to the overlying water in the first year of the simulation (Fig.7.5). Since the anaerobic layer is thinner than in Fig.7.18, the sediment concentrations respond more rapidly. From these results it appears that the thinner layer $H_2 = 2$ cm. is more representative of the short term response observed in these experiments.

It should be pointed out that the depth of the anaerobic layer is an artificial construct that is the consequence of the assumed two layer structure of the model. If the model had been constructed using multiple layers in the vertical, then the parameters that control the long term response are the mixing coefficient for particles and the depth of particle mixing. Although this formulation is preferable, it can add an unacceptably large computational burden if the model is to be applied as a part of a large water quality model with many individual sediment segments. The depth of

the active layer H_2 is a surrogate for these parameters and plays a similar role in the model.

8

Application of Iron Flux Model to Onondaga Lake

8.1 INTRODUCTION

This chapter presents the application of a iron sediment flux model to Onondaga Lake. The model is constructed in exactly the same way as the manganese sediment and water column flux model described in the previous chapters. Onondaga Lake was chosen because a complete eutrophication water column data set is available and has been modeled, and because iron data are also available. The hypolimnion of the lake becomes anaerobic each year, releasing significant quantities of iron to the water column. Thus Onondaga Lake provides a very good setting to test the validity of the iron sediment flux model.

8.1.1 Physical Characteristics

Onondaga Lake is located immediately north of the city of Syracuse, in Onondaga County, in Central New York State. The lake has a length of 7.6 km. and a width of 1.8 km. The outflow from the lake exits through a single outlet at the northern end and enters the Seneca River. A bathymetric map is shown in Fig. 8.1 and relevant physical data is given in Table 8.1. The is lake comprised of two basins, commonly referred to as the south and north basins, which are separated by a slight saddle region that is located approximately 3.6 km from the outlet. The north basin has a maximum depth of 18.9 m and the south basin has a maximum depth of 19.9 m.

Table 8.1 Physical characteristics of Onondaga Lake

Characteristic	Value
Surface Area (km^2)	12.0
Volume (m^3)	$131. \times 10^6$
Mean Depth (m)	10.9
Maximum Depth (m)	19.9
Watershed Drained (km^2)	689.
Detention Time (days)	90.0

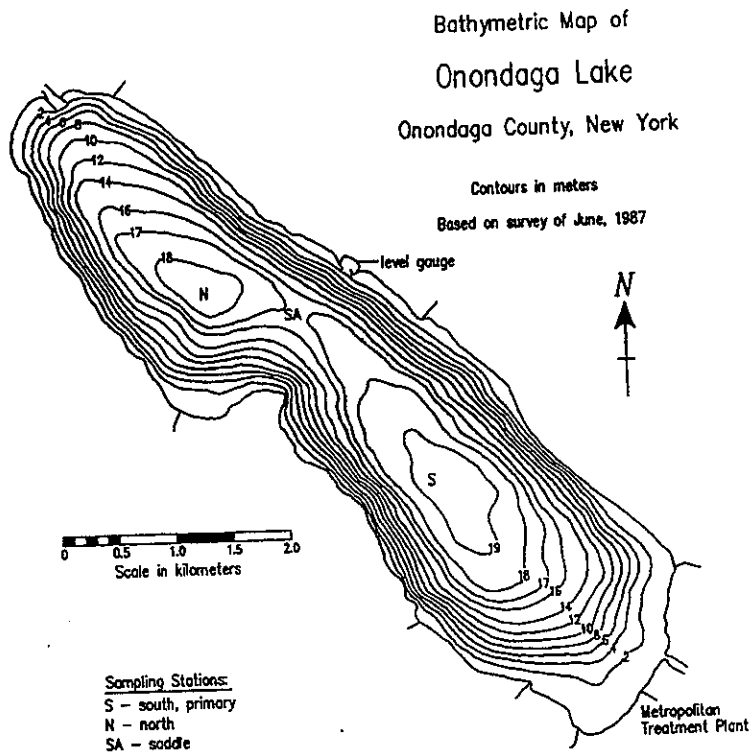

Fig. 8.1 Bathymetric map of Onondaga Lake

8.1.2 Tributaries

Onondaga Lake receives surface runoff from a drainage basin of 689 km^2 which is almost entirely located in Onondaga County. The major freshwater inputs are Ninemile Creek, Onondaga Creek, the Metropolitan Syracuse Sewage Treatment Plant (METRO), Ley Creek, Bloody Brook and Harbor Brook. Minor inputs include Sawmill Creek, Tributary 5A and the East Flume. Flow data for the tributaries for the period 1971–1989 is given in Table 8.2.

8.1.3 Loadings

As a result of urban and industrial development, Onondaga Lake has been used for both domestic and industrial waste disposal for over 100 years. Major industrial loadings include calcium, alkalinity, inorganic carbon and chlorides that were associated with the production of sodium carbonate (Na_2CO_3), commonly known as soda ash. The production of soda ash began on the shores of Onondaga Lake in 1884 and continued until 1986.

Table 8.2 Tributary flows into Onondaga Lake 1971-1989

Tributary	Drainage Area km^2	Average Flow (m^3/s)	% Contribution
Onondaga Creek	285	5.25	31.2
Ninemile Creek	298	5.29	31.5
METRO		2.99	17.8
Ley Creek	77	1.32	7.78
Harbor Brook	29	0.38	2.30
Other inputs		1.57	9.40
Total	689	16.80	100.0

The Metro wastewater treatment plant was upgraded in 1979 to secondary treatment. Tertiary treatment for phosphorus removal was added in 1981. By the early 80's the plant capacity was 80 MGD. Loading data are listed in Table 8.3

Table 8.3 Summary of loadings to Onondaga Lake 1971-1989

Constituent	1970's	early 1980's	late 1980's
Organic Carbon	45,000	18,000	7,000
Total nitrogen	8,000		6,000
total phosphorus	800		400
Silica	400		250
Calcium	1×10^6	0.6×10^6	0.2×10^6
Alkalinity	0.25×10^6	0.25×10^6	0.25×10^6
Total Inorganic Carbon		4.0×10^4	
Chloride	1.8×10^6	1.8×10^6	0.4×10^6

8.1.4 Water Quality

The water quality in Onondaga Lake during the period simulated below is characteristic of a highly eutrophic lake. Due to the large nutrient loadings, summer chlorophyll$_a$ concentrations can exceed 100 μg/L. The lake is stratified in the summer months from June to September with temperature differences exceeding 18 °C. Hypolimnitic hypoxia and anoxia exist for 9 to 10 months per year. Epilimnion dissolved oxygen

concentrations are generally above 6 mg/L throughout the year. Table 8.4 provides typical summer and winter concentrations.

Table 8.4 Onondaga Lake water quality overview.

Variable	Summer	Winter
Epilimnion Temp (°C)	22	3
Hypolimnion Temp (°C)	7	3
Epilimnion DO (mg/L)	13	8
Hypolimnion DO (mg/L)	0	1
Chlorophyll_a (μg/L)	40	8
Epilimnion Salinity (g/L)	1.5	1.5
Hypolimnion Salinity (g/L)	2.5	1.7
Epilimnion pH	7.8	7.8
Hypolimnion pH	7.3	7.3

8.1.5 Data Sets

A substantial data set is available for Onondaga Lake dating back to the late 1960's. A compilation and review of all data collected between 1968–1989 is available [Walker, 1991]. Data sources include Onondaga County Department of Drainage and Sanitation (D&S), Onondaga County Department of Health (DOH), New York State Department of Environmental Conservation (DEC), Upstate Freshwater Institute (UFI) and the United States Geological Survey (USGS). The data have been assembled onto a single database containing 186,000 water quality observations.

8.1.5.1 Iron and Manganese Dissolved iron data were collected by the Department of Drainage and Sanitation in the years 1968–1975. Dissolved iron data were also collected by the Upstate Freshwater Institute in 1980–1981, 1985–1986 and 1988–1989. Data were collected at station 41, in the southern basin of the lake. It is the data from this station that will be used subsequently. Data were collected at 1 m depth intervals on a weekly basis. In 1985 iron data was recorded from May to November. In 1986 iron data for March through November are available. In 1987 no iron data were recorded. In 1988 data were recorded from May to October. In 1989 iron data are available from June to August.

Dissolved manganese data were collected by the Department of Drainage and Sanitation in the years 1968–1970 which is the only manganese data available. Because of the age of these data and questions over their validity, manganese was not considered.

8.2 MODEL CONFIGURATION

The eutrophication model has been constructed for Onondaga Lake as part of another project. A detailed description of RCA, the water quality model employed, is available [HydroQual, 1992]. The model is direct descendent of the WASP model [Di Toro et al., 1981]. For Onondaga Lake the version of RCA used had 32 state variables, including the two iron state variables $Fe(II)$ and $FeOOH(s)$. The model is configured to simulate the annual cycle of phytoplankton production, nutrient cycling, and the resulting dissolved oxygen distribution. A sediment flux model which provides the fluxes of nutrients and oxygen, and is identical to that used for the MERL simulations, is coupled to the water column [Di Toro and Fitzpatrick, 1993]. A list of the systems used in the Onondaga Lake model are given in Table 8.5.

8.2.1 Iron Flux Model Equations

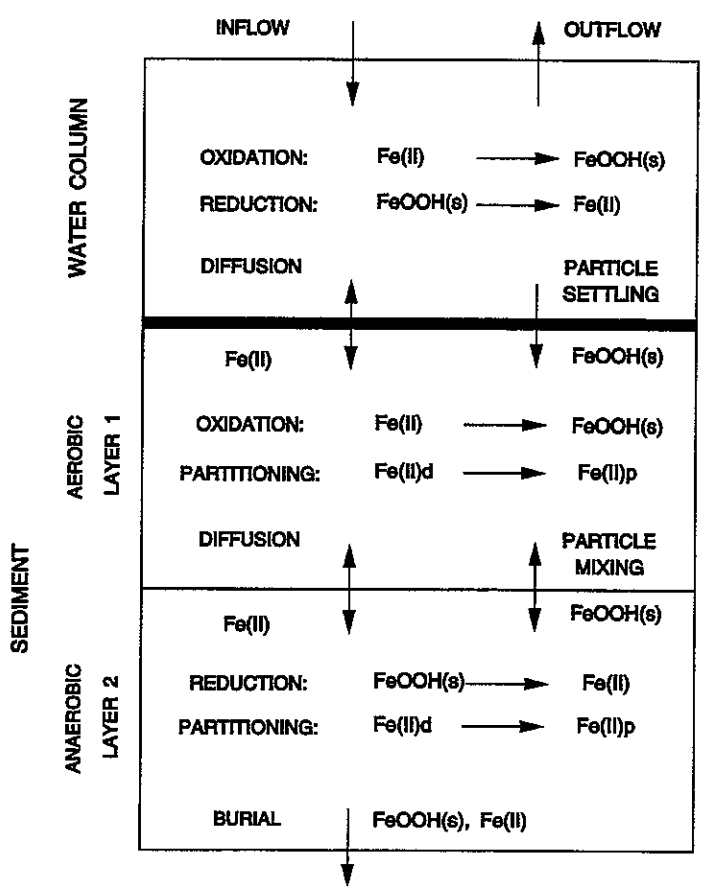

Fig. 8.2 Schematic diagram of the iron flux model

Table 8.5 Water quality model systems

Number	System
1	Salinity
2	Phytoplankton - diatoms
3	Phytoplankton - summer groups
4	Particulate Organic Phosphorus - refractory
5	Particulate Organic Phosphorus - labile
6	Dissolved Organic Phosphorus - refractory
7	Dissolved Organic Phosphorus - labile
8	Total Dissolved Organic Phosphorus
9	Particulate Organic Nitrogen - refractory
10	Particulate Organic Nitrogen - labile
11	Dissolved Organic Nitrogen - refractory
12	Dissolved Organic Nitrogen - labile
13	Total Ammonia
14	Nitrate + Nitrate
15	Biogenic Silica
16	Total Silica
17	Particulate Organic Carbon - refractory
18	Particulate Organic Carbon - labile
19	Dissolved Organic Carbon - refractory
20	Dissolved Organic Carbon - labile
21	Dissolved Organic Carbon - reactive
22	Dissolved Organic Carbon - algal exudate
23	Oxygen Equivalents
24	Dissolved Oxygen
25	Total Active Metal
26	Total Inorganic Carbon
27	Alkalinity
28	Calcitep
29	Calcium
30	Temperature
31	Dissolved Iron
32	Particulate Iron

The formulation of the sediment flux model for iron exactly parallels that developed for manganese. Iron is tracked both as dissolved Fe^{2+} and particulate $FeOOH\,(s)$ iron. A schematic is presented in Fig.8.2. The equations for the aerobic (1) and anaerobic (2) sediment layers are:

Layer 1 $Fe(II)$:

$$\begin{aligned} H_1\frac{dFe(1)}{dt} &= -s\left(f_{d1}Fe(1) - Fe\,(0)\right) + K_{L12}(f_{d2}Fe(2) - f_{d1}Fe(1)) \\ &\quad +w_{12}(f_{p2}Fe(2) - f_{p1}Fe(1)) - w_2Fe\,(1) \\ &\quad -k_{Fe,1}H_1\left(10^{2(pH_1-7)}\right)O_2\,(0)\,f_{d1}Fe(1) \\ &\quad +Fe\,(2)\,\dot{H}_1^+ - Fe\,(1)\left(\dot{H}_1 + \dot{H}_1^-\right) \end{aligned} \tag{8.1a}$$

Layer 2 $Fe(II)$:

$$\begin{aligned} H_2\frac{dFe(2)}{dt} &= -K_{L12}(f_{d2}Fe(2) - f_{d1}Fe(1)) \\ &\quad -w_{12}(f_{p2}Fe(2) - f_{p1}Fe(1)) - w_2\left(Fe(2) - Fe(1)\right) \\ &\quad +k_{Fe,2}H_2FeOOH(2) - Fe(2)\left(\dot{H}_2 + \dot{H}_1^+\right) + Fe(1)\dot{H}_1^- \end{aligned} \tag{8.1b}$$

Layer 1 $FeOOH\,(s)$:

$$\begin{aligned} H_1\frac{dFeOOH(1)}{dt} &= k_{Fe,1}H_1\left(10^{2(pH_1-7)}\right)O_2\,(0)\,f_{d1}Fe(1) - w_2FeOOH(1) \\ &\quad +w_{12}(FeOOH(2) - FeOOH(1)) + w_1FeOOH\,(0) \\ &\quad +FeOOH(2)\dot{H}_1^+ - FeOOH(1)\left(\dot{H}_1 + \dot{H}_1^-\right) \end{aligned} \tag{8.1c}$$

Layer 2 $FeOOH\,(s)$:

$$\begin{aligned} H_2\frac{dFeOOH(2)}{dt} &= -k_{Fe,2}H_2FeOOH(2) \\ &\quad -w_{12}(FeOOH(2) - FeOOH(1)) - w_2\left(FeOOH(2) - FeOOH(1)\right) \\ &\quad -FeOOH(2)\left(\dot{H}_2 + \dot{H}_1^+\right) + FeOOH(1)\dot{H}_1^- \end{aligned} \tag{8.1d}$$

where $FeOOH\,(0)$ and $Fe\,(0)$ refer to the particulate and dissolved iron concentrations in the bottom most water column segment, designated as segment 0, which overlays the sediment.

The water column equations for iron for this segment are

Layer 0 $Fe(II)$:

$$\begin{aligned} H_0 \frac{dFe(0)}{dt} &= s\left(f_{d1}Fe(1) - Fe\left(0\right)\right) - k_{Fe,0}H_0\left(10^{2(pH_0-7)}\right)O_2\left(0\right)Fe(0) \\ &\quad + k_{Fe,1}H_0\frac{K_{M,Fe,0}}{K_{M,Fe,0}+\left[O_2\left(0\right)\right]}FeOOH\left(0\right) \\ &\quad + E_{0,-1}\left(Fe\left(-1\right) - Fe\left(0\right)\right) \end{aligned} \tag{8.2a}$$

Layer 0 $FeOOH\left(s\right)$:

$$\begin{aligned} H_0 \frac{dFeOOH(0)}{dt} &= k_{Fe,0}H_0\left(10^{2(pH_0-7)}\right)O_2\left(0\right)Fe(0) \\ &\quad + w_1\left(FeOOH\left(-1\right) - FeOOH\left(0\right)\right) \\ &\quad - k_{Fe,1}H_0\frac{K_{M,Fe,0}}{K_{M,Fe,0}+\left[O_2\left(0\right)\right]}FeOOH\left(0\right) \\ &\quad + E_{0,-1}\left(FeOOH\left(-1\right) - FeOOH\left(0\right)\right) \end{aligned} \tag{8.2b}$$

where $E_{0,-1}$ represents the vertical mixing coefficient between the bottom layer and the layer immediately above. The concentrations in the water column are numbered in reverse order to preserve the notation used previously. Thus layer -1 refers to the layer just above layer 0 in the water column.

An additional term has been added to the water column equations (8.2) to include the reduction of $FeOOH$ if the dissolved oxygen concentration approaches zero. The rate of the reduction of $FeOOH$ to $Fe(II)$ is given

$$k_{Fe,1}H_0\frac{K_{M,Fe,0}}{K_{M,Fe,0}+\left[O_2\left(0\right)\right]}FeOOH\left(0\right) \tag{8.3}$$

where $k_{Fe,1}$ is the rate at which $FeOOH(s)$ is reduced to $Fe(II)$; $K_{M,Fe,0}$ is the half saturation constant for oxygen for this reaction which is set to a small number so that reduction occurs only occurs if the dissolved oxygen concentration is almost zero. The nitrogen, oxygen, phosphorus, and silica portions of the sediment model are identical to those used above.

8.2.2 Segmentation for Onondaga Lake

Onondaga Lake is represented by 10 vertical water column segments. Each segment has a depth of 2 meters and a surface area chosen to match the hypsometry of the lake. Table 8.6 gives the depth, surface area and volume of each vertical segment. The lake is assumed to be laterally well mixed, consistent with observations [Effler, 1996].

Table 8.6 Vertical segment depths, areas and volumes

Segment No.	Average Depth m	Surface Area $m^2 \times 10^6$	Volume $m^3 \times 10^6$
1	1	11.9	23.8
2	3	11.9	22.3
3	5	10.4	19.9
4	7	9.49	18.3
5	9	8.81	16.9
6	11	8.12	15.0
7	13	6.91	13.0
8	15	6.11	10.9
9	17	4.76	8.61
10	19	3.85	3.85

8.2.3 Iron Loading

Data for the composition of particles entering Onondaga Lake in 1981 have been reported [Yin and Johnson, 1984]. The loading rate in 1981 for a "Fe-Mn-rich" class of solids is reported that contains $Fe(OH)_3\,(s)$, $Fe_2O_3\,(s)$, $FeOOH\,(s)$, $MnO_2\,(s)$, and other Fe and Mn compounds. These are shown in Table 8.7. Since the concentration of manganese is much less than iron in typical soil particles [Lindsay, 1979] it is assumed that these loading rates represent only iron inputs. Using the average tributary flows an estimate of the influent concentration can be obtained. This concentration was then used to estimate daily loads for the calibration years 1985–1989.

Table 8.7 Iron loading to Onondaga Lake for 1981

Tributary	Flow 1981 m^3/s	Fe Load tons/yr
Onondaga Creek	5.1	315
Ninemile Creek	4.9	63
METRO	3.1	2
Ley Creek	1.2	22
Harbor Brook	0.4	2
Total	14.7	405

This loading represents all particulate iron compounds. In order to obtain the reactive iron load it is necessary to reduce the total load to account for the unreactive iron compounds. As there is no simple way to do this without sequential extraction information [Canfield, 1989], the load was reduced as part of the calibration procedure. A reduction of 40% was required in order to match the observations. This reduction was applied to all model year runs. All influent iron was assumed to be particulate since inflows to the lake were aerobic and the oxidation rate of ferrous iron is very rapid (Fig.2.4).

8.2.4 Dissolved Oxygen

The original development of the Onondaga Lake model focused on calcitep precipitation and deposition, with secondary emphasis on eutrophication. Although the model produced a reasonable fit of the dissolved oxygen profiles, it did not always reproduce the exact timing of the anoxia in Onondaga Lake. An example of model-data comparison for 1986 is shown in Figure 8.3. The model is unable to reproduce the observed hypolimnetic anoxia from February through May.Because of the strong relationship between iron flux from the sediment and the overlying water dissolved oxygen, it was decided to use the measured dissolved oxygen data rather than the model results to specify when anoxia was present. This was done for three reasons.

1. The dissolved oxygen data were very complete and thorough, with weekly dissolved oxygen profiles measured at 1 m depth intervals.

2. Because dissolved oxygen is coupled to so many other systems, achieving a better dissolved oxygen fit to the data would have essentially involved recalibrating the existing water quality model, which would have been time consuming.

3. Because the iron only responds to the dissolved oxygen but does not affect it, at least at these iron concentrations for which the oxygen consumed by iron oxidation is small, there is no loss of a feedback mechanism by specifying the dissolved oxygen directly.

8.2.5 Calibration Results

The model was run for 5 years, beginning January 1, 1985 to December 31, 1989. Iron loading was supplied via the tributaries based on the calculation procedure described above. The values of the constants used for the nutrients and oxygen sediment model, and iron model in the water column and sediment are given below in Tables 8.9 and 8.8. Note that the same oxidation and reduction rates are used for both the sediment and water column. This parallels the procedure followed in the manganese model. The model was cycled through 20 years of simulations—the 5 year sequence repeated

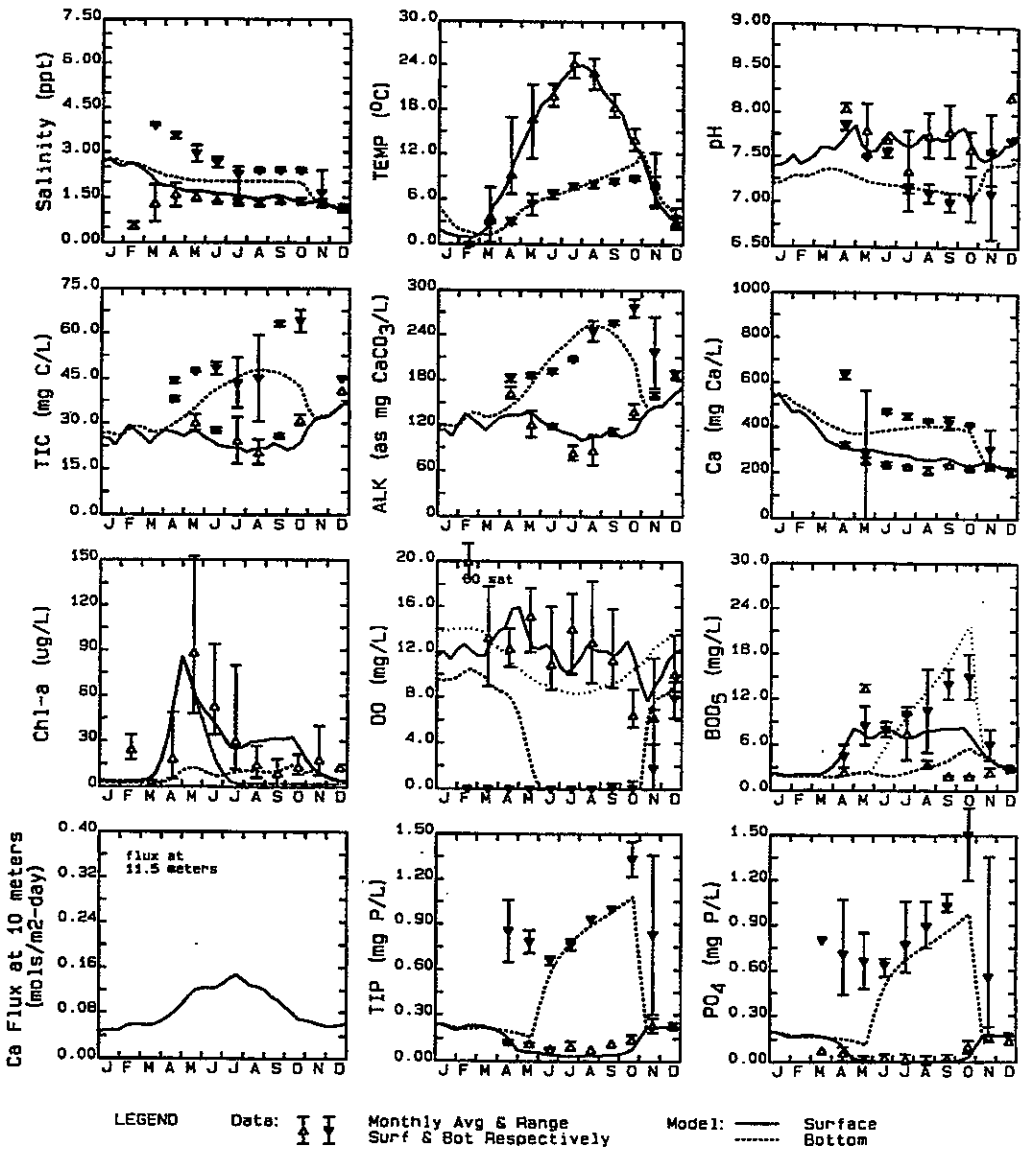

Fig. 8.3 Calibration results for RCA water quality model for 1986. Monthly averages for surface layer: model (solid line), data (▲) ± range; and bottom layer model (dotted line), data (▼) ± range.

four times—in order to generate equilibrium initial conditions. These were then used as the initial conditions for the final five year calibration run.

Table 8.8 Constants for the iron flux model – Onondaga Lake

Name	Value	Unit	Description
		Water Column	
$k_{Fe,1}$	10.0	day^{-1}	Oxidation rate
$\theta_{Fe,1}$	1.08	–	Temperature coefficient
$k_{Fe,2}$	4.0	day^{-1}	Reduction rate
$K_{M,Fe,0}$	0.2	mg O_2/L	Oxidation half saturation constant
		Sediment	
$\Delta\pi_{Fe,1}$	15.0	L/kg	Aerobic layer partition coefficient
$\pi_{Fe,2}$	3000.0	L/kg	Anaerobic layer partition coefficient
$O_{2,Crit,Fe}$	2.0	mg/L	Partition coefficient half saturation constant
$k_{Fe,1}$	10.0	day^{-1}	Aerobic layer oxidation rate
$\theta_{Fe,1}$	1.08	–	Temperature coefficient
$k_{Fe,2}$	4.0	day^{-1}	Anaerobic layer reduction rate
$\theta_{Fe,2}$	1.08	–	Temperature coefficient

Figure 8.4 shows the iron calibration results for 1986 using the fitted dissolved oxygen for the months of March to November when iron data were recorded. Also shown are temperature and dissolved oxygen. The measured data average (open symbols) and range (bars) and the model computed monthly averages (solid line) and range (shading) are compared. It is interesting to note how early in the year anoxia started and how long it persisted. In fact, in 1986 the bottom of the lake was essentially anoxic or hypoxic (DO $<$ 2 mg/L) for the whole year.

The dissolved iron concentrations, shown in the third row of panels in Fig. 8.4, increase as a consequence of the iron flux being generated by the sediment. The data for March were actually collected on March 30 and so the right edge of the shading should be compared to the data, to which it compares reasonably well. There is a continual buildup of dissolved iron due to an iron flux from the sediment.

The particulate iron concentrations are shown in the last row of Fig.8.4. When anoxia is not present the particulate iron will exhibit an increasing concentration with depth, due to the settling of particulate iron into the deeper parts of the lake where the volume is decreasing. As the particulate iron settles into the anoxic zone it is reduced to form Fe^{2+} . Thus the particulate concentration will initially increase and

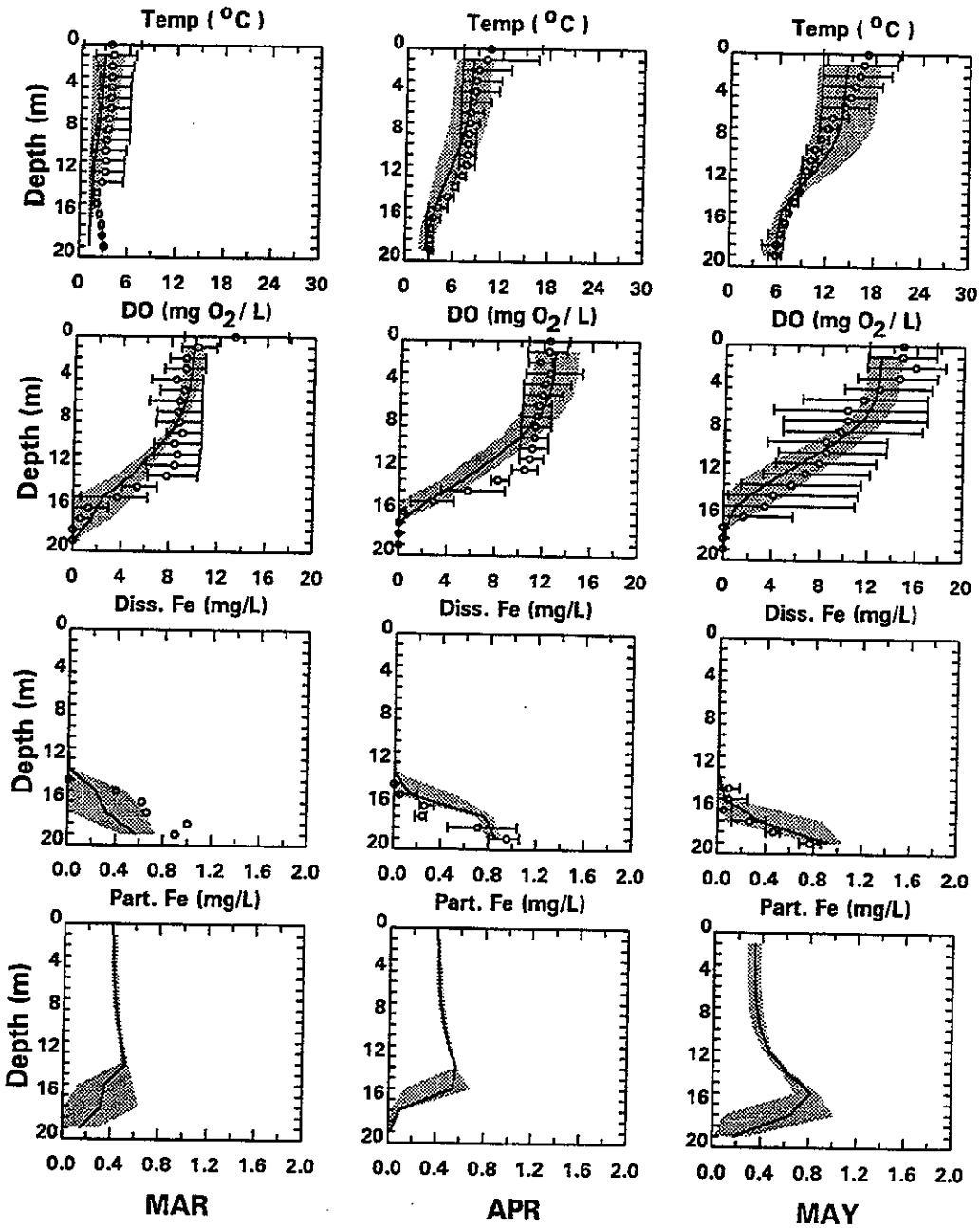

Fig. 8.4 Calibration results for Onondaga Lake. March–May, 1986; concentrations versus depth. Columns are each month. Rows are temperature, dissolved oxygen, dissolved iron, particulate iron.

Table 8.9 Sediment Model Parameters for Onondaga Lake

m_1 (kg/L) 0.5	m_2 (kg/L) 0.5	w_2 (m/d) 6.85×10^{-6}	H_2 (m) 0.10		
D_d (m^2/d) 5.0E-03	θ_{D_d} – 1.08	D_p (m^2/d) 1.2×10^{-4}	θ_{D_p} – 1.15	D_{d0} (m^2/d) 1.0×10^{-4}	$\theta_{D_{d0}}$ – 1.08
$\kappa_{NH_4,1}$ (m/d) 0.2	π_{NH_4} (L/kg) 1.00	θ_{NH_4} – 1.123	K_{M,NH_4} (mg N/L) 0.728	$\theta_{K_{M,NH_4}}$ – 1.125	K_{M,NH_4,O_2} (mg O_2/L) 0.74
$\kappa_{NO_3,1}$ (m/d) 0.15	$\kappa_{NO_3,2}$ (m/d) 0.25	θ_{NO_3} – 1.080			
$\kappa_{H_2S,d1}$ (m/d) 0.2	$\kappa_{H_2S,p1}$ (m/d) 0.4	$\pi_{H_2S,1}$ (L/kg) 100.0	$\pi_{H_2S,2}$ (L/kg) 100.0	θ_{H_2S} – 1.15	K_{M,H_2S,O_2} (mg O_2/L) 4.0
k_{Si} (/d) 0.5	$[\mathrm{Si}]_{sat}$ (mg Si/L) 30.	$\Delta\pi_{\mathrm{Si},1}$ – 6.0	$\pi_{\mathrm{Si},2}$ (L/kg) 175.0	θ_{Si} – 1.100	$K_{M,P\,\mathrm{Si}}$ (mg Si/L) 5.0×10^4
$\Delta\pi_{PO_4,1}$ – 65.0	$\pi_{PO_4,2}$ (L/kg) 225.0	$O_2\,(0)_{\pi,PO_4}$ (mg O_2/L) 2.0	K_{M,D_p,O_2} (mg O_2/L) 4.0	$O_2\,(0)_{\pi,\mathrm{Si}}$ (mg O_2/L) 1.0	

then decrease in the anoxic zone. The model computations are shown in Figure 8.4. Unfortunately there are no data with which to compare the model results.

From March to May the Fe^{2+} concentration at the hypolimnion continues to increase. However, once the overlying water column concentration reaches that of the sediment pore water, there is no longer a gradient and the sediment flux of iron from the sediment to the overlying water ceases. At this point the hypolimnion concentration remains approximately constant. It can be seen from Fig.8.4–8.5 that this occurs near the end of May and beginning of June when the bottom Fe^{2+} concentration reaches about ~ 0.8 mg/L. At this point two things happen. First, the depth of the thermocline increases, beginning from a depth of 13 m from the water surface and climbing to 10 m and then to 8 m from the water surface over a 30 day period. Secondly, although the concentration at the bottom will remain constant, the continued settling and subsequent reduction of particulate iron will continue. This source from the overlying oxic water eventually will cause a peak to occur in dissolved iron, not

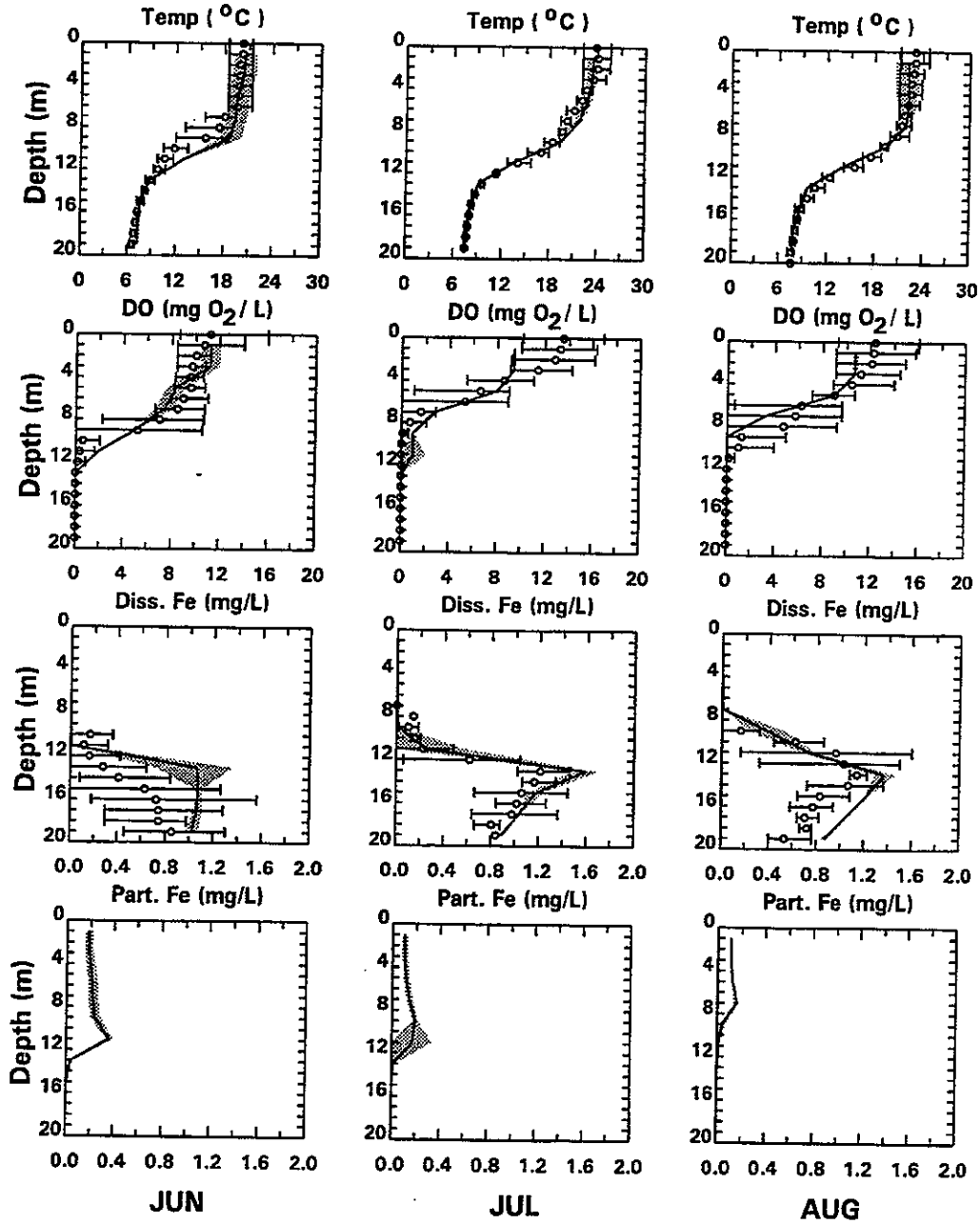

Fig. 8.5 Calibration results for Onondaga Lake. June–August, 1986; concentrations versus depth. Columns are each month. Rows are temperature, dissolved oxygen, dissolved iron, particulate iron.

at the bottom, but at a location just below the thermocline. This behavior is clearly shown in the months of June through September.

The model overestimates the amount of Fe^{2+} slightly in August, but more noticeably in September and October (Fig.8.6). One reason for this may be the formation and subsequent precipitation of iron sulfide, FeS. This mechanism is discussed in more detail in Section 8.2.6. Note that the Fe^{2+} data for November 1986 are only for one day, November 3.

A temporal summary of the calibration for 1986 is shown in Figure 8.7. The top plot is a temporal plot of epilimnion and hypolimnion temperatures. The depth of the thermocline was estimated at 8 m. The symbols represent the average observed epilimnion and hypolimnion concentrations. The solid line represent the model monthly averages with the shading representing the range. As can be seen, the model is reasonably well calibrated to the observed temperature.

Figure 8.7 also contains a similar plot for dissolved oxygen. Note the persistence of anoxia in the lake for 1986. This was not originally reproduced by the model and so had to be specified.

The bottom plot in Figure 8.7 shows Fe^{2+} concentrations. Since Fe^{2+} is rapidly oxidized in aerobic waters, it is only present during anoxic conditions in the hypolimnion. The model reproduces both the average and the range of the data. The exception is in September when both the model range and average overpredict the data, and in October when the model average is close but the range is too large. As mentioned previously, this could be the effect of precipitation of FeS, and will be discussed in Section 8.2.6.

In 1987 no iron data were collected. Figs. 8.8–8.9 show the calibration results for 1988 for the months of May through October. It is interesting to note that the data for both 1988 and 1989 exhibit much more short term variation than in 1986. It is not clear why this happens, and although the model fits the monthly concentration averages, it cannot reproduce the large variations. The observed dissolved oxygen data does not suggest any reaeration events occurring, which would cause large variations in Fe^{2+}.

Figure 8.10 is a temporal plot of the 1988 calibration for the epilimnion and hypolimnion. Again the large ranges in Fe^{2+} are noticeable.

Iron data were collected for only three months: June through August in 1989. The calibration is shown in Figure 8.11, and the temporal summary for the epilimnion and hypolimnion are presented in Figure 8.12. The model demonstrates good agreement with the data.

It is of interest to determine the extent to which the model predictions are dependent on an accurate representation of the dissolved oxygen concentrations. This is examined in the next three figures 8.13–8.15 which show temporal plots of the iron calibration using the dissolved oxygen concentrations calculated by the model. Note the marked

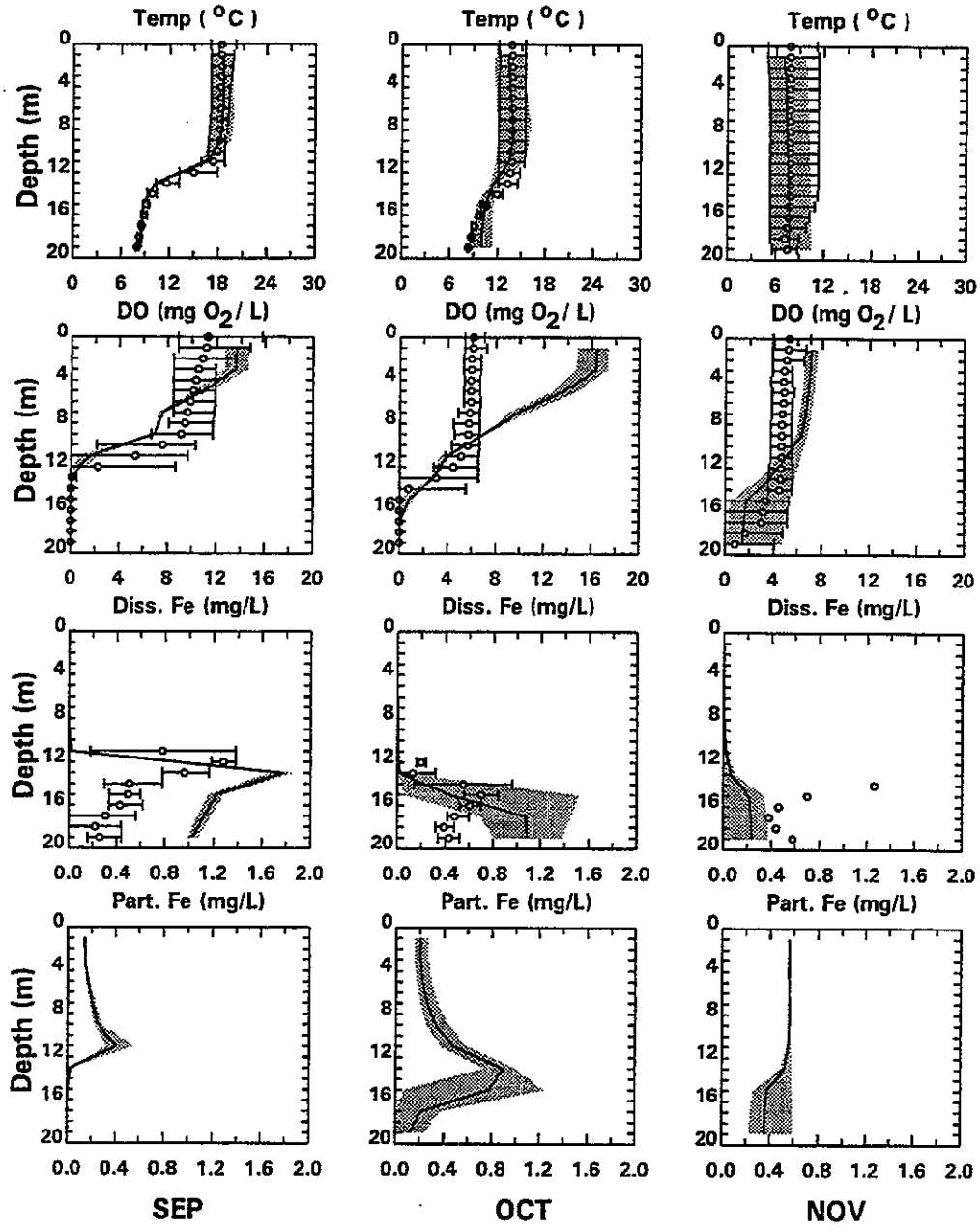

Fig. 8.6 Calibration results for Onondaga Lake. September–Noverber 1986; concentrations versus depth. Columns are each month. Rows are temperature, dissolved oxygen, dissolved iron, particulate iron.

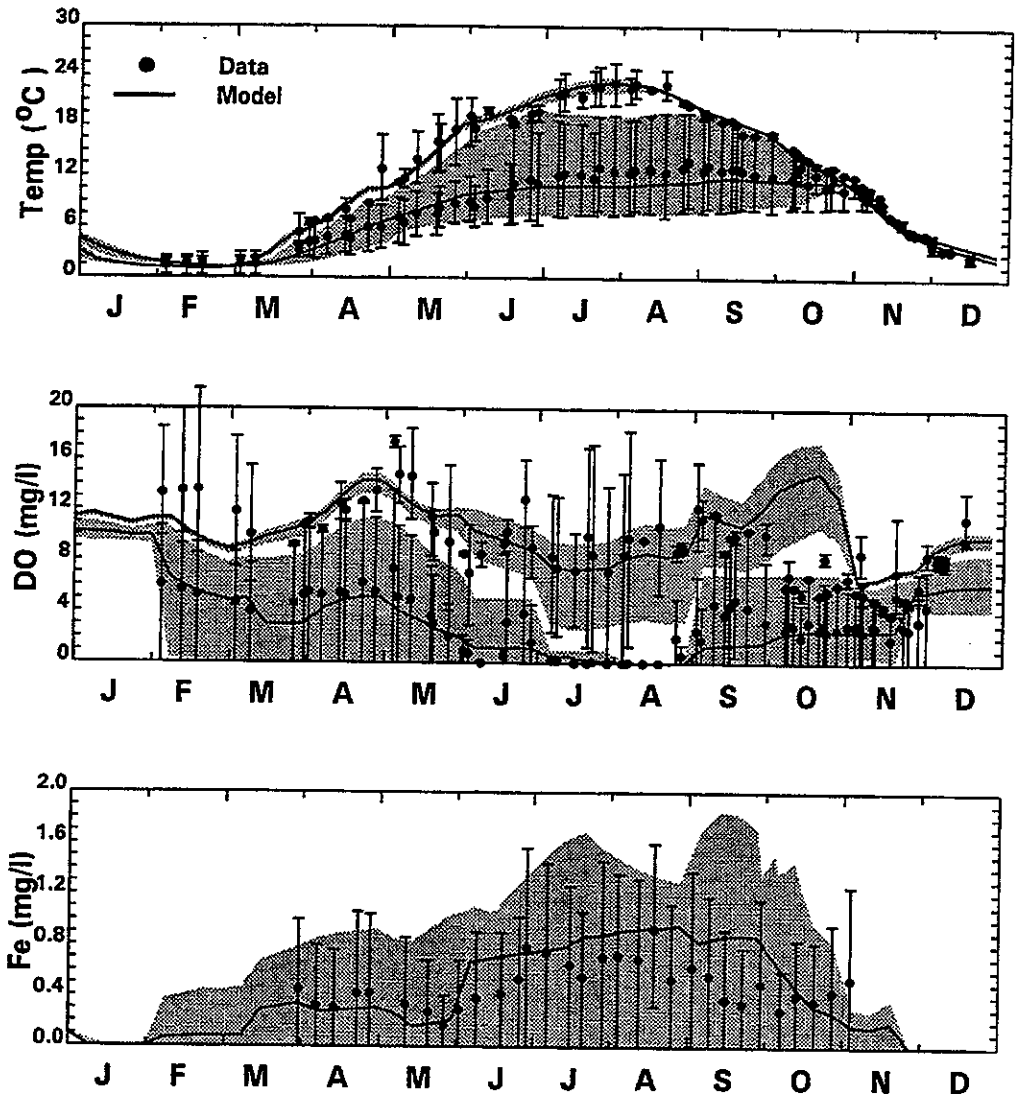

Fig. 8.7 Onondaga Lake. Temporal plot for 1986. Epilimnion and hypolimnion average concentration and ranges are plotted for both model (shaded) and data (bars).

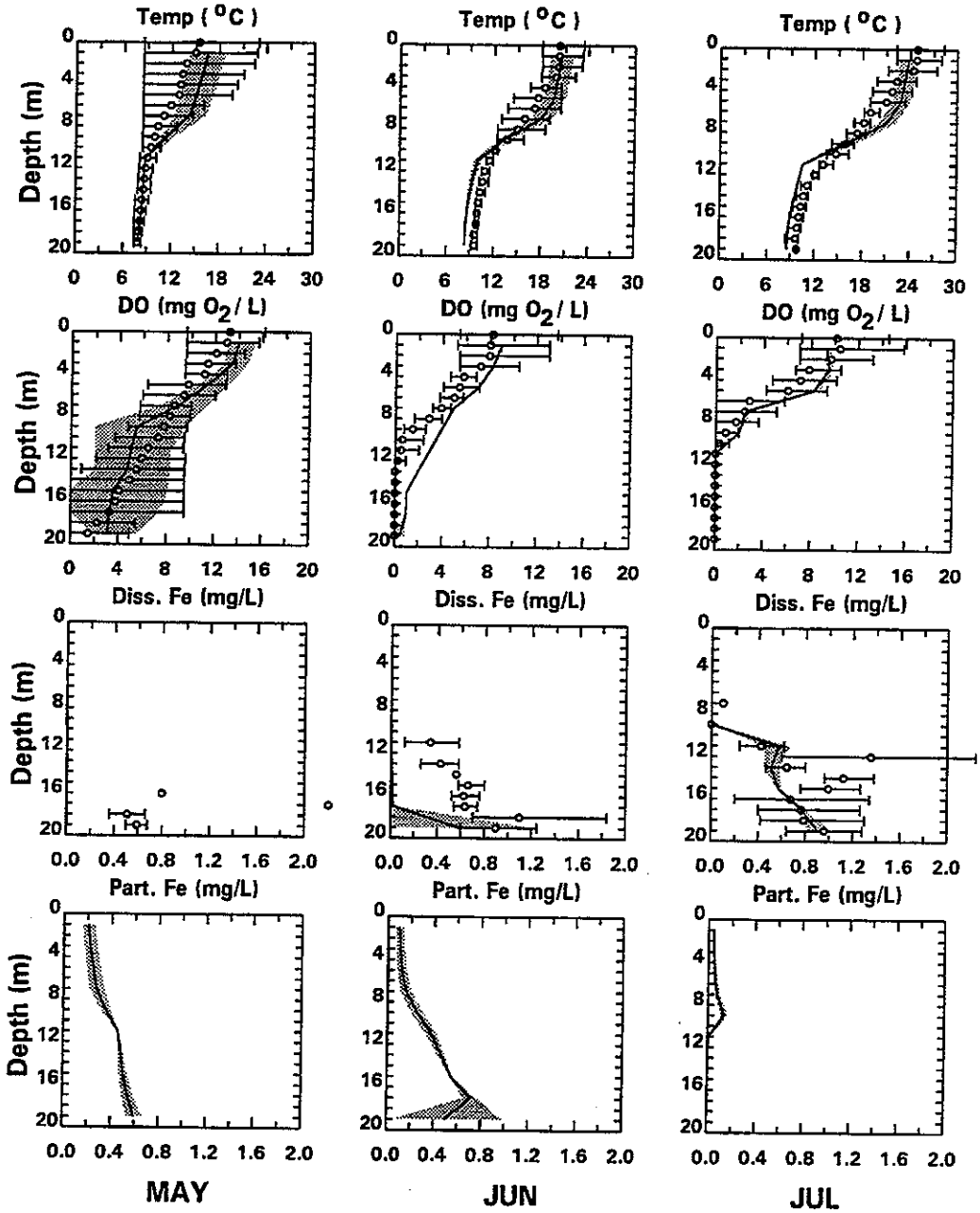

Fig. 8.8 Calibration results for Onondaga Lake. May–July, 1988.

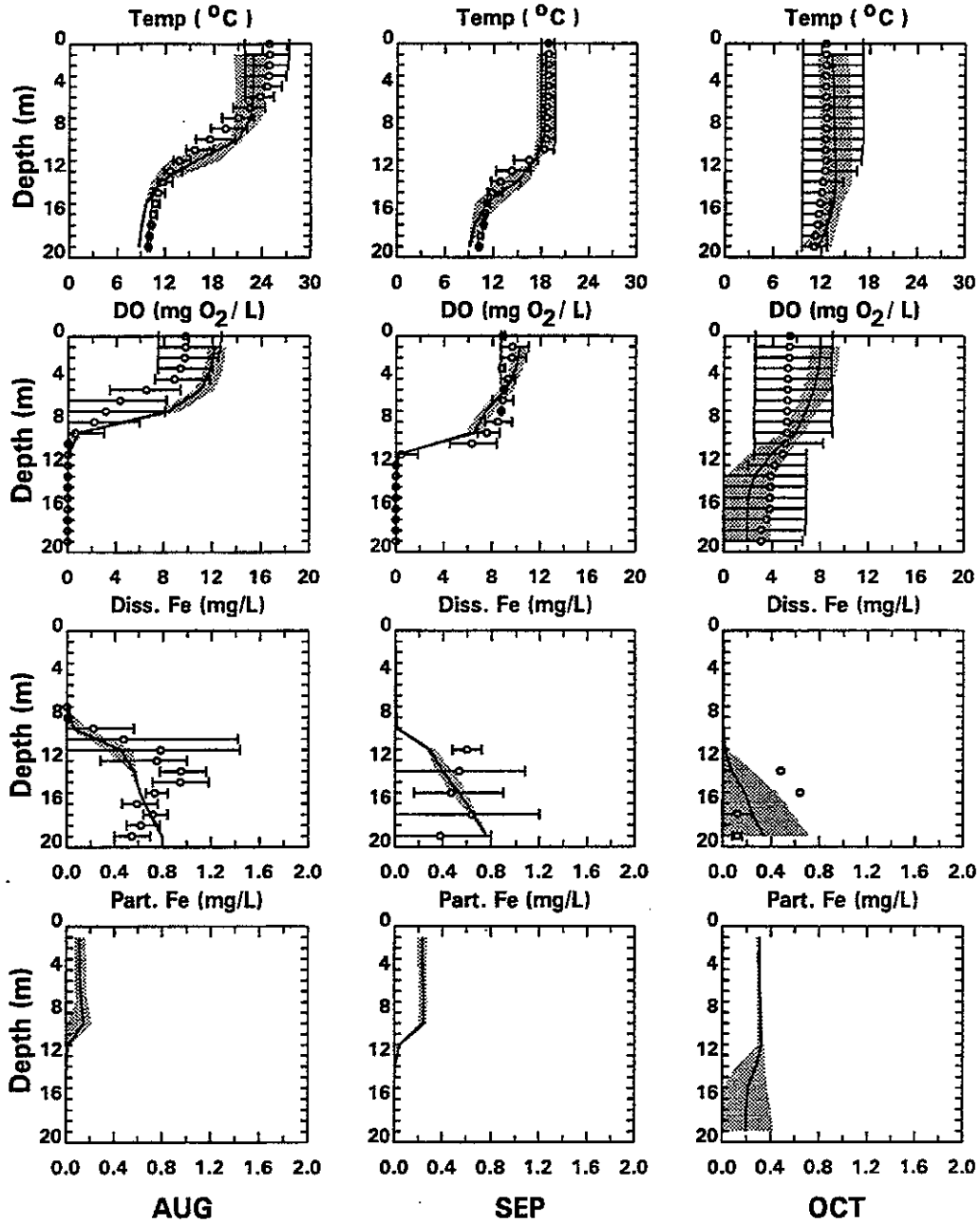

Fig. 8.9 Calibration results for Onondaga Lake. August–October, 1988.

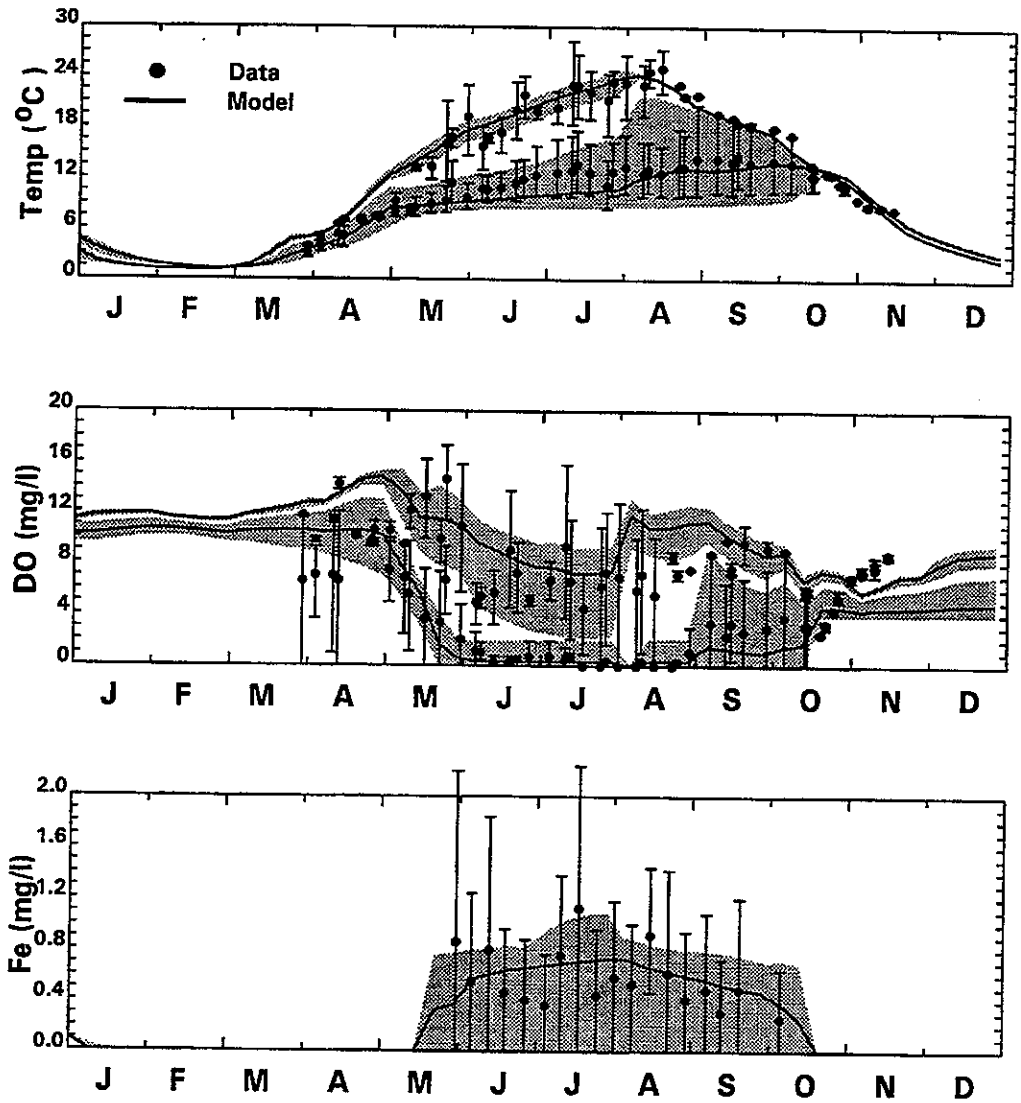

Fig. 8.10 Calibration results for Onondaga Lake. Temporal results, 1988.

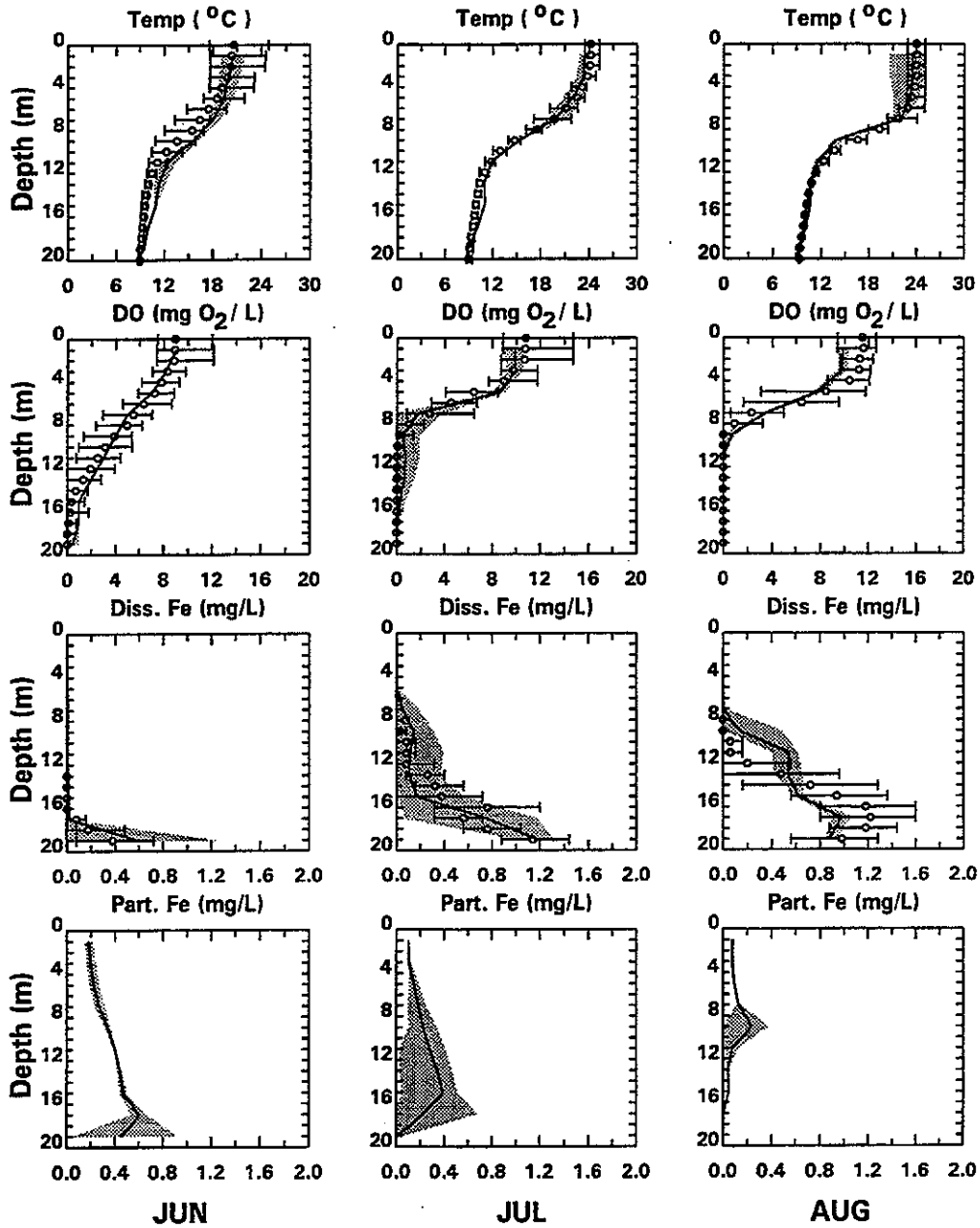

Fig. 8.11 Calibration results for Onondaga Lake. June–August, 1989

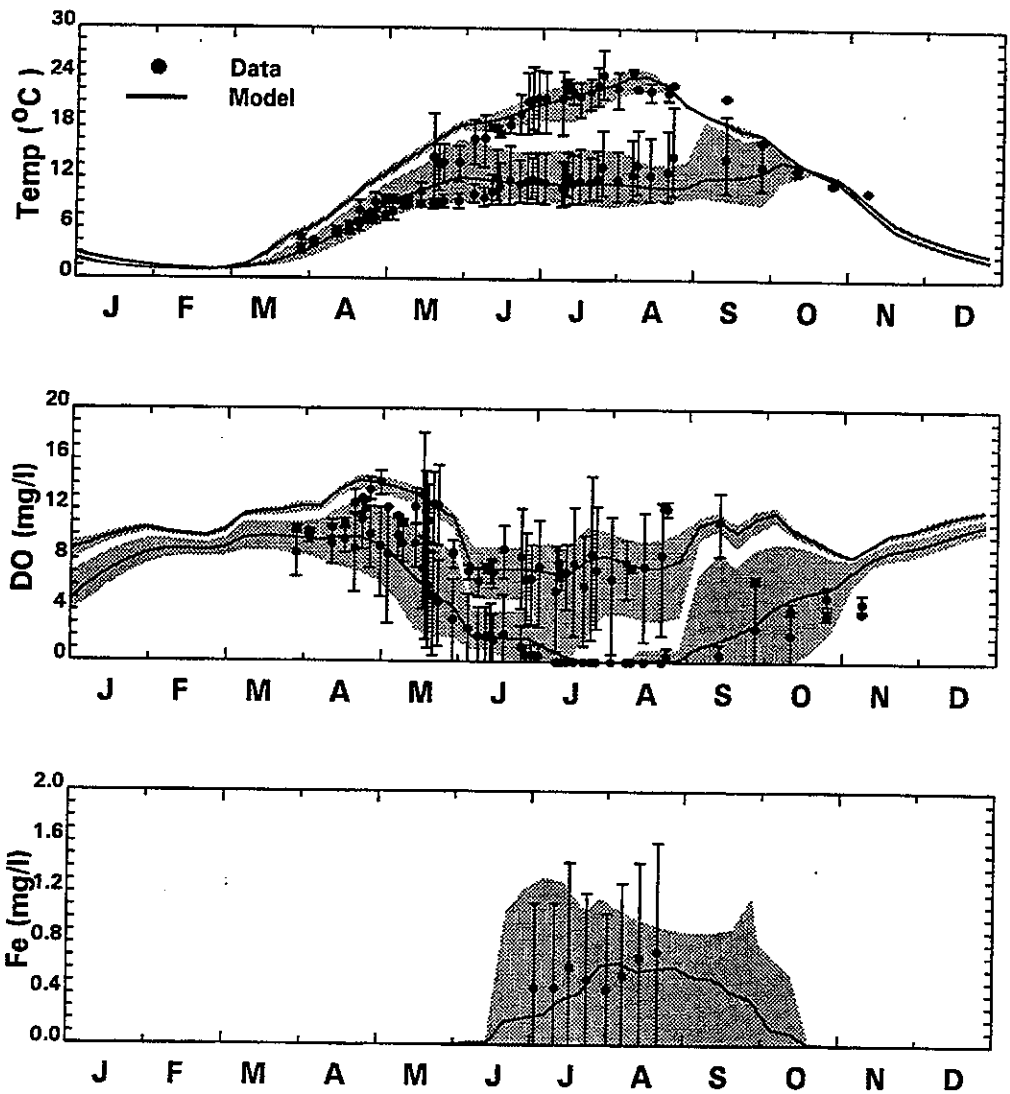

Fig. 8.12 Calibration results for Onondaga Lake. Temporal plot for 1989

effect on the 1986 calibration. The onset of iron generation from the sediment is delayed until the dissolved oxygen is zero at the sediment-water interface. The model predicted the period of anoxia in 1988 and 1989 and so there is little difference between the results where the period of anoxia is specified (Figs. 8.7, 8.10 and 8.12).

8.2.6 Iron Sulfide Precipitation

The suggestion was made above that the decline in dissolved iron in the latter portions of 1986 was due to the precipitation of iron sulfide. The sediment model computes sulfide fluxes and the water column model tracks the oxygen equivalents of dissolved sulfide. It is possible, therefore, to see if the sulfide concentrations are increasing to a point where precipitation is possible.

Figures 8.16, 8.17, and 8.18 are plots of sulfide and dissolved iron for the months of May through October for 1986, 1988 and 1989 respectively. For 1986 (Fig. 8.16) the buildup is reproduced until October when premature destratification in the model reduces the sulfide concentration. The computed sulfide concentrations for 1988 (Fig. 8.17) increase more rapidly than is observed, and the data for the two months in 1989 suggest the same overprediction. The magnitude of the sediment flux of sulfide during anoxia is influenced by the magnitude of the sulfide partition coefficients $\pi_{H_2S,1}$ and $\pi_{H_2S,2}$. These are empirical parameters that were calibrated using the Chesapeake Bay data set [Di Toro and Fitzpatrick, 1993]. Since these parameters have not been calibrated for Onondaga Lake, the results are encouraging.

The sulfide and iron data can be used to make a qualitative analysis of the likelihood that sulfide precipitation is the cause of the model overprediction of dissolved iron and sulfide. The excessive iron concentrations are occurring primarily in September and October of 1986 (Fig. 8.16). There is no indication that the sulfide concentrations are increasing rapidly enough to initiate precipitation of iron sulfide. It is possible, of course, that $FeS\,(s)$ is being formed continuously and that its addition as a mechanism would improve the model's predictive ability. However, a qualitative examination of the model-data discrepancies does not suggest that this is a first order effect.

8.2.7 Sediment Concentrations

Some limited data are available for both pore water dissolved iron and sediment iron concentrations in Onondaga Lake. The data are summarized in Table 8.10, which also shows the model's calculated annual average concentrations. Sediment iron data are available for 1986 [Yin and Johnson, 1984]. Pore water dissolved iron data are available for August and November 1991 [Cornwall, 1993]. The computed and observed pore water concentrations are in the same order of magnitude and the range is similar. The solid phase comparison is also reasonable when the observed concentrations are corrected for the reactive fraction, as shown.

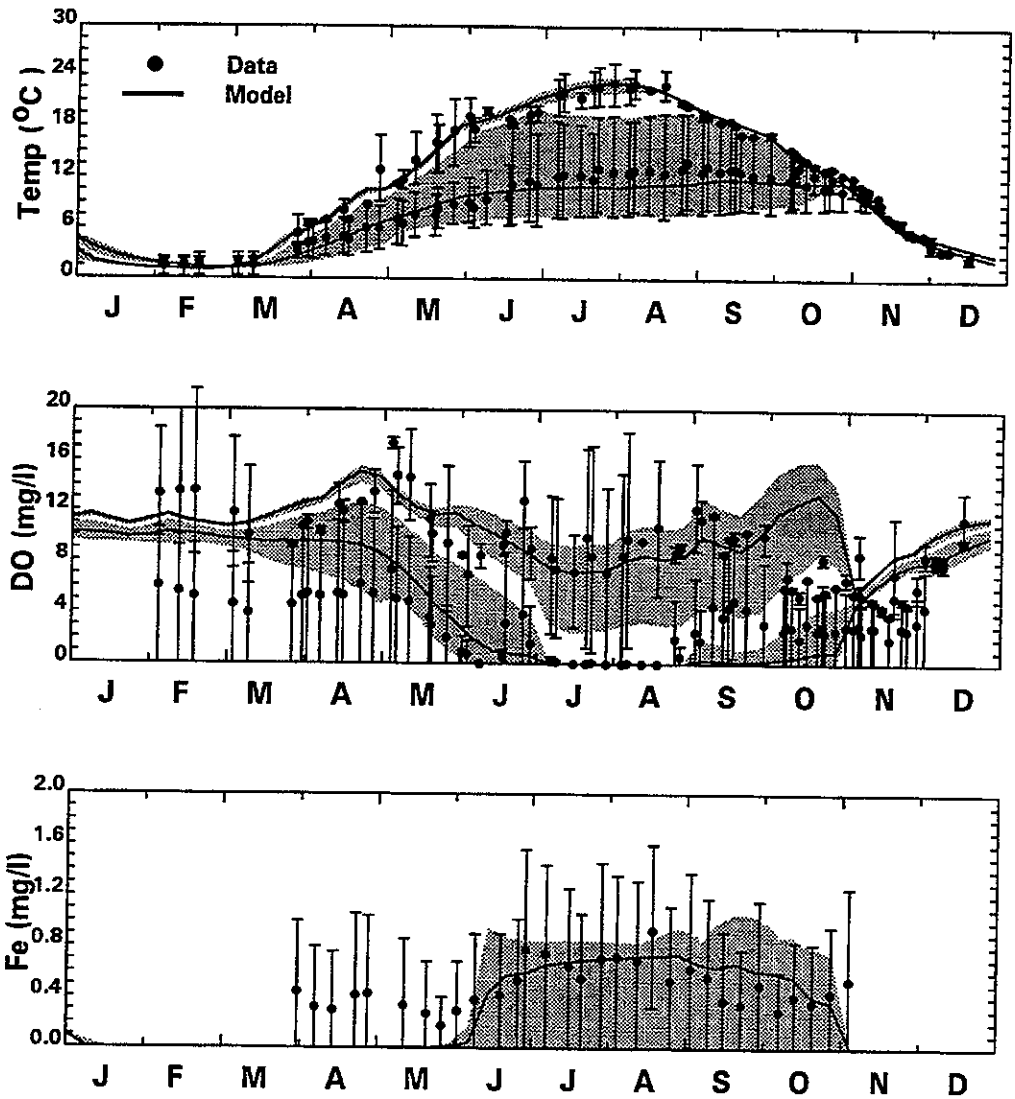

Fig. 8.13 Calibration results for Onondaga Lake using modeled DO. Temporal plot for 1986.

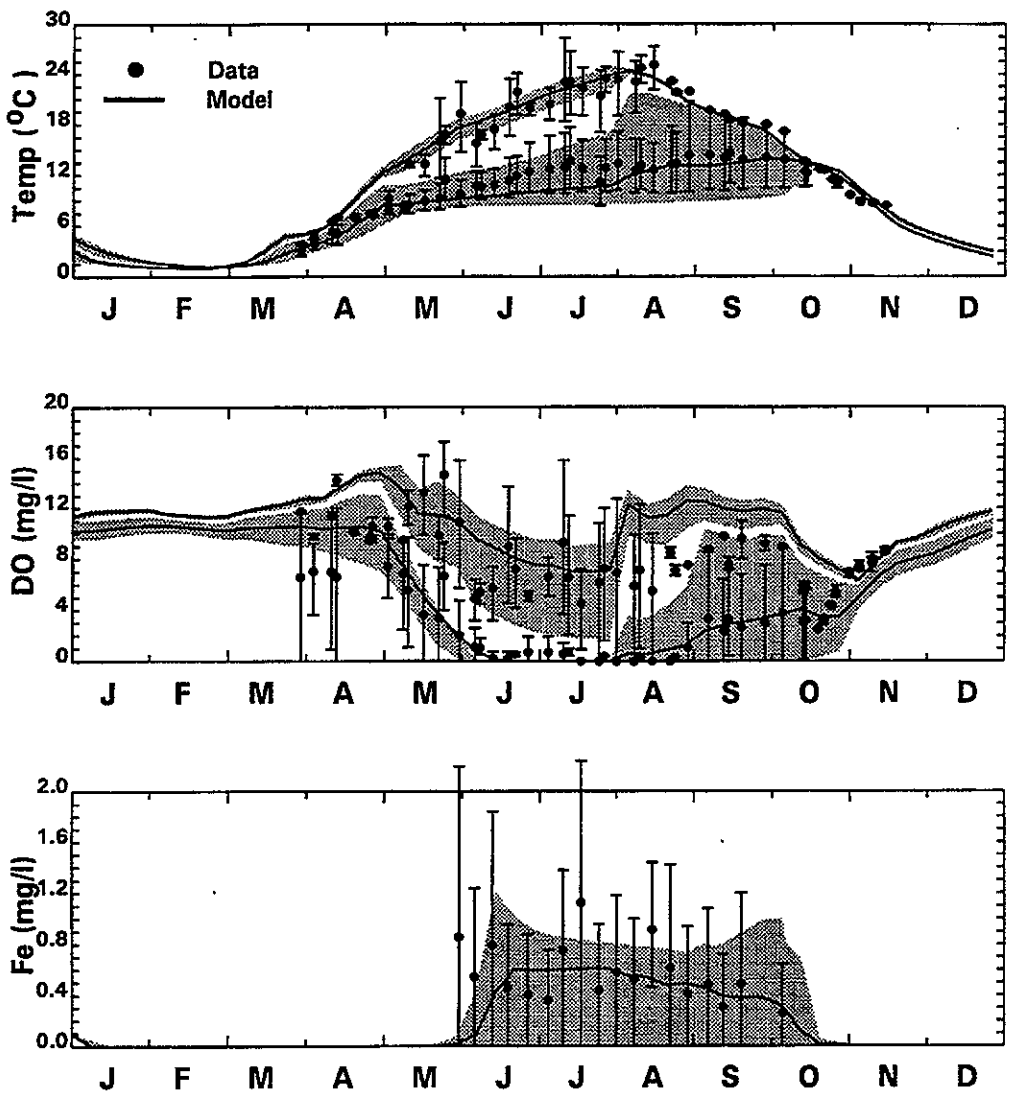

Fig. 8.14 Calibration results for Onondaga Lake using modeled DO. Temporal plot for 1988.

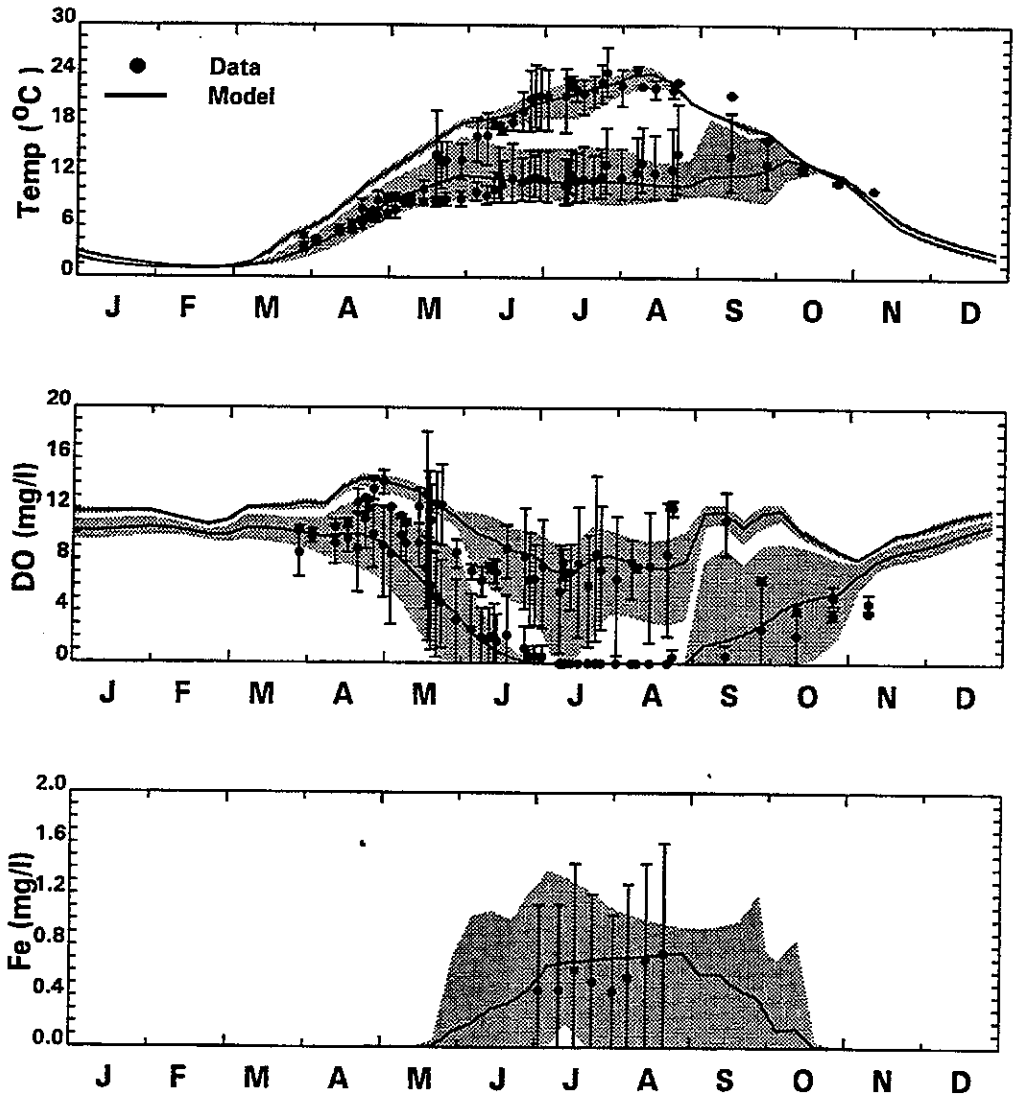

Fig. 8.15 Calibration results for Onondaga Lake using modeled DO. Temporal plot for 1989.

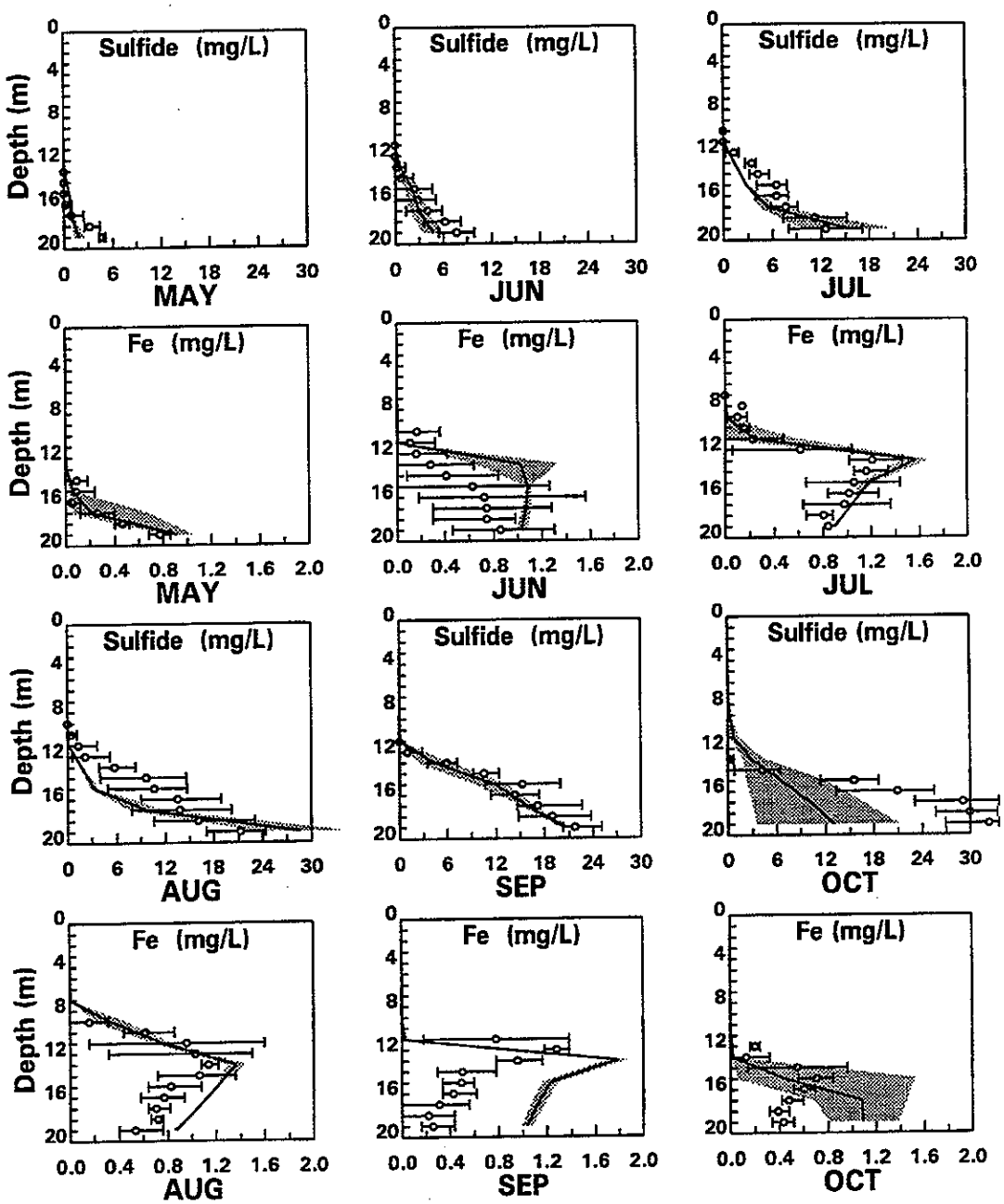

Fig. 8.16 Iron and sulfide calibration for Onondaga Lake. August–October, 1986

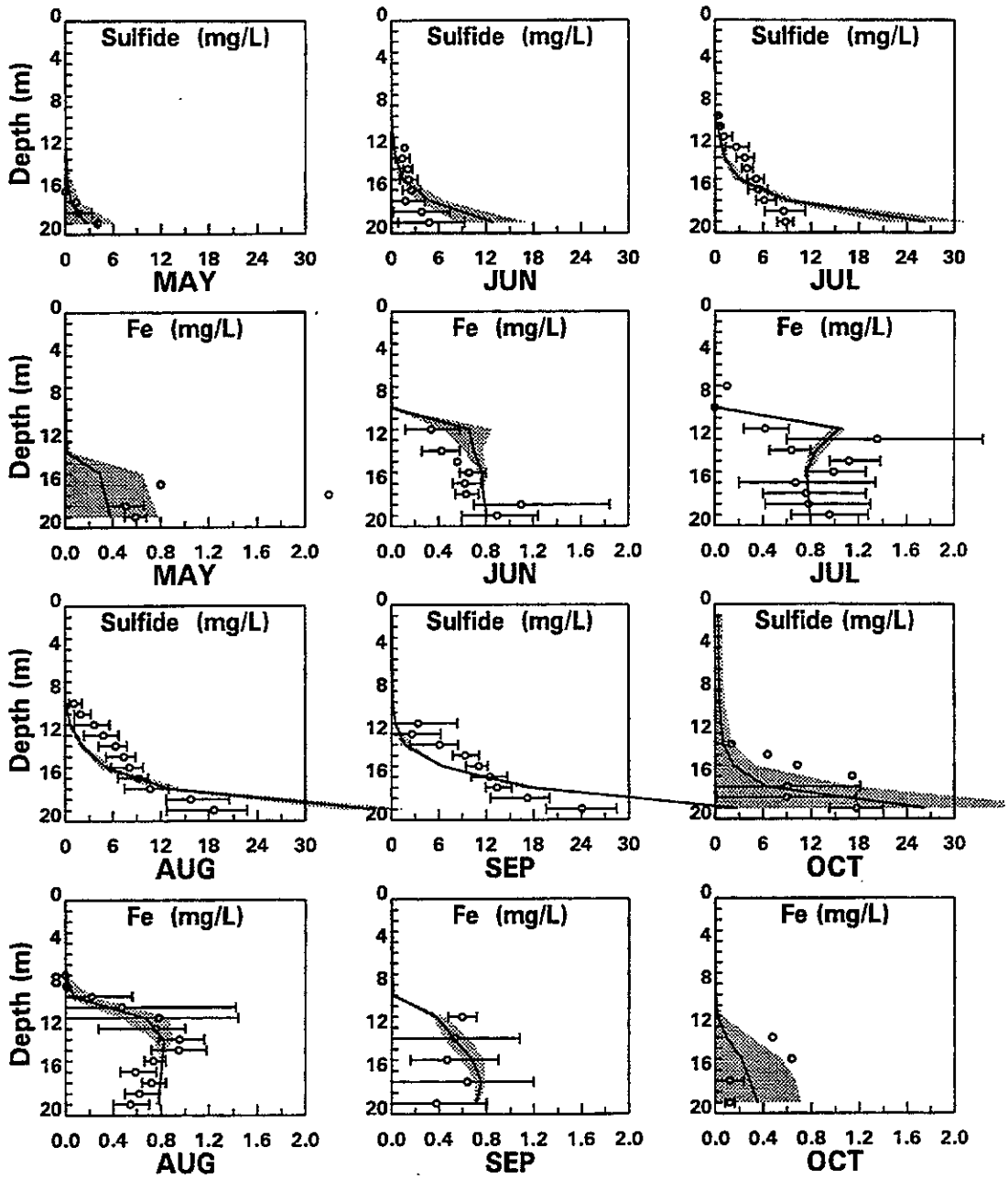

Fig. 8.17 Iron and sulfide calibration for Onondaga Lake. August–October, 1988

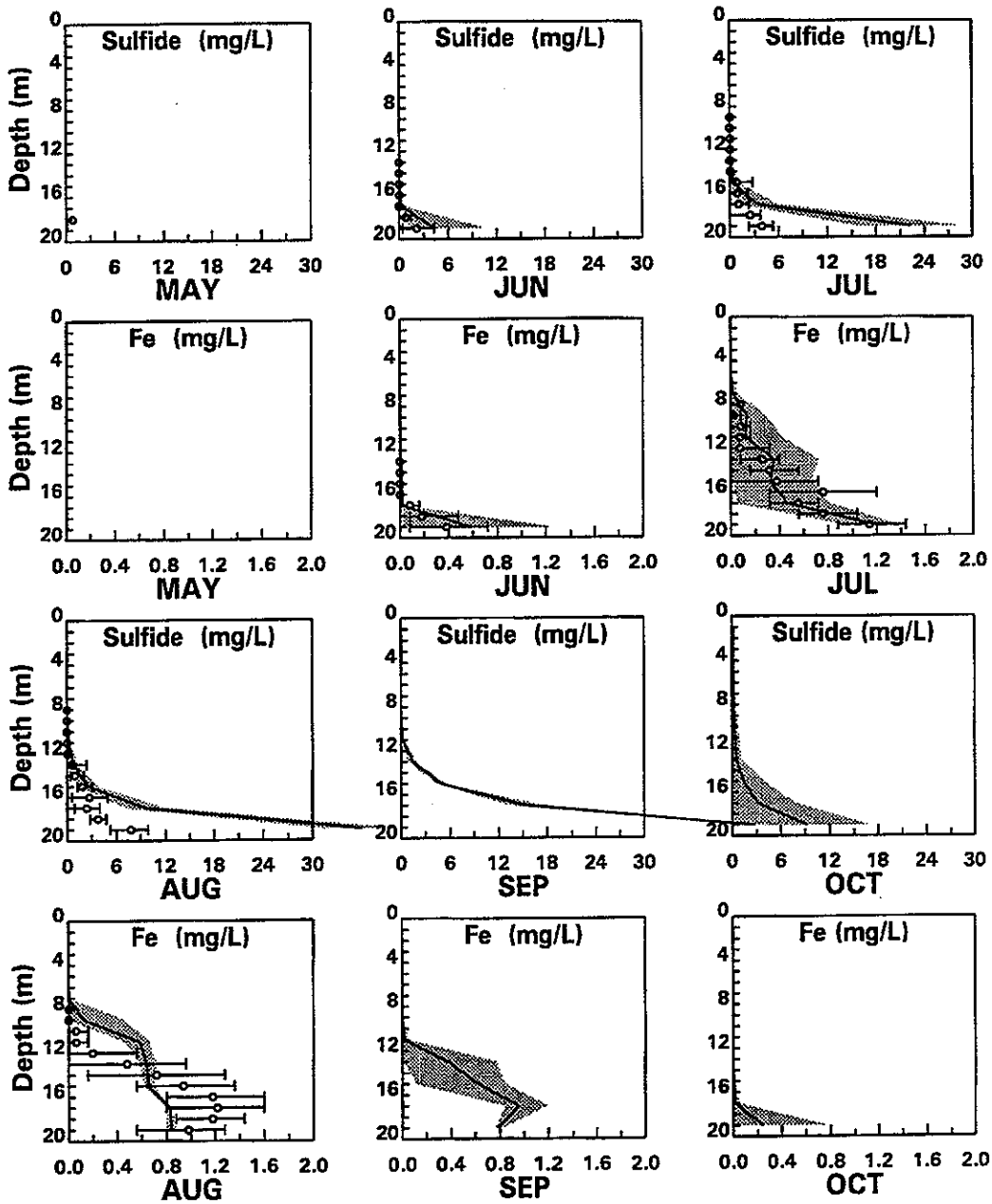

Fig. 8.18 Iron and sulfide calibration for Onondaga Lake. August–October, 1989

Table 8.10 Comparison of observed and computed sediment and pore water iron concentrations: annual average (range)

Phase	Model	Data
Pore water (mg Fe/L)	0.88	0.58
	(0.02–2.78)	(0.13–3.34)
Solid phase (mg Fe/g)	4.0	5.6[a]
	(3.0–5.5)	(3.6–7.8)[a]

[a]Reactive iron is estimated as 40% of total iron consistent with the reactive fraction assumption used to estimate the loading

8.2.8 Summary

The iron sediment and water column model formulated in this chapter can reproduce the available observations of water column and sediment concentrations in Onondaga Lake for three years with reasonable fidelity. The model is initialized to a periodic steady state and then run for 5 years, beginning in 1985 and ending in 1989. The same oxidation and reduction kinetic rate constants are used in both the water column and sediment, consistent with the procedure followed for the manganese model. The seasonal development of the vertical distribution of iron in the water column is correctly reproduced. An initial increase occurs at the sediment-water interface at the beginning of anoxia (March-May 1986), followed by an almost uniform concentration in the hypolimnion (June), and then the development of a maximum concentration at the thermocline (July-Sept.), and the subsequent decline at overturn.

The predicted sulfide concentrations are also in reasonable agreement with observations without any further calibration of the partitioning parameters for sulfide. There does not appear to be any strong evidence for the precipitation of iron sulfide if the criteria used is the discrepancy between model and data. This does not rule out the possibility and, therefore, the addition of this mechanism would be a logical next step. It would also remove the need to specify the partition coefficients for sulfide and iron, thereby removing a degree of freedom from the model.

9

Application to Croton Reservoir

9.1 INTRODUCTION

The eutrophication model for the Croton Reservoir was constructed as a part of a study of the water supply system for the City of New York [Metcalf et al., 1995]. The iron and manganese models developed in this study were incorporated in that model and the results are presented below.

9.1.1 Physical Characteristics

The Croton Reservoir is located approximately 40 miles north-east of New York City, in Westchester and Putnam Counties, in lower New York State. The reservoir represents part of the drinking water supply system for New York City and supplies on average about 140 million gallons per day of drinking water to the city. The Croton Reservoir was created by the impoundment of the Croton River by the New Croton Dam. At the northwest end of the reservoir is the Muscoot Dam which delineates the Muscoot Reservoir. Approximately 4 km upstream from the Croton Dam, in the Croton Reservoir (sometimes called the New Croton Reservoir), is a submerged dam that formed the original Croton Reservoir at this site.

The reservoir is oriented along a southeast-northwest axis, with the New Croton Dam located at the southeast end. A bathymetric map of the Croton Reservoir, which also outlines the model surface segmentation, and sampling sites, is shown in Fig.9.1. The length of the Croton Reservoir is approximately 14.6 km. The maximum depth when full is 36 m. The surface area when full is 92×10^6 ft^2 and the volume when full is 4.14×10^9 ft^3. The average residence time of the Croton Reservoir is 91 days. The direct drainage area is 56 square miles.

At the Muscoot Dam the depth of the Croton Reservoir is about 10 m depending on the water level in the reservoir. The depth increases to 16 m at sampling site 6. Upstream of the submerged dam, at sampling site 5, the depth is 20 m . At site 4, just after the submerged dam, the depth is 24 m. At the New Croton Dam the maximum depth of the reservoir is 40 m.

9.1.1.1 Tributaries Most of the inflow to the Croton Reservoir, 85–90%, comes from the adjoining Muscoot Reservoir. The rest is inflow from tributaries, groundwater

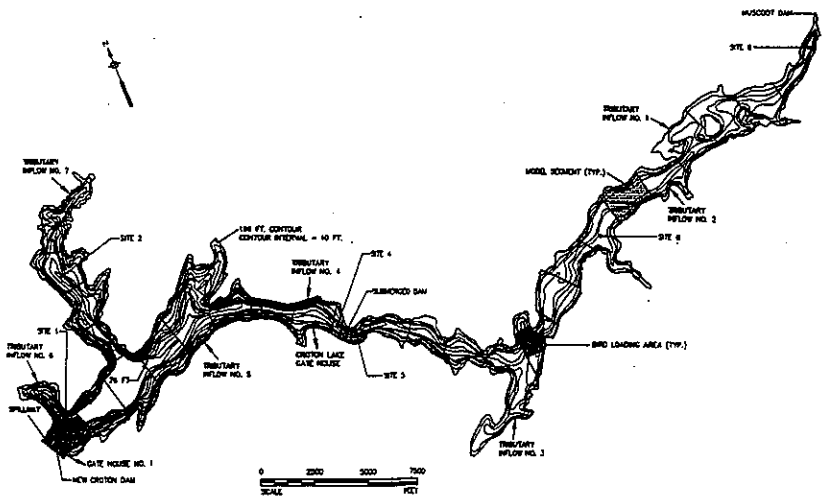

Fig. 9.1 New Croton Resevoir segmentation.

recharge, and surface runoff. The main tributaries are the Kisco River and Hunter Brook. The largest inflows occur in the months January through April. The smallest inflows occur in the months June through September. In order to maintain adequate stream conditions in the Croton River downstream of the reservoir, a minimum outflow of 5.5 MGD is required to be maintained. A summary of the inflow for 1993 is shown in Table 9.1.

9.1.2 Loadings

The nutrient loadings to the Croton reservoir are from the following sources: runoff, wastewater treatment plants, septic systems, atmospheric deposition, and the Muscoot Reservoir inflow. Phosphorus loading is of most interest in the Croton and Muscoot Reservoirs because it is the limiting nutrient. Phosphorus loading from the Muscoot Reservoir for 1993 was estimated to be 42 kg/day. The two tributaries, the Kisco River and Hunter Brook, together contribute an estimated additional 6 kg/day to the Croton Reservoir. Atmospheric deposition is estimated to contribute 0.6 kg/day to the Croton Reservoir.

9.1.3 Water Quality

The Croton reservoir is mesotrophic with intermediate levels of chlorophyll. It is highly stratified in the summer months from June to September with temperature differences exceeding 18°C . In 1993 hypolimnion hypoxia and anoxia at Stations 5 and 6 lasted from June through November. Epilimnion dissolved oxygen concentrations at these

Table 9.1 Inflow To Croton Reservoir in 1993 (MGD)[a]

Month	Muscoot inflow	Runoff	Other tributaries and groundwater
January	472	3	52
February	243	8	53
March	665	22	50
April	796	8	60
May	249	3	31
June	153	7	26
July	126	0	24
August	149	23	27
September	144	11	36
October	198	10	39
November	184	14	34
December	283	26	53
Average	305	11	39

[a] [Metcalf et al., 1995]

stations were above 8 mg/L all year. Table 9.2 shows some relevant water quality data on a seasonal basis for Stations 5 and 6.

Table 9.2 Croton Reservoir water quality overview for Stations 5 and 6 for 1993

Variable	Summer	Winter
Epilimnion Temp (°C)	24	6
Hypolimnion Temp (°C)	7	6
Epilimnion DO (mg/L)	9.0	11
Hypolimnion DO (mg/L)	0.0	11
Chlorophyll a (μg/L)	6.0	3.0
Epilimnion Chlorides (mg/L)	34	34
Hypolimnion Chlorides (mg/L)	34	34
Epilimnion pH	8.5	7.2
Hypolimnion pH	6.7	7.2

9.1.4 Data Sets

Extensive water quality monitoring of the Croton and Muscoot Reservoirs has been carried out by the New York City Department of Environmental Conservation since

1976. The parameters that have been measured include both iron and manganese. The location of the sampling sites is shown on Figure 9.1.

9.1.4.1 Iron and Manganese Two sites in particular have useful iron and manganese data, Stations 5 and 6. Station 5 is located just upstream of the submerged original Croton Dam. Station 6 is located approximately 4.5 km downstream of the Muscoot Reservoir.

For 1993, the data at Stations 5 and 6 was collected monthly from April to December. While many parameters such as dissolved oxygen and temperature were measured at 1 m depths, the sampling protocol for iron and manganese was different. Two grab samples were taken at a site: one sample above the thermocline and one sample below, near the reservoir bottom. Only dissolved iron and manganese were analyzed.

Monthly measurements of total iron and total manganese were made at the tributary inflows to the Muscoot and Croton Reservoirs. These data are used to generate the daily iron and manganese loads to the system. As all tributaries are aerobic, the influent iron and manganese loads are assumed to be particulate concentrations. At present there are no sediment iron or manganese data available at the Croton Reservoir.

9.2 MODEL SETUP

For the model of the Croton and Muscoot Reservoirs the water quality model, RCA, has 34 state variables. The first 32 variables are the same as used in the Onondaga Lake model and are listed in Table 8.5. An additional 2 variables were added for manganese. Like iron, manganese is modeled as dissolved $Mn\,(II)$ and particulate $MnO_2\,(s)$ manganese as in Chapter 7. Both the manganese and iron sediment model, discussed in the previous Chapter 8 are included. This application provides a test of both models.

9.2.1 Manganese Flux Model Equations

The manganese flux model is virtually identical to that applied to the MERL mesocosm data set (Chapter 7). The only change is the addition of the reduction reaction of $MnO_2\,(s)$ to $Mn\,(II)$ if the hypolimnion becomes anoxic. A schematic is presented in Fig.7.2. The equations for the aerobic (1) and anaerobic (2) sediment layers are:

Layer 1 $Mn(II)$:

$$\begin{aligned} H_1\frac{dMn(1)}{dt} &= -s\,(f_{d1}Mn(1) - Mn\,(0)) + K_{L12}(f_{d2}Mn(2) - f_{d1}Mn(1)) \\ &\quad + w_{12}(f_{p2}Mn(2) - f_{p1}Mn(1)) - w_2Mn\,(1) \end{aligned}$$

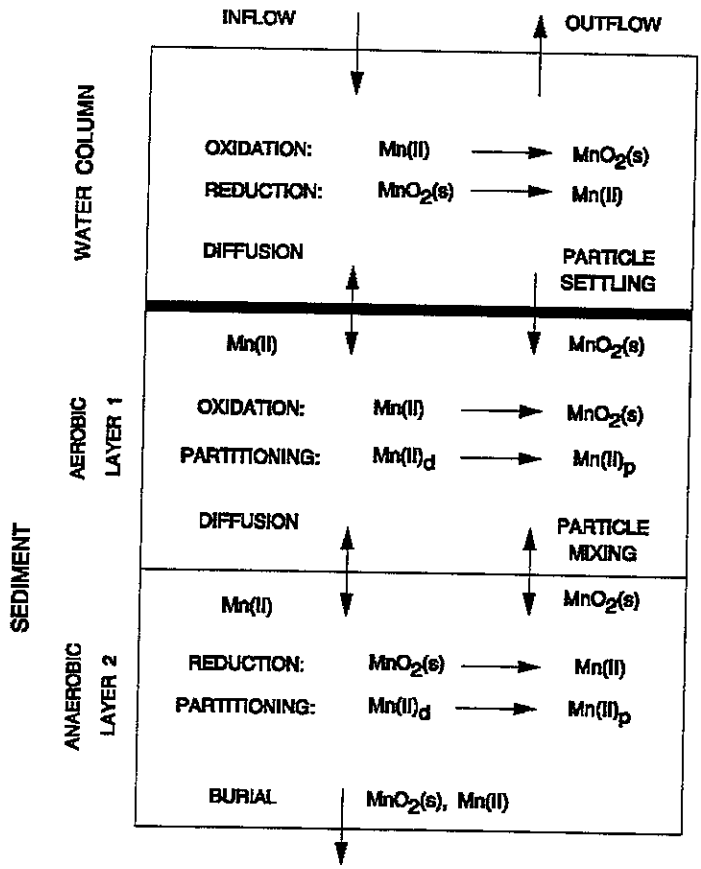

Fig. 9.2 Schematic diagram of the manganese flux model

$$-\frac{\kappa_{Mn,1}^2}{s}\left(10^{2(pH_0-7)}\right)O_2\left(0\right)f_{d1}Mn(1)$$

$$+Mn\left(2\right)\dot{H}_1^+ - Mn\left(1\right)\left(\dot{H}_1+\dot{H}_1^-\right) \tag{9.1a}$$

Layer 2 $Mn(II)$:

$$\begin{aligned} H_2\frac{dMn(2)}{dt} &= -K_{L12}(f_{d2}Mn(2)-f_{d1}Mn(1)) \\ &\quad -w_{12}(f_{p2}Mn(2)-f_{p1}Mn(1))-w_2\left(Mn(2)-Mn(1)\right) \\ &\quad +\kappa_{Mn,2}MnO_2(2)-Mn(2)\left(\dot{H}_2+\dot{H}_1^+\right)+Mn(1)\dot{H}_1^- \end{aligned} \tag{9.1b}$$

Layer 1 $MnO_2\left(s\right)$:

$$H_1\frac{dMnO_2(1)}{dt} = \frac{\kappa_{Mn,1}^2}{s}\left(10^{2(pH_0-7)}\right)O_2\left(0\right)f_{d1}Mn(1)-w_2MnO_2(1)$$

$$+w_{12}(MnO_2(2) - MnO_2(1)) + w_1 MnO_2(0)$$
$$+MnO_2(2)\dot{H}_1^+ - MnO_2(1)\left(\dot{H}_1 + \dot{H}_1^-\right) \tag{9.1c}$$

Layer 2 $MnO_2(s)$:

$$\begin{aligned} H_1 \frac{dMnO_2(2)}{dt} &= -\kappa_{Mn,2} MnO_2(2) \\ &\quad -w_{12}(MnO_2(2) - MnO_2(1)) - w_2(MnO_2(2) - MnO_2(1)) \\ &\quad -MnO_2(2)\left(\dot{H}_2 + \dot{H}_1^+\right) + MnO_2(1)\dot{H}_1^- \end{aligned} \tag{9.1d}$$

where $MnO_2(0)$ and $Mn(0)$ refer to the particulate and dissolved manganese concentrations in the bottom most water column segment, designated as segment 0, which overlays the sediment.

The water column equations for manganese for this segment are
Layer 0 $Mn(II)$:

$$\begin{aligned} H_0 \frac{dMn(0)}{dt} &= s(f_{d1} Mn(1) - Mn(0)) - \kappa_{Mn,0}\left(10^{2(pH_0-7)}\right) O_2(0)\, Mn(0) \\ &\quad +k_{Mn,0} H_0 \frac{K_{M,Mn,0}}{K_{M,Mn,0} + [O_2(0)]} MnO_2(0) \\ &\quad +E_{0,-1}(Mn(-1) - Mn(0)) \end{aligned} \tag{9.1e}$$

Layer 0 $MnO_2(s)$:

$$\begin{aligned} H_0 \frac{dMnO_2(0)}{dt} &= \kappa_{Mn,0}\left(10^{2(pH_0-7)}\right) O_2(0)\, Mn(0) + w_1(MnO_2(-1) - MnO_2(0)) \\ &\quad -k_{Mn,0} H_0 \frac{K_{M,Mn,0}}{K_{M,Mn,0} + [O_2(0)]} MnO_2(0) \\ &\quad +E_{0,-1}(MnO_2(-1) - MnO_2(0)) \end{aligned} \tag{9.1f}$$

where $k_{Mn,0}$ is the rate at which $MnO_2(s)$ is reduced to $Mn(II)$; $K_{M,Mn,0}$ is the half saturation constant for oxygen for this reaction; and $E_{0,-1}$ represents the vertical mixing coefficient between the bottom layer and the layer immediately above. The concentrations in the water column are numbered in reverse order to preserve the notation used previously. Thus layer -1 refers to the layer just above layer 0 in the water column. The remaining portions of the sediment model—the nutrient and oxygen components—are identical to those used above.

9.2.2 Model Segmentation for Croton and Muscoot Reservoirs

The surface segmentation for the Croton and Muscoot model is shown in Figure 9.1. The model has 55 surface segments, 32 in the Croton Reservoir and 23 in the Muscoot. Vertically the model has 10 layers and uses a stretching coordinate system to adjust the layer depth to fit the varying bathymetry.

9.2.3 Model Calculations and Results

9.2.3.1 Dissolved Oxygen It is critical that the timing of the onset of anoxia be calculated correctly since this event triggers the release of iron and manganese from the sediment. As with the Onondaga Lake application, it was decided that actual dissolved oxygen data would be used to specify when anoxia was present. This allows us to examine how the iron and manganese model would perform if the eutrophication-dissolved oxygen model was perfectly calibrated to the dissolved oxygen data.

9.2.3.2 Calibration Scenario The model was run for 1993, beginning January 1 to December 31, a total of 365 days. In order to ensure that the sediment had reached a steady state the model was cycled for several years before using the results as the calibration output.

The values of the constants used for the nutrients and oxygen sediment model are given below in Table 9.5 The values of the constants used for the iron and manganese models in the water column and sediment are given below in Tables 9.3 and 9.4. The nutrients, oxygen, and iron model values are identical to those used for Onondaga Lake with one exception noted below.

9.2.4 Calibration Results

As mentioned previously, the iron and manganese data for Croton Reservoir consisted of samples at two depths, which were collected approximately once a month. One sample was taken in the epilimnion, which was always oxic and hence yielded negligible dissolved iron and manganese. The hypolimnion sample was taken near the bottom. Therefore no comparison can be made to the computed vertical profile.

Figure 9.3 shows the calibration results for site 5. The surface and bottom model (lines) and data(symbols) are shown for temperature and dissolved oxygen. The bottom dissolved iron and dissolved manganese concentrations are compared to the model computations in the bottom-most layer of the model. The extended period of anoxia is clearly evident, from early June until early November. For these simulations the observed time for the both onset and end of anoxic was used to correct the bottom layer dissolved oxygen computed by the model.

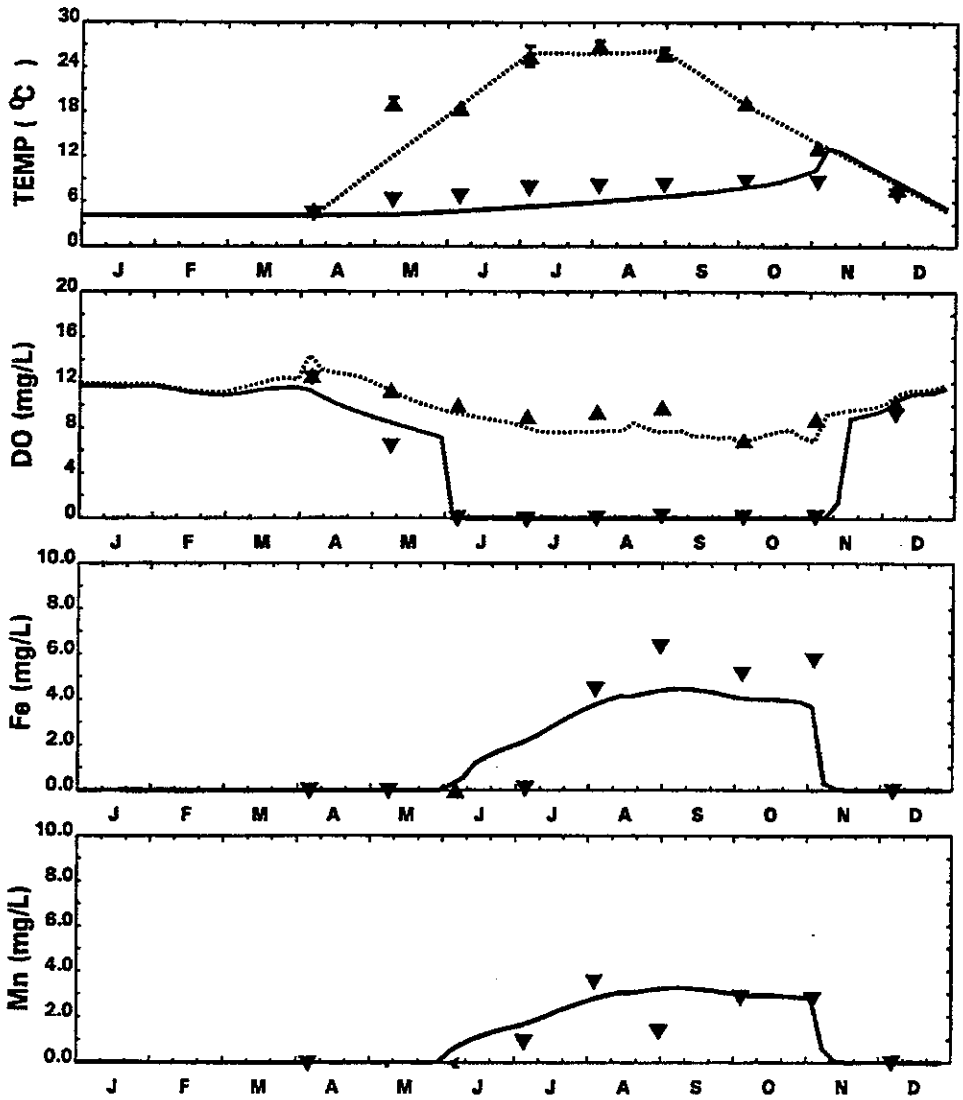

Fig. 9.3 Croton resevoir site 5 iron and manganese calibration, 1993.

Table 9.3 Constants for the iron flux model – Croton Reservoir

Name	Value	Unit	Description
		Water Column	
$k_{Fe,1}$	10.0	day^{-1}	Oxidation rate
$\theta_{Fe,1}$	1.08	–	Temperature coefficient
$k_{Fe,2}$	4.0	day^{-1}	Reduction rate
$K_{M,Fe,2}$	0.2	mg O_2/L	Oxidation half saturation constant
		Sediment	
$\Delta\pi_{Fe,1}$	15.0	L/kg	Aerobic layer partition coefficient
$\pi_{Fe,2}$	100.0	L/kg	Anaerobic layer partition coefficient
$O_{2,Crit,Fe}$	2.0	mg/L	Partition coefficient half saturation constant
$k_{Fe,1}$	10.0	day^{-1}	Aerobic layer oxidation rate
$\theta_{Fe,1}$	1.08		Temperature coefficient
$k_{Fe,2}$	4.0	day^{-1}	Anaerobic layer reduction rate
$\theta_{Fe,2}$	1.08		Temperature coefficient

The iron data shows very large Fe^{2+} concentrations during anoxia, between 4 and 6 mg/L. The results for site 6, which are shown in Figure 9.4, show markedly lower iron concentrations, $\sim$ 1 mg/L for July and August, but $\sim$ 4 mg/L for early September. By comparison, Onondaga Lake bottom iron concentrations were $\lesssim$ 1 mg/L.

In order to reproduce this difference, it is necessary to understand what controls the maximum hypolimnion iron concentration. The following observation is useful. Within $\sim$ 14 days from the onset of anoxia, the bottom concentration will be approximately the same as the pore water iron concentration. For Onondaga Lake this was $\sim$ 1 mg/L. Hence, in order for the model to calculate 4 mg/L in the bottom layer of the Croton reservoir, the sediment partition coefficient for iron must be reduced in order to increase the pore water iron concentration. The results, which are shown in Figures 9.3 and 9.4, was achieved by changing the anaerobic layer partition coefficient from $\pi_{Fe,2} = 3000$ L/kg, which was used for Onondaga Lake, to $\pi_{Fe,2} = 100$ L/kg.

It is not clear why the pore water iron concentration in the Croton reservoir is larger, and the partition coefficient is lower, than in Onondaga Lake. This is the principle drawback associated with using an empirical partition coefficient in the sediment flux model to determine the pore water-solid phase speciation . There is no guarantee that it, or any other of the partition coefficients used in the model, are transferable from one application to another.

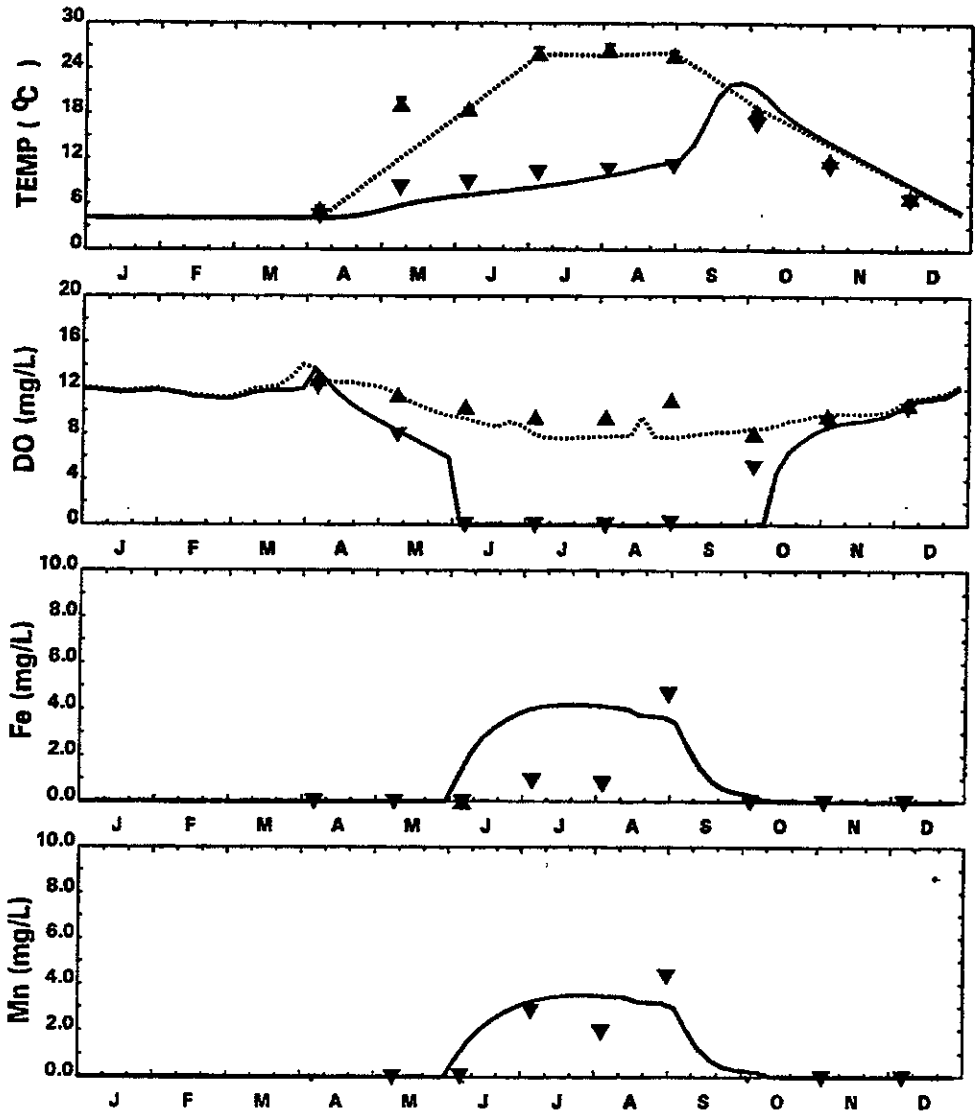

Fig. 9.4 Croton resevoir site 6 iron and manganese calibration, 1993.

Table 9.4 Constants for the manganese flux model – Croton Reservoir

Water Column			
Name	Value	Unit	Description
$k_{Mn,1}$	10.0	day^{-1}	Oxidation rate
$\theta_{Mn,1}$	1.08	–	Temperature coefficient
$k_{Mn,2}$	4.0	day^{-1}	Reduction rate
$K_{M,Mn,2}$	0.2	mg O_2/L	Oxidation half saturation constant
Sediment			
$\Delta\pi_{Mn,1}$	200.0	L/kg	Aerobic layer partition coefficient
$\pi_{Mn,2}$	8000.	L/kg	Anaerobic layer partition coefficient
$O_{2,Crit,Mn}$	2.0	mg/L	Partition coefficient half saturation constant
$k_{Mn,1}$	0.01	day^{-1}	Aerobic layer oxidation rate
$\theta_{Mn,1}$	1.08	–	Temperature coefficient
$k_{Mn,2}$	4.0	day^{-1}	Anaerobic layer reduction rate
$\theta_{Mn,2}$	1.08		Temperature coefficient

The manganese concentrations, by contrast, are about the same at site 5 and site 6. As can be seen, the model produces a good fit to the data with no need for further adjustments.

9.3 SUMMARY

The Croton reservoir was used as a field test of the iron and manganese model because data are available and the eutrophication model had been developed previously. The model was run for 1993, after equilibrating the sediment. The calibration for iron involved changing the anaerobic layer sediment partition coefficient from the value used for Onondaga Lake in order to compute the higher iron concentrations observed in the Croton reservoir. This difference in dissolved iron between the two lakes is unexplained at present. The calibrated manganese model was able to reproduce the observed data without any further adjustments.

Table 9.5 Sediment Model Parameters for the Croton Reservoir

m_1 (kg/L) 0.5	m_2 (kg/L) 0.5	w_2 (m/d) 6.85×10^{-6}	H_2 (m) 0.10		
D_d (m^2/d) 5.0E-03	θ_{D_d} – 1.08	D_p (m^2/d) 1.2×10^{-4}	θ_{D_p} – 1.15	D_{d0} (m^2/d) 1.0×10^{-4}	$\theta_{D_{d0}}$ – 1.08
$\kappa_{NH_4,1}$ (m/d) 0.2	π_{NH_4} (L/kg) 1.00	θ_{NH_4} – 1.123	K_{M,NH_4} (mg N/L) 0.728	$\theta_{K_{M,NH_4}}$ – 1.125	K_{M,NH_4,O_2} (mg O_2/L) 0.74
$\kappa_{NO_3,1}$ (m/d) 0.15	$\kappa_{NO_3,2}$ (m/d) 0.25	θ_{NO_3} – 1.080			
$\kappa_{H_2S,d1}$ (m/d) 0.2	$\kappa_{H_2S,p1}$ (m/d) 0.4	$\pi_{H_2S,1}$ (L/kg) 100.0	$\pi_{H_2S,2}$ (L/kg) 100.0	θ_{H_2S} – 1.15	K_{M,H_2S,O_2} (mg O_2/L) 4.0
k_{Si} (/d) 0.5	$[\mathrm{Si}]_{sat}$ (mg Si/L) 30.	$\Delta\pi_{\mathrm{Si},1}$ – 6.0	$\pi_{\mathrm{Si},2}$ (L/kg) 175.0	θ_{Si} – 1.100	$K_{M,P\mathrm{Si}}$ (mg Si/L) 5.0×10^4
$\Delta\pi_{PO_4,1}$ – 65.0	$\pi_{PO_4,2}$ (L/kg) 225.0	$O_2(0)_{\pi,PO_4}$ (mg O_2/L) 2.0	K_{M,D_p,O_2} (mg O_2/L) 4.0	$O_2(0)_{\pi,\mathrm{Si}}$ (mg O_2/L) 1.0	

Bibliography

Aller, R. (1980a). Diagenetic processes near the sediment-water interface of Long Island Sound. I. Decomposition and nutrient element geochemistry (S, N, P). In Saltzman, B., editor, *Estuarine Physics and Chemistry: Studies in Long Island Sound. Advances in Geophysics*, pages 237–350. Academic Press, New York.

Aller, R. (1980b). Diagenetic processes near the sediment-water interface of Long Island Sound. II. Fe and Mn. In Saltzman.B., editor, *Estuarine Physics and Chemistry: Studies in Long Island Sound. Advances in Geophysics*, pages 351–415. Academic Press, New York.

Aller, R. C. and Yingst, J. Y. (1980). Relationships between microbial distributions and the anaerobic decomposition of organic matter in surface sediment of Long Island Sound, USA. *Mar. Biol.*, 56:29–42.

Baes, C. F. and Mesmer, R. E. (1976). *The Hydrolysis of Cations.* Wiley, New York.

Brezonik, P. (1994). *Chemical Kinetics and Process Dynamics in Aquatic Systems.* CRC Press, Inc., Boca Raton, Florida.

Bricker, O., Matisoff, G., and Holdren, G. (1977). Interstitial water chemistry of Chesapeake Bay sediments. Basic data report No.9. Technical report.

Butler, J. (1991). *Carbon Dioxide Equilibria and Their Applications.* Lewis Publishers, Inc., Chelsea, Mich.

Canfield, D. E. (1989). Reactive iron in marine sediments. *Geochim. Cosmochim. Acta*, 53:619–632.

Chapra, S. (1997). *Surface Water-Quality Modeling.* McGraw-Hill, New York.

Cornwall, J. (1993). Preliminary data for onondaga lake sediment process study. *Personal Communication.*

Di Toro, D. and Fitzpatrick, J. (1993). Chesapeake Bay sediment flux model. Contract report EL-93-2.

Di Toro, D., Fitzpatrick, J., and Thomann, R. (1981). Documentation for water quality analysis simulation program (WASP) and model verification program (MVP). Epa-600-3-81-044.

Di Toro, D. M. (1976). Combining chemical equilibrium and phytoplankton models - a general methodology. In *Modeling Biochemical Processes in Aquatic Ecosystems*, pages 233–256. Ann Arbor Science Press, Ann Arbor, Mich.

Di Toro, D. M. (1985). A particle interaction model of reversible organic chemical sorption. *Chemosphere*, 14(10):1503–1538.

Dortch, M. and Hamlin Tillman, D. (1995). Disappearance of reduced manganese in reservoir tailwaters. *J. Environ. Engr.*, 121(4):287–297.

Dzombak, D. A. and Morel, F. M. M. (1990). *Surface Complexation Modeling. Hydrous Ferric Oxide.* John Wiley & Sons, New York, NY.

Effler, S. (1996). *Limnological and Engineering Analysis of a Polluted Urban Lake.* Springer-Verlag, New York.

Emerson, S., Jacobs, L., and Tebo, B. (1983). The behavior of trace metals in marine anoxic waters: Solubilities at the oxygen-hydrogen sulfide interface. In C.S. Wong, E. Boyle, K. B. and Burton, J., editors, *Trace Metals in Sea Water*, pages 579–608. Plenium Press, 'New York.

Gschwend, P. M. and Wu, S. (1985). On the constancy of sediment-water partition coefficients of hydrophic organic pollutants. *Environ. Sci. Technol.*, 19(1):90.

Hamming, R. (1962). *Numerical Methods for Scientists and Engineers.* McGraw-Hill Book Company, Inc., New York.

Holdren, Jr., G. (1977). *Distribution and behavior of manganese in the interstitial waters of Chesapeake Bay sediments during early diagenesis.* PhD thesis.

Holdren, Jr., G., Bricker, O., and Matisoff, G. (1975). A model for the control of dissolved manganese in the interstitial waters of Chesapeake Bay. In Church, T., editor,

Marine chemistry in the coastal environment, pages 364–381. ACS Symposium ser. 18, Am. Chem. Soc., Washington, DC.

Hunt, C. and Kelly, J. (1988). Manganese cycling in coastal regions: Response to eutrophication. *Est. Coast. and Shelf Sci.*, 26:527–558.

HydroQual, I. (1992). User's guide for RCA. Release 2.0. Technical report.

Jahnke, R., Craven, D., and Gaillard, J.-F. (1994). The influence of organic matter diagenesis on $CaCO_3$ dissolution at the deep-sea floor. *Geochim. Cosmochim. Acta*, 58(13):2799–2809.

Jaquet, J., Nembrini, G., Garcia, P., and Vernet, J. (1982). The manganese cycle in Lac Leman, Switzerland: The role of metallogenium. *Hydrobiol.*, 91:323–340.

Jenne, E. (1968). Controls on Mn, Fe, Co, Ni, Cu, and Zn concentration in soils and water: The significant role of hydrous Mn and Fe oxides. In Baker, R., editor, *Tracd Inorganics in Water*, volume Adv. Chem. Ser. 73. American Chemical Society, Washington DC.

Kelly, J., Berounsky, V., Nixon, S., and Oviatt, C. (1985). Benthic-pelagic coupling and nutrient cycling across and experimental eutrophication gradient. *Marine Ecology Progress Series*, 26:207–219.

Lindsay, W. L. (1979). *Chemical Equilibria in Soils.* J. Wiley & Sons, New York,N.Y.

Loewenthal, R. and Marais, G. (1976). *Carbonate Chemistry of Aquatic Systems: Theory & Application.* Ann Arbor Science, Ann Arbor, Mich.

Macsyma (1993). Macsyma. Technical report.

Mahony, J., Di Toro, D., Gonzalez, A., Curto, M., Dilg, M., De Rosa, L., and Sparrow, L. (1996). Partitioning of metals to sediment organic carbon. *Environ. Toxicol. Chem.*, 15(12):2187–2197.

Metcalf, Eddy, I. H., and Sawyer, P. (1995). The Croton water treatment plant at Jerome Park reservoir. Appendix E. Volume II. Technical report.

Morel, F. M. M. (1983). *Principles of Aquatic Chemistry.* J. Wiley & Sons, New York, N.Y.

Morgan, J. (1967). Chemical equilibria and kinetic properties of manganese in natural water. In Faust, S. and Hunter, J., editors, *Principles and Applications of Water Chemistry.* J. Wiley, New York.

Morse, J. and Mackenzie, F. (1990). *Geochemistry of Sedimentary Carbontes.* Elsevier, New York.

Nixon, S., Oviatt, C., Frithsen, J., and Sullivan, B. (1986). Nutrients and the productivity of estuarine and coastal marine ecosystems. *J. Limnol. Soc. Sth. Afr.*, 12(1/2):43–71.

Pankow, J. F. (1979). *The Dissolution Rates and Mechanisms of Tetragonal Ferrous Sulfide (Mackinawite) in Anoxic Aqueous Systems. Ph.D. Thesis.* California Institute of Technology, Pasadena, CA.

Press, W., Flannery, B., Teukolsky, S., and Vetterling, W. (1989). *Numerical Recipes. The Art of Scientific Computing. (FORTRAN Version).* Cambridge University Press, New York, NY.

Schnoor, J. (1996). *Environmental Modeling.* John Wiley & Sons, New York.

Stumm, W. and Morgan, J. (1981). *Aquatic Chemistry.* John Wiley & Sons, New York.

Stumm, W. and Morgan, J. (1996). *Aquatic Chemistry. Chemical Equilibria and Rates in Natural Waters.* John Wiley & Sons, New York.

Stumm, W. and Morgan, J. J. (1970). *Aquatic Chemistry.* J. Wiley & Sons, New York.

Sundby, D., Anderson, L. G., Hall, P. O. J., Iverfeldt, A., Rutgers, L., Michiel, M., and Westerlund, S. F. G. (1986). The effect of oxygen on release and uptake of cobalt, manganese, iron and phosphate at the sediment-water interface. *Geochim. Cosmochim. Acta*, 50(6):1281–1288.

Thomann, R. and Mueller, J. (1987). *Principles of Surface Water Quality Modeling and Control.* Harper & Row, New York, NY.

Walker, W. (1991). Compilation and review of Onondaga lake water quality data. Technical report.

Westall, J. and Hohl, H. (1980). A comparison of electrostatic models for the oxide/solution interface. *Adv. Colloid Interface Sci.*, 12:265–294.

Yin, C. and Johnson, D. (1984). Sedimentation and particle class balances in onondaga lake. *Limnol. Oceanogr.*, 29:1193–1201.

REPORT DOCUMENTATION PAGE

Form Approved
OMB No. 0704-0188

Public reporting burden for this collection of information is estimated to average 1 hour per response, including the time for reviewing instructions, searching existing data sources, gathering and maintaining the data needed, and completing and reviewing the collection of information. Send comments regarding this burden estimate or any other aspect of this collection of information, including suggestions for reducing this burden, to Washington Headquarters Services, Directorate for Information Operations and Reports, 1215 Jefferson Davis Highway, Suite 1204, Arlington, VA 22202-4302, and to the Office of Management and Budget, Paperwork Reduction Project (0704-0188), Washington, DC 20503.

1. AGENCY USE ONLY ***(Leave blank)***

2. REPORT DATE
September 1998

3. REPORT TYPE AND DATES COVERED
Final report

4. TITLE AND SUBTITLE
Sediment Flux Model for Manganese and Iron

5. FUNDING NUMBERS
Work Unit No. 32694

6. AUTHOR(S)
Dominic DiToro, Scott Lowe, James Fitzpatrick, Richard Isleib

7. PERFORMING ORGANIZATION NAME(S) AND ADDRESS(ES)
HydroQual, Inc.
One Lethbridge Plaza
Mahwah, NJ 07430

8. PERFORMING ORGANIZATION REPORT NUMBER

9. SPONSORING/MONITORING AGENCY NAME(S) AND ADDRESS(ES)
U.S. Army Corps of Engineers, Washington, DC 20314-1000
U.S. Army Engineer Waterways Experiment Station
3909 Halls Ferry Road, Vicksburg, MS 39180-6199

10. SPONSORING/MONITORING AGENCY REPORT NUMBER
Contract Report W-98-1

11. SUPPLEMENTARY NOTES
Available from National Technical Information Service, 5285 Port Royal Road, Springfield, VA 22161.

12a. DISTRIBUTION/AVAILABILITY STATEMENT
Approved for public release; distribution is unlimited.

12b. DISTRIBUTION CODE

13. ABSTRACT ***(Maximum 200 words)***

Iron and manganese were installed as state variables in a previously developed sediment diagenesis model. The comprehensive model now incorporates nutrients, oxygen and sulfide, and iron and manganese. The model was initially calibrated using long-term mesocosm data. The mesocosms contained water and sediments removed from Narragansett Sound, an estuarine environment. Validation of the model was conducted using in situ data from two freshwater systems, Onondaga Lake and Croton Reservoir.

14. SUBJECT TERMS
Iron, Manganese, Model, Sediments

15. NUMBER OF PAGES
172

16. PRICE CODE

17. SECURITY CLASSIFICATION OF REPORT
UNCLASSIFIED

18. SECURITY CLASSIFICATION OF THIS PAGE
UNCLASSIFIED

19. SECURITY CLASSIFICATION OF ABSTRACT

20. LIMITATION OF ABSTRACT